

# Authigenic carbonates of the South China Sea Archives for geochemical cycling and geodynamic activity

Dissertation

zur Erlangung des

Doktorgrades der Naturwissenschaften

Doctor rerum naturalium

(Dr. rer. nat.)

am Fachbereich Geowissenschaften

der Universität Bremen

vorgelegt von

Yiting Tseng

Bremen, 2022



## **Gutachter**

Prof. Dr. Gerhard Bohrmann  
Universität Bremen

MARUM – Zentrum für Marine Umweltwissenschaften  
Klagenfurter Strasse 2–4  
28359 Bremen, Deutschland

Dr. habil. Ingo Klaucke  
GEOMAR | Helmholtz-Zentrum für Ozeanforschung Kiel  
Gebäude 8/C, Ostufer  
Wischhofstraße 1-3  
24148 Kiel, Deutschland

Datum des Kolloquiums: 18 November 2022





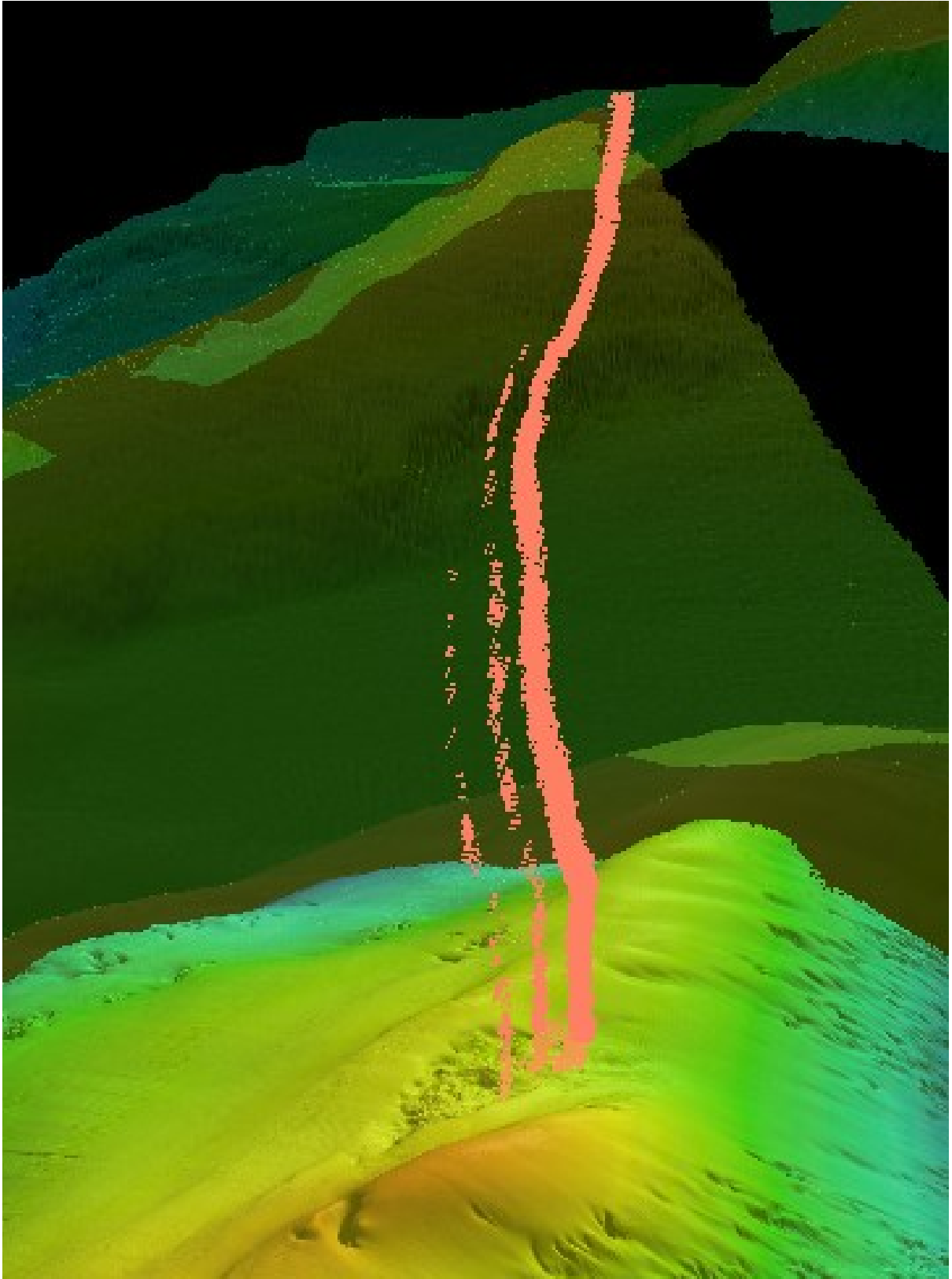
*„Es gibt kein schlechtes Wetter, nur schlechte Kleidung.“*

German Folk



## Erklärung

Hiermit versichere ich, Yiting Tseng, die vorliegende Arbeit ohne Hilfe Dritter und nur mit den angegebenen Quellen und Hilfsmitteln angefertigt zu haben. Alle Stellen, die Quellen entnommen wurden, sind als solche kenntlich gemacht worden. Diese Arbeit hat in gleicher oder ähnlicher Form noch keiner Prüfungsbehörde vorgelegen. In der abgegebenen Arbeit stimmen die schriftliche und elektronische Fassung überein.



*Perspective view (to the north) of Yam Seep on Four-Way Closure Ridge (FWCR) at water depth ~1400m in the South China Sea. The rough seafloor of Yam Seep is situated at the northern summit of FWCR. Gas flares (orange color) rise from the eastern flank of Yam Seep reaching 550 m above the seafloor.*

## Preface

3<sup>rd</sup> December 2018, shortly after “Mahlzeit” (lunch break) on RV Sonne, the calling of scientists to come to the deck was announced as the drilling ware MeBo was coming back on deck. After only a few hours of drilling, the video playback showed the gas bubbles gradually blocking the camera, from a few rising bubbles to a massive escape of bubble streams. Back on deck, core MeBo-24 was pulled out from the drilling liner. Through the transparent core liner, the 5-meter carbonate core consisting of grey, white, and pink colours appeared in front of us. Many of the scientist including me had not seen another similar core like MeBo-24 before. This core and the seep area became the “rock” of my PhD study in the next four year (2018-2022).

Methane-derived carbonates are crucial for archiving seepage episodes in the past and present. Methane seepage occurring at continental margins is one of the most important windows for buried carbon re-entering the hydrosphere. Under certain pressure and temperature conditions, methane migrating to and within subsurface forms gas hydrate. Gas hydrate is an ice-like compound, largely occurring in oceans, lakes, or permafrost regions, and considered important for many reasons. The vulnerability of gas hydrate is that it might dissociate under variations of temperature and sea level. With 1 m<sup>3</sup> of gas hydrate, a maximum of 164 m<sup>3</sup> of sequestered methane can be measured at standard temperature and pressure. It is on one side a potential geohazard as it might release great amounts of greenhouse gas. On the other side, if only a small amount of methane hydrate occurs in an extractable concentration, it might provide a significant energy resource. Moreover, the interplay of gas hydrates and authigenic carbonates at cold seeps reshape the seafloor and the subsurface morphology which leads to the discussion of seepage episode related to climatic changes. I investigated Four-Way Closure Ridge since 2013 funded by National Energy Program, Taiwan focusing on the gas hydrate survey and pore water chemistry, seepage and early sediment diagenesis. Since 2018, a scholarship of the German Academic Exchange Service (DAAD) allowed me to conduct the project for this PhD thesis “Authigenic carbonates of the South China Sea – archives for geochemical cycling and geodynamic activity”. The authigenic carbonate core providea an excellent archive for chronology and environmental proxies. I realized that I have not left Four-Way Closure Ridge for almost a decade. In ten years’ time, I have not only gone deep into it but also travelled in the time dimension of up to ~40 thousand years to resolve the history of Yam Seep at Four-Way Closure Ridge.

## Table of contents

Preface .....	ii
Table of contents .....	iii
Table of Abbreviations .....	v
Abstract .....	vi
Outline and contributions to manuscripts.....	ix
1. Introduction .....	1
1.1. Cold seeps and their role in the global carbon cycle.....	1
1.2. Occurrence of gas hydrate and their climate interaction.....	3
1.3. Seepage manifestations and investigations .....	5
1.4. Authigenic carbonate precipitates at cold seeps .....	8
1.5. Marine biogenic carbonates archives .....	11
2. Study area .....	17
3. Motivation and objectives .....	20
3.1. Overarching goal.....	20
3.2. Open questions and aims of the three manuscripts .....	20
3.3. Open questions and aims of the preliminary studies .....	21
4. Manuscript I: Seep area morphology, active seepage and evolution .....	23
4.1. Introduction.....	26
4.2. Regional setting of the study area .....	29
4.3. Materials and Methods.....	31
4.4. Results and Discussion .....	35
4.5. Conclusions and outlook.....	52
5. Manuscript II: Seep carbonates microfacies and chronology .....	54
5.1. Introduction.....	56
5.2. Geological setting .....	58
5.3. Materials and Methods.....	59

## *Table of contents*

---

5.4. Results.....	61
5.5. Discussion.....	68
5.6. Conclusions.....	76
6. Manuscript III: Seep carbonates environmental archives .....	84
6.1. Introduction.....	87
6.2. Study area.....	89
6.3. Materials and Methods.....	89
6.4. Results.....	91
6.5. Discussion.....	92
6.6. Conclusion .....	101
7. Computer tomography scanning of carbonate consolidated gas hydrates bearing sediments at Yam Seep, Four-way Closure Ridge SW offshore Taiwan .....	115
8. Conclusion and outlook.....	123
8.1. Summary of findings.....	123
8.1. Outlook .....	127
9. References .....	128
Acknowledgments .....	144
致謝 Acknowledgments in Mandarin .....	146
Appendix .....	147
Conference contribution.....	147
Cruise participation.....	149
Affirmation in lieu of an oath .....	150

## Table of Abbreviations

<b>Abbreviations</b>	<b>Full form</b>
AUV	Autonomous Underwater Vehicle
BGHSZ	Base of gas hydrate stability zone
cmbsf	Centi-meter below seafloor
CTD	Conductivity, temperature, density
CT	Computer tomography
DAAD	German Academic Exchange Service
DIC	Dissolved inorganic carbon
FWCR	Four-Way Closure Ridge
GHSZ	Gas hydrate stability zone
LGM	Last Glacial Maximum
MBES	Multi-beam Echosounder system
mbsl	Meter below sea level
OFOS	Ocean Floor Observation System
REE	Rare Earth Elements
SD-AOM	Sulphate-dependent anaerobic oxidation of methane
SMI	Sulphate methane interface
U-Th	Uranium thorium



## Abstract

Cold seeps are areas where hydrogen sulphide, methane and other hydrocarbon-rich fluids occur at the ocean floor and produce specific seafloor features including chemosynthetic communities and authigenic minerals precipitation. Mostly present at continental margins, seepages characterise with various features responding to the influence of tectonic, climate and gas hydrate dynamics at different locations. Therefore, the evolution of the seep area and its influence of diagenesis provide archives of geochemical cycling and geodynamic activities. The formation of gas hydrates sequesters methane gas in the subsurface of seep areas under critical low temperature and high pressure conditions. Authigenic carbonate is one of the most common manifestations at seep sites, in which the precipitates provide the chronology of seepages and environmental archives. Therefore, it is ideal for inferring evidence to resolving geochemical cycling and geodynamic activities at cold seep. In deep water setting ( $>1000$  mbsl), gas hydrates are predominantly stable, active seepages are contributing the critical amount of methane. Active seepages in deep water are under presumably less climatic influence such as sea level and temperature variations. However, factors that control seepages and the evolution of long-term seepages under such environmental conditions are poorly constrained.

This study aims at investigating the processes that govern the activity and evolution of cold seeps on active margin and their potential as environmental archives by studying the morphology of Yam Seep and its authigenic carbonates. The seep area is located at Four-Way Closure Ridge, offshore southwestern Taiwan, which is an accretionary ridge at the active margin between the Eurasian Plate and the Philippine Sea Plate. This study is based on data from two research cruises (RV SONNE SO266 and RV Ocean Researcher I OR1-1163). They were obtained using inter-disciplinary investigations include: (1) shipborne and autonomous underwater vehicle hydroacoustic seafloor and water column echosounder (2) visual observations system, (3) coring and drilling samplers e.g. gravity core and drill rig MeBo200 and (4) water sampling. In addition, various analyses such as U-Th radiometric dating, stable isotope analyses, mineralogy analyses, microscopic petrography analyses, gas analyses were carried out after the cruise on selected samples.

Results of this study are presented in three manuscripts and a report. In the first manuscript, high-resolution hydroacoustic bathymetry, backscatter map and TV-sled observations revealed a 49,000 m<sup>2</sup> carbonate paved area called Yam Seep. The entire area is covered by a heavily fractured methane-derived carbonate crusts and build-ups indicating long-term influence of

seepages on seafloor morphology. Representing current active seepage, hydroacoustic anomalies so-called “flares” that indicate gas bubbles in the water column can be compiled with high methane concentration (up to 18 nM) in the water column and abundant chemosynthetic communities within carbonate fractures. The inter-disciplinary investigation of the Yam Seep demonstrated that its discharging at the seafloor and seabed properties can be attributed to continuous uplifting of Four-Way Closure Ridge.

The second manuscript presents the petrography and stratigraphy of a 5-meter-long carbonate core that distinguishes three distinct microfacies in which the sediment consolidated 1) micrites are intercalated by 2) clear aragonites and 3) grey aragonites (intercrystal of different aragonite forms, not discussed in the second manuscript) in the entire core. Uranium thorium (U-Th) dating on clear aragonites and shells reveals a persistent seepage over a time-span ranging from ~40 to 2 ka. Intercalated clear aragonites also present a general precipitation progress of cementing the fractured micrites, in which the oldest aragonites occur at fractured boundaries or unconformities. Dating on the fractured boundaries and unconformities suggests a cycle of tectonic and seepage activities that consists of an active period from ~37 to 27 ka, a relatively quiet period from ~27 to 16 ka and another active period from ~16 to 12 ka.

The third manuscript aims at confining the characteristic of seep aragonite isotopic archives that revealed the interplay between seawater, gas hydrate and seepage methane using  $\delta^{13}\text{C}$ ,  $\delta^{18}\text{O}$  and  $\delta^{234}\text{U}$  isotopes. Seep aragonite  $\delta^{234}\text{U}_i$  is a back calculated value that represents the seawater  $\delta^{234}\text{U}$  during seep aragonite precipitation. Seep aragonite  $\delta^{234}\text{U}_i$  archives represent the paleo seawater indicating the sea-water like archive in seep pure aragonites. Seep aragonites  $\delta^{18}\text{O}$  values present a trend following a paleo seawater profile with a generally depleted variability. Depleted values suggest the influence of gas hydrate formation environment and fractionation differences between different aragonite forms. Seep aragonites  $\delta^{13}\text{C}$  variations represent (1) the mixing of  $\delta^{13}\text{C}$  of seawater dissolved inorganic carbon (DIC) and seepage methane and (2) a decoupling of isotopic archives during aragonite precipitation.

The last part of the thesis is a report presenting significant results of computer tomography scanning on the 5-meter carbonate core revealing the porosity variations within the consolidated rock. Pores within MeBo-24 present two distinct intensities which represent open pores and filled pore in which lateral precipitation grows within open pores without completely cementing the pore space. The scanning reconstructing porosity of carbonate presents a systematic trend correlating to the microfacies observed in the second manuscript. Therefore, this study provides

useful evidence for reconstructing gas bubbles migration and gas hydrate formation in the sediments in the earliest stage.

Yam Seep's morphology, authigenic carbonates chronology, and the seep aragonites archives provide an phenomenal record of ~40,000-year-old long-term seepage under tectonic influenced in the deep water area and a new insight of seep aragonites environmental archives.

## Outline and contributions to manuscripts

This cumulative thesis focuses on authigenic carbonates at a cold seep site at an active continental margin, using high-resolution seafloor mapping, visual imaging and to complement the dataset including drilling of a carbonate core. The structure of this work aims to follow the approach by giving a summarized introduction of the carbon cycle, cold seeps, gas hydrates dynamics and authigenic carbonates (Chapter 1) and then focuses on the geological setting of the accretionary ridge south western offshore Taiwan as the main study area (Chapter 2). This is followed by the knowledge gap and scientific questions that serve as motivations (Chapter 3). The first manuscript (Chapter 4) provides dataset of investigations on the seep area, Yam Seep, suggesting the active seepage and seafloor morphology that is paved by carbonate crust, and a 5-meter-long core MeBo-24 drilling at Yam Seep. Studies on this carbonate core are later documented in the second manuscript (Chapter 5) regarding the chronology petrography of this seep carbonate core. The third manuscript (Chapter 6) focuses on isotope archives in this seep carbonates, which provide new insights of environmental archives. The manuscripts mentioned above are discussed and prepared for publication. Other important results, detailed computer tomography scanning and analysis had been carried out on MeBo-24. This provides the discussion of porosity variations in a draft result (Chapter 7). Finally, a summary and conclusion of the main findings of this study can be found in Chapter 8. The acknowledgments, reference, and appendix are attached at the end of this thesis.

Yiting Tseng is the primary contributor to all chapters presented in this cumulative thesis and is responsible for the drafting of the context, which are supported by contributions from selected co-authors. A list of authorship and their contribution is outlined in the table below.

Manuscript I: Yam Seep at Four-Way Closure Ridge – a prominent active gas seep system at the accretionary wedge SW offshore Taiwan

Author name	Statement of contribution
Yiting Tseng	The principal author of this manuscript and responsible for producing all figures; analyzing and integrating all data, designing and drafting the manuscript.
Miriam Römer	Hydroacoustic data evaluation and interpretation on backscatter results, manuscript reviewing and editing.

<b>Saulwood Lin</b>	Chief scientist of the cruise SO266. Data analysis and interpretation.
<b>Thomas Pape</b>	Manuscript reviewing and data interpretation.
<b>Christian Berndt</b>	Chief scientist of the cruise SO266. Design of field work.
<b>Tzu-Ting Chen</b>	AUV acquisition high resolution bathymetry map of Yam Seep and interpretation.
<b>Charles K. Paull</b>	AUV acquisition high resolution bathymetry map of Yam Seep and interpretation.
<b>David W. Caress</b>	AUV acquisition high resolution bathymetry map of Yam Seep and interpretation.
<b>Gerhard Bohrmann</b>	Chief scientist of the cruise SO266, contributed to the design and implementation of the research.

Manuscript II: Fluctuations of authigenic carbonate precipitation by geochemical variations due to continuous uplifting and fracturing of Four-Way Closure Ridge

<b>Author name</b>	<b>Statement of contribution</b>
<b>Yiting Tseng</b>	The principal author of this manuscript and responsible for producing all figures; analyzing and integrating all data, designing and drafting the manuscript.
<b>Daniel Smrzka</b>	Carbonate petreography and microfacies interpretations, manuscript reviewing and editing.
<b>Saulwood Lin</b>	Chief scientist of the cruise SO266, contributed to the design and implementation of the research.
<b>Andrea Schröder-Ritzrau</b>	Carbonate U-Th dating and interpretation.
<b>Norbert Frank</b>	Carbonate U-Th dating and interpretation.

---

<b>Gerhard Bohrmann</b>	Chief scientist of the cruise SO266, contributed to the design and implementation of the research.
-------------------------	--

---

Manuscript III: A new  $\delta^{238}\text{U}$  and  $\delta^{18}\text{O}$  record of seawater and decoupling isotopes over the last glacial maximum provided by seep carbonates offshore Taiwan

---

<b>Author name</b>	<b>Statement of contribution</b>
<b>Yiting Tseng</b>	The principal author of this manuscript and responsible for producing all figures; analyzing and integrating all data, designing and drafting the manuscript.
<b>Daniel Smrzka</b>	Data interpretation. Manuscript reviewing and editing.
<b>Thomas Pape</b>	Gas analysis and data interpretation.
<b>Saulwood Lin</b>	Chief scientist of the cruise SO266. Data analysis and interpretation.
<b>Andrea Schröder-Ritzrau</b>	Carbonate U-Th dating and interpretation.
<b>Norbert Frank</b>	Carbonate U-Th dating and interpretation.
<b>Gerhard Bohrmann</b>	Chief scientist of the cruise SO266, contributed to the design and implementation of the research.

---

## 1. Introduction

### 1.1. Cold seeps and their role in the global carbon cycle

The marine environment has been referring to be the major sink of carbon in the global carbon cycle. Dissolved organic carbon is carried by weathering particles from the continent into the ocean and finally deposit as sediments at the seafloor (Bernier, 1982). However, hydrocarbon seeps and hydrothermal vents characterize fluid venting from subsurface sediments exuding fluids rich in CH<sub>4</sub> and H<sub>2</sub>S and create specific seafloor morphologies and deep-water ecological habitats (Hinrichs & Boetius, 2003; Campbell, 2006; Boetius & Wenzhöfer, 2013; Suess et al., 2014; Suess et al., 2018). Such environments are implicated as source of methane to the hydrosphere and partially atmosphere and the crucibles of life origin. Ancient vents and seeps are increasingly recognized, presenting different sizes, lithologies, biota, geotectonic settings, and ages (Campbell, 2006). The oldest metazoans fossils of seep deposit were purported in the age of Silurian (Barbieri, 2004). Quantification of active seeps and vent flows enable the estimation of total volatile output and the role of geological derived methane in the global carbon cycle. Therefore, studies of vents and seeps are critical for the process of organic matter accumulation, burial, hydrocarbon generation, fluid migration as well as biogeographic patterns that reflect plate tectonic configurations and paleo seawater variation (Moore et al., 1992; Paull et al., 1992; Fischer et al., 1997; Peckmann et al., 1999; Suess et al., 2014).

Hydrocarbon seeps, or cold seeps mainly occur at tectonic boundaries, where faulting, thrusting at the collision or deformation zone create pathways to allow the hydrocarbons to migrate to shallower depths (Campbell, 2006) (Fig. 1.1). Various cold seep areas were described at active margins including eastern South China Sea, off Costa Rica, off Chile, Gulf of Cadiz, and off New Zealand Hikurangi. Others are located at passive margins including Black Sea, Mexico, eastern Mediterranean Sea, and western South China Sea (Suess, 2018) (Fig. 1.1). Hydrocarbon seeps at all settings yield distinct seafloor deposits characterized by diverse seafloor morphologies, fossils and authigenic carbonate precipitation, implicating paleo seepage or recent seep activities.

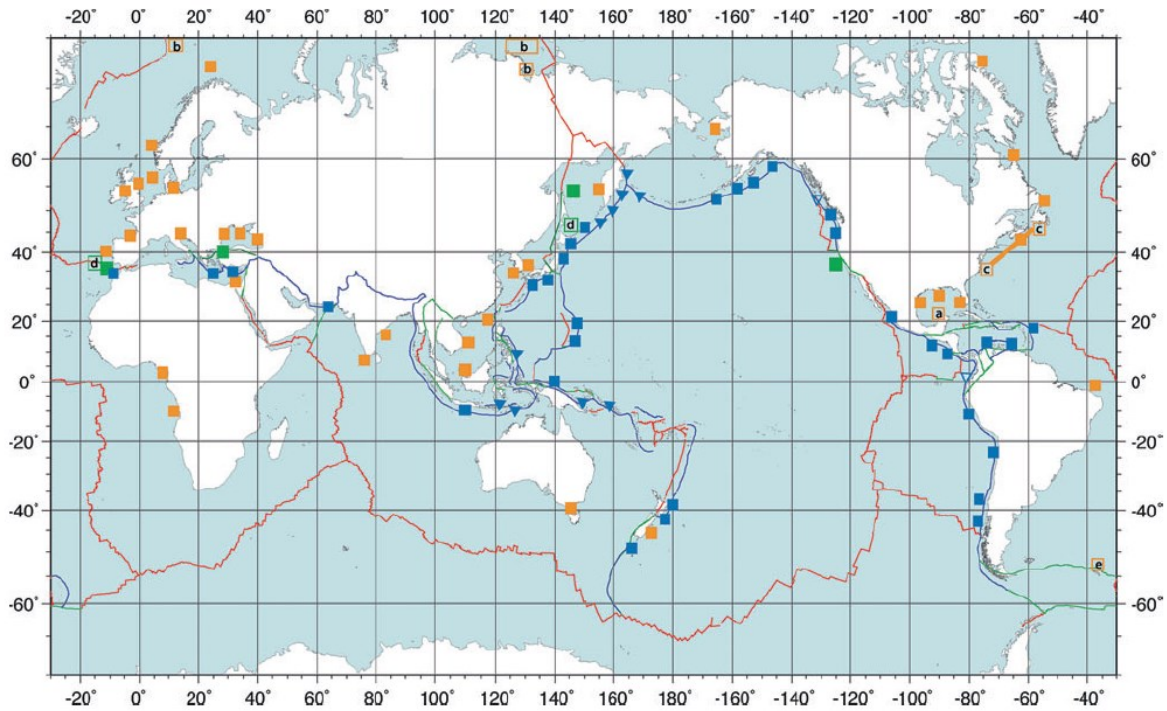
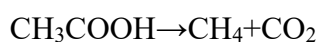


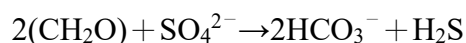
**Fig. 1.1** Global distribution of seeps; sites at transform and strike-slip faults; places with hydrocarbon-metazoan-microbe-carbonate associations at active margins (= blue squares); similar at passive margins including groundwater seeps (= orange squares); Site references are given for the data in Campbell (2006) and Suess (2010, 2014). New locations (= lettered open squares): (a) Asphalt seeps (Sahling et al. 2016); (b) East Siberian Shelf and Svalbard edge (Shakova et al. 2016); (c) Atlantic margin (Skarke 2014); (d) Sakhalin strike-slip and Africa-Eurasia strike-slip (Derkachev et al. 2015); (e) South Georgia Island fjords (Römer et al. 2014). Figure after Suess, 2018.

Methane released at cold seeps is produced by methanogenesis, occurring within the anoxic methanic zone in the sediment, below the sulfidic zone (Berner, 1980, 1982). Methanogenesis is using buried organic matter via thermogenic or microbial processes to consequently produce methane. Thermocatalytic breakdown of organic matters reacts in higher temperature zone and produces various hydrocarbons, i.e. methane, ethane, propane, up to hexane (Davis & Spies, 1980; Paull et al., 1985; Roberts & Anaron, 1994; Sherwood et al., 2013), while microbial methanogenesis reacts in a moderate high temperature zone producing predominantly methane and carbon dioxide (Whiticar et al., 1986; Whiticar, 1999):

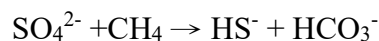


In the sulfidic zone, sulphate reduction uses sulphate as the terminal acceptor to produce sulphide. Dissimilatory sulphate reduction (SR) occurs under oxidation of organic matters and reduction of sulphate that consequently produces bicarbonate and sulphide (Berner, 1980; Berner, 1982; Jørgensen et al., 2001):





Another scenario of sulphate reduction is the sulphate-dependent anaerobic oxidation of methane (SD-AOM) which is a reaction taking place within the consortium of sulphate reducing bacteria (SRB) and methanotroph archaea (Boetius et al., 2000, 2013). Reduction of sulphate and oxidation of methane consequently produces hydrogen sulphide and bicarbonate:



At seep sites, ample methane migrates towards the sulfidic zone. The consumption of methane and sulphate produces high concentrations of sulphide and bicarbonate that increase alkalinity at a depth is called the sulphate-methane interphase (SMI), or sulphate-methane transition zone (SMTZ) (Leloup et al., 2007). In this depth, abundant carbonate precipitates and pyrites are typical authigenic products of SD-AOM and are important manifestations of seepage (Berner, 1982; Peckmann et al., 2001).

### 1.2. Occurrence of gas hydrate and their climate interaction

Gas hydrate, a frozen, concentrated form of methane, occurs naturally and stores significant carbon in the global environment under a range of low-temperature and moderate-pressure conditions (Sloan et al., 2007) (Fig. 1.2). Gas hydrate is widespread along continental margins where methane occurs in marine sediments and in permafrost areas. Criteria for gas hydrate formation is determined by a phase boundary of temperature and pressure conditions which varies according to gas composition and salinity (Kvenvolden, 1993). Temperature and pressure conditions in the marine environment are generally depending on bottom water temperature and varying depth of water column (i.e. temperature) and vary with changing sediment temperature profiles below seafloor (Fig. 1.2) (Kvenvolden & McMennamin, 1980; Bohrmann & Torres, 2006). In general, sea-surface temperature depends on local weather conditions. Below sea-surface, seawater temperature at greater depth varies, for example the thermocline characterizes with rapid temperature changes that are boundaries of upper and lower water masses. At seafloor, sediment temperature typically presents the seawater temperature at seabed and increasing with depths and varying with density variation (Kvenvolden and McMennamin, 1980). The intersection of the phase boundary, water column temperature and sediment temperature profiles define the limits of the gas hydrate stability zone (GHSZ), e.g. the upper and lower depth of the boundary crossing represent the stability depth of the GHSZ (Fig. 1.2 left).

Bottom water temperature is critical for GHSZ (Fig. 1.2 right). Gas hydrates in shallow depth (< 200 m) mostly occurs in high latitudes. Along the continental slope and continental rise, the

thickness of the gas hydrate zone within the seafloor increases with increasing water depth (Fig. 1.2 right).

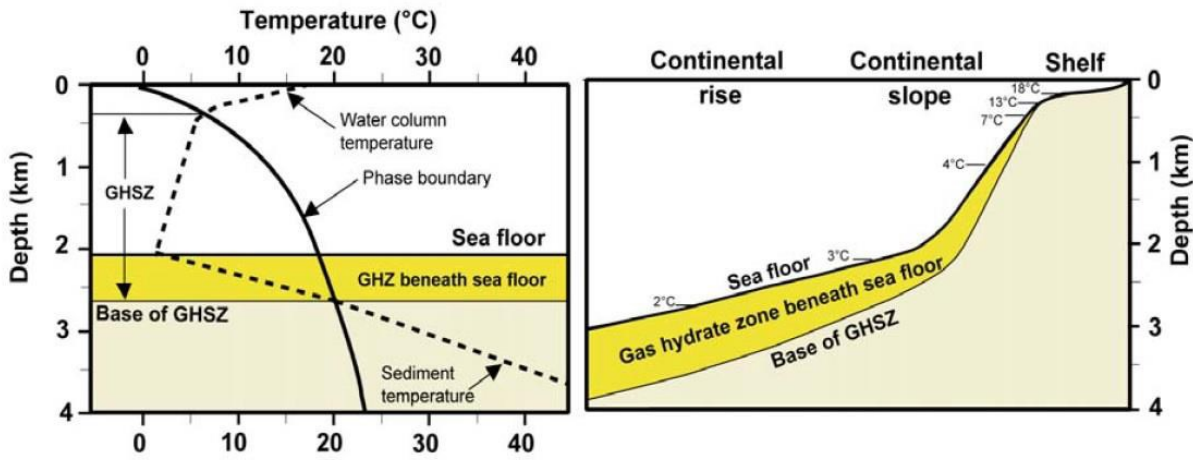


**Fig. 1.2** Left: Calculated stability field of gas hydrate (pure methane), as defined by pressure (expressed as water depth) and temperature. Right: Assuming a typical geothermal gradient of 28°C/ km, the inferred thickness of the gas hydrate zone beneath the seafloor at the continental margin is shown. Typical bottom water temperatures are marked, ranging from 2 °C at the bottom of the continental rise to 18° C at the shelf (after Bohrmann and Torres (2006) and Kvenvolden and McMenamin (1980)).

The interaction of climate change and gas hydrate stability is one of the most important issues among the global carbon system. Dissociation of gas hydrates is sensitive to both temperature and pressure changes. During the Last Glacial Maximum (LGM), sea level was 120 m lower than current sea level (Clark et al., 2009). Pressure and temperature changes affected by sea level variation consequently influences the depth of the base of the gas hydrate stability zone and drives gas hydrate dissociation. This phenomenon is especially critical along continental slope at water depths between ~200 to 1000 m. At the continental slope, changes of bottom water temperature have an impact on the stability of shallow gas hydrates. Therefore, seepages at water depths of ~200-1000 m is suggested to be mediated by gas hydrate dissociation episodes related to sea level fluctuations. This can be observed at e.g. the South China Sea, Sea of Marmara, Central American forearc and Black Sea (Chen et al., 2019; Cremier et al., 2013; Han et al., 2014; Liebetrau et al., 2010, 2014). Temperature sensitivity is particularly pronounced in the shallow sea (< 200 m) and polar regions, where +1 °C variation can lead to methane releasing episodes. While, gas hydrates at deep waters (water depth > 1000 m) is relatively insensitive to temperature changes (F. Chen et al., 2019; Ruppel & Kessler, 2017). Gas hydrates in deep water depths (>1000m) typically acquire most substantial gas hydrate stability in which bottom water remain constant through climate changes (Ruppel & Kessler, 2017). Even if the bottom water temperature would increase several degrees, the ambient

hydrostatic pressure regime still keeps gas hydrates in shallow sediments stable (Ruppel & Kessler, 2017).

### 1.3. Seepage manifestations and investigations

Cold seeps, including mud volcanos, at various geological settings transport fluids, water dissolved compounds, and/or free gasses through the seafloor to the ocean and present different anomalies (Feng et al., 2018; Suess, 2018) (Fig. 1.3). These anomalies indicate present and paleo seepage and can be observed and investigated using various approaches. At many seep areas, free gas rises from the sediment into the water column as bubble streams that appear as flare-like anomalies (Fig. 1.3) in hydroacoustic echograms (Römer et al., 2014; Dupre et al., 2015; Loher et al., 2018; Hsu et al., 2019). These commonly called “flares” are typically used to locate active seepage areas. Dissolved methane in bottom water is also an important indicator at active seep sites. In general, in-situ methane concentrations in seawater vary from 2.1 to 3.7 nM from sea surface to 2000 m depending on its thermodynamic equilibrium (Mau et al., 2020). At seep areas, high methane concentration of over ten-fold can be measured close to the seafloor (Mau et al., 2020). Both gas flares and dissolved methane indicate currently active seepage. Evidences of paleo or long-lasting seepage that produces seafloor morphology anomalies can be observed via hydroacoustic systems (Römer et al., 2014; Loher et al., 2018) such as side-scan or multi-beam hydroacoustic backscatter signals are typically used for distinguishing seafloor textures of different physical property (Fig. 1.3). Seafloor covered by sediments is generally characterized by low-backscatter intensity while high seafloor backscatter signals are potentially indicating seep related manifestations such as carbonate crusts and bioclasts, mussel or clam shells (Hsu et al., 2019; Orange et al., 2002; Papenmeier et al., 2020; Römer et al., 2014; Sahling et al., 2008a; B. Wang et al., 2021).

Chemosynthetic organisms and microbes fuelled by methane, sulphide or other chemicals survive devoid of primary production beneath the euphotic zone. Chemosynthetic living microbes (archaea and bacteria) occur at sediments or use other macrofauna such as mussels tubeworms and crabs as inhabitant and sometimes provide sustenance for the macrofauna (Sibuet & Olu, 1998; Cordes et al., 2003; Campbell, 2006; Watsuji et al., 2017; Kuo et al., 2019). Mussels are stationary at hard substrate carbonate and feeding by microbial symbiosis that are fuelled by dissolved methane (Feng et al., 2015; Kuo et al., 2019; Rubin-Blum et al., 2017). Therefore, the presence of mussels indicates both carbonate paved seafloor and active seepage. *Vestimentiferan* tubeworms live in symbiosis with chemoautotrophic sulfur-oxidizing bacteria and are considered as one of the primary producers in seep communities due to the fact

of they often dominate seep sites in the earlier stage (Freytag et al., 2001; Sahling et al., 2008a). Moreover, their relatively long lifespan which can live up to 250 years (Cordes et al., 2003) indicates a rather long-term seepage environment. Other common organisms frequently observed at seep areas are opportunistic or endemic and include fish, *galatheid* crabs, polychaetes, sponges (Sibuet & Olu, 1998; Vacelet et al., 1995) which are not chemosynthetic living organisms but using the organic matters and debris at the periphery of chemosynthetic communities (Sibuet & Olu, 1998; Campbell, 2006).

Investigations on seep manifestations can be conducted via different approaches (Fig. 1.3). Gas flares, high methane concentration of bottom water, carbonate paved seafloor anomalies and chemosynthetic communities can be observed and studied using ship-borne and autonomous underwater vehicle (AUV) multi-beam echosounder system (MBES), conductivity-temperature-depth (CTD) and water sampling, and ocean floor observation system (OFOS). Sampling for further analysis can be conducted via coring and drilling devices, like the Meeresboden Bohrgerät (MeBo), or remotely operated underwater vehicle (ROV).

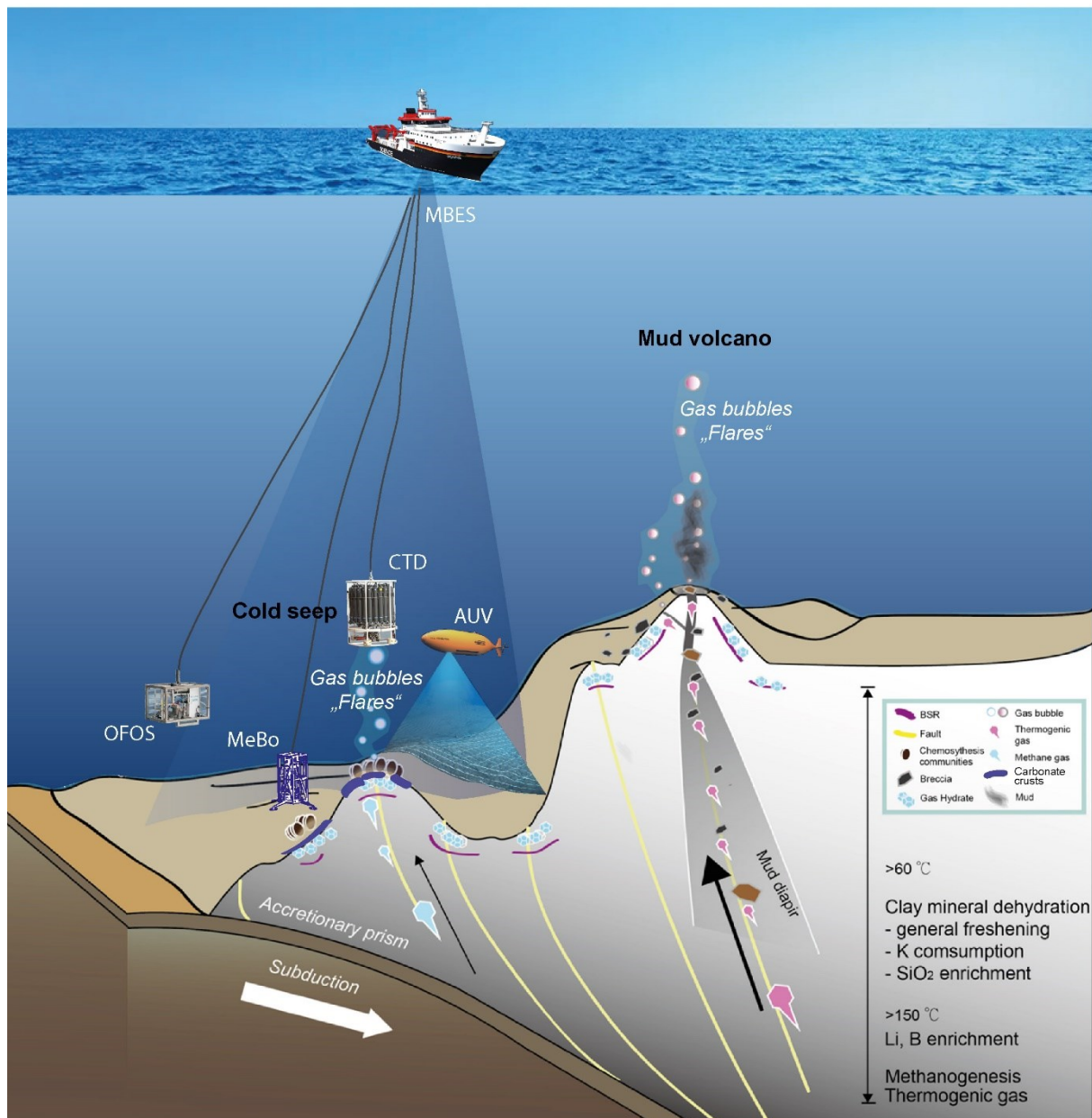


**Fig. 1.3** Cold seep and mud volcano and the approaches that are applied for studying seepages. AUV: Autonomous Underwater Vehicle; MBES: Multi-beam Echo Sounder; OFOS: Ocean Floor Observation System; MeBo: Meeresboden Bohrgerät.

#### 1.4. Authigenic carbonate precipitates at cold seeps

Authigenic carbonate is one of the most common features at all the seepage areas (Robert & Aharon, 1994; Peckmann et al., 2001; Peckmann & Thiel, 2004). Precipitation of seep carbonate changes the seabed morphology in different scales and meanwhile providing information regarding seepage chronology and seep fluids and potentially indicating the archive of the tectonic activity and geochemical cycling in wider extend.

Exposed carbonate pavements typically create a rough seafloor morphology, such as at Central Nile Deep Sea Fan (Fig. 1.4 left) (Römer et al., 2014) and Venere mud volcano central Mediterranean (Loher et al., 2018). Carbonate geomorphologies at seafloor under influence of tectonic activities, erosion, or sedimentation rate produce various shapes like pockmarks, mounds, knolls, chimneys, build-ups etc. Carbonate pockmarks or geomorphological depressed seep areas can be found at Congo Fan area (Marcon et al., 2014; Sahling et al., 2008a), Vestnesa Ridge, North Atlantic (Himmeler et al., 2019), Pacific margin, off North America (Paull et al., 2015), northern Gulf of Mexico, presenting brine-filled pockmarks (MacDonald et al., 1990), and off south western Taiwan, comet-shape-depressions (T.-T. Chen et al., 2019). Seep areas characterised with carbonate mounds or knolls had been observed at Central American forearc offshore Nicaragua and Costa Rica (Kutterolf et al., 2008; Liebetrau et al., 2014), Black Sea (Bahr et al., 2007; Mazzini et al., 2008; Bahr et al., 2010), Gulf of Mexico (Hsu et al., 2019), and at the passive and active margins of South China Sea (F. Chen et al. 2019; X. Q. Han et al., 2013; Klaucke et al., 2016; B. Wang et al., 2021). Other build-ups on the accretionary ridge are at Cascadia margin Hydrate Ridge (Fig. 1.4 right) (Bohrmann et al., 1998; Teichert et al., 2005; Teichert et al., 2005). Special lamination seep carbonates can be found at minimum oxygen zone at Makran continental margin, Arabian Sea, (Himmeler et al., 2010, 2015, 2016). Widespread varieties of carbonates indicate correlation of seepage and regional setting and activities of sedimentation, uplifting, erosion, or slumping. Areas of long-term seepages produce various carbonate shapes and compositions preliminarily suggesting the evolution of a seep site.

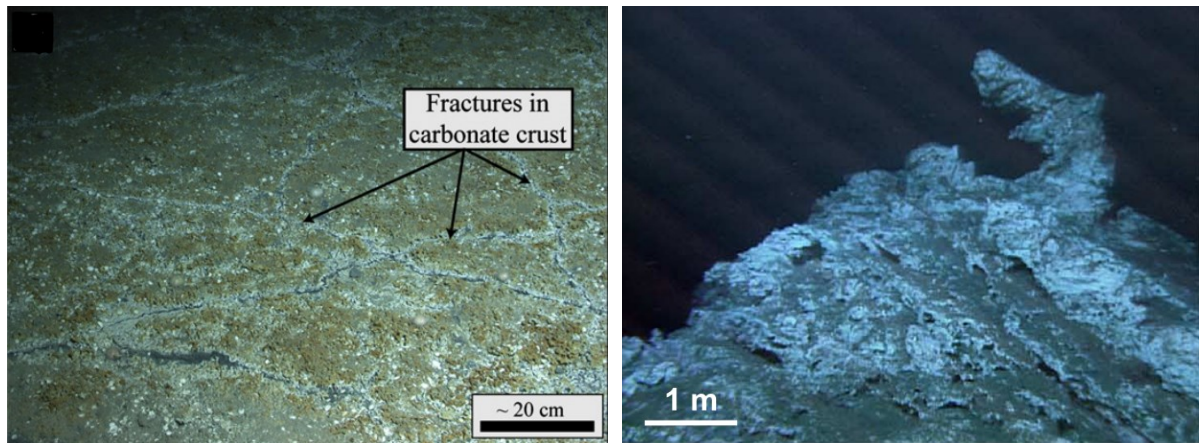


**Fig. 1.4** Carbonate paved seafloor and fractures (left) at central Niles Deep Sea Fan, Eastern Mediterranean Sea (Römer et al., 2014) and chemoherm carbonates (right) at Hydrate Ridge, Cascadia continental margin (Teichert et al., 2005).

Despite the variety of carbonate geomorphology, carbonate precipitates provide records of environmental archives at the time of its precipitation (Teichert et al., 2003; Wiedicke & Weiss, 2006; Libertrau et al., 2014). Studies focus on oxygen and carbon stable isotopes and uranium radiometric to determine the seep fluid sources and to establish the chronology of seepage episodes (Bohrmann et al., 1998; Teichert et al., 2003, 2005; Feng et al., 2018; F. Chen et al., 2019).

Typically, micritic carbonates that consist of microcrystalline aragonites or low and high magnesium calcites (LMC, HMC) consolidate sediments with precipitations in interstitial pore spaces and result in large scale carbonate paved seafloor that can extend over hundreds of square meters (Greinert et al., 2001). In marine environment, aragonite, LMC and HMC are more common comparing to calcite as for the composition of sulphate, phosphate and calcium and magnesium ratio in seawater favour the thermodynamic of the precipitation of aragonites, LMC and HMC (Berner, 1975; Sun et al., 2015). Clear seep aragonites, devoid of sediments, are commonly found cementing micritic carbonate fractures as aragonite veins or overgrowth structures up to decimetres in thickness (Himmler et al., 2015; Teichert et al., 2003; Liebertrau et al., 2014). These seep aragonites are close to the depth of gas hydrate bearing sediment, therefore, it has been suggested that these clear aragonites precipitations are the result of replacing gas hydrate filled spaces (Bohrmann et al., 1998). Some of these pure aragonites are called chemoherms that are define as the microbial derived carbonate build-ups precipitate fully or partially into water column (Teichert et al., 2005). These clear aragonites present different aragonite forms such as crystalline banded and botryoidal or spheroidal and cryptocrystalline yellow aragonites (Peckmann et al., 2002; Himmlar et al., 2013; Smarzka et al., 2015; Zwicker et al., 2018). Studies on lipid biomarkers further differentiated the influences of microbial



reactions on aragonite forms, (i.e. crystalline, cryptocrystalline, and microcrystalline) and suggested the presence of bicarbonate producing microbes (Hagemann et al., 2013). Lately, drilled carbonate cores revealing micritic carbonates over few meter long intercalated succession (> 50 cm) of clear aragonites have been recovered at e.g. Hydrate Ridge (Hagemann et al., 2013; Leefmann et al., 2008), the Central America Forearc (Liebetrau et al., 2014), and the South China Sea (F. Chen et al., 2019). These cores provide an extraordinary volume of carbonate precipitates implicating potential long-term archives.

Dating on banded and botryoidal crystalline aragonites that are isopaches implicates the seepage chronology and the sequence of precipitation (Teichert et al., 2003; Han et al., 2014; Liebetrau et al., 2014). Widely applied on carbonates, speleothems, aragonitic corals, and seep carbonates, radiometric U-Th dating provides precise and systematic chronology. Dating aragonitic corals are calibrated by radiocarbon foraminifera time scale, which implicate the absolute chronology of sea level changes of Late Quaternary (T. Chen et al., 2016; Chutcharavan et al., 2018). However, Coralline and seep aragonites are vulnerable to post-depositional alteration of its original geochemistry. Therefore, a screening technique is applied to identify the unaltered carbonates (Chutcharavan et al., 2018) via the back-calculation of carbonate initial  $^{234}\text{U}/^{238}\text{U}$ . The seawater  $\delta^{234}\text{U}$  was suggested to be a constant value of  $\sim 146\text{‰}$  (Andersen et al., 2010). The reliable carbonates were therefore assumed to reflect the seawater  $\delta^{234}\text{U}$  to represent the un-altered condition from the time of their precipitation (Aharon et al., 1997; Chen et al., 1986; Cheng et al., 2000; Dunk et al., 2002; Henderson et al., 2003; Robinson et al., 2004; Esat et al., 2006; Andersen et al., 2010; T. Chen et al., 2016). Seep aragonites present well preserved initial  $\delta^{234}\text{U}$  and are devoid of sediment that has minimized the age contamination from ancient thorium in sediment (Bayon et al., 2009). Therefore, U-Th dating is ideal for providing precise chronology during seep aragonites precipitation (Bayon et al., 2009; F. Chen et al., 2019; Liebetrau et al., 2014).

Dating on seep carbonates suggest the seepage episodes and sometimes present the correlate with paleo ocean sea level variations of  $\sim 200\text{ ka}$  (F. Chen et al., 2019). The glacial-interglacial interval resulted in a 120 m sea level variation (Clark et al., 2009). If seep sites are classified according to the respective seafloor depths into three classes a)  $< 200$ , b) 200-1000 and c)  $> 1000$  mbsl (Fig 1.5), sea level fluctuations are most likely to affect gas hydrate stability at seeps in class b ( $\sim 200$ -1000), as seeps  $< 200$  and  $> 1000$  mbsl do not encounter dramatic temperature and pressure variations. Thus, seep sites within water depths of 200 -1000 mbsl are suggested to have seepage episodes effected by gas hydrate dissociation during sea level low stands (Fig.



1.5). Therefore, dating on seep carbonates also allow for hypothesizing about the mechanisms controlling seepage in water depths  $< 200$  and  $> 1000$  mbsl, for example geological events, including ice volume waxing and waning and tectonic controls. As seepage in the water depths  $< 200$  mbsl are mostly found at permafrost and polar areas, they might correlate with the coverage of ice shelf, which is influenced by global temperature variations. Seep sites below a water depth of 1000 m are the most substantial seepages throughout the climatic variation. However, the correlation between seepage episodes and sea level variations are not sufficient to provide a direct evidence of gas hydrate influenced fluid isotopic imprint in the carbonates.

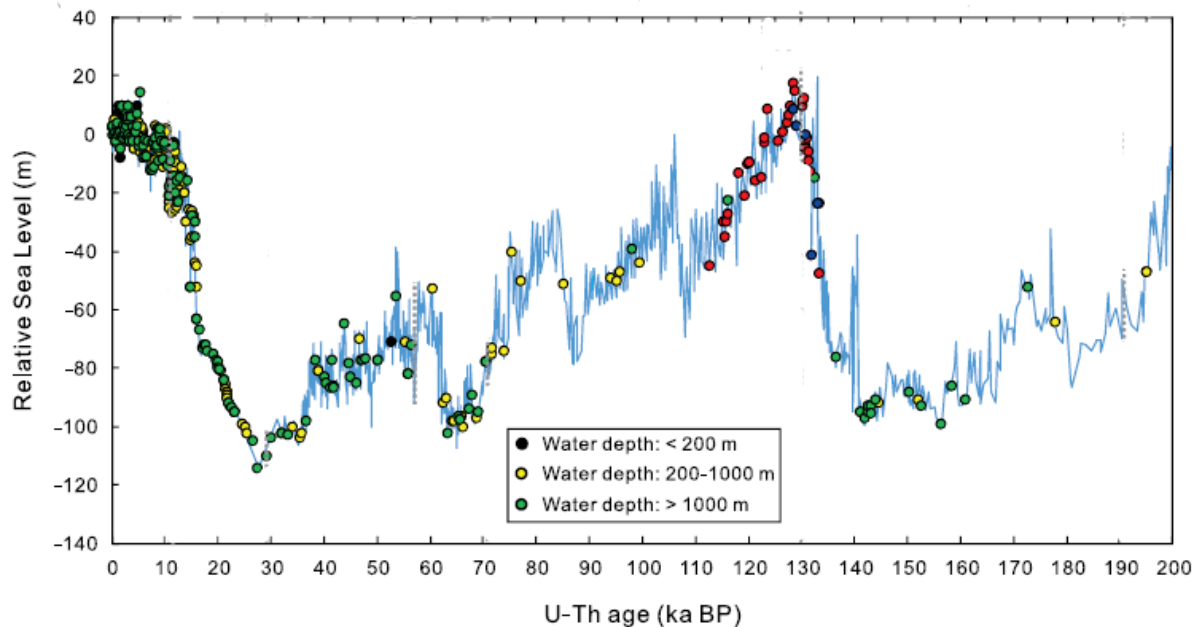


**Fig. 1.5** Previously reported seep carbonates grouped by water depth (black, yellow, and green circles) (modified after F. Chen et al., 2019).

### 1.5. Marine biogenic carbonates archives

Carbonates such as speleothems, foraminifera, molluscs and corals of tropical and deep sea, have been used to investigate the land, sea, and atmosphere climatic variation, via investigating carbonate isotope archives (Swart, 2015). Speleothems, stalagmites and stalactites of cave environments provide records of rainwater as well as regional and global temperature and  $\text{CO}_2$  records (Douville et al., 2010; Gasse, 2000; Spötl et al., 2019). In marine environment, marine biogenic carbonates provide excellent seawater archives. Foraminifera are applicable for reconstructing paleo seawater temperature and water mass variations in local and global scale

(Urey, 1947; Hillaire-Marcel & Ravelo, 2007; Marchitto et al., 2014). Tropical corals provide records of sea level fluctuations as well as shallow seawater temperature variations (Fairbanks & Matthews, 1978; Roder et al., 2013; Chutcharavan et al., 2018). Typical carbonates proxies for environmental archives are oxygen and carbon isotopes (Swart, 2015) (Fig 1.6).  $\delta^{18}\text{O}$  and  $\delta^{13}\text{C}$  values of carbonate minerals are influenced by several factors that affecting system such as open (global) ocean and ambient (local) water and sometimes the fractionation exists during precipitation (Swart, 2015) (Fig 1.6). Foraminifera oxygen isotopes values have been studied for decades and implicate open seawater variations that influenced by (i) salinity, (ii) ice volume and (iii) mixing of deep water masses; and the precipitation fractionation are affected by (i) temperature, (ii) mineral type, (iii) vital effect and (iii) carbonate ion concentration (Fig. 1.6) (Hillaire-Marcel & Ravelo 2007). Laboratory experiments and field studies established equations of temperature sensitivity that have been expended for wider temperature ranges and between different species (Mucci, 1983; Grossman & Ku, 1986; Hillaire-Marcel & Ravelo, 2007; Marchitto et al., 2014). Planktonic and benthic foraminifera generally represent the different characteristics of water column and water masses near seafloor during carbonate precipitation (Hillaire-Marcel & Ravel, 2007; Swart, 2015). Species of different mineralogy, calcitic and aragonitic, present an offset of  $\sim 0.6$  to  $1\%$  in oxygen isotope values during precipitation (Grossman & Ku, 1986; Marchitto et al., 2014; Swart, 2015). Carbonate carbon isotope values characterize the dissolved inorganic carbon (DIC) in the open seawater, which is influenced by (i) carbon from lithosphere, (ii) respiration and photosynthesis, (iii) mixing of water masses and (iv) mixing of deep water masses; and also the precipitation fractionation that is affected by (i) temperature, (ii) mineral type and (iii) precipitation rate (Fig 1.6) (Hillaire-Marcel & Ravel, 2007; Swart, 2015). The factors that affect the fractionation precipitation are similar to the oxygen isotopes, however, the factors that causing open seawater dissolved inorganic carbon (DIC) variation represent more regional variation. Therefore, carbon isotopes do not imply a similar effect as oxygen isotopes (Hillaire-Marcel & Ravel, 2007).

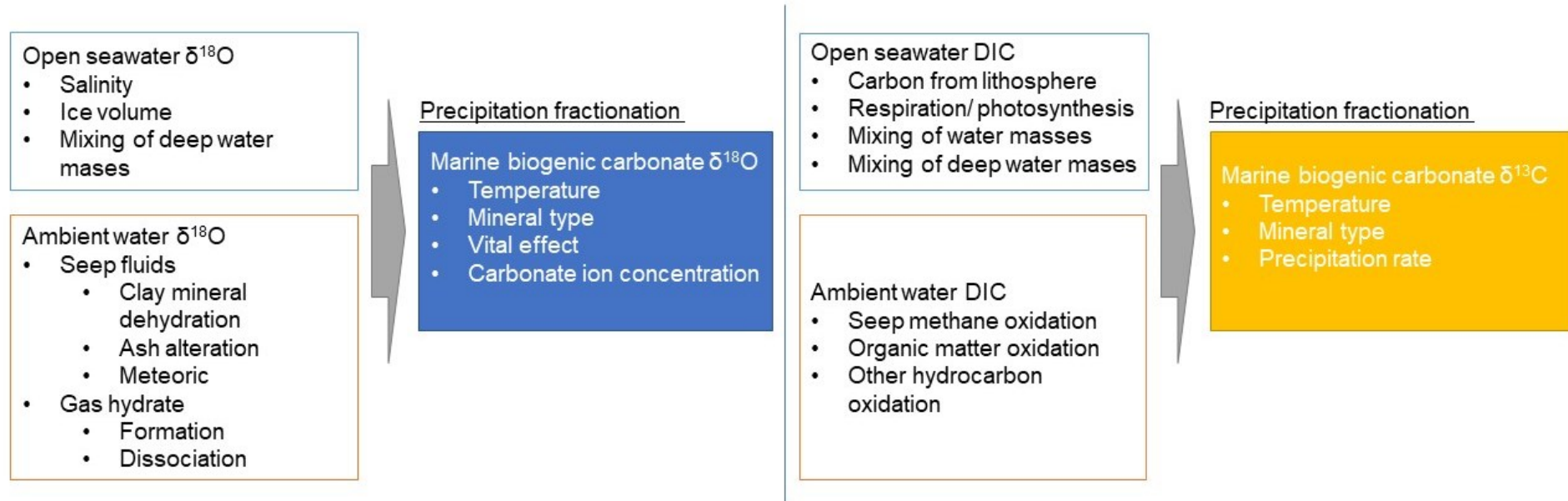


**Fig. 1.6** Factors that influence the  $\delta^{18}\text{O}$  and  $\delta^{13}\text{C}$  of marine biogenic carbonates from the impacts on systems of open (global) seawater, ambient (local) water and the fractionation of oxygen and carbon isotopes during precipitation.

Seawater  $^{234}\text{U}/^{238}\text{U}$  provide crucial information for the global-scale continental weathering and as the quality screening for marine uranium-series geochronology (Robinson, et al., 2004a; T. Chen et al., 2016). It has been expected that the seawater  $^{234}\text{U}/^{238}\text{U}$  is constant within the Late Quaternary due to the long residence time of U in seawater (~300-500 thousand years) (Henderson, 2002; Dunk et al., 2002), in which the equilibrium response to external inputs should be more than an order of magnitude longer than glacial-interglacial cycle (~10 thousand years). However, increasing studies suggesting that the seawater  $^{234}\text{U}/^{238}\text{U}$  might have been lower during LGM than the Holocene and previous interglacial (Robinson et al., 2004a, 2004b; Cutler et al., 2004; Esat & Yokoyama, 2006; Thompson et al., 2011). The timing and amplitude of  $^{234}\text{U}/^{238}\text{U}$  variability had been recently confined via well-preserved deep-sea corals from the low-latitude Atlantic and Pacific Ocean and suggesting the subglacial melting of Northern Hemisphere ice sheet and ocean mixing are account for the Seawater  $^{234}\text{U}/^{238}\text{U}$  evolution (T. Chen et al., 2016).

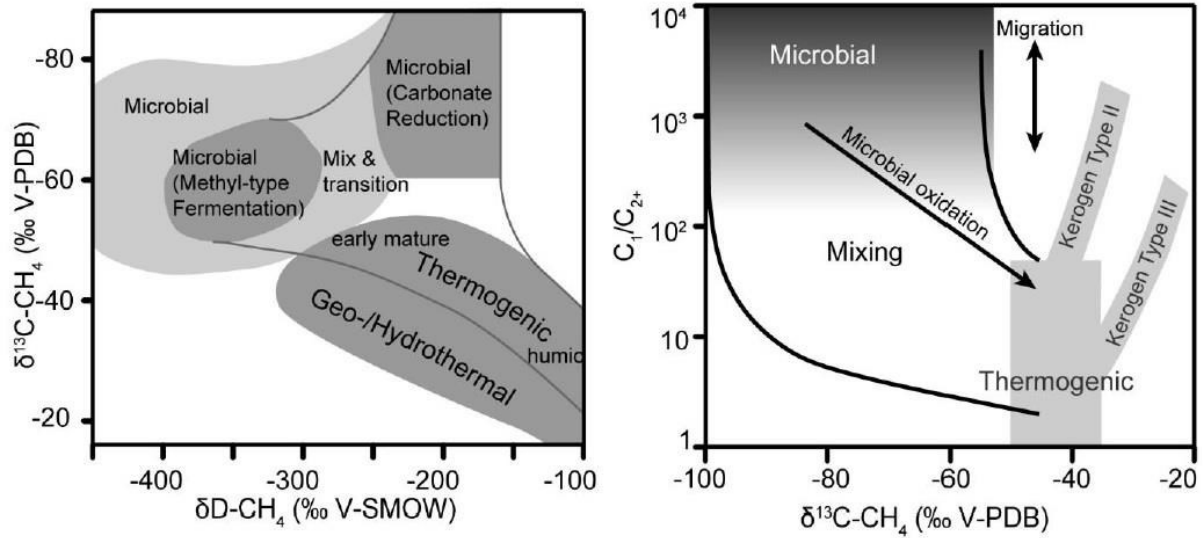
Between various marine biogenic carbonates, the preservation potential of carbonate isotope signals for representing seawater isotopes are different. It is depending on the preservation of predominant mineralogy, precipitation fractionation (temperature, vital effect and growth rate) and degree of diagenetic alteration (Table 1.1). Environments that cause the precipitation fractionation can alter the isotopic values and the sometimes the limitation of habitant, e.g. temperature, available of light and symbionts, however result in providing relative consistent values that are suitable for represent the environmental variation. For instance, tropical corals that are limited to live within the temperature of 20 to 28°C, in which the symbiont of this temperature range have also allow for a certain pH for precipitation, and therefore, the isotopic values of tropical corals are normally well correlated in representing environmental archives (Wellington et al., 1996; Grottoli et al., 2000). As for the cold-water corals that are not limited by the temperature, their oxygen and carbon isotope values are not applicable for represent seawater isotope values (Freiwald, 2003). On the other side, uranium archives in corals of both tropical and cold-water have high potential to represent the seawater evolution after a screening technique that recognizing the altered carbonates (Chutcharavan et al., 2018). Diagenesis can obscure the origin composition of isotope during carbonate precipitation. Foraminifera are excellent for providing oxygen and carbon isotopic archives (Swart, 2015). However, the diagenesis of mineral after foraminifera buried in depth that the changing of alkalinity lead to incorporation of uranium isotopes in down core (Russel et al., 1994; Keul et al., 2013), and the issue of removing thorium in foraminifer are both problematic for represent seawater uranium archives (Delaney & Boyle, 1983) (Table 1.1).

Table 1.1 The preservation potential of isotope signals for representing seawater isotopes in different marine biogenic carbonates.

<i>Isotope signals and properties</i>	<b>Marine biogenic carbonates</b>					
	Planktonic foraminifera	Benthic foraminifera	Tropical corals	Cold-water corals	Seep carbonates (micrite)	Seep aragonites (chemoherm)
Oxygen isotope signals	High (Swart, 2015)	High (Swart, 2015)	High (Wellinton et al., 1996)	Low (Freiwald, 2003)	Low (Wiedicke & Weiss, 2006)	Good (Teichert et al., 2003) and in this study chapter 6
Carbon isotope signals	High to Moderate (Swart, 2015)	High to Moderate (Swart, 2015)	Moderate (Grottoli, 2000)	Low (Freiwald, 2003)	Low (Wiedicke & Weiss, 2006)	In this study chapter 6
Uranium isotope signals	Low (Delaney & Boyle, 1983)	Low (Delaney & Boyle, 1983)	High (Chutcharavan et al., 2018)	High (Chutcharavan et al., 2018)	Low (Teichert et al., 2003)	Good (Teichert et al., 2003) and in this study chapter 6
Properties of marine biogenic carbonates	Representing water column	Representing deep water masses.	Only apply for limited areas and time-scales	Only apply for limited areas and time-scales	Presenting mixing signals due to cementation of various sources	Different aragonite forms

Seep carbonates oxygen and carbon isotopes archive the environment affected by ambient water that influenced by seep fluid, gas hydrate and other diagenesis influenced ambient water e.g. DIC (Fig 1.6). Clear aragonites are suitable for studying a comprehensive archives of seepage chronology as well as for understanding the influence of carbonate precipitation in relation to seawater and seepage fluid. Himmler et al. (2010) investigated pure aragonites (crystalline) exhibiting seawater-like rare earth elements (REE), indicating the influence of seawater, while micritic aragonites (microcrystalline) reflect porewater-like REE. At seep site, ambient water  $\delta^{18}\text{O}$  is affected by seep fluids depending on the geological setting, whereas fluid sources include clay mineral dehydration, ash alteration, meteoric water etc. (Dählmann et al., 2003) (Fig 1.6). Moreover, presence of gas hydrate potentially cause the  $^{18}\text{O}$  enriching or depleting through gas hydrate dissociation or formation (Bohrmann et al., 1998; Feng et al, 2018; Chen et al., 2019, Deng et al., 2021) (Fig 1.6). Seep carbonates  $\delta^{13}\text{C}$  archived DIC consists of certain different sources including seawater dissolved DIC and DIC generated during oxidation of organic matters, methane, and other non-methane hydrocarbon (Formolo et al., 2004) (Fig 1.6). Methane  $\delta^{13}\text{C}$  is generally determined by the methanogenesis, e.g. whether the methane is of biogenic or thermogenic source. Methane  $\delta^{13}\text{C}$  of biogenically produced gases is depleted

compared to thermogenic gas, and range from  $-50$  to  $-100$  ‰, and  $-35$  to  $-50$  ‰, respectively (Whiticar, 1999) (Fig. 1.7). Methane-derived microbial reaction produced authigenic carbonates are generally low in  $\delta^{13}\text{C}$  due to  $^{13}\text{C}$ -depleted methane source that produce  $^{13}\text{C}$ -depleted DIC (Aloisi et al., 2000; Peckmann et al., 2001; Ritger et al., 1987; Thiel et al., 2001).



**Fig. 1.7** Left: Stable Carbon-hydrogen isotope diagram for classification of biogenic and thermogenic methane (modified after Whiticar (1999)); Right: “Bernard” diagram for classification of hydrocarbon gas based on  $\delta^{13}\text{C-CH}_4$  values and  $\text{C}_1/\text{C}_{2+}$  ratios with theoretical mixing lines and relative compositional effects of oxidation as well as migration (modified after Whiticar (1999)).

## 2. Study area

Taiwan characterizes with one of the most unique tectonic settings in the world, the plate tectonic of Eurasian plate was subducting and transformed into collision as a result of gradual underlying of Luzon arc from Philippine sea plate (Fig 2.1a)(C.-S. Liu et al., 1997). Due to the collision, formation of Taiwan Mountain belt began since the late Cenozoic (Teng, 1990). Later in late Pleistocene, formation of faulting systems in the southern Taiwan e.g. Hengchun Fault generally exposed the Hengchun peninsula and formed series of thrust faults, anti-clinal ridges in the south western offshore and onshore (W.-S. Chen et al., 2005; S.-C. Liu et al., 2021). In the most recent record, Philippine sea plate is moving north eastward in the rate of 8 cm /yr (C.-S. Liu et al., 1997) and Hengchun Fault is uplifting in the rate of  $5.0 \pm 1.2$  mm/yr since Holocene (C.-H. Wang et al., 1990). Under rapid uplifting and collision, south western off Taiwan generally succeed the tectonic structure (e.g. faults, thrust faults, and anticlinal ridges) until Deformation Front (Fig 2.1a) (C.-S. Liu et al., 1997). Characterized with some of the highest denudation rate in the world, surrounding Taiwan island consist of high orogenic sediments from mountain belt through submarine canyons (Dadson et al., 2003). Canyons, such as Penghu, Kaoping, and Fangliao canyon, are important for shaping the submarine ridges in the study area (Lin et al., 2014). Ample buried organic rich sediments provide the source for methanogenesis. Offshore south western Taiwan is divided into upper slope and lower slope; upper slope underlay with series of mud diapirs and overlay with various mud volcanos, while lower slope characterizes with accretionary ridges and hydrocarbon seeps (C.-S. Liu et al., 1997). Beside active hydrocarbon seepages, south western offshore Taiwan is suggested to contain over 15,000 km<sup>2</sup> gas hydrates at both accretionary ridges and in South China Sea (C.-S. Liu et al., 2006).

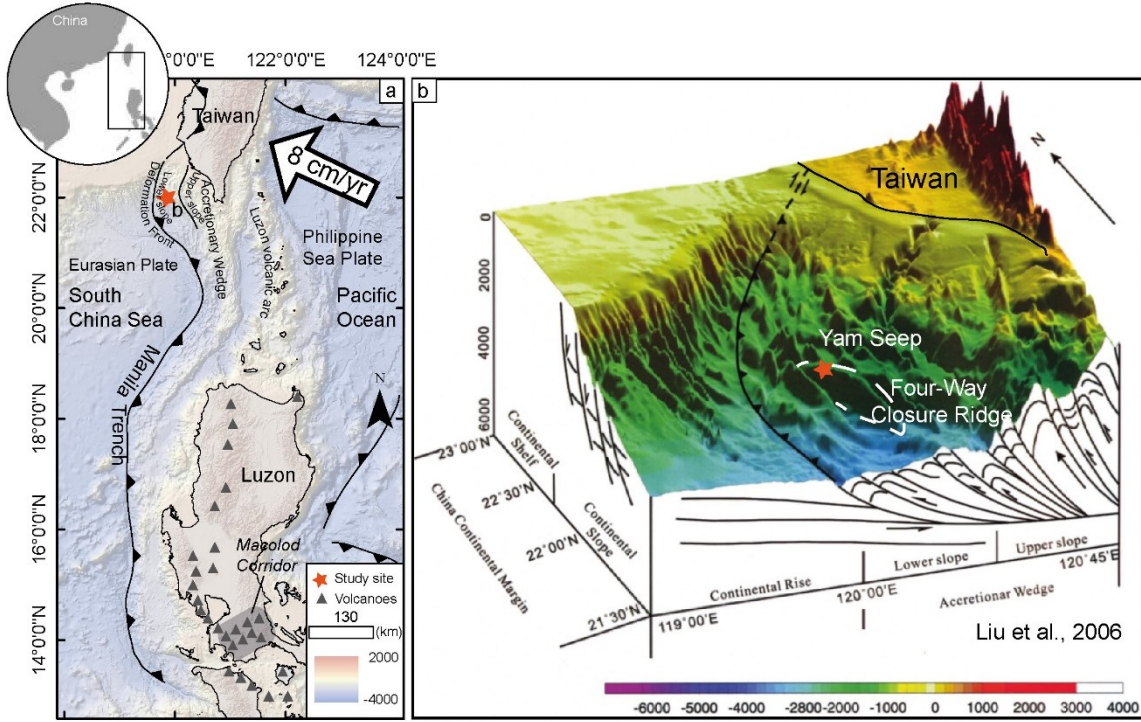


**Fig. 2.1** Tectonic setting of study area. (a) General plates structure. (b) Accretionary ridges offshore south western Taiwan. Orange star: study area Yam Seep.

Four-Way Closure Ridge (FWCR) is located at the lower slope of the active margin close to the deformation front in the water depth of ~2000 to 1400 mbsl (Fig. 2.1b). Base of GHSZ in FWCR is located at ~450 m below seafloor, which agrees with theoretical bottom-simulating reflections (BSR) (Kunath et al., 2020). The erosional features at the east flank of Four-Way Closure Ridge suggests the influence from the paleo Penghu Canyon on the eastern Four-Way Closure Ridge (Klaucke et al., 2016). Yam Seep is located at the northern summit of FWCR at the water depth of ~1400 mbsf. The seep area is over 49,000 m<sup>2</sup> and generally characterized with rough topography (T.-T. Chen et al., 2019). The active seepage at Yam Seep has been reported since 2013 by Klaucke (2015). The thrust fault on the western limb of Four-Way Closure Ridge suggests the hydrocarbon migrations along this faults networks that fuels Yam Seep (Kunath et al., 2020). At Yam Seep, chaotic reflections and multiple BSR between 250-150 mbsf further suggest a gas hydrate and free gas co-existing zone in the subsurface (Kunath et al., 2020). Given the wide salinity range (0.5 to 3.5 %) and temperature-pressure profile (e.g. in 2018; CTD02, GeoB 23208; Bohrmann et al., 2019) of South China Sea water masses (Fig. 2.2), the GHSZ is below water depth of ~600 mbsl which is far above the water depth of Yam Seep (Fig. 2.2). This poses the occurrence of gas hydrate at the Yam Seep to the base of FWCR.



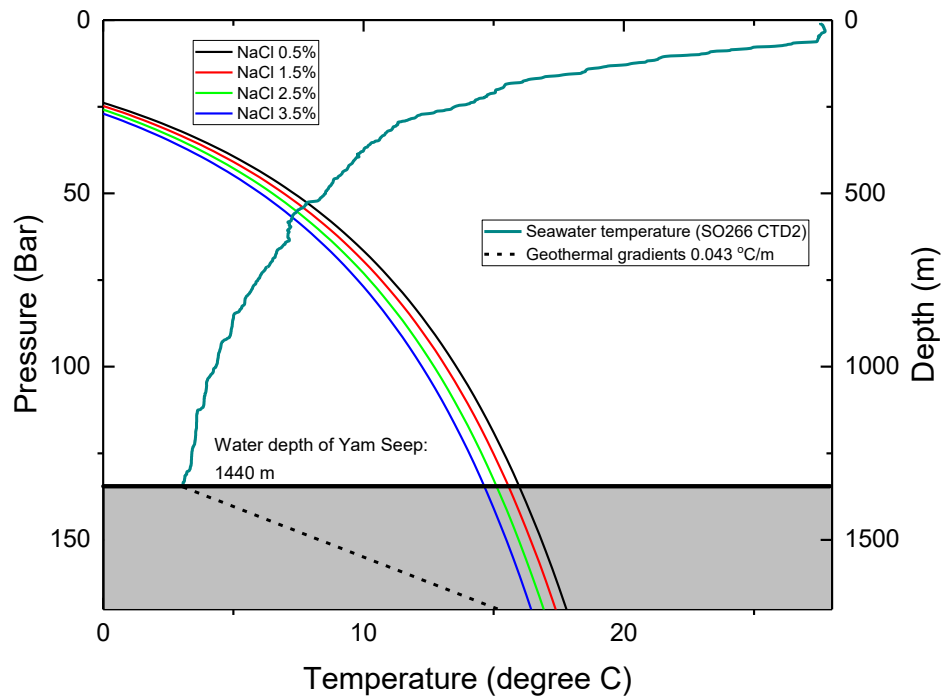


**Fig. 2.2** Phase boundaries of gas hydrate stability zone (GHSZ) calculated for gas hydrate structure I at Yam Seep. Phase boundaries (solid lines) of different salinities, 0.5 (black), 1.5 (red), 2.5 (green) and 3.5 % (blue). Seawater depth-temperature profile is determined using CTD2 SO266 (Bohrmann et al., 2019). Dashed line indicate thermal gradient of 0.043 °C/m (Bohrmann et al., 2019).

### 3. Motivation and objectives

#### 3.1. Overarching goal

This study focuses on authigenic carbonate at an active margin accretionary ridge in deep water setting (>1000m) and aims to understand the geochemical cycling and geodynamic activity. The open questions and aims of the manuscripts and preliminary studies include: (a) providing a comprehensive seabed morphology of Yam Seep regarding active seepages and carbonate depositions, (b) petrography and chronology of the carbonates precipitations, (c) the diagenetic implication and the environmental archives in the seep carbonates, (d) reconstructing the stratigraphy of free gas and gas hydrate bearing sediment during the cementing process.

#### 3.2. Open questions and aims of the three manuscripts

##### **i) Shed light on the processes: seep area morphology, active seepage and evolution**

Previous FWCR studies revealed several fossil and active seep areas that presenting hydro-acoustic water-column and morphology anomalies of rough seafloor, high backscatter signals and gas bubble “flares”. Yam Seep at the northern FWCR regarded as the active seep area, the actual seabed topography and lithology and sedimentology below Yam Seep were however had yet been proofed. Therefore, TV-sleds, and multiple coring and drilling were deployed in order to ground-truthing the Yam Seep and for better describing the distribution of seep sites, the chemosynthetic communities, the roughness that resulting from fractured carbonate crust and build-ups in the area. The aim of the first manuscript is to provide a comprehensive description of Yam Seep by correlating data of images, sampling and hydroacoustic with previous studied side-scans and high-precision bathymetry. Images and videos provide the details of carbonate crusts and build-up indicating the factors that shaping the seep area. In addition, the distribution of chemosynthetic communities suggests the hot spot of discharging, in which according to the life cycle of fauna and indicating the life span of seep episode at different region of the seep area. Finally, the objective through the comprehensive study on the seabed morphology and preliminary study on sampling is to provide an aspect of the evolution of Yam Seep.

##### **ii) Through the dimension of time: Seep carbonate microfacies and chronology**

The drilling at north western Yam Seep recovered a 5-meters-long carbonate core, MeBo-24, which presenting well consolidated carbonate rocks consist of different microfacies. Thick-succession (>50 cm) of isopaches clear aragonites are intercalated within grey micritic carbonates. As one of the key manifestations of seep site, carbonate studies have provided ample evidence regarding seep fluid sources, seepage episodes, and the interplay of gas hydrate

at seep sites. However, previous studied seep carbonates are mostly recovered from seafloor and lacking of a continuous record. Located at deep water area (>1000 mbsl), active seepage at Yam Seep potentially characterize with seepage that is devoid of the impact from climate and sea level changes. Massive well-consolidated carbonates in MeBo-24 potentially indicating long-term seepage at Yam Seep. Therefore, the objective of studying MeBo-24 is to confine the chronology and decipher the cause of different carbonate microfacies. U-Th dating provides age of aragonite precipitation suggest the sequence of precipitation regarding to the boundaries of fractured micrites. The petrography reveals that aragonite is the dominant the carbonate mineral in which consist of different aragonite forms and three different microfacies that suggesting distinct precipitate environments. Transition of microfacies and the precipitation sequence of clear aragonites project the phenomenon of fractured micritic carbonate later cementing by clear seep aragonites. Via these studies, this manuscript is resolving this the formation of the extraordinary carbonate core that interplaying the tectonic activity, carbonate fracturing, free gas and gas hydrate bearing, and clear aragonite precipitation.

### **iii) New insight of the role of seep carbonate: seep carbonates environmental archives**

Seep carbonates isotope indicate the seep fluid sources that typically characterize with positive oxygen isotope values and extremely negative carbon isotope values. Among seep carbonates, pure aragonites that are devoid of sediments and cementing micritic carbonate fractures, however, presenting seawater-like REE and uranium isotopes. The pure aragonites ambient that interplaying seawater and seep fluids and the extend of its environmental archives from uranium, oxygen and carbon isotopes have not yet by confined. Moreover, seawater oxygen isotope values does not remaining constant through the geological time thus the seep carbonate archives seepage fluid potentially be misleading due to the time of precipitation. Chronology of MeBo-24 revealed long-term seepage from 37 to 2 ka, in which ample pure aragonites providing adequate materials for establishing the isotopic values variations through LGM. Therefore, the objective of this manuscript is analysis the variation of isotopic archives of uranium, oxygen and carbon in seep aragonites.

### **3.3. Open questions and aims of the preliminary studies**

Additional findings are reported in their preliminary form, along with their tentative interpretations (Chapters 7). The following issues are the focus:

**Application of computer tomography (CT) scanning well-consolidated carbonate core for reconstructing free gas and gas hydrate bearing sediments**

CT scanning provides non-intrusion analysis for complete core composition in terms of the density and porosities, therefore it has been largely applied on sediment samples that consist of coral skeletons, breccias and other buried debris. MeBo-24 is a cavity-riched and well-consolidated carbonate core intercalate with different minerals, aragonite forms, shells and breccias. Applying CT scan on MeBo-24 is therefore perfect for archiving the comprehensive condition that intercalate shells, breccias, and different minerals potentially provide the evolution of consolidation, diagenesis and chemosynthetic communities at the seep site. Previous study suggested that the massive gas hydrates are replacing carbonate and result in clear aragonite precipitation within micritic carbonates near surface. However, the relation of gas hydrate, free gas and hosting sediments is difficult to be observed in situ. By reconstructing the structure, density and porosity of the consolidated carbonates potentially provide the evidence of the hydrate and free gas co-existing environment.

#### 4. Manuscript I: Seep area morphology, active seepage and evolution

## **Yam Seep at Four-Way Closure Ridge – a prominent active gas seep system at the accretionary wedge SW offshore Taiwan**

Yiting Tseng<sup>1</sup>, Miriam Römer<sup>1</sup>, Saulwood Lin<sup>2</sup>, Thomas Pape<sup>1</sup>, Christian Berndt<sup>3</sup>, Tzu-Ting Chen<sup>1</sup>, Charles K. Paull<sup>4</sup>, David W. Caress<sup>4</sup>, Gerhard Bohrmann<sup>1</sup>

(Published in International Journal of Earth Science, 24 December 2022)

<sup>1</sup> MARUM - Center for Marine Environmental Sciences and Faculty of Geosciences,  
University of Bremen, Klagenfurter Str., 28359 Bremen, Germany

<sup>2</sup> Institute of Oceanography, National Taiwan University, Roosevelt Road, 10617 Taipei,  
Taiwan

<sup>3</sup> GEOMAR Helmholtz-Zentrum for Ocean Research Kiel, Wischhofstr. 1-3, 24148 Kiel,  
Germany

<sup>4</sup> Monterey Bay Aquarium Research Institute, Moss Landing, 95039 California, USA

### **Keypoints**

- 1) Active Yam Seep SW off Taiwan investigated for seafloor topography, backscatter, nature of deposits and distribution of seep sites
- 2) Widespread, m-thick, fractured authigenic carbonate crusts indicate long-lasting methane seepage and tectonic activity
- 3) Clustering of active seep sites along the edges of the seep area suggests seafloor sealing by carbonates and lateral deflection of rising gas

## **Abstract**

Hydroacoustic surveys at the accretionary wedge southwest of Taiwan identified a confined active hydrocarbon seepage area of  $\sim 49,000 \text{ m}^2$  in  $\sim 1,350 \text{ m}$  water depth on the northern crest of the Four-Way Closure Ridge, which we called Yam Seep. In this study, multibeam and side-scan sonar data acquired during surveys with an AUV during an expedition with RV Ocean Researcher I in 2017 showed that the seep area is characterized by rough topography and high seafloor backscatter. Seafloor observations with a video sled and sediment sampling with gravity cores and MeBo drillings during an expedition with RV SONNE in 2018 revealed that the area is almost entirely covered by heavily fractured methane-derived carbonates, which indicate that seepage has been ongoing for thousands of years. Hydroacoustic anomalies ('flares') in the water column indicated the presence of several gas bubble emission sites mostly at the center and eastern flank of the area in 2019. Drilling through massive carbonates in the northwestern part of the seep area induced free gas escape from a depth of  $\sim 5 \text{ m}$ . As the seep area is located within the gas hydrate stability zone, the presence of gas hydrates in the subsurface is inferred. The inter-disciplinary investigations of the Yam Seep demonstrate that upward migration of methane from the accretionary ridge and its discharge at the seafloor has a considerable influence on the seabed properties. Development of the Yam Seep is attributed to the continued lateral compression and uplifting within the accretionary wedge.

## **Keywords**

Methane seepage, authigenic carbonates, chemosynthetic fauna, gas hydrate

## **Statements and Declarations**

The authors declare that they have no known competing financial interests or personal relationships that could have appeared to affect the work reported in this paper.

#### 4.1. Introduction

Fluid flow, dewatering and the ascent of gassy hydrocarbons through ocean sediments are fundamental processes of the Earth's carbon cycle. Such processes not only affect geochemical budgets of the ocean, but migration of fluids and volatiles also plays an essential role in triggering geologic processes like submarine landslides, earthquakes, and mud volcanism (Kastner et al., 2014). Subsurface fluid circulation systems at the seafloor can result in focused emission of fluids and/or gaseous compounds into the ocean as cold seeps. These sites are geological windows that can provide important information on the transfer processes and reactions in the geosphere below (Suess, 2014). Chemosynthetic communities that utilize the chemical energy of reduced compounds such as CH<sub>4</sub>, H<sub>2</sub>S and other light hydrocarbons are frequently associated with fluid outflow at seeps (Rubin-Blum et al., 2017; Sahling et al., 2002). Similar to hot vents, cold seeps support the growth of tube worms, vesicomyid, and mytilid bivalves, as well as sulfide-oxidizing bacteria (Sibuet and Olu, 1998). Biomass production by these communities can be several orders of magnitude higher than typical densities at non-seep environments on the nearby ocean floor (MacAvoy et al., 2002). Authigenic mineral precipitates are further obvious seafloor manifestations of cold seep. Methane-seep deposits are typically dominated by carbonates, but a variety of other precipitates including barite, iron sulfides and gas hydrates are also common (e.g., Bohrmann et al., 1998; Fan et al., 2018; Tong et al., 2013; Torres et al., 1996). Mineral authigenesis is linked to biogeochemical cycling of carbon and sulfur (Claypool and Kaplan, 1974; Berner and Raisell, 1983; Berner, 1990). Carbonate precipitation is induced by the anaerobic oxidation of methane (AOM), and typically occurs at the base of the sulfate reduction zone, which, at methane seeps is often situated close to the seafloor (Paull et al., 1992; Boetius et al., 2000). Due to highly dynamic processes at seeps, the morphology of the seafloor may change during the seepage processes and distinct bottom features are created, like pockmarks, bulges or very irregular surfaces instead of otherwise plain seafloor (Judd and Hovland, 2007; Paull et al. 2015).

Cold seeps occur along all continental margins. At active margins, plate convergence and strike-slip faulting are driving tectonic fluid expulsion by dewatering of sediments, which is generating seep fluids from different depths (Scholl and von Huene, 2007). Cold seeps at active plate boundaries were reported from Aleutian trench (Suess et al., 1998), Cascadia margin (Suess et al., 1985;), Costa Rica (Bohrmann et al., 2002), Hikurangi Margin (Greinert et al., 2010), Makran Trench (Römer et al., 2012), Nankai Trough (Sato et al., 2012) and many other oceanic to continental plate collision zones. Fluid expulsion at passive margins is frequently driven by sediment loading, differences in compaction, saline fluids resulting from contact with



evaporitic rocks, and migrating hydrocarbons. Such seep sites were documented at margins of the North Atlantic (Paull et al. 1995; Skarke et al., 2014), in the Gulf of Mexico (MacDonald et al., 1990), the Black Sea (Klaucke et al., 2006), the Congo deep-sea fan (Sahling, et al., 2008; Pape and Bohrmann, 2021) and many other locations of passive margins.

The area studied herein is located in the South China Sea. Convergence of the Philippine Sea plate and the Eurasian plate form an active margin in the east and rifting formed the passive margin in the west (Bowin et al., 1978). Seep research was first focused on the passive margin of the South China Sea, where a Chinese-German research cruise in 2004 discovered seep carbonates being exposed in a large area named “Jiulong methane reef” (Han et al., 2008). Similar methane-derived carbonates, dead and living chemosynthetic bivalves and other seep manifestations were found at northern and southern continental margins of the South China Sea (Feng , Yang, et al., 2018). Detailed investigations using diving platforms like submersibles and ROVs have been performed at active seep sites on Formosa Ridge (Lin et al., 2007; Fujikura et al., 2007; Machiyama et al., 2007) on the Northeastern slope and at “Haima” seep on the Southwestern slope of the South China Sea. Both sites are well known for their active gas emissions, methane-derived carbonate precipitates, specific biomarkers and chemosynthetic bivalves (Feng, Qiu, et al., 2018; Liang et al., 2017; Wei et al., 2020).

In contrast to the passive margins, seeps at active margins in the South China Sea are less well investigated, although elevated concentration of methane are known to commonly occur within the seafloor sediments and lowermost water column (Chen et al., 2017; Chuang et al., 2019; Chuang et al., 2013; Chuang et al., 2010). Geophysical indications for the widespread presence of gas hydrates also occur within the accretionary prism southwest of Taiwan (Schnürle et al., 2011). Klaucke et al. (2016) investigated seepage at ~1,500 meters below sea level (mbsl) at the so-called Four-Way Closure Ridge (FWCR) by analyzing high-resolution bathymetry, deep-towed side-scan sonar imagery, high-resolution seismic profiling and towed video observations. A prominent seep area was identified on top of the northern FWCR characterized by patches of high seafloor backscatter. Seafloor video observations showed active gas emissions, the presence of extensive authigenic carbonate slabs and chemosynthetic bivalves (Klaucke et al. 2016).

During a drilling cruise in 2018 using the remotely operated drill rig MeBo200 onboard RV SONNE we re-visited the main seep area described by Klaucke et al. (2016) in order to characterize this seep area. Since the shape of the seep area resembles the root vegetable “yam”, which is a very popular local food, especially when it was made into QQ ball, we call the area “Yam Seep”. In this study, we present new and comprehensive results with high resolution

video survey from the Yam Seep together with micro-bathymetry data collected with an autonomous underwater vehicle during a previous cruise.

#### 4.2. Regional setting of the study area

Located at the convergent margin of the Eurasian plate and the Philippine Sea plate, southwestern offshore Taiwan is characterized by a deformation front where the South China Sea lithosphere is subducted underneath the Philippine Sea plate. The Philippine Sea plate is moving in a northwestern direction against the Eurasian plate (Fig. 4.1a) with a convergence rate of  $\sim 8$  cm/yr (Ustaszewski et al., 2012). The collision initiates during middle and late Miocene (Bowin et al., 1978) causing the formation of a series of accretionary ridges, faults and thrust faults, which consequently creating pathways for fluid and gas migration, mud volcanoes, and cold seeps at the seafloor (Liu et al., 1997; Liu et al., 2006). The accretionary wedge has been divided into an upper slope and a lower slope (Fig. 4.1a) (Klaucke et al., 2016; Liu et al., 1997; Liu et al., 2006). The upper slope domain in shallow water hosts a series of mud diapir intrusions, mud volcanism, and related active gas and mud extrusion (Chen et al., 2020; Chen et al., 2014). The relatively deeper, lower slope domain includes ridges of active thrusting and folding and cold seep sites (Chuang et al., 2019; Chuang et al., 2013; Chuang et al., 2010; Fan et al., 2018). The Four-Way Closure Ridge (FWCR), which hosts the seep area studied herein forms one of the well-developed accretionary ridges (Fig. 4.1b).

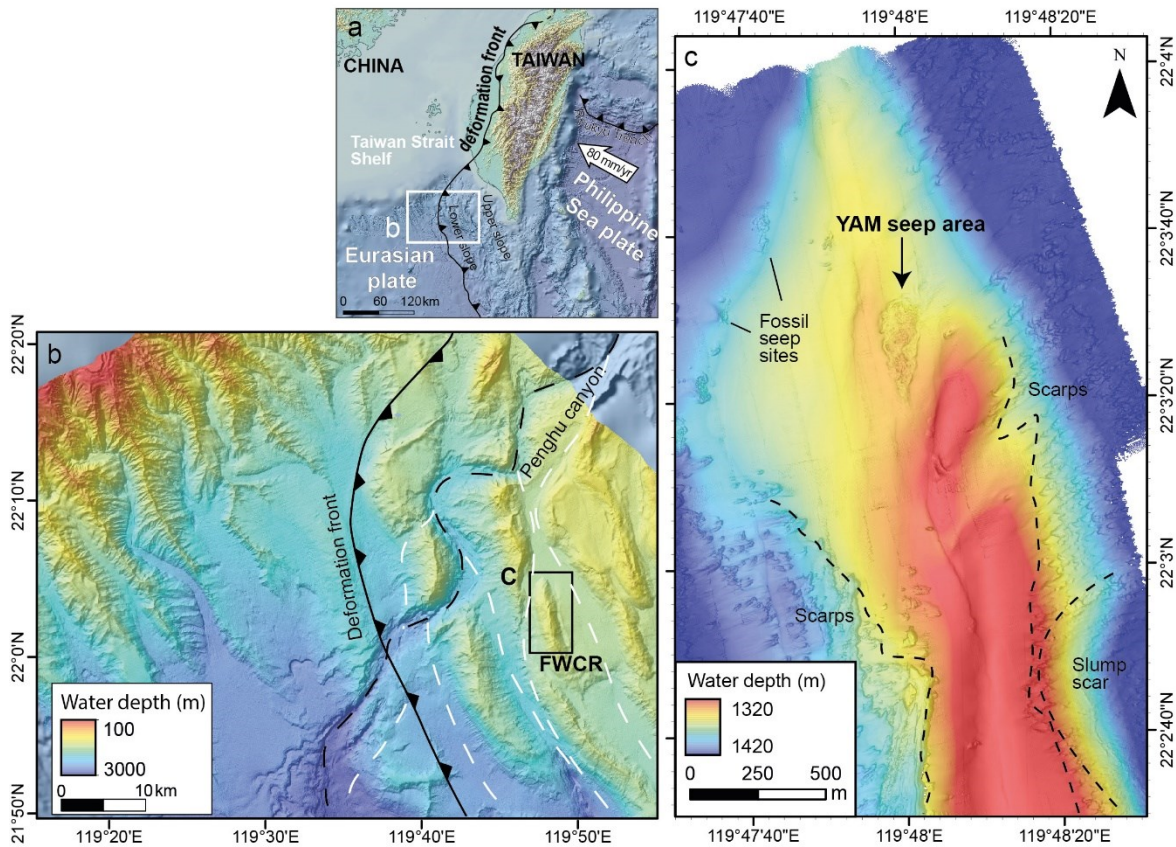


**Fig. 4.1** Tectonic setting of offshore SW Taiwan. (a) Location of accretionary prism SW offshore Taiwan: the deformation front, which is forming the boundary of the Philippine Sea

plate and the Eurasian plate at the seafloor. (b) Detailed bathymetric map of the transition area from the passive margin in the west to the active margin in the east showing locations of the deformation front (black solid line with arrows) and of NE-SW-trending ridges. Present Penghu canyon is shown with a black dashed line and the former canyons are marked by white dashed lines (Klaucke et al., 2016; Liu et al., 1997; Yu and Chang, 2002). (c) AUV-derived 1-meter scale bathymetry map showing the northern sector of Four-Way Closure Ridge (FWCR) and Yam Seep. Several fossil seep sites, scarps, and slump scars in the area had been reported by Klaucke et al. (2016) and Chen et al. (2020).

FWCR is a complex anticlinal elongated structure of approximately 10 km in length. It is orientated in a NNW-SSE direction parallel to the deformation front. It is located at ~1,500 mbsl and towers up to 350 m above the surrounding seafloor (Fig. 4.1c). Chen et al. (2020) identified scarps associated with the western and eastern flank of FWCR and Klaucke et al. (2016) suggested the presence of slump scars on its eastern flank (Fig. 4.1c).

The south-western Taiwan accretionary prism is characterized by one of the highest weathering rates in the world, and the sediment flux toward SW offshore is estimated to account for 99 Mt/yr (Dadson et al., 2003). These sediments are transported into the South China Sea through submarine canyons, including the Penghu canyon, which controls the erosion of slope sediments along the submarine ridges, and are prominent erosive conduits on the active margin. Penghu canyon was probably once located closed to FWCR, as revealed by seismic data showing similarities of deposits at the eastern flank of FWCR, suggesting removal of paleo seafloor (Klaucke et al., 2016; Kunath et al., 2020).

The Yam Seep studied herein is located at the northern crest of FWCR. It is situated on top of an extensional fault network with the main thrust fault structures on its western limb (Kunath et al., 2020). Fluids ascend along the thrust faults and extensional fault systems at shallow depth (Kunath et al., 2020). Bubble emission activity at the seafloor of the Yam Seep has been reported by Klaucke et al. (2016). Mau et al. (2020) reported enrichments of dissolved methane in near-bottom water samples collected in 2018 and showed that the Yam Seep is generally bathed in high salinity deep water. Several fossil seep sites inferred from backscatter anomalies were reported from a close-by area to the northwest of the Yam Seep (Klaucke et al., 2016; Chen et al., 2020) (Fig. 4.1c).

#### 4.3. Materials and Methods

This study is based on data obtained during a research cruise with RV Ocean Researcher I (ORI-1163) conducted in May 2017 and during research cruise SO266/1 on RV SONNE conducted in October/November 2018. Multibeam bathymetry, seafloor backscatter and side-scan sonar data conducted via autonomous underwater vehicle (AUV) were also collected in May 2017 during cruise ORI-1163. Multibeam bathymetry, seafloor and water column backscatter via the ship-borne system, seafloor observation image, sediment cores, and seawater samples were collected during cruise SO266/1. The geo-information system (GIS) software ESRI ArcGIS™ vers. 10.4 was used to create maps and sustainable spatial management of the data obtained during the cruises. The correlated bathymetry and backscatter intensity profiles along the studied track lines were plotted using ArcMap 10.7 3D analyst tool.

##### 4.3.1. Multibeam echosounder data acquisition and processing

A Dorado class autonomous underwater vehicle (AUV) developed and operated by the Monterey Bay Aquarium Research Institute (MBARI) (Caress et al., 2008) was used to collect multibeam bathymetry and side-scan sonar backscatter of the FWCR, including the Yam seep site. The AUV was equipped with a Reson 7125 400 kHz multibeam and Edgetech 110 kHz chirp side-scan sonar, both yielding mapping data with a lateral resolution of 1 meter. The survey was flown at a 50 meter altitude with a 150 meter survey line spacing. The AUV survey starting position was initialized using tracking from the GPS navigated ship using an ultra short baseline (USBL) sonar. The realtime survey navigation derived from a Kearfott inertial navigation system that limits navigation drift to less than 0.05% of distance traveled when aided by velocity estimates from a 300 kHz Doppler velocity log.

Seafloor bathymetry, seafloor and water column backscatter were also obtained using the hull-mounted Kongsberg EM122 multibeam echosounder during RV Sonne cruise SO266. The sonar frequency of the EM122 is 12 kHz with an angular coverage sector of up to 150° and 288 beams per ping.

The open source software package MB-System (vers. 5.5.2213 & 5.5.2289; Caress and Chayes, 1995) was used for post-processing of multibeam bathymetry and AUV sidescan data. The AUV navigation was adjusted so that features match in overlapping and crossing swathes using the MB-System tool MBnavadjust. Water column data were displayed and edited to extract hydroacoustic anomalies attributed to rising gas bubbles ('flares') and allowed for manual flare identification and geo-picking of flare sources at the seafloor using the QPS software FMMidwater tool box and Fledermaus. The seafloor footprint of a flare in the multibeam

records was measured at ~50 m in diameter, revealing the approximate error of the seep location. Flare sources of different crossings located within the seafloor footprint were grouped in flare source areas. The 3D projection of extracted anomalies was edited and displayed using the QPS software Fledermaus (Version 7.7.2). The position of AUV multibeam grids was adjusted to fit with the GPS navigated ship-based bathymetry using the Global Mapper ® (Blue Marble Geographics) application software. The water column flare data sets and detailed bathymetric data were displayed using the 3D Fledermaus software (QPS).

#### 4.3.2. Coring and drilling

During cruise SO266/1, sediment and carbonate cores offshore SW Taiwan were drilled at two sites using the MARUM seafloor drill rig MeBo200 (Table 4.1, Fig. 4.2b). Sediment core MeBo-28 (GeoB23234-1) was drilled at the eastern flank of the Yam Seep at 1,348 mbsl (Fig. 4.2b). At this station, a drilling depth of 59.9 meters below seafloor (mbsf) with a core recovery of 50.5 m was achieved. Hole MeBo-24 (GeoB23225-1) was drilled in the northwestern part of the seep area at 1,347 mbsl, down to ~5.1 mbsf. At this station, cemented carbonates were drilled with a core recovery of 4.7 m and the drilling was aborted when significant amounts free gas started to escape from the borehole.

Four gravity cores were designed to core shallow deposits at the Yam Seep and its periphery (Fig. 4.2b). Two cores GC-1 and GC-2 (GeoB23203-1 and GeoB23203-2, respectively) were located in the central area of the seep area, whereas cores GC-4 and GC-8 (GeoB23211-1 and GeoB23233-1, respectively) were taken close to the eastern rim of the seep area (Table 4.1, Fig. 4.2b).

**Table 4.1:** List of gravity coring sites and MeBo drilling sites.

Tool	GeoB No./ Station	Water depth (mbsl)	Lat. (N)	Lon. (E)	Sampling depth (mbsf)	Comment
Gravity cores	23203-1/ GC-1	1,358	22°03.518	119°48.007	0	No recovery
	23203-2/ GC-2	1,359	22°03.521	119°48.014	0	No recovery

	23211-1/ GC-4	1,354	22°03.465	119°48.036	5.1	Carbonates at 4.7 and 4.8 mbsf
	23233-1/ GC-8	1,356	22°03.478	119°48.039	7.2	Carbonates at 5.1 mbsf and pyrite at 5.9 mbsf; erosional surface at 5.1 mbsf
MeBo core	23225-1/ MeBo-24	1,352	22°03.487	119°47.979	5.1	Interrupted due to gas eruption. 4.7 m core recovery; almost entirely carbonate.
	23234-1/ MeBo-28	1,355	22°03.461	119°48.049	59.9	50.5 m core recovery; erosional surface at ~6 mbsf.

#### 4.3.3. Stable carbon isotope analysis of authigenic carbonates

Powdered carbonate sub-samples were reacted to carbon dioxide (CO<sub>2</sub>; by 100% phosphoric acid at 75 °C) and stable carbon isotope ratios (<sup>13</sup>C/<sup>12</sup>C reported as δ<sup>13</sup>C in ‰ vs. V-PDB) of the released CO<sub>2</sub> were analyzed with a Finnigan MAT 251 mass spectrometer at the Stable Isotope Laboratory at MARUM. For details of the procedure see Loher et al. (2018)

#### 4.3.4. Visual seafloor observation

The towed Ocean Floor Observation System (OFOS) on RV SONNE was used for visual seafloor documentation of the Yam Seep during two surveys (OFOS-1 (GeoB23202-1); OFOS-2 (GeoB23206-1); Fig. 4.2a). The OFOS was equipped with a HD dynamic color video camera (Micro Sea Cam 2002) and a high resolution still frame camera (Canon EOS 5D Mark IV). Positioning of the OFOS was tracked by the IXSEA ultra short baseline (USBL) system. Scale at the seafloor was provided by three laser pointers (Micro-Sea-Laser) of known distance between two laser points (20 cm).

#### 4.3.5. Spatial distribution of dissolved methane in the near-seafloor water body

Four vertical hydrocasts were conducted along a 220 m long transect across the Yam area on October 20, 2018 (GeoB23208-1, -2, -3, and -4, Table 4.2). The concentration of dissolved methane in the near-bottom waters was previously reported by Mau et al. (2020) in a study off methane over a larger region. In this study, differences in concentrations of dissolved methane are presented with respect to relative positions above the seep structure.

**Table 4.2:** List of CTD sampling sites and depths. GeoB no.: Internal code for stations and samples.

<b>GeoB No.</b>	<b>Station</b>	<b>Water depth</b>	<b>Lat.</b>	<b>Lon.</b>	<b>Sampled water depth</b>
		(m)	(N)	(E)	(m)
23208-1	CTD-2-1	1,349	22°03.428	119°47.963	1,339, 1,334, 1,329, 1,324, 1,319
23208-2	CTD-2-2	1,347	22°03.461	119°48.000	1,337, 1,332, 1,327, 1,322, 1,317, 1,311
23208-3	CTD-2-3	1,355	22°03.471	119°48.039	1,345, 1,340, 1,334, 1,329, 1,325, 1,320
23208-4	CTD-2-4	1,357	22°03.479	119°48.064	1,347, 1,342, 1,337, 1,333, 1,327, 1,322



#### 4.4. Results and Discussion

##### 4.4.1. Seafloor bathymetry and general composition of deposits

The Yam Seep is located on the summit line of the FWCR at ~1,347 mbsl (Fig. 4.1c, 4.2a). The seep area is identified as an area with distinctly rougher seafloor, compared with the relatively smooth seafloor in the surrounding area. The seafloor is also characterized by anomalously high seafloor backscatter (Fig. 4.2b). Together they form a triangular-like shape of ~400 m maximum length and ~175 m maximum width (Fig. 4.2b). The total seafloor area characterized by rugged bathymetry is ~49,000 m<sup>2</sup>, whereas the area showing relatively higher seafloor backscatter accounts for ~37,000 m<sup>2</sup>. Both the rough seafloor and high backscatter are considered to seepage-related features, such as high density of authigenic carbonate crusts.

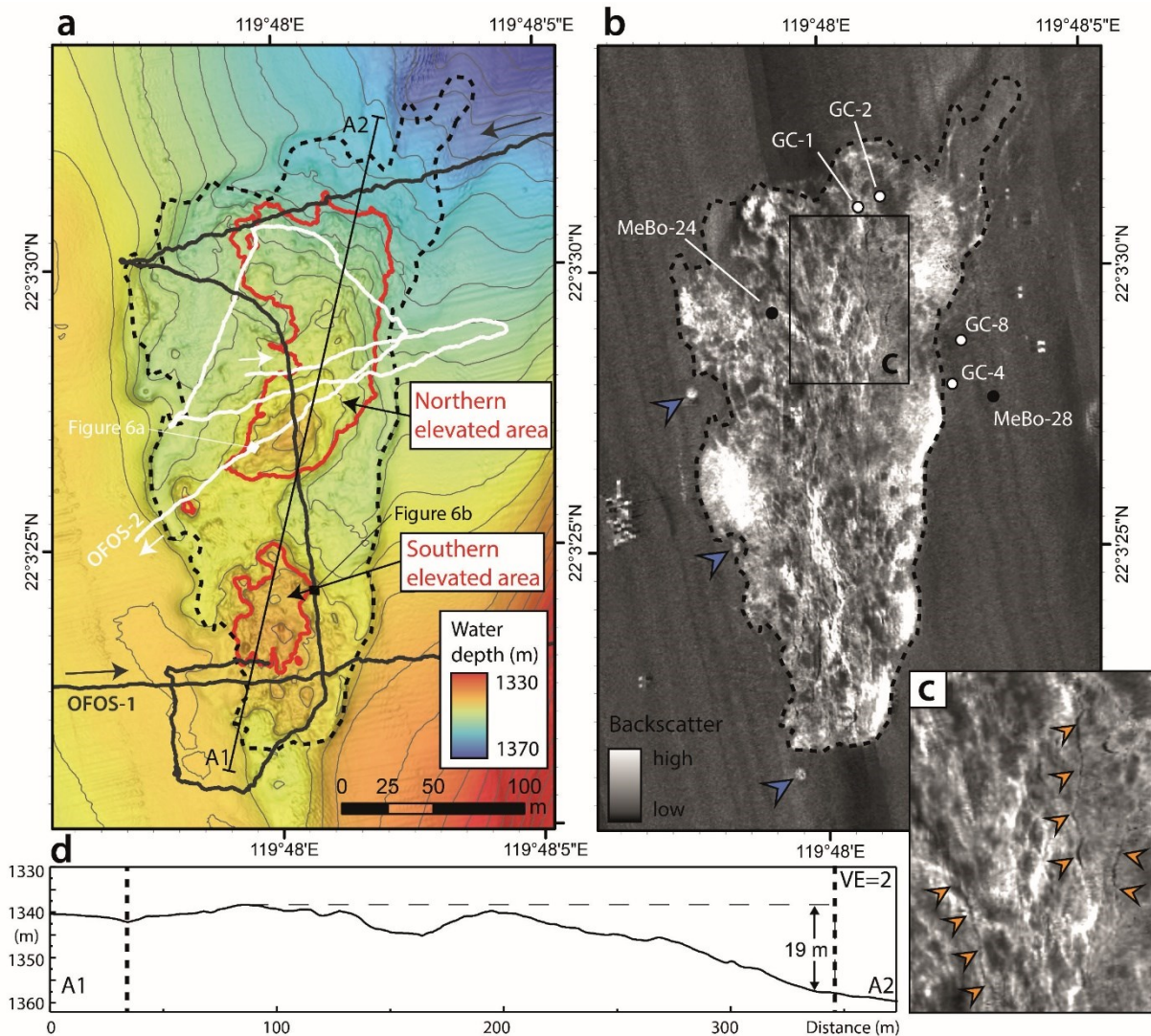


**Fig. 4.2.** (a) AUV-based micro-bathymetry of the Yam Seep with tracks of the two OFOS deployments. Black dashed line outlines the area of relatively high backscatter, i.e. the main seep structure (adopted from Figure 2b). Red outlined areas illustrate relatively elevated. (b) AUV-based seafloor backscatter map of Yam Seep illustrating relatively higher backscatter values in contrast to homogeneous, low seafloor backscatter in the surrounding. Blue arrows indicate separate, small sized high-backscatter patches outside the perimeter of the main seep

area. White and black dots indicate locations of gravity cores (GC) and MeBo drill sites. (c) AUV-based seafloor backscatter map outlined in Fig. 4.2b with the lighter color being higher backscatter. Orange arrows mark pronounced linear features. (d) Topographic profile 'A1-A2' (location depicted in Fig. 4.2a) indicating a general incline of the seafloor towards northeast with a slope angle of  $\sim 2.8^\circ$ . Dashed line indicates the highest elevation along the profile, which is about 19 m lower at A2.

In order to distinguish relative depths within the seep area, a reference plane was created assuming an undisturbed seafloor (Fig. 4.2a). The intersection between this plane and the measured seep influenced seafloor separates the so-called northern and southern elevated areas to the surrounding deeper seafloor regions. Within the Yam Seep there are two elevated areas (Fig. 4.2a). The southern elevated area is an elliptically-shaped mound that peaks at a water depth of 1,337 mbsl (Fig. 4.2a). The northern elevated area is characterized by an elongated structure, which reveals two peaks located in its central and western parts. The SW-NE trending topographic profile (profile A1-A2, Fig. 4.2d) crossing two local elevated areas shows a general seafloor tilting of  $\sim 2.8^\circ$  and a total water depth variation of 19 m.

The seep area shows an inhomogeneous, reticular appearing backscatter pattern, which is mainly N-S to NW-SE directed. Highest intensities were found along the rim of the seep area, with the largest high-backscatter area at the western rim (Fig. 4.2b). N-S-oriented high backscatter branch-like patterns correlate well to the location of seafloor fractures illustrated in the micro-bathymetry map (Fig. 4.2a and 4.2b). Three separate high seafloor backscatter patches of  $\sim 7$  m in diameter were identified a few meters to the west and south of the main seep structure within circular seafloor depressions (Fig. 4.2a and 4.2b).

The failure of two gravity corer deployments (GC-1 and GC-2) to recover sediments (Fig. 4.2a, Fig. 4.3) are assumed to result from the presence of carbonates in near-surface sediments, which prevented penetration. Visual inspection during landing of the MeBo system at station MeBo-24 showed a flat sediment covered surface. Drilling at this station had to be aborted at a coring depth of  $\sim 5$  m (Fig. 4.3), because of virulent escape of bubble-forming gas that apparently was ascending from below this depth. Core MeBo-24 revealed about 5 m of carbonates consisting of whitish botryoidal and acicular aragonite mineral, grayish micrite, and cemented shells, which likely have sealed the pathway to rising free gas from the deeper accretionary structure. Stable carbon isotope signatures of the carbonates ( $\delta^{13}\text{C-CaCO}_3$ ) ranging from  $-37.9\text{‰}$  to  $-58.3\text{‰}$  V-PDB, suggest that they represent methane-derived authigenic carbonates (Naehr et al., 2007) with the carbon incorporated primarily resulting from the AOM.

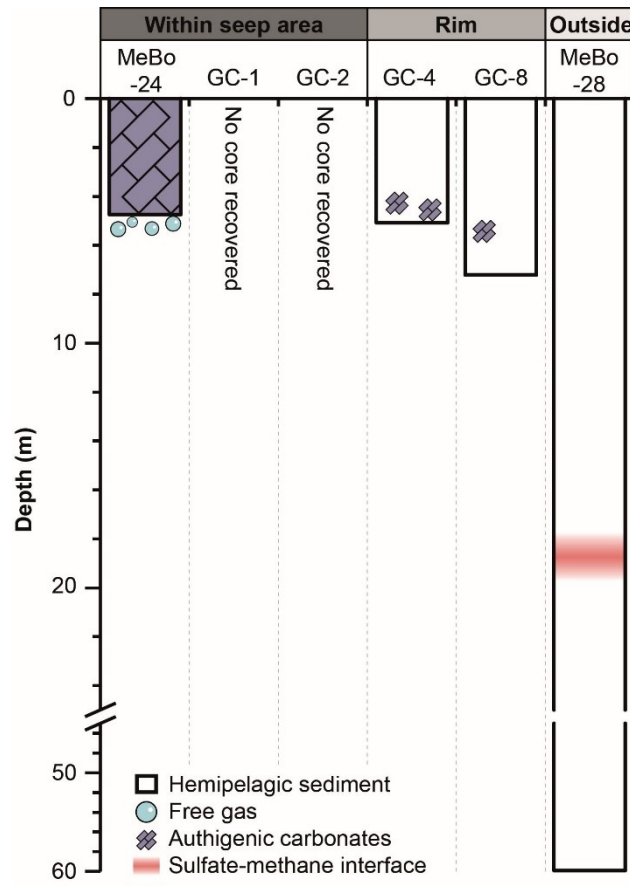


**Fig. 4.3.** Schematic core descriptions of MeBo and gravity cores (GC) taken within, at the rim, and outside the Yam Seep. See Fig. 4.2a for core locations.

Sediments were recovered at stations GC-4 and GC-8 close to the eastern rim of the Yam Seep and at station MeBo-28 further east of the seep area (see Fig.4.2b for locations). Concentrations of sulfate dissolved in pore waters extracted from these cores showed only slight depletions with depth (Lin et al., personal communication). This indicates that the zone of the sulfate-methane-interface (SMI) was situated well below 4.8 mbsf (GC-4) and 6.9 mbsf (GC-8), respectively these cores penetrated and indicates the present methane upward flux of methane is low at these sites at present (see e.g., Borowski et al., 1996). Core MeBo-28 was located further east of the seep area (Fig. 4.2b) and recovered sediments down to 59.8 mbsf. The pore water sulfate concentrations indicate a modern SMI located at ~14-20 m (Lin et al. personal communication; Fig. 4.3). Carbonate precipitates were present in core GC-4 at 4.7 m and 4.8 mbsf depth, and in core GC-8 at 5.1 mbsf (Fig. 4.3).

#### 4.4.2. Spatial distribution of seepage sites and temporal variability of gas ebullition

During the Sonne cruise in October 2018 hydroacoustic anomalies in the water column indicative of seafloor gas bubble emissions, called flares, were recorded during eight crossings of the Yam Seep. Vertical seafloor projections of the flares, called flare source points, suggested seafloor gas emissions from 41 seafloor sources (Fig. 4.4b). However, due to echosounder footprint and the corresponding uncertainties of the flare source point locations, we postulate a minimum of eight flare source areas (Fig. 4.4a) including repeated sightings of flares from the same source areas. Flare source points interpreted in 2018 were mainly concentrated along the north-eastern rim and the center of the seep area. Such flares could be traced from the seafloor to about 880 m above seafloor (550 mbsl) (Fig. 4.4c). The AUV flare survey conducted in spring 2017 revealed the presence of two bubble emission sites located at the northern center of the seep area (Fig.4.4a). While one site was located inside the flare source area interpreted from the ship-based flare detection in 2018, no gas emission was observed for the other site in 2018.

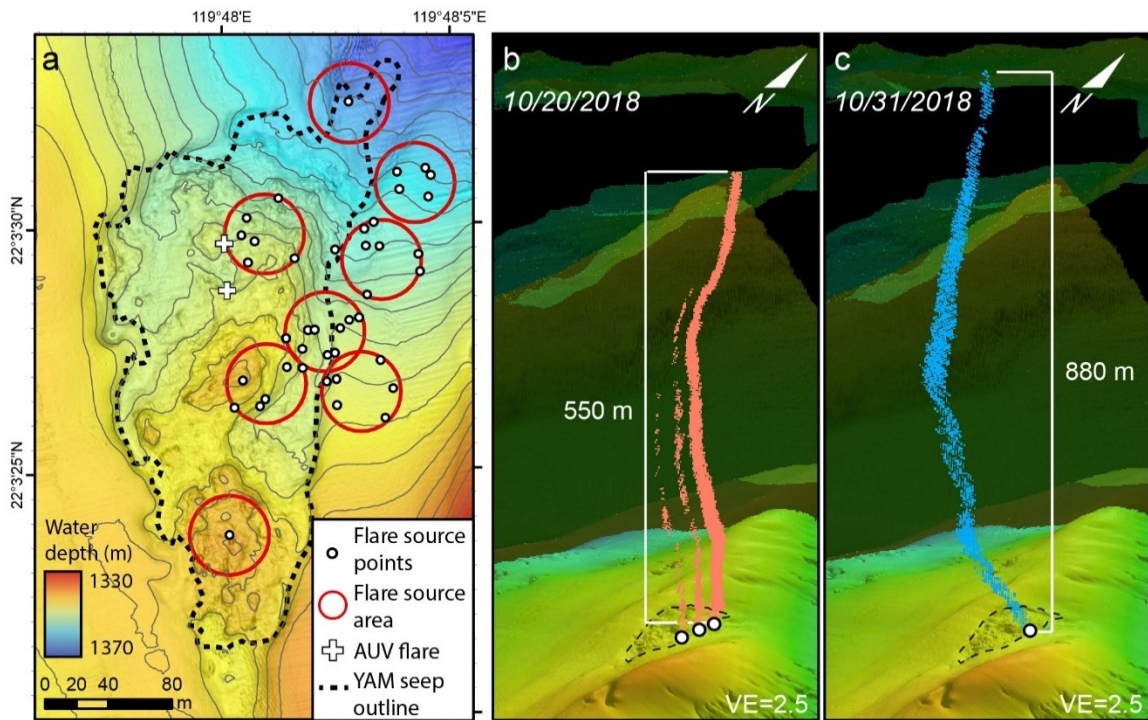


**Fig. 4.4.** Positions of gas seepage sites and shape of hydroacoustic anomalies in the water column that are diagnostic of rising gas bubbles ('flares') at the Yam Seep. (a) Positions overlying the Yam Seep. (b) Perspective view from SE showing three separate flares above the north-eastern rim on October 20, 2018. (c) Perspective view from SE showing one flare above the north-eastern rim on October 31, 2018.



3D flare extractions enabled the variation of bubble emission sites, bubble rise, and intensity to be illustrated. Multiple flares were sometimes observed to occur simultaneously, with three simultaneous flares on 10/20/2018 with heights of maximum 550 m (Fig. 4.4b). The highest single flare during a crossing on 10/31/2018 reached a height of ~880 m above the seafloor (Fig. 4.4c).

These results indicate that while gas bubble seepage has persisted for at least several years within the Yam Seep, the particular venting sites varies spatially and temporally. Our flare analysis revealed that gas bubble emission in 2018 was sourced from at least eight areas along the north-eastern rim and from central areas of the Yam Seep. However, the bubble ebullition was spatially and temporally variable during different years and even different days of observation.

The variations in the dissolved methane concentrations in discrete water samples collected over the Yam Seep in 2018 (Mau et al., 2020) while the pattern of variation might match with the pattern suggested by the hydroacoustic investigations. Maximum concentrations of dissolved methane (18.2 nmol/L) were measured in a water sample collected ~5 meter above seafloor (1,399 mbsl) at the western rim of the seep area during station CTD-2-1 (Fig.4.5). Elevated methane concentrations of up to 10.3 nmol/L were also measured in samples taken at the eastern rim of the seep area at ~5 and 10 meter above seafloor (1,340-1,345 mbsl) during CTD-2-3. Concentrations of dissolved methane in water samples from above the central seep area (cast CTD-2-2) ranged between ~5.5 and ~6.4 nmol/L, with highest relative concentrations close to the seafloor. Water samples from about 50 m east of the seep area (cast CTD-2-4) showed similar concentrations ranging from ~6.0 to ~6.6 nmol/L, again with a slight decrease with decreased water depth.

Although bottom water currents have not been investigated in this study, the relatively low CH<sub>4</sub> concentrations measured in water samples collected at casts CTD-2-2 and CTD-2-4 support the observation that most of seafloor gas emissions at the Yam Seep occurred from its rim in 2018. Seepage of dissolved methane from the northern central sector of the seep area cannot be excluded. According to seawater temperature and salinity, methane concentration in-situ atmospheric equilibrium would be 3.6 nM, our measured concentrations are all much higher. Therefore, it is probably focused at spatially limited areas like fractures, might be temporally more variable and, thus, less significant. The cause(s) for the methane enrichments in water samples collected from the western rim of the Yam Seep (cast CTD-2-1) may be explained by i) the presence of diffusive gas seepage sites, ii) temporal variability of gas seepage, and iii) lateral transport of water masses enriched in methane. It should be noted, however, that data

from a single station conducted are not representative for the entire seep area, as visual observations revealed the heterogeneity of recently active areas and carbonate precipitates partly preventing and focusing fluid flow.

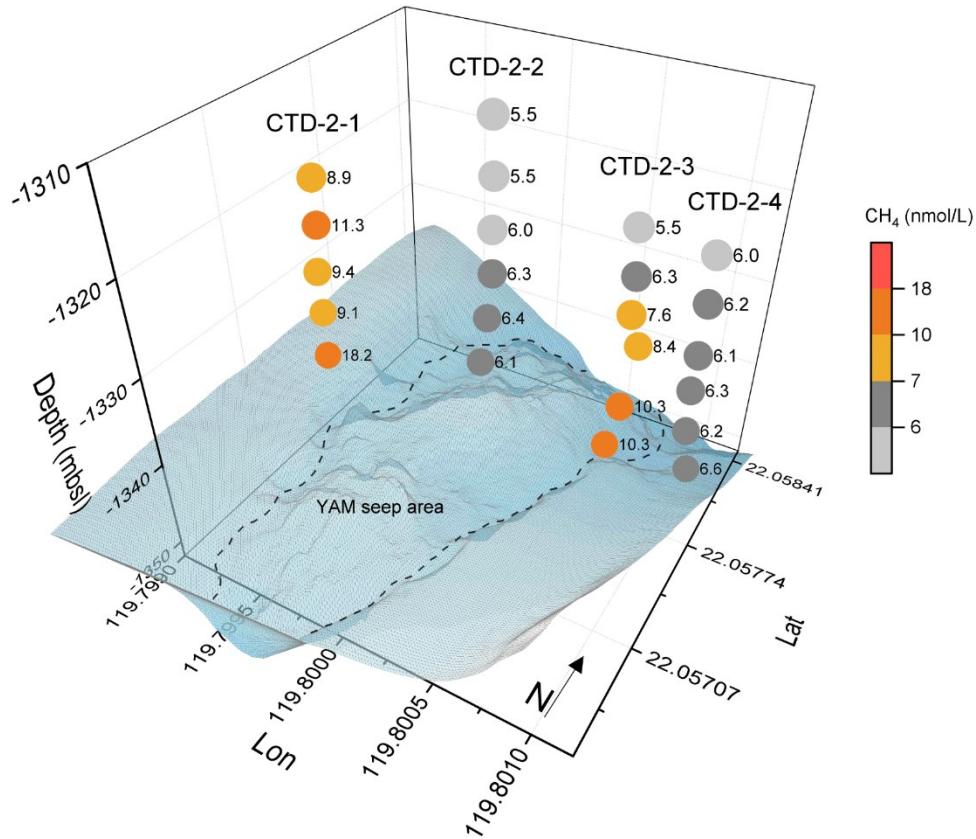


**Fig. 4.5.** Ex-situ concentrations of methane dissolved in water samples taken during CTD station GeoB23208 (4 separate casts) across the center of the Yam Seep in W-E direction on October 20, 2018 (Mau et al., 2020). Numbers at circles indicate concentrations of dissolved methane (in nmol/L) VE = 5.

#### 4.4.3. Visual seafloor observations of seep indicators

Visual seafloor observation during surveys with the OFOS enabled analyzing the characteristics of seafloor deposits and distributions of hydrocarbon seep-related benthic fauna along the tracks. Constrained by the life cycle, living chemosynthetic fauna indicate recent fluid availability, while authigenic carbonates document long-lasting (paleo)-seepage.

#### 4.3.1. Properties and distributions of exposed carbonates as indicators of paleo-seepage

The rough topography of the Yam Seep, in general, is associated with exposed carbonates, which occur widespread as crusts, and/or irregular outcrops. Carbonate crusts are relatively massive and thick carbonate formations occasionally seem to comprise several layers (e.g., Fig.4.6a and 4.7b) or form comparably thin layers with smooth surfaces (e.g., Fig. 4.9c). Irregular shaped masses of free-standing carbonates are also seen (e.g., Fig. 4.6b).

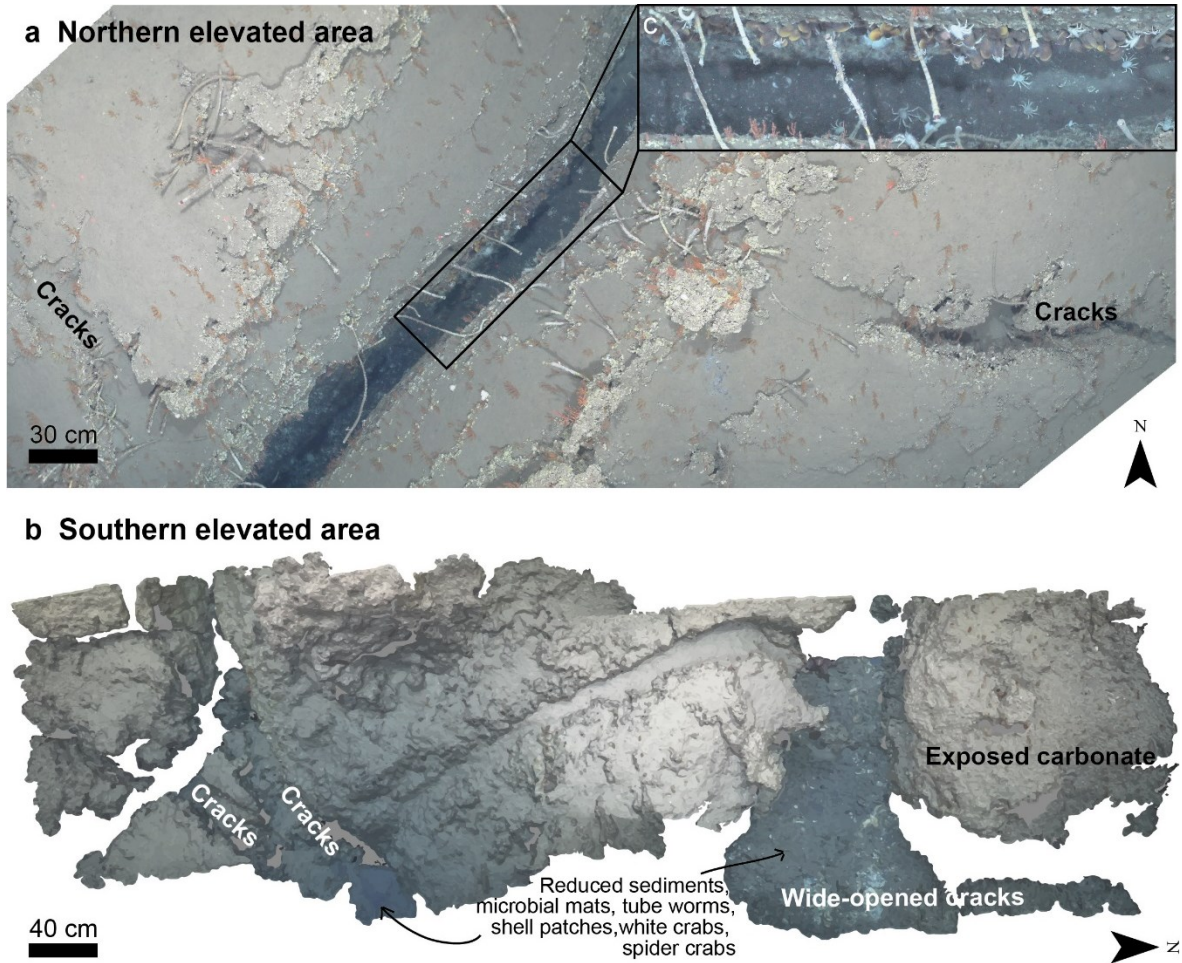


**Fig. 4.6.** Seafloor pictures taken during OFOS deployments at the Yam Seep. (a) Photomosaic of fractured carbonate crust at the northern elevated area. Individual tube worms rooting below the carbonates. Enlarged section shows mussels, crabs, and anoxic sediments at the bottom of the fracture. Photographs taken during OFOS-2. (for exact position see Fig. 4.2a) (b) Orthomosaic of fractured authigenic carbonates at the southern elevated area. Anoxic sediment and fauna, including tube worms, vesicomyid clams, galatheid crabs and spider crabs colonized the fractures. Photographs taken during OFOS-1 (for exact position see Fig. 4.2a).



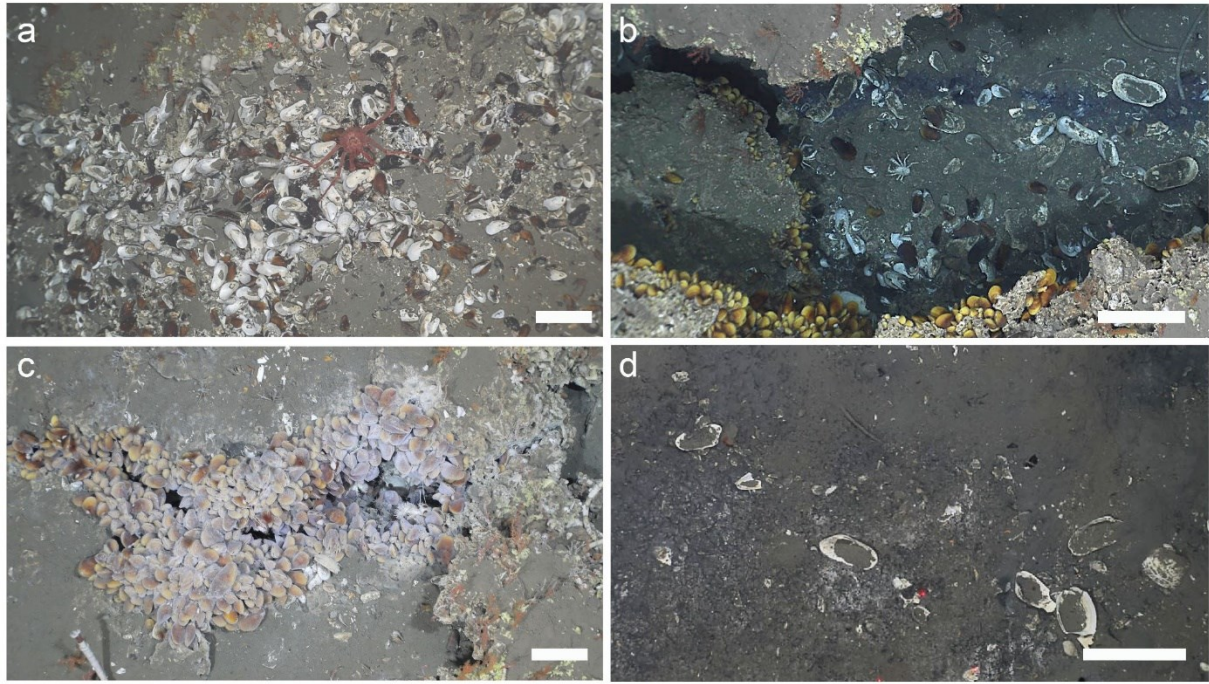


**Fig. 7.** Images of the seafloor taken with the OFOS at the Yam Seep (for locations see Fig. 4.8d). All scale bars are 20 cm. (a) Bivalve shells on a carbonate paved seafloor within a wide-opened crack in carbonate crusts. (b) Chemosynthetic communities clinging on the vertical wall of cracks in carbonate crusts, and dark stained (presumably anoxic) sediment on the floor of the fracture. (c) Mussels covered by microorganisms (white) within cracks of carbonate slabs. (d) Anoxic sediments and shells in an apparently poorly cemented stage.

Evaluation of seafloor pictures revealed that almost all areas along the tracks hosted dense carbonate formations. Elevated areas revealed mainly flat carbonate surfaces or irregularly-formed carbonate outcrops. The southern elevated area was found to be characterized by sediment draped carbonate (Fig. 4.6b). Carbonate crusts over several decimeters were observed in areas of plain seafloor. Such crusts were partially draped by sediment and colonized by clams (Fig. 4.9c). Exposed flat carbonate crusts were dominant in elevated area showing thick formation, including several fields of oblique thick carbonate crusts. We couldn't assume a clear trend in the distribution of the different type of carbonate formation as the carbonate crusts at plain seafloor are less exposed. And perhaps plain areas are also paved by flat carbonate crusts, for example, failure of sediment recovery at plain seafloor (Fig. 4.9b) during GC-2 coring (Fig. 4.2) suggesting hard carbonate substrate beneath.



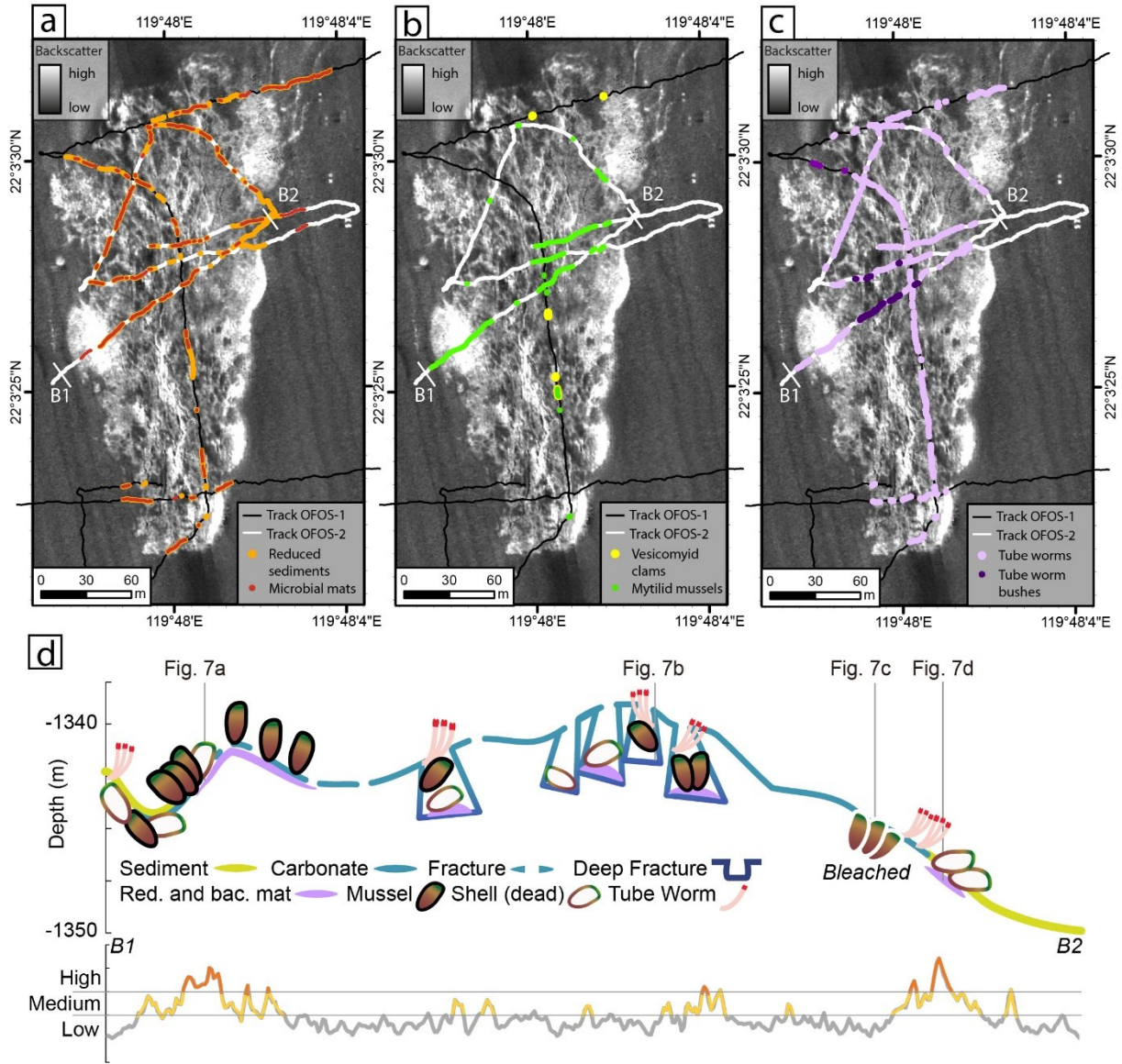


**Fig. 4.8.** Distribution of (a) anoxic sediments and microbial mats, (b) vesicomyid mussels and mytilid clams, and (c) tube worms at the Yam Seep as observed by video footage recorded during OFOS surveys (tracks marked in white) during cruise SO266/1. (d) a SW-NE section of OFOS-2 (B1 - B2) crossing the central Yam Seep was studied for seep indications and backscatter intensity. Seafloor photos of specific locations along the topographic profile can be found at Fig. 4.7a – 4.7d.

#### 4.3.2. Appearance and distributions of fractures in carbonates

Heavy fracturing of the carbonate structures adds to the rough topography of the area. The fractures generally have a N-S orientation (Fig. 4.2b and 4.2c). In the AUV- derived high-resolution backscatter map, fractures can be observed at the northern and southern elevated areas as linear areas of low backscatter (Fig. 4.2b and 4.2c). The southern elevated area was visually observed to be characterized by fracturing (e.g., Fig. 4.6b). Fractures and cracks of the

carbonate paved seafloor occur with different sizes and dimension. They often are linear troughs with steep and sharp-separated walls (Fig. 4.6a) are likely caused by tectonic movements within the accretionary ridge whereby the north-south orientation is fitting to normal faults of the structure (Kunath et al. 2020). Fractures range from ~15 cm to ~100 cm in width. They are more common in the center of the seep area. At the northern elevated area, a several m-long and dm-wide, SW-NE oriented fracture was discovered (Fig. 4.6a). Other cracks are more irregular structures with uneven walls (Fig. 4.6b). Therefore, the observed cracks and build-ups can be regarded as erosive structures. Cracks with variable orientations separated carbonate slabs at the northern elevated and the southern elevated area (Fig. 4.6b).

Along the OFOS tracks, fractures were often found to be partly filled with sediments that are characterized by dark stained patches suggesting near-surface anoxic conditions and are presumably caused by the occurrence of H<sub>2</sub>S near the seafloor (Fig. 4.6a and 4.6b; Fig. 4.7b). Such staining was not observed for sediments covering carbonate slabs (Fig. 4.6a and 4.7c). The majority of anoxic sediments were also found to host microbial mats (Fig. 4.8a). Microbial mats and anoxic sediment patches occur in the entire seep area including the rim of the seep area and its close surrounding, which suggest that fluid migration is happening in shallow sediments even outside the morphologically identified seep area. The most extensive area (>40 m in length) characterized by dark stained sediments and microbial mats was located at the NE rim of the Yam Seep (Fig. 4.8a).

#### 4.3.3. Chemosynthetic animals as indicators of recent seepage

Hydrocarbon seep-related animals documented at the Yam Seep include bathymodiolid mussels (Fig. 4.7a, 4.7b, 4.7c), which harbor symbiotic chemoautotrophic bacteria (Duperron et al, 2005). *Bathymodiolus platifrons* and *Bathymodiolus securiformis* have been reported to occur at Yam Seep before (Kuo et al., 2019). In this study, dense accumulations of mytilid mussels were discovered in the northern elevated area (Fig. 4.8b) within the bottom of fractured carbonate precipitates. In the center of the seep area, mussel accumulations were also found on subvertical walls of fractures (Fig. 4.6a, 4.7b). Mytilid mussels were also found at the northern elevated area settling mostly within the fractures, cracks, or clinging at the steep fracture flanks. Additional dense mussel accumulations were observed at the eastern rim of the seep area (Fig. 4.9d).

Apart from living mussels, the massive extent of shell accumulations provides evidence of past occurrences of living mussels in a certain density, which hence indicate active seepage at the

Yam Seep in the past. Shell accumulations occurred between carbonate fractures at the central and western parts of the seep area. Shell accumulations of dead mussels were present at the rim of the seep area and frequently found peripheral to living mussel accumulations. In some areas, a transition of dense mussel communities to dense shell accumulations was observed and some regions were characterized by a mixture of living mussels and shells of mussels and clams (Fig. 4.7a). At the western rim of the Yam Seep a field containing shells was found to extend 10 m along the track of OFOS-2 (Fig. 4.8d). At the eastern rim, shell debris was found partly covered and buried by sediment with dark sediment patches and potentially slightly cemented (Fig. 4.7d and 4.8d). This observation suggests the past activity of fluid flow with dissolved methane at specific locations to sustain the chemoautotroph living communities, and may indicate a regional variation of the fluid transporting dissolved methane to the seafloor.

Living vesicomyid clams were barely spotted as they live buried in soft sediments. In some areas clams were seen embedded in soft sediments within fractures (Fig. 4.9c), e.g. at the northern and southern parts of the seep area (Fig. 4.8b). The presence of vesicomyid clams implies that soft sediments fills the fractures between the authigenic carbonates. The colonization at the fractures additionally suggests a supply of sulfide to support the vesicomyid clams communities. Such environments have been suggested to be the precursor stage towards the capping of sediments by carbonate precipitation (Sahling et al., 2008).

The occurrence of chemoautotroph living mussels and clams are key indicators for present hydrocarbon seepage. They suggest different scenarios due to the habitat requirement and chemical fuels. Mussels cling to a hard stratum and require dissolved methane flow as fuel for their symbionts, whereas clams burrow into soft sediments fueled by hydrogen sulfide (Dubilier et al., 2008). The different settlements of mussel accumulations at the Yam Seep (surface covering in the western part and attached on vertical outcropping carbonate walls in the central area) suggest varying dissolved methane emissions depending on the carbonate structures at these different locations. Such differences can be argued to be related to the structures of the whole carbonate paved area, in which fluids with dissolved methane only occurred at a certain level. The spatial differences might be attributed to the occurrence of gas hydrate accumulations underneath the fractured carbonate slabs.

Vestimentiferan tube worms (polychaetes), were widely observed on carbonates (Fig. 4.6a). Vestimentiferan tube worms live in symbiosis with chemoautotrophic, sulfur-oxidizing bacteria and are considered as one of the primary producers in seep communities (Sahling et al., 2008). They require hard grounds as habitat for settling and grow with the posterior tube until extending into the sediments. Since tube worms are sessile and live for a century or more there

presence indicates seepage activity persisted for decades (Bergquist et al., 2000; Fisher et al., 1997).

At the Yam Seep, tube worms occurred in bushes composed of up to several tens of individuals, but also of only 2-3 single tube worms in some places (Fig. 4.8c). Tube worms were generally rooted below the carbonate slabs and extended out from fractures. Tube worm bushes were mainly found at shallow fractures, single tube worms occur on isolated carbonate masses or at the edges of carbonate slabs. At a deeply incised fracture in the central part of the seep area, tube worm bushes were attached along the vertical flanks of exposed carbonate layers (Fig. 4.6a). Individual tube worms were observed to reach lengths of up to ~1 m. The widespread occurrence of authigenic carbonates and tube worms substantiates the long-lasting history of gas seepage in the study area.

Other non-chemosynthetic faunal elements, such as corals and anemones, were frequently observed attached to carbonates and along fractures. Such organisms might not indicate seepage, but indicate the long-term exposition of the carbonate precipitate as hard ground for settlement and nutrients supply through water currents (Deng et al., 2019; Hovland and Risk, 2003). Other mobile organisms such as galatheid crabs or spider crabs were widely found close to or within the fauna communities of the seep area. Such an abundance of organisms suggests a sufficient food source.

#### 4.4.4. Seafloor backscatter characteristics related to the seep system

Joint evaluation of the bathymetric and seafloor backscatter data, and visual seafloor observation enabled a spatial correlation of seafloor deposit characteristics and faunal distribution (Fig. 4.9a – 4.9d). Sediment draped areas correlate with relatively smooth seafloor as revealed from the bathymetric map and with low backscatter intensities (Fig. 4.9b). The different backscatter intensities of carbonate covered and fractured areas seem to be caused by the density of colonization by clams as observed at the site characterized by medium intensity (Fig. 4.9c). High backscatter intensities were also detected in areas colonized by living mytilid mussels (Fig. 4.9d).

Not all mytilid mussel accumulations observed along the OFOS tracks are associated with high backscatter intensity, for instance when located within deeply incised fractures or covered by sediments. Numerous sites with chemosynthetic communities, including extensive accumulations of shells from vesicomid clams (Fig. 4.7a), mytilid mussels (Fig. 4.7c), and mytilid mussels attached to vertical fracture walls (Fig. 4.7b) were observed during the seafloor visual survey (OFOS-2) in the central elevated area (Fig. 4.8d). At the eastern rim, an extensive area with dark stained sediments has been observed, adjacent to a field of shell accumulations,



which mostly correlate to high backscatter characteristics. At the western periphery, shells were seen to be covered by sediments (Fig. 4.7d).

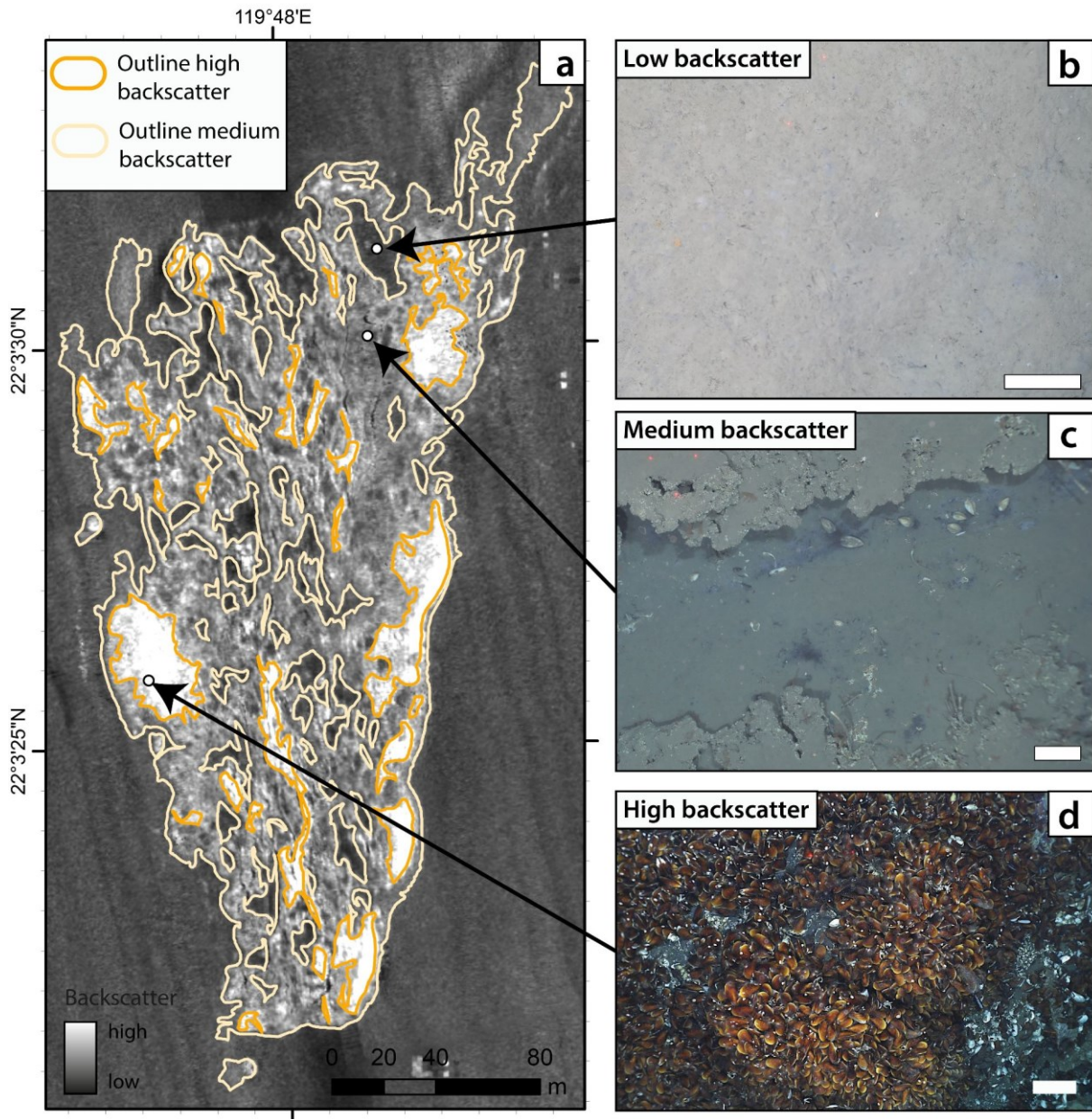


**Fig. 4.9.** (a) Seafloor backscatter map of the Yam Seep with outlines of medium and high seafloor backscatter areas. (b) Soft sediments characterize low backscatter values. (c) Carbonate crusts partly covered by a thin layer of sediments produce medium backscatter values. Clams were found to live in the sediments. (d) Dense faunal assemblages dominated by mytilid mussels and crabs covering the seafloor were seen in areas of high seafloor backscatter. White scale bar in (b), (c), and (d) is 20 cm.

According to our observations we conclude that a) high backscatter intensities areas are mostly related to shells and living mytilid mussels; b) medium backscatter intensity correspond to

authigenic carbonates partly hosting active chemosynthetic communities; c) low backscatter relates to soft sediments (even when covering authigenic carbonates in greater depth). Backscatter intensity of shells or fractures is strongly affected (lowered) by sediment draping. The backscatter values recorded within the seep area are not homogeneous, but widely scatter and range from low to high (Fig 4.9a). Most of the seep area is characterized by medium backscatter values (>70%), which separates the seep area to the surrounding seafloor of homogeneously low backscatter. However, low backscatter areas occur also within the seep area, but accounting for less than 15% of the total and in relatively small patches distributed within the entire area (maximum <500 m<sup>2</sup>). About 15% of the seep area is characterized by high backscatter, with the largest coherent areas of ~1000 m<sup>2</sup>.

#### 4.4.5. Evolution of the Yam Seep

Swath-bathymetry, side-scan sonar imaging, and OFOS seafloor imagery showed that the seafloor topography of the active YAM seep system is dominated by authigenic carbonate. The carbonate precipitates which are the result of anaerobic methane oxidation are either exposed or covered by thin layers of sediments. The presence of heavily fractured authigenic carbonates suggest that formation and exposure of the Yam Seep on top of the FWCR anticline is strongly controlled by tectonic compression, uplifting of the accretionary ridge, gas migration and seafloor seepage, and focused seafloor erosion. Ongoing AOM results in the formation of authigenic carbonates and sediment cementation (Bayon et al., 2009; Hovland, 2002). Further carbonate precipitation at newly developed gas emission pathways expands the carbonate paved area (Liebetrau et al., 2014; Loher et al., 2018). Gas bubble discharge recorded in 2013, 2017, and 2018 along with seawater methane enrichments measured in 2018 indicate that i) the Yam Seep is an actively methane seeping area and ii) up to meter-thick carbonate pavements result from long-term seepage. Seepage areas characterized by similar features have been documented in other active margins at accretionary ridges, i.e. Hydrate Ridge (Teichert et al., 2005; Paull et al. 2015) and offshore southern Nicaragua, both linked to underlying fault systems (Moerz et al., 2005; Sahling, et al., 2008;).

Tectonically, implying the thrusting and the uplifting of the submarine ridge and potentially effects the fracturing and exposure of the seep region. Yam Seep is generally tilted to the northeast and following with an even tilted northeastern slope of FWCR. Erosion at scarps was observed at FWCR, which were reported as the results of over-tilting of the ridge uplifting (Chen et al., 2020; Klaucke et al., 2016). In addition to tectonic influence, we argue that seafloor erosion due to currents and biology might have been involved in shaping the Yam Seep.

Stronger currents result in unconsolidated sediment being carried away, exposing the consolidated authigenic carbonates on the seafloor which in general formed hardgrounds for filter-feeder fauna. Internal waves (Alford et al., 2015) were reported to occur peripheral to FWCR at canyons adjacent to the upper slope and shelf, and especially related to records of Penghu canyon (Klaucke et al., 2016; Kunath et al., 2020; Yu and Chang, 2002), which effect the region including our study area by scavenging on the surface sediments. Bioerosion is also a potential erosion force in our study area as we observed abundant chemosynthetic community along or within the edge of cracks (Paull et al., 2005).

Beside tectonic processes affecting seepage sites, the formation of gas hydrates in shallow sediments can have an important influence on the seep evolution, especially when gas bubbles are emanating at the seafloor (Marcon et al. 2014). Since the Yam Seep is located well within the gas hydrate stability zone, gas upward migration would lead to the deposition of gas hydrate (Sloan and Koh, 2007) underneath the exposed carbonates. Examples from several studies reported wide areas of updoming or collapsing of carbonate paved seafloor related to gas hydrate accumulation or dissociation (Matsumoto et al., 2009; Sahling et al., 2008). A good example was described recently from the Calabrian arc in the Mediterranean where massive gas hydrate below a thin carbonate crust was dissolved and the carbonate crust collapse (Loher et al., 2018). Methane migrated below the cemented and sealed layer of precipitated authigenic carbonates, where it formed massive gas hydrates in contact with water. An accumulation of gas hydrate at such shallow sediment depth inhibits an increased buoyancy but also could push the overlying sediments up (Barry et al., 2012). Because the Yam Seep is situated ~700m below the upper boundary of the gas hydrate stability zone (GHSZ) and above the lower boundary of GHSZ at ~650 mbsl marked by a bottom simulation seismic reflector (Kunath et al., 2020). Thermal and pressure effects by glacial/interglacial changes which move the seafloor and shallow sediments out of the stability zone can be neglected.

The local presence of gas hydrates is causing a heterogeneous distribution of methane availability for chemosynthetic community settlements. Clams and microbes found within shallow fractures at relatively smooth areas and covered by sediment suggest that the area and close surrounding are characterized by methane supply. Tube worms are commonly found adhering to carbonate crusts of different sizes and shapes, and prove that seepage has been around for a longer time. Mytilid mussels suggest a later stage of seepage when carbonate hard ground are available where mytilid larvae initially can settle down and benefit from the dissolved methane-rich bottom which they use for their metabolism and thrive via their microbes in the gills (Sibuet and Olu, 1998). Corals colonizing carbonate build-ups were found

frequently over the paved area, indicating sufficient nutrients for filter-feeders and indicate that currents exposed the hard carbonate substrates (Hovland and Risk, 2003; Roberts et al., 2009). Summarizing our results presented in this study, we established a simplified conceptual model with four evolutionary stages (Fig. 4.10) in order to discuss the dominant processes at the Yam Seep:

#### Stage I & II– Initial seepage and carbonate precipitation

Initially methane begins to migrate along permeable fault networks to the shallow subsurface. When methane comes in contact with seawater-derived sulfate, AOM produces sulfide and initiates the production of authigenic carbonate. The sulfide-rich environment enable colonization by vesicomyid clams. Authigenic carbonates form hard substrates on which vestimentiferan tube worms can settle (Cordes et al., 2005; Cordes et al., 2003; Freytag et al., 2001; Sahling et al., 2008).

#### Stage III - Increasing precipitation and seafloor sealing

The continued supply of methane enhances the amount of authigenic carbonates and carbonate slabs that increasingly seal the seafloor and deflect upward migration fluids. Gas hydrate (blue gradient shaded hexagons in Fig. 4.10) formation underneath the carbonate slabs may also be induced. Because near-seafloor carbonates and gas hydrates hamper direct fluid upward migration and gas escape, fluids are preferentially deflected towards the edges of the carbonate crust, causing lateral growth of the seep-influenced area. Chemosynthetic organisms settle at the rim of the seep area, where gas can migrate through higher permeability sediments.

#### Stage IV – Erosion and seafloor morphology re-shaping

In this stage, partial exposure of the paved carbonate area, fracturing of carbonate slabs, and fauna colonization occur. We postulate that tectonic movement causes the ridge uplifting and erosion along tilted flanks. Carbonate crusts are partly exposed by sediment removal. Thrusting and faulting affect the cemented carbonate slab and cause fracturing and re-opening of the pathways for gas ebullition. Repeated sealing within cracks and fracturing of the lower cemented crusts shaped the (a) deeply fractured crusts. Meanwhile, (b) carbonate precipitation occurs in the exposed sediments at the more profound depth within deep fracture. (c) Free gas migrated along the extensional fault and leave the sediment but trapped underneath the fractured carbonate crusts potentially form gas hydrate, and fueling chemosynthetic communities along the fractured carbonate area. Peripheral to the profoundly fractured carbonates area, scenarios



of (d) shallow fractured crusts and (e) anoxic sediment showing the progress of stage I to III of newly occurred seepage pathway, consequently extended the carbonate paved area. Anoxic sediments and vesicomysid clams bearing sediments within fractures are the key features occurring at the rim and the relatively plain regions.

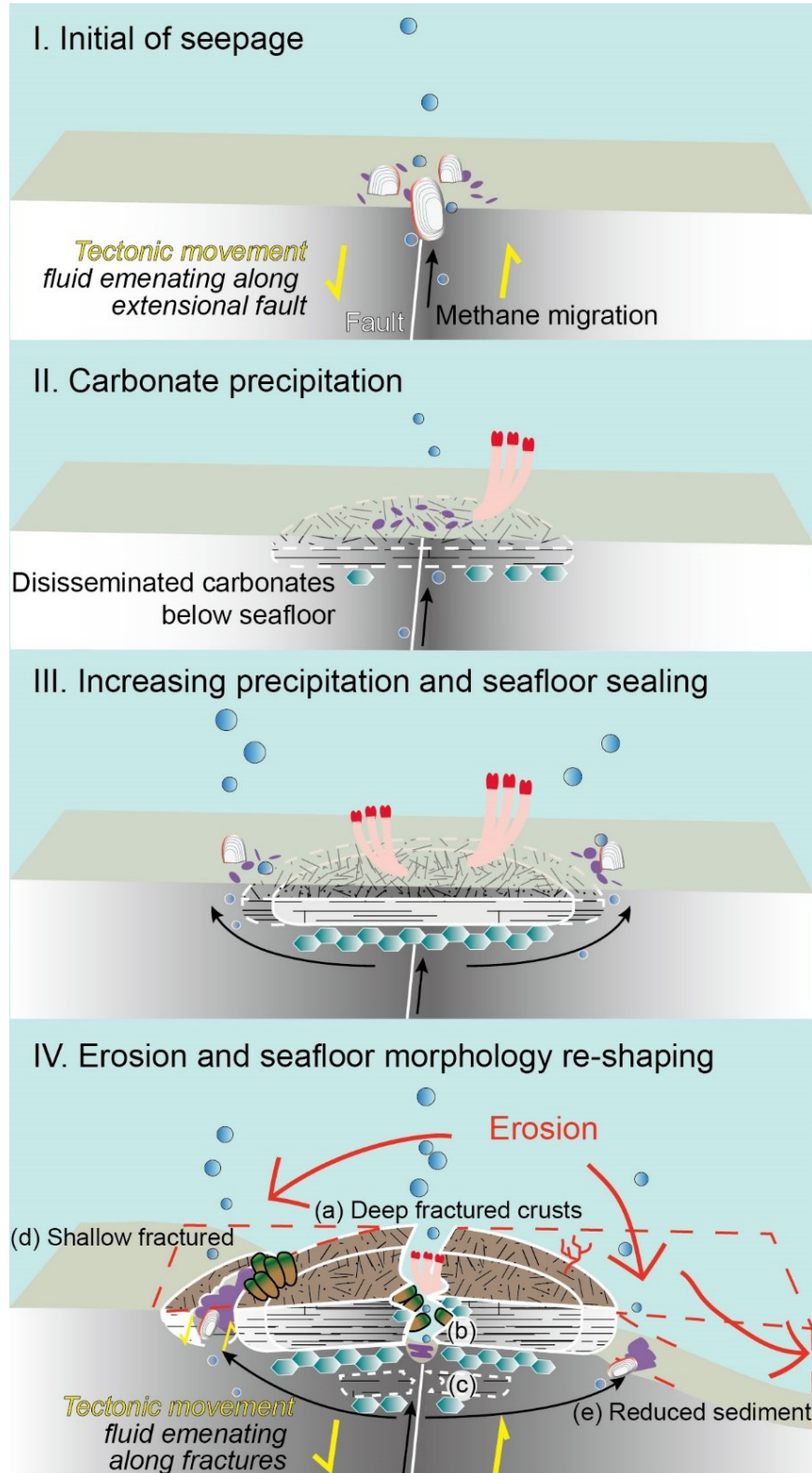


**Fig. 4.10.** Schematic model of the evolution of the Yam Seep compiling the results of this study.

#### 4.5. Conclusions and outlook

In addition to previous seismic and side-scan sonar studies since 2013, our study reveals the effects and mechanisms acting at the Yam Seep and characterizes the cemented, fractured, and exposed region. Hydro-acoustic data documented several flare sightings and defined eight source areas for recent gas bubble ebullition at the center and the eastern flank of the Yam Seep and further illustrated its spatial and temporal variability. The backscatter results extend the seafloor condition and backscatter intensity, showing the highest intensity shell distribution and middle-intensity-patterned fractures and cracks. Enrichments of dissolved methane were found at the rim of the seep area. Ample seep-related and non-seep-related fauna were observed in HD video. The widespread occurrence of authigenic carbonates illustrates the long-term seep evolution and the chemosynthetic community suggests recent seep activities,

The diverse evidence observed at the Yam Seep were used to propose an active margin seep area evolution of under dynamic tectonics, geochemical, and biological interaction, involving four stages: (I) Initial of seepage, (II) Carbonate precipitation, (III) Increasing precipitation and seafloor sealing, (IV) Erosion and seafloor morphology re-shaping. Stage I to III relate to the geochemical progress of methane seepage and carbonate precipitation and its indicator fauna. Stage IV includes the exposure of the seep carbonates under tectonic faulting, uplifting, over-tilting and the expansion of the seep area with repeating stages I-III at its periphery.

Further analysis of chronology measurements on the carbonate core material, which archived environment information as it precipitated, can further answer its time-constrained and complete the fragmentary stages from this current study. In addition, the chronology of seepage, deposition of gas hydrate, and the potential correlation to paleoclimate in relation to tectonic activities are promising studies to be discovered in the future.

### **Acknowledgment**

R/V SONNE cruise SO266 was financed in Germany by the Ministry of Education and Science, project TaiDrill – SO266 (Ref. #03G0288A). The project was funded in Taiwan by the Ministry of Science and Technology (MOST) Project TaiGer drill (MOST107-3113-M- 002-004). We are grateful to the master of the vessel, Lutz Mallon, and to Susan Mau, Tzu-Hsuan Tu, Jhen-Nien Chen, Janice Malnati for collecting and analyzing water samples during SO266. The AUV survey was also supported by Ministry of Science and Technology (MOST) through the master gas hydrate program and the David and Lucile Packard Foundation.

## 5. Manuscript II: Seep carbonates microfacies and chronology

**Fluctuations of authigenic carbonate precipitation at Yam Seep controlled by continuous fracturing and uplifting of Four-Way Closure Ridge offshore SW Taiwan**

**Yiting Tseng<sup>1\*</sup>, Daniel Smrzka<sup>1</sup>, Saulwood Lin<sup>2</sup>, Andrea Schröder-Ritzrau<sup>3</sup>, Norbert Frank<sup>3</sup>, Gerhard Bohrmann<sup>1</sup>**

**(Under review by Geochemistry, Geophysics, Geosystems)**

<sup>1</sup>MARUM, Center of Environmental Sciences, and Department of Geosciences, University of Bremen, Germany (\*correspondence: tiffni37@gmail.com)

<sup>2</sup>Institute of Oceanography, National Taiwan University, Taiwan

<sup>3</sup>Institute of Environmental Physics, Ruprecht Karl University of Heidelberg, Germany

Corresponding author: Yiting Tseng (tiffni37@gmail.com)

**Key Points:**

- A nearly 40-thousand-years-old history of hydrocarbon seepage at active margin accretionary ridge SW offshore Taiwan.
- Tectonic fractured micrites are cemented by aragonites, which present the oldest age on fracture boundaries and precipitation inward.
- Dating on fracture boundaries provides episodes of tectonic and seepage activities.

## **Abstract**

Fracturing of carbonate crusts and occurrence of gas hydrates are common at hydrocarbon seeps in marine sediments. However, the fate of long-lasting seepage within the gas hydrate stability zone (GHSZ) at active margins, where the interplay of faulting, seepage, fracturing, and gas hydrate accumulation is poorly constrained. This study presents an unusually long and complete record of hydrocarbon seepage from a ~5-meter long core composed almost entirely of authigenic carbonates from Yam Seep area, Four-Way Closure Ridge off SW Taiwan. Detailed petrography enabled the identification of three distinct microfacies, A, B and C. Microfacies B composed mostly pure aragonite, forms 10 ~50 cm thick intervals that are intercalated by sediment consolidated microcrystalline aragonite microfacies A, whereby the transitions between microfacies are interpreted as fracture boundaries. High resolution U-Th dating revealed that the microfacies B fills previously formed fractures, precipitating from the fracture boundary inwards. The chronology of aragonite throughout the core revealed consistent seepage from ~41 to 2 ka that fluctuated its intensity over this time. The chronology of observed fracturing and precipitation suggests (1) an active period of fracturing and seepage from ~37 to 27 ka, (2) a more quiescent period from ~27 to 16 ka, followed by (3) another active period from ~16 to 12 ka. A schematic model illustrates the evolution of carbonate formation within the core influenced by faulting, fracturing, erosion, gas hydrate accumulation, and aragonite precipitation, suggesting a unique record of ~40,000 years of seepage and crucial insights into long-term seepage systems at active margins.

### **5.1. Introduction**

At plate boundaries, faults, accretionary ridges and mud diapirs provide conduits for methane gas derived from deep methanic sediments to migrate towards shallower sediments and the seafloor. Hydrocarbon seepage is sometimes associated with the presence of gas hydrates, which are widely distributed along continental margins and are stable at water depths greater than 300-500 m (Kvenvolden, 1993; Suess et al., 2001). Seepage at active margins at such water depths, where gas hydrate stability is unaffected by climate related variations, contributes a significant amount of methane to the water column and the atmosphere (Ruppel et al., 2017). The sulfate-driven anaerobic oxidation of methane (SD-AOM) mediated by a consortium of sulfate reducing bacteria and methanotrophic archaea, consumes methane and increases alkalinity in sedimentary pore water enabling the precipitation of authigenic carbonate (Paull et al., 1992; Ritger et al., 1987). SD-AOM generally consumes methane and sulfate in the same sediment depth, usually denoted as the sulfate-methane interface (SMI), and carbonate precipitation is therefore confined to an anoxic environment (Aloisi et al., 2000; Peckmann et al., 2001). The formation of carbonate crusts at and below the seafloor may

potentially hamper fluid migration and methane expulsions into bottom waters (Bayon et al., 2015; Solomon et al., 2008).

Carbonate crusts exposed at the seafloor have been observed at Hydrate Ridge (Greinert et al., 2001) at the Nile deep-sea fan (Bayon et al., 2009; Römer et al., 2014), the Northern Congo Fan (Bayon et al., 2009; Haas et al., 2010; Sahling et al., 2008), the Black Sea (Bahr et al., 2010; Mazzini et al., 2008), as well as in the periphery of mud volcanos in the Eastern Mediterranean (Himmler et al., 2011; Loher et al., 2018). In some cases, however, authigenic carbonates occur as build-ups, chimneys or chemohierms that protrude into the water column. Formation of these carbonates may be mediated either by physical exposure such as erosion, winnowing, or pockmark formation (Srnzka et al., 2019), or be facilitated by a combination of anoxic bottom waters (Bayon et al., 2013; Himmler et al., 2018) and/or microbial growth into oxic seawater (Teichert et al., 2003, 2005). These seep carbonates sometimes consist of pure aragonites (Naehr et al., 2007) that provide a reliable stable isotopic and chronologic record, and are therefore suitable for reconstructing paleo seepage activity (Feng et al., 2018). Additionally, carbonate cores had been recovered via subsurface drilling, revealing massive successions of authigenic carbonates at Hydrate Ridge (Leefmann et al., 2008), the Central America Forearc (Liebetrau et al., 2014) and the South China Sea (F. Chen et al., 2019). Although such cores provide an excellent record of carbonate precipitation and potential deep-water tectonic activity through time, the chronology of tectonic events and the timing and duration of carbonate precipitation in relation to tectonics still remains poorly constrained.

Uranium Thorium (U-Th) dating is a high precision radiometric method that is widely applied to precipitated carbonate minerals, including speleothems, corals and shells (Chutcharavan et al., 2018; Spötl et al., 2019; Frank and Hemsing, 2021). U-Th dating of seep carbonate has been used to constrain the chronology and duration of venting at hydrocarbon seeps (Bayon et al., 2009; Bayon et al., 2015; F. Chen et al., 2019; Feng et al., 2010; Himmler et al., 2019). These studies have shown how seepage activity can be initiated by the perturbation of shallow gas hydrates within gas hydrate stability zone (GHSZ) during sea-level lowstand. Seepage triggered by tectonic activity in the forearc mound structures off Central America was studied by Kutterolf et al. (2008), who were able to constrain the duration and cyclicity of fluid venting. U – Th dating of seep deposits can be applied on both microcrystalline carbonate (i.e. micrite), as well as on various types of carbonate cements (Teichert et al., 2003). However, due to the high concentration of thorium in clay minerals, dating of micrite that lithified the host sediments is not ideal, as potential contamination may easily compromise the dating results (Cochran et al., 1986). Aiming at acquiring precise chronology thus U-Th dating only applied on clear aragonites.

This study presents an extraordinary record of seepage activity that may be correlated with fracturing of the uplifted accretionary ridge and subsequent precipitation of massive authigenic carbonates, and provides a precise chronology of events that occurred at this highly active seepage site at GHSZ.

## 5.2. Geological setting

The South China Sea lithosphere, as part of the eastern Eurasian plate, subducts eastward beneath the Philippine Sea Plate along the Manila trench (Sibuet et al., 2021) (Fig. 5.1a). The Northern Manila Trench overlying the Luzon arc and the Ryuku arc juncture, as well as the mountain belt and accretionary prism of Taiwan formed during the collision of the Philippine Sea Plate moving northwestward at a rate of 8 cm/yr (Ustaszewski et al., 2012). Offshore south-western Taiwan, a series of accretionary ridges and mud diapirs align parallel to the deformation front (N.-C. Chen et al., 2020; S.-C. Chen et al., 2014; T.-T. Chen et al., 2020; Lim et al., 2011). To the south of the Manila Trench where the South China Sea lithosphere is subducted, chains of active volcanoes above the subduction zone are aligned parallel to the trench on Luzon Island (Ku et al., 2009; Wei et al., 2003). The Yam Seep site at Four-Way Closure Ridge, located offshore south-western Taiwan (Fig. 5.1b), is characterized by widespread carbonate pavements on the seafloor (~49,000 m<sup>2</sup>), as well as large carbonate crusts and build-ups related to active seepage (Tseng et al., 2022). It has been suggested that the area has been exposed by seafloor erosion due to observed erosion surfaces related to the paleo channel of Peng-Hu canyon on the eastern flank of Four-Way Closure Ridge (Kunath et al., 2020). Four-Way Closure Ridge is located below the thermocline at a water depth of ~1400 to 1600 m, where gas hydrate stability is not perturbed by sea level change during interglacial – glacial cycles. Because a main thrust fault was reported at western Four-Way Closure Ridge, the Yam Seep fluid expulsions were suggested to be fueled by fault networks (Kunath et al., 2020). The MeBo-24 carbonates were recovered from the northwest of Yam Seep, and revealed stable carbon isotope values ranging from –37.9‰ to –58.3‰ V-PDB, suggesting methane-derived carbonate precipitation (Tseng et al., 2022).



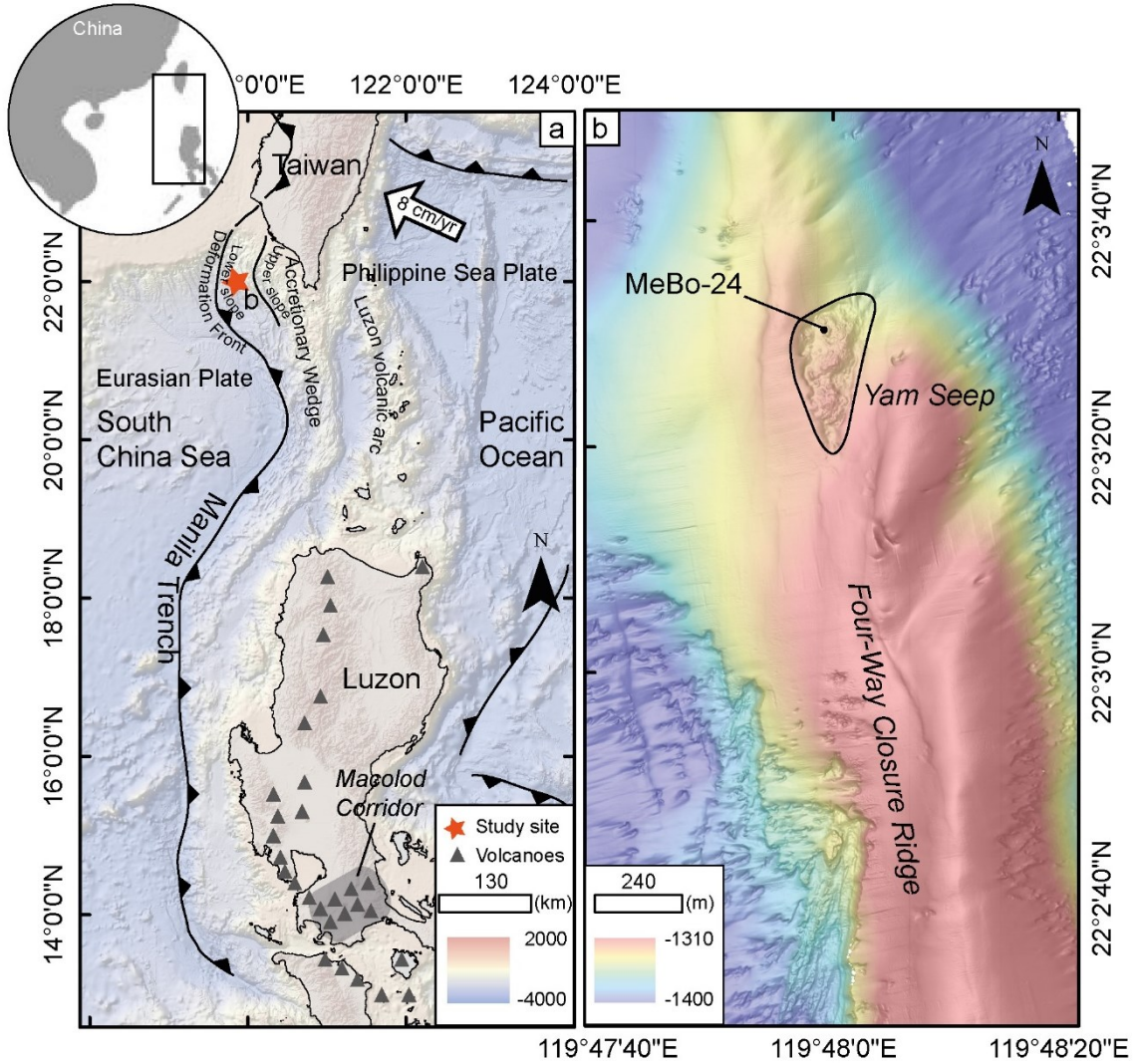


**Fig. 5.1.** Tectonic setting and the location of the sampling area. (a) Full extend of Manila Trench and Deformation Front of Eurasian Plate and Philippine Sea Plate. Grey triangles: volcanos; Star sign: location of study seep area. (b) Location of drilled carbonate core, MeBo-24, at Yam Seep, at the northern part of Four-Way Closure Ridge.

### 5.3. Materials and Methods

#### 5.3.1. Petrography, mineralogy, and stable oxygen isotopes of authigenic carbonates

The carbonate core MeBo-24 was collected during RV Sonne cruise 266 (Bohrmann et al., 2019). The 4.95 m-long core was cut into two equal halves, the working and the archive halves. The working halves were partially cut into slabs in order to subsample specific carbonate lithologies. A total of 16 carbonate slabs were obtained from the core at specific depths (black boxes, Fig. 5.2), which were subsequently used for the preparation of thin sections. Thin section petrography was conducted on a Zeiss Axioskop 40A polarization microscope. Photomicrographs were taken with a AxioCam MRc camera coupled to the MRGrab software (vs. 1.0.0.4) for image analysis and camera control.

A total of 23 powdered samples were selected for X-ray diffraction (XRD), total organic carbon (TOC) and carbonate content, and for stable oxygen and carbon isotope analyses (Fig. 5.2, black circles).

Some of these samples were micro-drilled along a cut surface, others were hand-picked and milled by hand to fine powder using an agate mortar and pestle. XRD analyses were conducted on a Scintag X-ray diffractometer with a Cu K $\alpha$  radiation ( $\lambda = 1.5405 \text{ \AA}$ ) in the range of  $5^\circ$ – $60^\circ$   $2\theta$  at  $0.02^\circ/\text{s}$ , using a 40 kV accelerating voltage and a 30 mA current at the Department of Geoscience, University of Bremen. Peak identification and relative abundance of minerals estimation were performed using the PANalytical and MacDiff® interpretation software packages. As the intensity of the diffraction pattern of a mineral in a mixture is proportional to its concentration, estimates of the relative proportions of the minerals in each sample were made by measuring their relative peak areas. Total carbon (TC), TOC and TIC were determined on an IR spectrometer (Vario EL III) at the Department of Geoscience, University of Bremen. A fraction of the subsample powders (20–25 mg) was selected for TC composition. The remaining subsamples ( $\sim 1 \text{ g}$ ) were treated with 3M HCl for 24 hours in order to completely dissolve carbonate. The remaining subsamples were washed and freeze-dried, and then weighed and analyzed for TOC content. TIC contents were determined by subtracting TOC from TC and converted to calcium carbonate contents.

For stable oxygen and carbon isotopes in carbonate, powdered samples were reacted with carbon dioxide in 100% phosphoric acid at  $75^\circ\text{C}$ . The stable oxygen and carbon isotopes of released  $\text{CO}_2$  were analyzed using a Thermo Fisher Scientific 253 plus gas isotope ratio mass spectrometer coupled to a Kiel IV automated carbonate preparation device at the Stable Isotope Laboratory at MARUM Center for Marine and Environmental Sciences, University of Bremen. Stable oxygen and carbon isotope ratios are reported as  $\delta^{18}\text{O}$  and  $\delta^{13}\text{C}$  in ‰ vs. the Vienna PeeDee Belemnite (V-PDB). Replicate analyses of a laboratory standard show a standard deviation  $< 0.03 \text{ ‰}$  for  $\delta^{18}\text{O}$  and  $\delta^{13}\text{C}$ , respectively. All the data are reported relative to the VPDB standard. Acid fractionation factor of aragonites  $\delta^{18}\text{O}$  are calculated following Kim et al., (2007)

### 5.3.2. Uranium-Thorium dating

Sample preparation and measurements for U-Th dating were carried out at the Institute for Environmental Physics at the University of Heidelberg. Carbonate chips were cut along the edge of sample slabs using a small precision diamond wire saw in order to obtain sample sizes of  $1\text{--}1.5 \times 0.1\text{--}0.2 \times 0.4 \text{ cm}$  (L $\times$ W $\times$ H), weighing between 50 to 100 mg. The diamond wire width at 0.28 mm is controlled by operating at a fixed spooler spin speed and an elevated stage that provide steady movement along the z-axis. Bivalve shells were cut and polished to the same size as the carbonate chips. All sampled chips were leached using  $\sim 1\text{N}$   $\text{HNO}_3$  for 15–20 seconds in order to remove potential environmental contaminations during sampling. U-Th dating was conducted following the method of Wefing et al., (2017) and Frank and Hemsing (2021). All carbonate samples were dissolved in supra-pure 7N  $\text{HNO}_3$ . Chemical Th and U separation and purification is based on ion exchange processes using UTEVA resin following sample dissolution. Subsequently, isotopes of U and Th were analyzed with a Thermo Fisher Neptune MC-ICPMS at the Institute of Environmental Physics, Heidelberg

University. For age calculations  $^{234}\text{U}$  and  $^{230}\text{Th}$  half-lives published in Cheng et al. (2013) were used. Ages were corrected for  $^{230}\text{Th}$  not derived from ingrowth but from detrital contamination fraction according to measured  $^{232}\text{Th}$  concentration of the sample assuming a  $^{230}\text{Th}/^{232}\text{Th}$  ratio of  $8 \pm 4$  for the contaminating fraction and given with as 2 sigma error.

## 5.4. Results

### 5.4.1. Macroscopic examination of lithologies

The MeBo24 core consists almost entirely of dark grey carbonates intercalated with sections of white carbonates. A total length of 495 cm was recovered with one major gap between 202 to 274 centimeters below seafloor (cmbsf, Fig. 5.2). The entire core is well consolidated, and only little soft sediment fills closed bivalve shells. Dark grey carbonates are mostly composed of cementing breccia including clasts and bioclasts like foraminifera, bivalves and gastropods shell fragments, in which cemented bivalve shells are present from the top to 316 cmbsf. The bivalve shells are clearly remaining from chemosynthetic clams which are well known from surface investigation of the YAM seep (Tseng et al. 2022). The shells are generally fractured and feature surface precipitation of isopachous white carbonate. Dark grey carbonates are porous below 85 cmbsf, exhibiting a texture reminiscent of moussy sediment. The white carbonate is present as isopachous cement or spherules, which appear opaque to translucent in hand samples. Successions of white carbonate layers may reach up to 10 cm in thickness at 15.5-25.6, 192-202 and 475-490.5 cmbsf, and up to 50 cm in thickness at 105-155 and 319-385 cmbsf (Fig. 5.2). Additional white carbonates veins are present throughout the core, measuring up to 5 cm in thickness at 42-43 cmbsf and 70-74 cmbsf. The interface between dark grey and white carbonates are lithological boundaries, whereby the white carbonates represent disconnected unconformities. A total of 15 sections were selected (Fig. 5.2) which represent lithological boundaries and disconnected unconformities for further analyses.

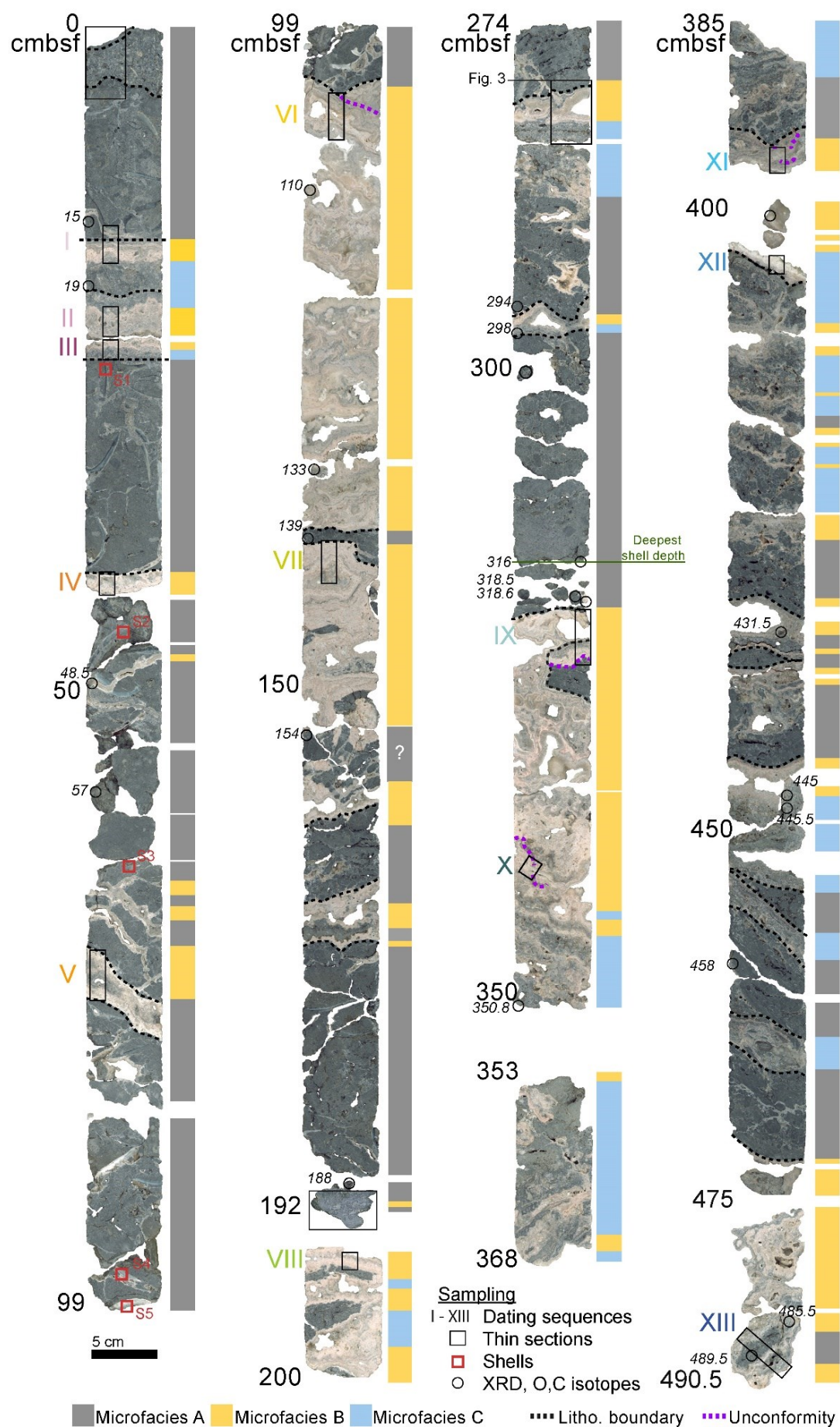




**Fig. 5.2.** Photograph of MeBo-24 (GeoB23225-1). Sample depths for XRD, TOC, TIC,  $\delta^{18}\text{O}$  are shown with black circles and by cm below seafloor (cmbsf). Samples from bivalve shells are shown by red squares. Petrographic interpretation of microfacies A, B, and C are shown by bars in different colour. Fracture boundaries of lithologies are marked with black dotted line and unconformities are marked with purple dotted line. Sections for U-Th dating sequences I to XIII marked with roman numerals. Thin sections were performed at section I to XIII and 0-5, 278-283, and 190-192 cmbsf (black boxes).

#### 5.4.2. Thin section petrography and microfacies subdivision

Thin section petrography on 16 thin sections (Fig. 5.2, black boxes), including 13 sequences in these sections labeled as I to XIII, which were dated (Table 5.2, Fig. 5.2), allowed for the distinguishing of three microfacies, A, B, and C. The three microfacies differ in terms of rock fabric, carbonate phase distribution, and crystal habitus. A representative example of all three microfacies is shown in a thin section scan from a sample retrieved at 278-283 cmbsf (Fig. 5.3a). Microfacies A is composed mainly of microcrystalline aragonite (referred to as micrite) that fills the pore space in the hemipelagic host sediment (Fig. 5.3b). Microfacies A is generally porous and fractured, and contains breccias of rock fragments and bioclasts whereby the latter includes bivalve shell fragments, foraminifera, and gastropod shells that are commonly observed within the microcrystalline aragonite matrix. Cemented shell fragments at 0-5 and 190-192 cmbsf exhibit irregular shell margins aligned with a dark, unidentified material (Fig. 5.4a).

Microfacies B comprises three distinct carbonate phases; (1) a yellowish to brownish cryptocrystalline aragonite phase referred to as yellow aragonite (Fig. 5.3c), (2) banded and botryoidal aggregates of clear, fibrous crystals referred to as banded and botryoidal aragonite (Fig. 5.3d), and (3) spheroidal aragonite featuring crystal aggregates of various sizes (Fig. 5.4b). Banded and botryoidal aragonite appears translucent, whereas cryptocrystalline yellow aragonite exhibits a yellowish to brownish color, and occasionally contains opaque inclusions of an unidentified material. Banded and botryoidal aragonite is by far the volumetrically dominant carbonate phase in this microfacies, although yellow aragonite is also present as prominent thick bands. Spheroidal aragonite is a subordinate phase and less common. The paragenesis within microfacies B is typified by intercalations of banded and botryoidal aragonite and yellow aragonite (Fig. 5.3d), whereby the former phase usually fills most of the void space in the rock. In some other cases the banded and botryoidal aragonite occurs as fractured botryoids with a yellowish to brownish color as observed in section XI, 396.7 cmbsf (Fig. 5.4d), and at section XII, 403 cmbsf.

Microfacies C is darker in appearance and composed of a matrix of microcrystalline aragonite with the interstitial pore space filled by banded and botryoidal aragonite and subordinate yellow aragonite (Fig. 5.3e). In contrast to microfacies B, the microcrystalline and banded and botryoidal aragonites are roughly equal in volume, whereby microcrystalline aragonite often exhibits a clotted fabric in microfacies C.

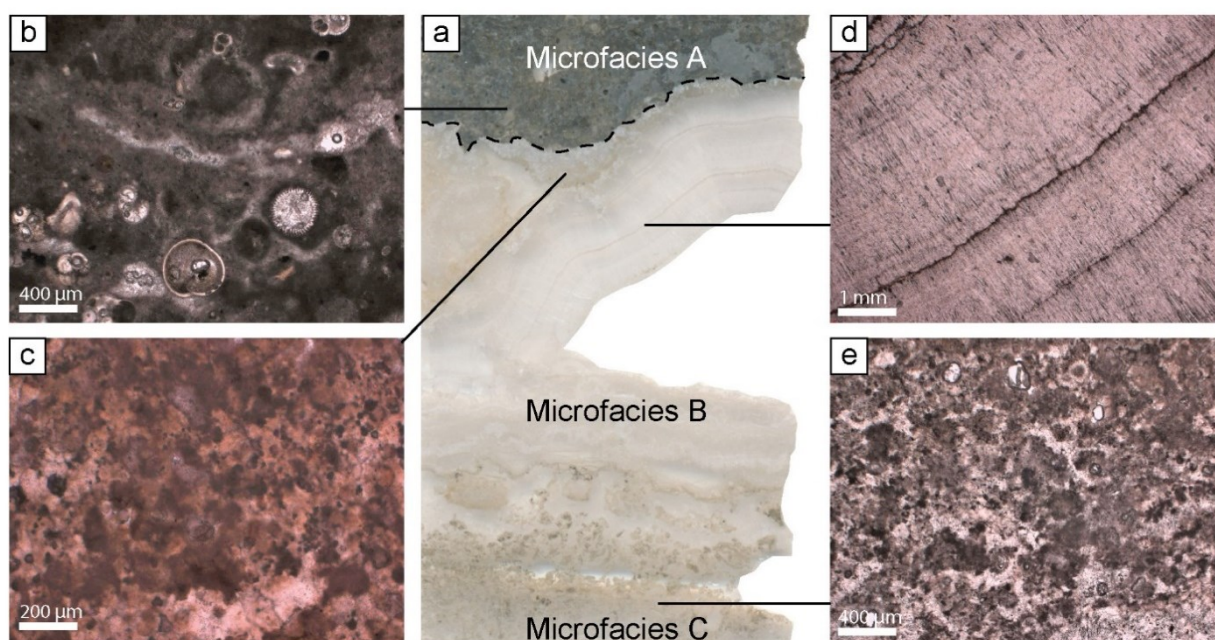


**Fig. 5.3.** Microfacies and aragonite forms. (a) Thin section scan between 278-283 cmbsf. Microfacies A-C represent micrite, light aragonites, and dark aragonites. Lithological boundary marked with dotted black line between microfacies A and microfacies B. (b) Microfacies A: lithified sediment by microcrystalline aragonite precipitation. (c) Microfacies B: yellow aragonites. (d) Microfacies B: banded aragonites. (e) Microfacies C: clear aragonites interspersed microcrystalline aragonites.

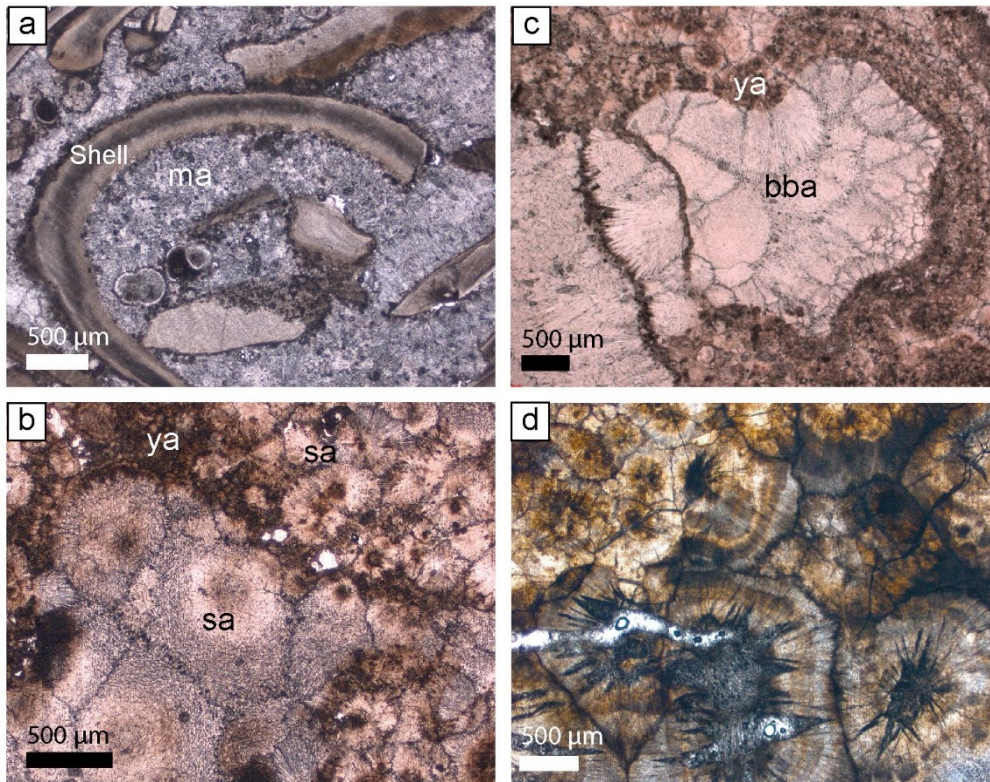


**Fig. 5.4. Corrosion features and varieties of aragonites from Core MeBo-24.** (a) microcrystalline aragonites (ma) lithified dark-stain coated corroded shell surfaces (section 0-5 cmbsf). (b) Spheroidal aragonite (sa) precipitations of variable sizes (section 64-68 cmbsf). (c) yellow aragonite (ya) framework and zonation of banded and botryoidal aragonite (bba) precipitation (section 70-75 cmbsf). (d) Fractured botryoidal aragonite filled with microcrystalline aragonite precipitation (section 392-397 cmbsf).

#### 5.4.3. Carbonate mineralogy, carbon contents, and stable isotope geochemistry

The mineralogy of carbonate phases within the three microfacies was determined via XRD, revealing aragonite as the dominant carbonate mineral among all investigated microfacies and phases (Table 5.1). Carbonates from microfacies A are volumetrically dominant in the core (Fig. 5.2) and consist of aragonite (50 – 60% of the total volume) with subordinate calcite (3 – 7%) that has lithified the host sediments composed of mostly quartz and clay minerals. Several carbonate samples contain less aragonite at 25-30%, and exhibit between 16 – 18% high Mg-calcite. TOC contents of samples from microfacies A samples lies between 0.2 to 0.4 %. Carbonates from microfacies B are very pure aragonites (99-100% of the total volume) with almost no measurable TOC content. Microfacies C consists of 87-94 % aragonite with accessory non-carbonate minerals such as quartz and clay minerals accounting for roughly 10% of the total volume and little to no TOC content. Stable oxygen isotope values ( $\delta^{18}\text{O}$ ) of the different microfacies show little variation, and the mean value of all sampled carbonates was determined at 4.7 ‰, with a standard deviation of 0.4 ‰, whereby the minimum and maximum values are 4.2 and 5.5 ‰, respectively (Table 5.1). Stable carbon isotopes value  $\delta^{13}\text{C}$  have a mean of all sampled carbonates was determined at -46.7 ‰, with a standard deviation of 3.7‰, whereby

the minimum and maximum values are -52.2 and -38.2 ‰, respectively. Average microfacies B  $\delta^{13}\text{C}$  (-48 ‰) is slightly depleted than Microfacies A (-44 ‰).

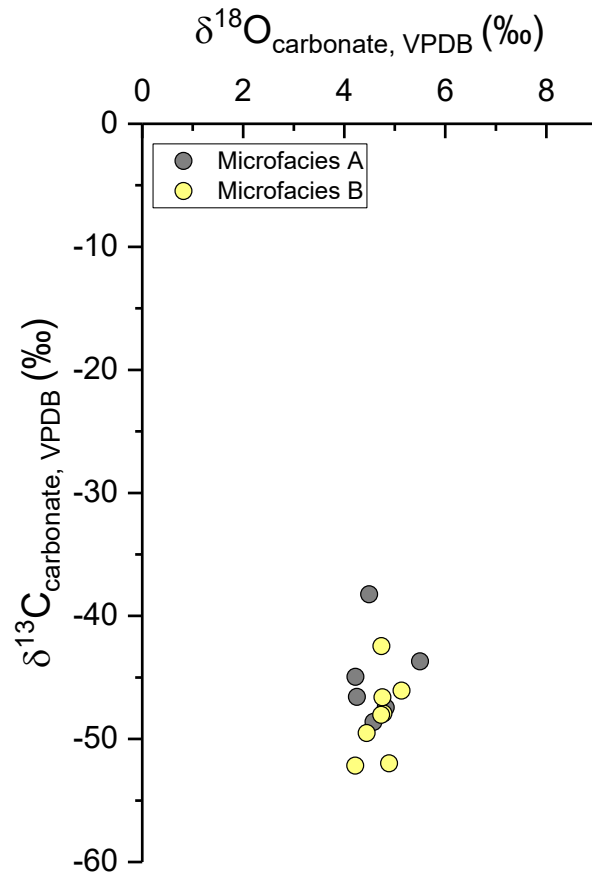


**Fig. 5.5.** Oxygen and carbon isotopes of carbonate samples.



**Table 5.1.** Carbonate mineralogy, total organic carbon (TOC), total inorganic carbon (TIC),  $\delta^{18}\text{O}$  and  $\delta^{13}\text{C}$  values.

Depth (cmbsf)	Classification	Aragonite * (%)	Calcite * (%)	Mg- Calcite * (%)	Quartz * (%)	TO C (%)	Carbonat e (%)	$\delta^{18}\text{O}$ (‰ VPDB )	$\delta^{13}\text{C}$ (‰ VPDB )
15.0	Microfacies A (micrite)	67	8	--	8	0.24	84	--	--
57.0		66	7	--	10	0.22	79.9	4.3	-46.6
139.0		58	--	4	20	0.32	72.7	--	--
154.0		55	10	--	10	0.3	80	--	--
188.0		60	4	--	16	0.25	73.7	4.5	-38.2
294.0		68	5	--	7	0.32	83.3	--	--
300.0		56	5	--	13	0.23	77.5	4.2	-45.0
316.0		40	5	--	17	0.27	67.7	--	--
318.6		51	3	--	20	0.25	69.8	4.6	-48.6
458.0		25	4	16	22	0.26	73.7	4.8	-47.5
489.5		31	5	18	15	0.42	85.6	5.5	-43.7
48.5	Microfacies B	100	--	--	--	n.d.	100	4.8	-47.9
110.0		100	--	--	--	n.d.	100	5.1	-46.1
133.0		96	1	--	2	n.d.	100	4.9	-52.0
318.5		99	--	--	--	n.d.	100	4.7	-42.5
400.0		100	--	--	--	n.d.	100	4.2	-52.2
431.5		100	--	--	--	n.d.	100	4.4	-49.5
445.0		100	--	--	--	n.d.	100	4.7	-48.0
485.5		100	--	--	--	n.d.	100	4.8	-46.6
19.0	Microfacies C	87	2	--	3	n.d.	100	--	--
298.0		79	--	7	3	n.d.	100	--	--
350.8		92	--	--	3	n.d.	100	--	--
445.5		94	--	--	3	n.d.	100	--	--

\*: XRD calculation are normalized to 100 % and were presented with database standard patterns.

n.d.: Not detectable. Remaining bulk carbonate after acid treatment was scarce for carbon content analysis.

#### 5.4.4. Carbonate Chronology

Samples from microfacies B were selected for detailed U-Th dating because of their high content in pure aragonite cements. A total of 104 samples from microfacies B were obtained from the 13 sections (I to XIII, Fig. 5.2), and revealed 13 distinct sequences of aragonite precipitation (Table 5.2). The determined ages range from  $2.50 \pm 0.18$  to  $36.65 \pm 0.12$  ka, respectively. Calculated age errors are between 0.03 and 2.5ka, and except for a couple of samples showing elevated  $^{232}\text{Th}$  concentrations, relative age errors are  $<1\%$  (Fig. 5.6, Tab. 5.2). Sequence VIII features the oldest age at a depth of  $\sim 192$  cmbsf, and the youngest sequence is XIII at a depth of  $\sim 486$  cmbsf (Figs. 5.2, 5.6). Plotting the sequence age against sediment depth reveals a younger precipitation age above and below the earliest precipitation sequence VIII (Fig. 5.6). Additionally, U-Th dating of 5 bivalve shell samples obtained from the core (Fig. 5.2) revealed the age when the bivalve died and its shells started to take up uranium from seawater. These shells exhibit ages ranging from  $41.4 \pm 1.5$  to  $32.71 \pm 0.40$  ka (Fig. 5.6), whereby shell samples collected from 27.5, 45, 62.5, 98.5, and 99 cmbsf have ages of  $34.64 \pm 0.93$ ,  $39.97 \pm 0.15$ ,  $40.48 \pm 0.26$ ,  $32.71 \pm 0.40$ , and  $41.4 \pm 1.5$  ka, respectively (Table 5.3, Fig. 5.6).

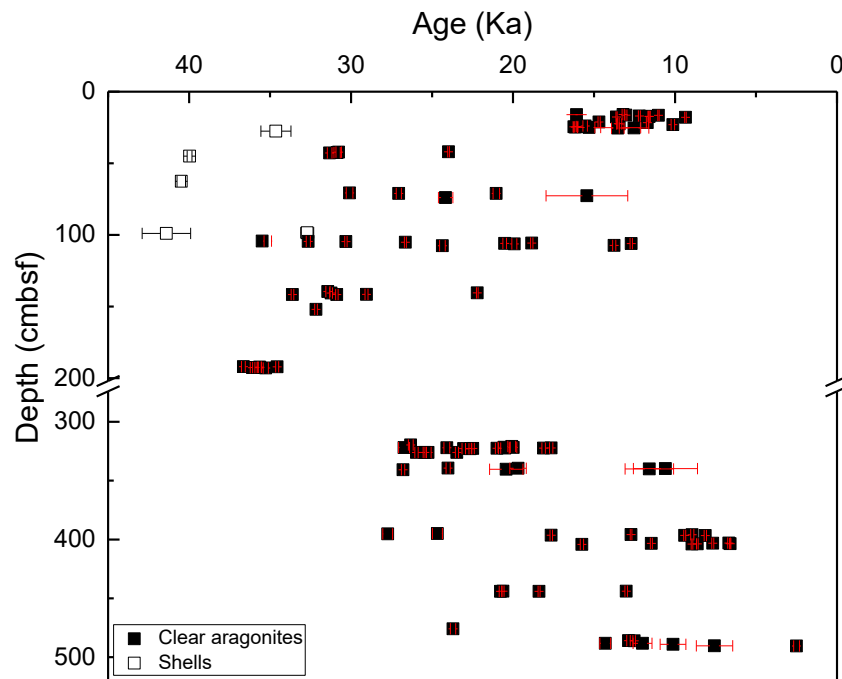


**Fig. 5.6.** U-Th ages of clear carbonates and shells against depth. Black squares are clear aragonites. Red lines are 2 sigma error bars of each dated aragonite. Empty squares are dates from bivalve shells with 2 sigma error bars.

#### 5.5. Discussion

##### 5.5.1. Carbonate formation at the Yam seep site

Authigenic carbonates are a common manifestation of hydrocarbon seepage today, and are a reliable recorder of ancient seepage events in seafloor sediments (Feng et al., 2018; Greinert et al., 2010; Roberts et al., 2010). Breccias and bioclasts, including bivalve shell fragments, present within the

seepage-impacted host sediment were cemented by micrite of microfacies A, providing evidence for an active macrofaunal chemosynthetic community present at the seep site prior to lithification. Bivalve shells are present from the top of the core to a depth of 316 cmbsf, indicating that the chemosynthetic community was fueled by a continuous supply of methane for a long period of time. Furthermore, parts of the Mebo24 carbonates show a porous structure resembling a moussy fabric usually found in unconsolidated sediments where most of the pore space is occupied by gas hydrate. This is a strong indication that methane in the form of dissolved gas, gas bubbles, and as solid gas hydrate was present at this seep site.

The very low  $\delta^{13}\text{C}$  carbon isotope values in carbonates from all three microfacies (Fig. 5.5) suggest that methane is the main carbon source for carbonate precipitation throughout the core (Tseng et al., 2022). The significantly enriched oxygen isotopes values (Fig. 5.5) may either be due to an influence of gas hydrate dissolution, clay mineral dehydration, or other water-rock reactions in the sediments (Aloisi et al., 2000; Bohrmann et al., 1998; Greinert et al., 2002; Han et al., 2004). Due to the absence of mud diapirs and ash layers at the study site, which would have also altered the primary  $\delta^{18}\text{O}$  composition during diagenesis (Dählmann et al., 2003), the enriched oxygen isotopes of MeBo-24 carbonates likely represent paleo-seawater  $\delta^{18}\text{O}$  compositions influenced by gas hydrates in sedimentary pore water (Han et al., 2014).

The three distinguishable microfacies represent different stages and extents in methane flux, microbial activity, and gas hydrate formation and dissolution. Micrite as present in microfacies A is a common early diagenetic phase in many modern and ancient seep limestones, representing the early occlusion of primary porosity and sediment lithification (Peckmann et al., 2001; Zwicker et al., 2015). Early diagenetic lithification is testified by the presence of microfossils such as foraminifera and shell fragments of chemosynthetic macrofauna dwelling at the seep, which are successively consolidated and incorporated as bioclasts (Figs. 5.2, 5.3a). Microfacies B, composed almost entirely of banded and botryoidal aragonite with some yellow aragonite, is devoid of host sediment and micrite. Banded and botryoidal aragonite and yellow aragonite represent two end-member varieties of aragonite at seeps. The former phase is a direct product of sulfate-driven AOM forming in larger voids within the host sediment lithified by micrite, or by direct replacement of solid gas hydrate within semi-lithified sediments (e.g. Bohrmann et al., 1998, 2006). Yellow aragonite is less commonly observed in modern seeps, yet has been linked to the direct encrustation and lithification of microbial mats of the AOM community (Hagemann et al., 2013; Zwicker et al., 2018). The observed variation in texture and fabric of these aragonite phases has been suggested to be a result of different growth modes. Yellow aragonite is thought to form at the hotspot of AOM activity in direct proximity of microbial biofilms, whereas banded and botryoidal aragonite requires more pore space for mineral growth, and is driven by the diffusion of carbonate ions from the AOM hotspot towards the locus of precipitation (Hagemann et al., 2013; Zwicker et al., 2018). Microfacies C is likewise devoid of host sediment, yet features smaller aggregates and bands of botryoidal aragonite interspersed between clotted microcrystalline aragonite.

The different textures of the carbonate phases reflect mineral growth at different rates under different degrees of supersaturation, as well as within larger and smaller available pore space (Flügel, 2004). Whereas micrite likely grew in small voids between the host sediments, the large, acicular crystals of banded and botryoidal aragonite grew inwards around the rims of larger cavities, slowly filling the available void space. The clotted fabric observed within microfacies C is essentially composed of micrite, and is a typical primary feature of seep limestones interpreted as a product of microenvironmental changes in mineral saturation by microbial metabolic activity (Peckmann et al., 2002, 2004).

The classification of carbonate microfacies enables the identification of fracture boundaries within the core. Boundary features in MeBo-24 include lithological boundaries, unconformities and corrosion layers (Fig. 5.2). Both lithological boundaries and unconformities can be well identified by the lateral precipitation of aragonite from microfacies A and B on fractured surfaces. Fracturing of lithified sediments and authigenic carbonates is a common feature found at many modern seeps (Bayon et al., 2009; Loher et al., 2018; Römer et al., 2014; Teichert et al., 2005; Wang et al., 2021). Previous studies investigating pockmark formation have shown that the cemented seafloor can expand due to the accumulation of free gas or the buoyancy of gas hydrates (Loher et al., 2018). At the Yam Seep site on the top of the accretionary ridge, uplifting and faulting are more feasible mechanisms inducing fracturing, because paleo sea level variations are unlikely to induce gas hydrate dissociation at a water depth of ~1400 m by pressure changes due to sea-level fall or small temperature changes of the bottom water. Similar thick aragonite successions cementing large void spaces have previously been reported for two other seep sites, the Dongsha area in the South China Sea (F. Chen et al., 2019), and the Jaco Scarp in the Central American forearc (Liebetrau et al., 2014). The precipitation mechanisms for the Jaco Scarp carbonate core is an upwardly-directed, chemoherm-type build up, yet such a conclusion was based on dating of just two separated aragonite samples located at both ends of a thick aragonite section within the core. Without continuous and detailed dating, the formation process and timing such thick aragonite successions remains unclear.

#### 5.5.2. Chronology of carbonate precipitation within fractures

Dating aragonites of microfacies B aragonites revealed that mineral authigenesis was active from ~37 to ~2 ka (Fig. 5.6), suggesting a persistent supply of methane over long timescales at the Yam Seep site. However, the depth of aragonite precipitation does not follow a continuous upward or downward temporal progression. Instead, the earliest instances of aragonite precipitation occur in the shallowest and deepest sections of the core. Assuming that fracturing of semi-lithified to lithified sediments produced conduits for methane ascent and sulfate infiltration from seawater, as well as providing available space for aragonite precipitation (specifically microfacies B), the chronology of fracturing will therefore be recorded by aragonite precipitation on the fracture boundaries. To evaluate the correlation of host rock fracturing and cementation of fractures by aragonite, U-Th dating was conducted systematically along the isopachous aragonite bands from the lithological boundary towards the center of the fracture (Fig. 5.7). Microsampling of the 13 investigated precipitation sequences of

microfacies B throughout the core generally suggest a precipitation direction from the fracture boundaries inward towards the void space.

Sequences VI and VII are the most consistent in terms of an identifiable precipitation direction. Sequence VI is one of the thickest sequences of microfacies B in the core measuring ~50 cm (Fig. 5.2), and only the top 3 cm of this sequence were sampled, and dated at ~35 to ~13 ka from the lithological boundary (Fig. 5.7a). This sequence represents a well-laminated botryoidal aragonite band with a linear precipitation direction in space and time for the upper 5 sample points corresponding to ~1.5 cm, followed by non-linear ages below (Fig. 5.7a). Sequence X consists of an unconformity, where the isopachous banded and botryoidal aragonite can be observed on the fractured boundaries (Fig. 5.7b). Three bands of aragonite can be observed on both surfaces, in which the upper layers are generally thicker than the lower. The precipitation from the upper boundary into the center of the fracture is dated at ~24, ~20, and ~11 ka, whereas for the lower isopachous aragonite band only two dates are available, providing ages from the center of the fracture towards the boundary of ~12 ka and 20 ka, respectively (Fig. 5.7b). This provides evidence that aragonite precipitated from the fracture boundaries inwards, filling out the fracture from both directions (Fig. 5.7b). Beside the continuous precipitation, detailed dating in several sequences reveals a hiatus in aragonite formation. Sequence IV shows an average age of ~29 ka from the lower three yellow aragonite samples, and a younger age of ~24 ka at the upper boundary succeeding a void space between microfacies B and A (Fig. 5.7c). Since this hiatus is dated between 30 to 24 ka, fracturing possibly occurred at around ~30 ka, producing space for aragonite precipitation. Alternatively, the hiatus in precipitation may have also resulted from methane or sulfate limitation, or the occupation of pore space by gas hydrate.

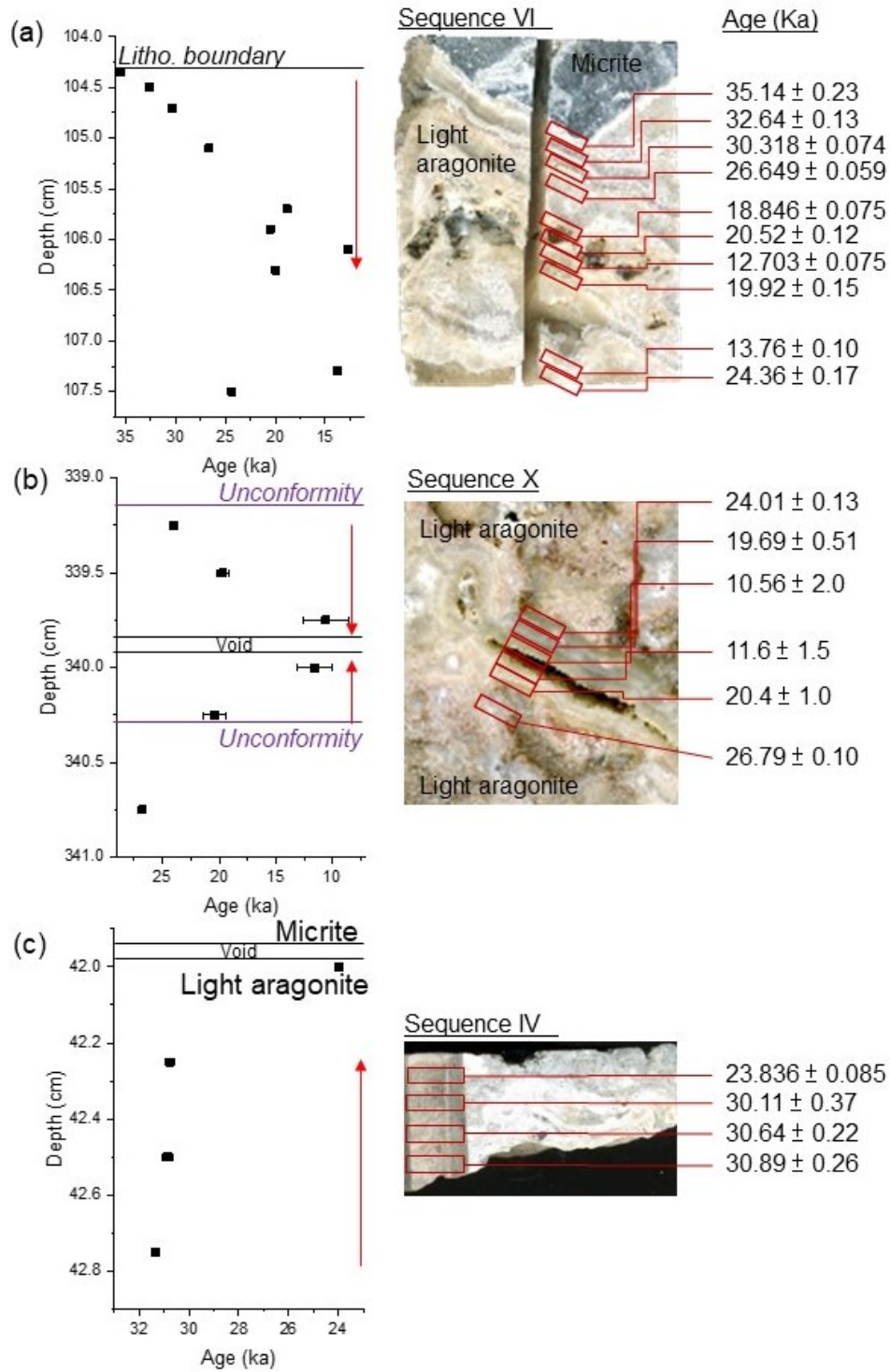


**Fig. 5.7. Aragonite precipitation ages in correspondence to microfacies in detail.** Sequences and directions of (a) lithological boundary precipitations: Sequence VI; (b) unconformity precipitations: Sequence X (c) rapid precipitation and hiatus: Sequence IV. Red arrows are general precipitation directions. Ages are given with 2 sigma error.

### 5.5.3. Timing of fracturing at Yam seep

The timing of 13 distinct precipitation sequences analyzed with 103 U-Th ages can be identified from the bands of aragonite on fracture boundaries, revealing (1) a period of vigorous fracturing and

seepage from ~37 to ~27 ka, (2) a subsequent quiet period of fracturing quiescence and lower seepage activity that lasted ~10 ka, and (3) a further, active period of fracturing and seepage between ~16 and ~12 ka (Fig. 5.8). Several aragonite bands from microfacies B were dated individually (grey squares), providing additional ages to further constrain the depth of precipitation (Fig. 5.8). Vertical lines in Fig. 5.8 indicate the aragonite samples closest to the fracture boundaries, different thickness represent the different fracture sizes ( $\geq 50$  cm or  $< 10$  cm), and the purple lines indicating the unconformities, dotted black line indicates the aragonite samples closest to its cemented breccia.

(1) Active period from ~37 to ~27 ka

Thick aragonite successions ( $\geq 50$  cm, thick black lines, Fig. 5.8) comprising sequences VIII, VI, VII and IX dated at ~36.6, 35.5, 33.6 and 26.7 ka, respectively, represents a period of intense fracturing and seepage that resulted in large-scale fractures and potential dramatic expulsion events that enabled the precipitation of massive aragonite bands (cf. Figs. 5.2, 5.7). Sequences IV, V, XI represent thinner layers of aragonite ( $< 10$  cm, thin black lines, Fig. 5.8), with ages of ~31.3, 30, 27.7 ka, respectively, indicating less intense fracturing around this time interval.

(2) Quiet period from ~27 to ~16 ka

Precipitation of microfacies B generally succeeds the formation of fractures. Whereby the unconformity of sequence X presents the only phase of fracturing during this period representing a period of fracturing quiescence. Aragonite precipitation at various depths (~42 to 476 cmbsf) suggests a cavity-rich environment potentially hosting free gas or, more likely, gas hydrate at sequences III, IV, V, VI, IX, X and the in sediments between sequence XII and XIII. At the end of this period, at around 16 Ka, aragonite precipitation ceased in all sequences of this period (V, VI, VII, VIII, and IX).

(3) Active period from ~16 to ~12 ka

After ~10 ka of quiescence, seepage recommenced at ~16 ka manifested by precipitation of sequence I, II, and III (~27 cmbsf). Additionally, a deeper precipitation event occurred at 403 cmbsf represented by sequence XII. Later aragonite precipitation occurred at a deeper depth in sequence XIII (486 cmbsf) that cemented the micritic breccia (dash dotted line in Fig. 5.7). The most recent precipitation event from ~12 to 2 ka is also the result of the formation of available pore space. Precipitation within sequences I, II, III stopped after ~10 ka. The unconformity at sequence XI was dated at ~9 ka, and coincides with the precipitation of sequence XII after a hiatus in which the latest precipitation event is dated at ~6 ka.

Fracturing of carbonates at many cold seeps is the result of buoyancy of gas hydrate accumulating beneath carbonate crusts (Loher et al., 2018). However, the topography of Yam Seep does not show a dome shape or pock mark-like surface that would indicate a previously sealed seafloor (cf. Loher et al., 2018). Instead, the non-homogeneous carbonate pavements and extended cracks suggest a preliminary influence of tectonic activity (Tseng et al., 2022). Therefore, fracturing in the core likely results from faulting, and the chronology of fracturing may represent a chronology of tectonic activity. The period of active fracturing at ~37 ka agrees with tephrochronology data from Luzon volcanic

eruptions at 39 ka (Ku et al., 2009), suggesting a period of tectonic activity between the Eurasian Plate and the Philippine Sea Plate that would have affected the Yam Seep at the time. The period of active fracturing at ~12 ka possibly affected both active and passive margins of the South China Sea lithosphere according to the chronology of massive seep aragonite at the Dong Sha seep site, which were dated at 11 ka (Deng et al., 2021). The chronology of aragonite precipitation at ~6 ka following a hiatus (Fig. 5.8) fits the record of other seepage sites at active margins in the South China Sea such as Yuan-An Ridge, that provides evidence for an episode of seepage during ~4.4 ka at accretionary ridges SW off Taiwan (Fan et al., 2018). Suggesting the dominant tectonic influence on fracturing, the chronology of tectonic activities is matching with climatic cooling events such as the Heinrich events HS-4 (~38 Ka), HS-2/ Last Glacial Maximum (LGM) (~24 Ka), HS-3 (~31Ka), HS-1(~16.8 Ka), and Younger Dryas (YD, ~12 Ka) regarding to fracturing of VIII, IV, X, III+XII and I+XI, respectively (Fig. 5.8). Whether there is a causal relationship remains to be clarified. Hypothesis of volcano eruptions triggering cooling events YD (Sun et al., 2020) can possibly assess by the fracturing age at active margin cold seep carbonates.

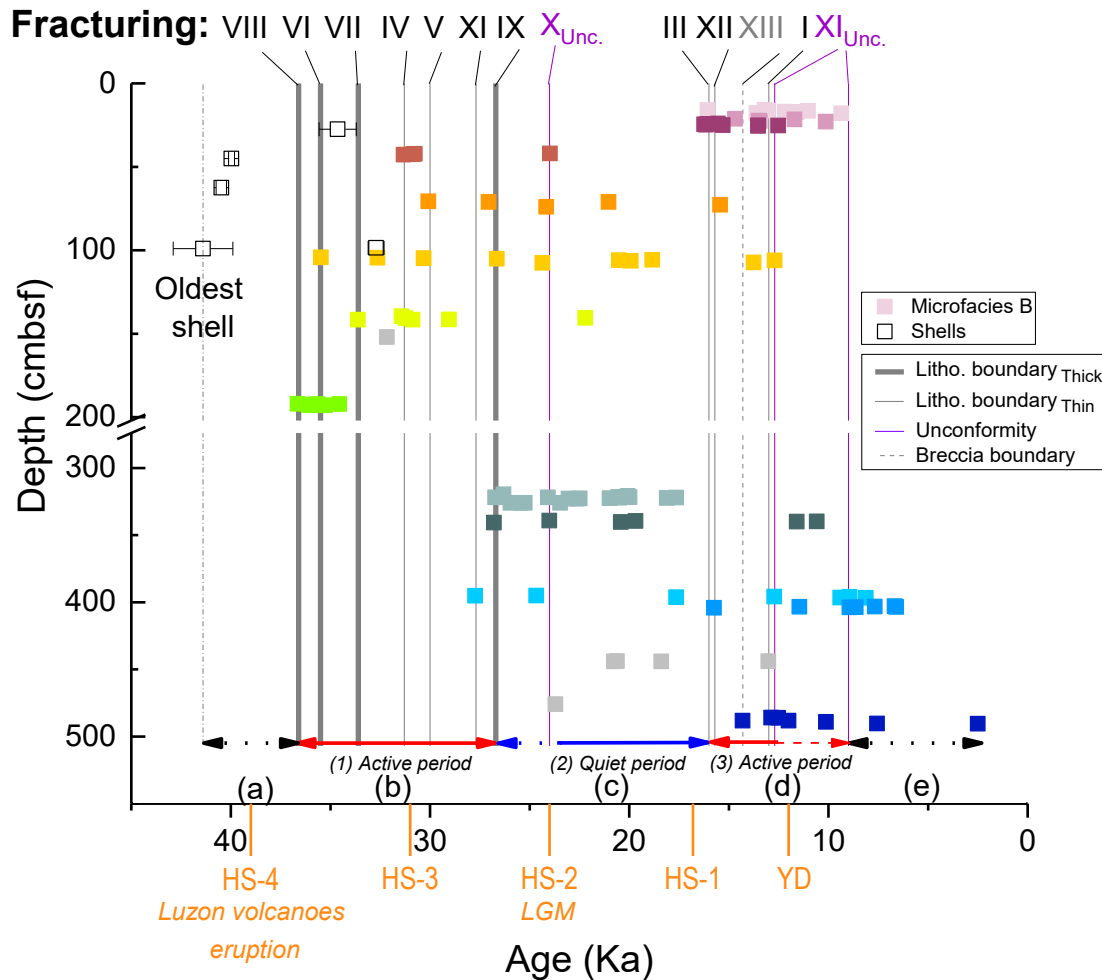


**Fig. 5.8.** Precipitation sequence chronology, shell ages and fracture boundaries. Microfacies B aragonites are shaded in 14 colors, 13 colors of 13 sequences and 1 non-sequenced sample color



(grey); for age error bars see Fig. 5.6 Dash-dotted line confines the oldest bivalve shell. Solid black lines of thick and thin representing fracture boundaries of  $\geq 50$  and  $<10$  cm, respectively, which are the oldest dated age of each microfacies B sequences occurring at the lithological boundaries. Purple dotted lines represent the age of microfacies B on unconformities. Black dotted line represents the precipitation age of microfacies B cemented breccia (microfacies A). Climatic events abbreviations (orange) of HS-1 to 4: Heinrich-Events; LGM: last glacial maximum; YD: Younger Dryas.

#### 5.5.4. Mechanisms and chronology of fracturing and carbonate precipitation at Yam seep

In order to discuss the modes and mechanisms of aragonite precipitation at Yam Seep, we illustrate how these are related to an interplay of faulting, methane seepage, rock fracturing, gas hydrate accumulation, and replacement of gas hydrates in space and time. The chronology of precipitation events is confined to a period between  $\sim 41$  and  $\sim 2$  ka, which can be illustrated in 5 stages (a to e, Fig. 5.9, Fig 5.8).

(a) Ages of chemosynthetic bivalve shells older than seep carbonates (Fig. 5.8 dotted, dashed line) suggest that the seafloor was affected by hydrocarbon seepage and colonized by chemosynthetic communities in the region since at least  $\sim 41$  Ka. Sediments near the SMI are gradually cemented and lithified, and form thin carbonate crusts near the seafloor. Intense methane seepage drives the SMI towards the seafloor where the oxidation of sulfide may induce carbonate corrosion in the upper most layer (0-5 cmbsf). Corrosion is observed on cemented shell fragments at 0-5 and 190-192 cmbsf exhibiting irregular shell margins lined with a dark, unidentified material (Fig. 5.4a), possibly induced by microenvironments of low pH due to oxidation of  $H_2S$  during erosion and exposure to oxygenated seawater (Himmler et al., 2011). At this point host sediments within microfacies A were already consolidated and lithified, and according to shells ages the consolidation of the sediments layer reached 1 mbsf at that point. Faulting within microfacies A would have provided conduits for methane seepage to the seafloor (Fig. 5.9a). The porous, moussy texture of the consolidated micrite of microfacies A (Fig. 5.2) also indicates the presence of gas hydrate and/ or free gas in the sediments (Torres et al., 2004).

(b) At this stage, the previously formed massive gas hydrate layers are replaced by aragonite (cf. Bohrmann et al., 1998). After aragonite precipitation this stage includes two major fracturing events. The earliest fracturing event at  $\sim 37$  ka caused microfacies B to crack at a depth of  $\sim 202$  cmbsf, after which further fracturing at  $\sim 27$  ka produced a wide fracture at a depth of 322 cmbsf (Fig. 5.9b). These fractures allowed for massive gas hydrates to accumulate at the active margin, which are then again consumed by aragonite precipitation.

(c) Followed by a period of comparable quiescence and moderate seepage intensity, aragonite growth at the expense of gas hydrates fills the fractures and results in the almost complete reduction of all available fracture porosity in the core, after which a pulse of moderate seepage re-opened the

aragonite veins at ~340 cmbsf (Fig. 5.9c). Incidentally, this period of quiescence coincides with the sea level rise after the Last Glacial Maximum (LGM, Clark et al. (2009). Seepage intensity was diminished by the increasing hydrologic pressure due to a sea level highstand after LGM (17 ka, Ruppel and Kessler (2017)), which may explain why later phases of aragonite precipitation occurred at a deeper depth within the core.

(d) Vigorous seepage commences again at ~16 ka, in which the entire cemented sections in shallow and deeper depths of the core (~27 and 403 cmbsf) are fractured. Due to the large supply of methane gas, massive gas hydrates accumulate within these fractures, which are again replaced by aragonite over time. Seepage activity continued until ~12 to 9 ka, enabling aragonite formation until ~5 ka (Fig. 5.9d).

(e) Carbonate precipitation ceases between ~5 and 2 ka. The present situation is characterized by the occurrence of free gas or gas hydrate accumulating below ~490 cmbsf, evidenced by large quantities of free gas released during drilling (Fig. 5.9e).

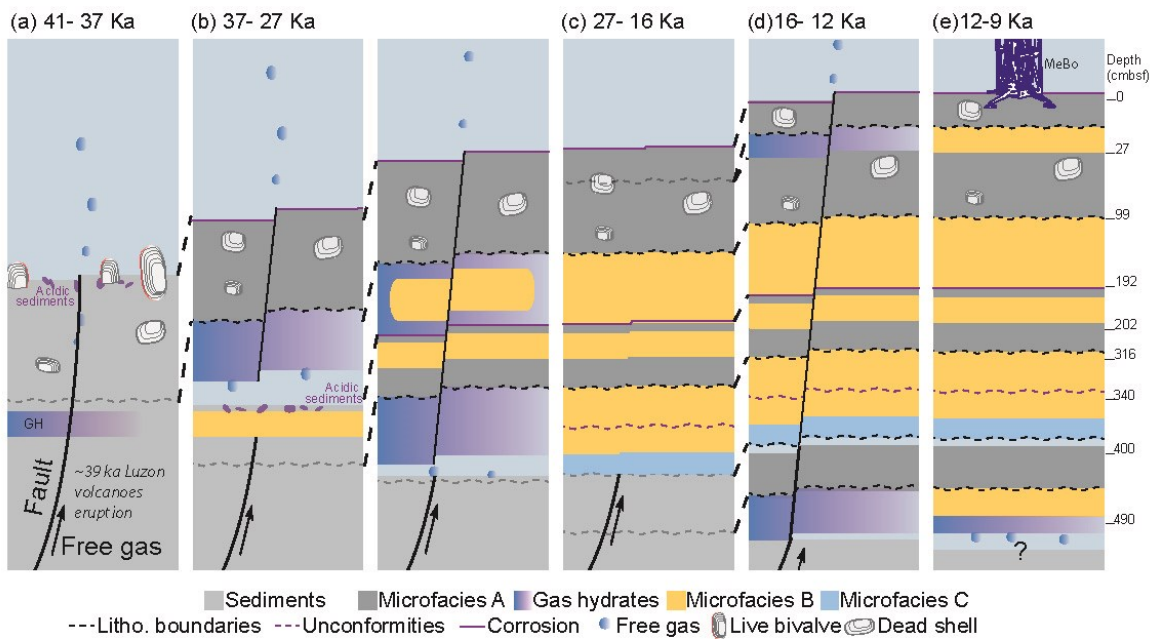


**Fig. 5.9.** Sketch to illustrate evolution of seepage, activities chronology, and fracture filling precipitations.

## 5.6. Conclusions

Petrography of carbonates within the MeBo-24 core reveals three distinct microfacies of aragonite that could further be classified into precipitation sequences separated by fracture boundaries and unconformities. Carbonate chronology of microfacies B and bivalve shells indicate persistent methane seepage occurred between ~41 and 2 ka, enabling multiple precipitation events within the core. Detailed U-Th dating of several pure banded and botryoidal aragonite cements located close to fracture boundaries measuring up to ~ 50 cm in thickness shows that the direction of precipitation is directed inward from fracture boundaries, slowing closing up the fractures and producing aragonite veins within

the core. These carbonates were dated in order to reconstruct the chronology of methane seepage and fracturing over the past 40 ka and suggest a period of active fracturing between ~37 to 27 and again between ~16 to 12 ka interrupted by a period of relative quiescence between ~27 to 16 ka potentially related to the global sea level rise at the end of the Last Glacial Maximum.

The major cause for the repeated occurrences of fracturing and intensification of seepage at the Yam Seep is most likely the waxing and waning of tectonic activity over time. Gas hydrate accumulates and forms massive layers of hydrate in the sediment in the early stages, whereas later accumulations of gas hydrates are mostly with fractured microfacies A and replaced by thick aragonite successions of microfacies B. This study revealed a 5-meter-thick carbonate deposition at Yam Seep, extended our knowledge of active seepage at active margin in GHSZ.

Table 5.2. U-Th isotope systematic and geochronology of clear aragonite.

IUP ID No.	ID GeoB 23225-1			Description	Depth (cmb sf)	Age corr. (ka)	$\pm$ (abs.)	$\delta^{234}\text{U}$ ini. (‰)	$\pm$ (abs.)	$^{238}\text{U}$ ( $\mu\text{g/g}$ )	$\pm$ (abs.)	$^{232}\text{Th}$ (ng/g)	$\pm$ (abs.)	$^{230}\text{Th}/^{238}\text{U}$ act. Ratio	$\pm$ (abs.)	$^{230}\text{Th}/^{232}\text{Th}$ act. Ratio	$\pm$ (abs.)	$\delta^{234}\text{U}$ m. (‰)	$\pm$ (abs.)	Age (ka)	$\pm$ (abs.)
IUP - 10479	I	15-19	La-04	Crystalline bands	15.88	13.201	0.067	140.02	0.50	4.34746	0.00018	1.9373	0.0032	0.13055	0.00033	903.9	2.8	134.89	0.48	13.313	0.036
IUP - 10480	I	15-19	La-05	Crystalline bands	16.04	16.08	0.28	142.0	1.0	4.2784	0.0018	9.248	0.016	0.16079	0.00047	232.49	0.79	135.68	0.98	16.620	0.058
IUP - 10572	I	15-19	La-07	Crystalline bands	16.36	13.034	0.061	141.07	0.87	5.61531	0.00023	0.4522	0.0023	0.12828	0.00055	4874	32	135.97	0.84	13.055	0.063
IUP - 10481	I	15-19	La-08	Cryptocrystalline bands	16.52	11.024	0.039	138.00	0.71	4.78172	0.00018	0.3998	0.0011	0.10927	0.00035	4039	17	133.77	0.69	11.045	0.039
IUP - 10573	I	15-19	La-11	Crystalline bands	17	12.200	0.061	140.80	0.67	6.05966	0.00027	0.2202	0.0010	0.12042	0.00057	10129	67	136.03	0.65	12.209	0.060
IUP - 10574	I	15-19	La-12	Crystalline filling fractured cryptocrystalline bands	17.16	11.602	0.052	141.6	1.1	5.58036	0.00035	0.2757	0.0012	0.11496	0.00047	7109	43	137.1	1.1	11.615	0.052
IUP - 10575	I	15-19	La-13	Crystalline filling fractured cryptocrystalline bands	17.32	11.598	0.064	144.2	1.2	6.16888	0.00029	0.2892	0.0015	0.11517	0.00059	7510	54	139.6	1.1	11.610	0.063
IUP - 10482	I	15-19	La-15	Cryptocrystalline bands	17.64	13.612	0.033	141.34	0.49	6.42764	0.00028	0.2975	0.0005	0.13355	0.00030	8898	26	136.00	0.48	13.624	0.033
IUP - 10483	I	15-19	La-17	Crystalline bands	17.96	9.352	0.046	137.0	0.70	4.83932	0.00020	0.5509	0.0014	0.09354	0.00041	2537	13	133.80	0.70	9.380	0.045
IUP - 10462	II	19-23	La-07	Crystalline bands	21.18	14.688	0.063	142.15	0.71	4.91444	0.00020	1.6017	0.0034	0.14412	0.00042	1409.7	5.1	136.37	0.68	14.770	0.046
IUP - 11085	II	19-23	La-10	Cryptocrystalline clotted crystalline	21.65	11.708	0.060	142.36	0.64	5.10385	0.00040	0.3954	0.0012	0.11624	0.00056	4577	26	137.74	0.61	11.727	0.064
IUP - 10463	II	19-23	La-12	Cryptocrystalline clotted crystalline	22.3	13.506	0.055	141.92	0.76	5.82977	0.00033	0.9810	0.0021	0.13292	0.00046	2561	10	136.60	0.74	13.548	0.052
IUP - 10464	II	19-23	La-13	Cryptocrystalline clotted crystalline	22.6	13.44	0.16	143.3	2.1	5.0542	0.0025	5.714	0.016	0.13474	0.00066	387.3	2.2	138.0	2.0	13.727	0.081
IUP - 10465	II	19-23	La-18	Botryoidal crystalline and cryptocrystalline bands	22.99	10.13	0.11	138.6	0.6	4.63312	0.00023	3.8256	0.0071	0.10273	0.00035	392.2	1.5	134.66	0.57	10.341	0.036
IUP - 11043	III	24-28	La-01	Cryptocrystalline	24	15.55	0.14	143.58	0.71	4.13395	0.00024	4.4627	0.0061	0.15398	0.00035	432.2	1.2	137.42	0.68	15.817	0.039
IUP - 11044	III	24-28	La-03	Crystalline bands	24.33	16.044	0.051	142.81	0.70	4.09805	0.00020	0.7069	0.0012	0.15630	0.00041	2746.2	8.6	136.49	0.67	16.087	0.040
IUP - 11045	III	24-28	La-04	Cryptocrystalline clotted crystalline	24.49	16.241	0.056	142.26	0.79	4.86014	0.00028	1.1360	0.0019	0.15814	0.00042	2052.9	6.4	135.89	0.75	16.299	0.050
IUP - 11046	III	24-28	La-06	Crystalline bands	24.82	16.14	0.11	140.84	0.67	4.62127	0.00036	3.5218	0.0067	0.15826	0.00046	630.3	2.2	134.57	0.64	16.334	0.055
IUP - 11047	III	24-28	La-07	Shells and cryptocrystalline	24.98	15.30	0.71	142.48	0.73	5.11137	0.00038	28.575	0.042	0.16191	0.00034	87.86	0.23	136.46	0.64	16.709	0.037
IUP - 11048	III	24-28	La-08	Cryptocrystalline clotted crystalline	25.15	13.5	1.4	142.50	0.80	5.21136	0.00043	57.220	0.096	0.15842	0.00044	43.78	0.14	137.16	0.55	16.311	0.053
IUP - 11049	III	24-28	La-09	Crystalline clotted cryptocrystalline	25.31	12.53	0.92	140.19	0.64	5.36342	0.00038	38.479	0.061	0.14022	0.00033	59.36	0.17	135.32	0.51	14.338	0.037
IUP - 11050	III	24-28	La-10	Crystalline clotted cryptocrystalline	25.47	13.53	0.39	140.78	0.79	5.21670	0.00036	16.112	0.033	0.13996	0.00038	137.71	0.47	135.50	0.74	14.308	0.042
IUP - 10252	IV	42-43	--	Crystalline bands	42	23.836	0.085	136.37	0.79	3.35356	0.00028	1.6459	0.0025	0.22324	0.00047	1385.6	3.6	127.50	0.74	23.959	0.063
IUP - 10338	IV	42-43	--	Cryptocrystalline	42.25	30.11	0.37	137.8	1.6	3.74838	0.00028	10.011	0.019	0.2784	0.0012	317.7	1.5	126.6	1.5	30.79	0.17
IUP - 10337	IV	42-43	--	Cryptocrystalline	42.5	30.64	0.22	138.5	2.2	3.58980	0.00032	2.8442	0.0068	0.2789	0.0014	1071.6	6.0	127.0	2.1	30.84	0.19
IUP - 10336	IV	42-43	--	Cryptocrystalline	42.75	30.89	0.26	141.0	1.6	4.35343	0.00038	7.538	0.018	0.2833	0.0011	498.1	2.3	129.2	1.4	31.32	0.15
IUP - 10494	V	70-75	La-03	Cryptocrystalline	70.7	30.09	0.20	145.1	1.9	3.99567	0.00031	5.5167	0.0086	0.27702	0.00073	613.3	1.9	133.3	1.8	30.43	0.11

IUP -	104 97	V	70-75	La-16	Crystalline bands	71	21.04	0.20	142.5	1.2	2.2060 00	0.0000 87	3.2843	0.0040	0.2026 6	0.000 52	419.5	1.2	134. 3	1.1	21.4 10	0.06 5
IUP -	104 98	V	70-75	La-17	Crystalline bands	71.1	27.05	0.16	140.2	1.6	3.3353 6	0.0001 8	3.8104	0.0052	0.2513 5	0.000 64	672.6	2.0	129. 8	1.5	27.3 41	0.09 2
IUP -	104 95	V	70-75	La-08	Crystalline bands	72.7	15.4	2.5	141.7	2.0	2.4919 3	0.0001 6	47.854	0.084	0.1937 5	0.000 70	30.85	0.12	135. 7	1.6	20.3 50	0.08 8
IUP -	104 96	V	70-75	La-13	Cryptocrystalline	74	24.16	0.45	135.7	1.2	4.4682 7	0.0002 7	14.885	0.024	0.2315 1	0.000 71	214.24	0.74	126. 7	1.1	25.0 06	0.08 8
IUP -	104 56	VI	103-108	La-02	Crystalline bands	104.3	35.14	0.23	146.9	3.6	3.8599	0.0025	0.8131	0.0026	0.3139	0.001 4	4611	25	133. 0	3.3	35.2 0	0.24
IUP -	104 84	VI	103-108	La-03	Crystalline bands	104.5	32.64	0.13	138.4	1.4	3.3153 3	0.0001 9	0.1463 7	0.0006 0	0.2925 6	0.000 93	20969	109	126. 2	1.3	32.6 5	0.13
IUP -	104 85	VI	103-108	La-04	Crystalline bands	104.7	30.31 8	0.07 4	138.5 1	0.87	3.5898 5	0.0001 6	0.3349 6	0.0007 0	0.2747 4	0.000 54	9153	26	127. 14	0.80	30.3 42	0.07 7
IUP -	104 86	VI	103-108	La-06	Crystalline bands	105.1	26.64 9	0.05 9	136.9 0	0.59	3.6079 0	0.0001 3	0.0584 5	0.0002 1	0.2450 9	0.000 47	46601	186	126. 97	0.55	26.6 53	0.05 3
IUP -	104 87	VI	103-108	La-09	Crystalline and Cryptocrystalline	105.7	18.84 6	0.07 5	133.3	1.4	2.9981 1	0.0001 7	0.7946	0.0015	0.1796 5	0.000 54	2126.0	7.5	126. 3	1.3	18.9 13	0.06 2
IUP -	104 88	VI	103-108	La-10	Crystalline bands	105.9	20.52	0.12	134.3	1.6	2.6363 3	0.0002 0	1.6170	0.0034	0.1949 3	0.000 70	995.5	4.2	126. 7	1.5	20.6 70	0.09 0
IUP -	105 76	VI	103-108	La-11	Crystalline bands	106.1	12.70 3	0.07 5	136.8	1.7	2.5094 8	0.0001 2	0.0343 0	0.0002 6	0.1246 0	0.000 67	27916	258	132. 0	1.7	12.7 07	0.06 6
IUP -	105 77	VI	103-108	La-12	Crystalline bands	106.3	19.92	0.15	139.4	1.7	3.0627 7	0.0001 9	2.0686	0.0085	0.1908	0.001 1	864.0	6.0	131. 7	1.6	20.0 9	0.12
IUP -	105 78	VI	103-108	La-17	Crystalline bands	107.3	13.76	0.10	132.5	1.8	2.9335 3	0.0001 8	0.0751 1	0.0005 9	0.1338 0	0.000 88	15972	164	127. 4	1.7	13.7 64	0.09 9
IUP -	105 79	VI	103-108	La-18	Crystalline bands	107.5	24.36	0.17	138.7	1.9	2.5415 4	0.0002 0	0.2500	0.0012	0.2270	0.001 4	7054	55	129. 5	1.8	24.3 9	0.18
IUP -	110 84	VII	138-144	La-03	Cryptocrystalline	139.5 1	31.43	0.13	137.2 8	0.88	4.7166 7	0.0003 5	2.5352	0.0061	0.2843 0	0.000 79	1613.3	5.9	125. 63	0.80	31.5 7	0.10
IUP -	104 99	VII	138-144	La-09	Crystalline bands	140.4 5	22.20 7	0.05 1	132.3 6	0.71	3.9911 2	0.0001 3	0.2728 5	0.0004 7	0.2077 5	0.000 36	9360	23	124. 31	0.67	22.2 24	0.04 5
IUP -	105 00	VII	138-144	La-10	Cryptocrystalline	140.6 1	31.23 5	0.08 4	134.9 3	0.65	4.5056 7	0.0002 3	0.9958	0.0014	0.2812 6	0.000 58	3914.0	9.8	123. 53	0.59	31.2 90	0.07 1
IUP -	105 01	VII	138-144	La-16	Crystalline clotted cryptocrystalline	141.5 4	29.05 0	0.09 2	136.8 5	0.99	4.8333 8	0.0003 0	1.1616	0.0023	0.2647 0	0.000 60	3397	10	126. 07	0.91	29.1 11	0.07 6
IUP -	105 02	VII	138-144	Lb-05	Cryptocrystalline	141.6	33.62 3	0.08 2	136.9 9	0.70	4.2384 3	0.0001 9	0.3978 3	0.0008 9	0.2997 5	0.000 59	9832	29	124. 57	0.63	33.6 47	0.08 2
IUP -	105 03	VII	138-144	Lb-11	Crystalline clotted cryptocrystalline	141.6 01	30.87 7	0.08 0	134.5 4	0.48	6.6485 9	0.0002 3	1.4441	0.0026	0.2784 0	0.000 57	3943	11	123. 30	0.44	30.9 32	0.06 8
IUP -	103 03	--	52-53	--	Cryptocrystalline	152	32.16 3	0.08 5	136.9 1	0.63	5.1807 3	0.0005 3	2.7741	0.0079	0.2885 4	0.000 65	1658.8	6.0	125. 01	0.58	32.1 76	0.08 6
IUP -	110 36	VIII	192-202	La-01	Crystalline and cryptocrystalline	192	36.65	0.12	140.8	1.1	3.8245 3	0.0003 4	1.6810	0.0028	0.3243 1	0.000 73	2237.1	6.2	127. 0	1.0	36.7 56	0.09 8
IUP -	110 37	VIII	192-202	La-02	Crystalline and cryptocrystalline	192.1 4	34.56 3	0.09 3	139.7 8	0.58	4.7454 4	0.0003 4	1.7286	0.0033	0.3084 2	0.000 60	2570.0	7.0	126. 79	0.53	34.6 54	0.07 4
IUP -	110 38	VIII	192-202	La-03	Cryptocrystalline	192.2 9	35.65	0.10	139.5 9	0.52	4.8922 0	0.0003 9	1.3925	0.0025	0.3163 5	0.000 70	3376.8	9.5	126. 23	0.47	35.7 23	0.09 2
IUP -	110 39	VIII	192-202	La-04	Cryptocrystalline	192.4 3	35.63	0.10	138.7 1	0.54	4.4983 5	0.0003 5	2.1858	0.0037	0.3163 3	0.000 58	1981.5	4.9	125. 44	0.49	35.7 52	0.07 5
IUP -	110 40	VIII	192-202	La-05	Cryptocrystalline	192.5 7	35.94	0.14	137.2 6	0.85	3.8925 6	0.0003 8	2.8103	0.0065	0.3186 9	0.000 75	1344.9	4.4	124. 02	0.76	36.1 22	0.10 4
IUP -	110 41	VIII	192-202	La-06	Cryptocrystalline	192.7 1	36.08	0.15	137.5 0	0.62	4.5249 5	0.0003 4	4.0854	0.0075	0.3201 3	0.000 66	1080.0	3.0	124. 19	0.55	36.3 07	0.08 9
IUP -	110 42	VIII	192-202	La-07	Cryptocrystalline	192.8 6	35.27	0.16	138.1 2	0.63	4.7751 2	0.0003 3	4.1807	0.0078	0.3142 1	0.000 83	1090.3	3.5	125. 03	0.57	35.4 9	0.12
IUP -	104 89	IX	319-326	Lb-02	Cryptocrystalline and fractured crystalline botryoids	319.6 4	26.31	0.15	133.3	2.6	3.3710 4	0.0002 6	0.9018	0.0023	0.2422	0.001 1	2869	14	123. 7	2.4	26.3 8	0.14
IUP -	104 90	IX	319-326	Lb-07	Crystalline bands	320.8 6	20.08	0.24	142.2	3.0	1.6860 7	0.0001 2	2.8427	0.0051	0.1948 1	0.000 86	360.4	1.7	134. 4	2.9	20.5 0	0.12
IUP -	104 91	IX	319-326	Lc-01	Crystalline bands	321.6	20.56	0.37	137.2	1.5	2.4023 6	0.0001 4	6.892	0.011	0.2006 6	0.000 71	218.36	0.85	129. 5	1.4	21.2 79	0.08 5

IUP -	104 92	IX	319-326	Lc-02	Cryptocrystalline	321.7 3	19.98	0.21	131.2	1.0	5.2613 1	0.0003 1	8.257	0.016	0.1919 5	0.000 66	380.0	1.5	124. 00	0.95	20.3 78	0.06 9
IUP -	105 80	IX	319-326	Lc-03	Crystalline botryoids	321.8 6	26.73	0.34	137.2	1.0	6.0081 0	0.0004 0	15.460	0.035	0.2510 5	0.000 66	298.5	1.0	127. 19	0.94	27.3 79	0.08 6
IUP -	105 81	IX	319-326	Lc-04	Cryptocrystalline	321.9 9	24.09	0.18	133.7 0	0.82	6.0314 7	0.0004 5	7.749	0.017	0.2262 0	0.000 60	537.5	1.8	124. 90	0.76	24.4 12	0.07 6
IUP -	105 82	IX	319-326	Lc-05	Crystalline botryoids	322.1 3	17.65	0.11	133.6	1.0	7.2152 3	0.0004 4	4.2288	0.0093	0.1699 5	0.000 66	883.4	3.9	127. 11	0.96	17.7 93	0.07 1
IUP -	105 83	IX	319-326	Lc-06	Crystalline and Cryptocrystalline	322.2 6	20.50	0.26	135.4	1.4	5.3935 0	0.0004 7	10.665	0.019	0.1979 3	0.000 62	305.3	1.1	127. 8	1.3	20.9 96	0.08 2
IUP -	105 84	IX	319-326	Lc-07	Cryptocrystalline	322.3 9	18.11	0.10	132.8 4	0.79	4.6655 1	0.0003 0	3.0859	0.0077	0.1740 9	0.000 53	804.0	3.2	126. 21	0.75	18.2 80	0.06 3
IUP -	105 85	IX	319-326	Lc-08	Cryptocrystalline	322.5 2	20.99	0.10	133.7	1.1	4.0185 8	0.0002 3	2.1278	0.0033	0.1987 1	0.000 60	1146.8	3.9	126. 0	1.0	21.1 25	0.07 6
IUP -	105 86	IX	319-326	Lc-09	Cryptocrystalline	322.6 5	22.48 4	0.09 4	133.9	1.1	3.6468 2	0.0001 7	1.6218	0.0040	0.2111 5	0.000 60	1447.0	5.5	125. 7	1.0	22.5 96	0.07 5
IUP -	105 87	IX	319-326	Lc-10	Crystalline and cryptocrystalline	322.7 8	23.05	0.11	134.1	1.2	3.6331 4	0.0002 3	1.4831	0.0037	0.2158 1	0.000 77	1613.9	7.0	125. 6	1.1	23.1 51	0.09 3
IUP -	104 93	IX	319-326	Lc-11	Crystalline clotted cryptocrystalline	322.9 1	22.63	0.09	128.8	1.8	3.4693 0	0.0001 8	1.0788	0.0022	0.2112 0	0.000 54	2132.5	7.0	120. 8	1.7	22.7 13	0.07 8
IUP -	110 86	IX	319-326	Lf-01	Crystalline and cryptocrystalline	326	25.45	0.11	137.5 4	0.90	3.2360 3	0.0002 0	0.5690	0.0019	0.2361 0	0.000 83	4095	20	128. 01	0.84	25.4 9	0.10
IUP -	110 88	IX	319-326	Lf-08	Crystalline and cryptocrystalline	326	23.47	0.10	136.5 9	0.80	5.3286 6	0.0004 7	3.0461	0.0061	0.2203 8	0.000 53	1173.3	3.7	127. 84	0.75	23.6 10	0.06 0
IUP -	110 89	IX	319-326	Lf-09	Crystalline and cryptocrystalline	326	25.24	0.19	135.7 6	0.99	4.7720 7	0.0002 9	6.205	0.014	0.2364 0	0.000 76	552.6	2.1	126. 42	0.92	25.5 71	0.09 7
IUP -	110 87	IX	319-326	Lf-07	Crystalline and cryptocrystalline	326	25.96	0.11	136.6 1	0.67	4.8561 0	0.0005 9	3.1421	0.0056	0.2410 6	0.000 53	1136.8	3.2	126. 96	0.62	26.1 24	0.06 7
IUP -	105 04	X	338-342	La-06	Crystalline bands	339.2 5	24.01	0.13	137.5 9	0.93	3.8374 4	0.0002 1	2.9132	0.0045	0.2252 0	0.000 65	914.7	3.0	128. 57	0.87	24.2 01	0.07 2
IUP -	105 05	X	338-342	La-07	Crystalline bands	339.5	19.69	0.51	143.0	2.0	2.2727 7	0.0001 1	9.013	0.014	0.1965 6	0.000 69	152.97	0.59	135. 3	1.9	20.6 83	0.07 3
IUP -	105 06	X	338-342	La-08	Crystalline bands	339.7 5	10.6	2.0	153.4	5.2	1.1302 61	0.0000 75	17.073	0.026	0.1422 5	0.000 79	28.87	0.17	148. 9	4.9	14.3 9	0.11
IUP -	105 07	X	338-342	La-09	Crystalline bands	340	11.6	1.5	143.9	2.5	1.2828 1	0.0001 2	13.935	0.025	0.1405 0	0.000 61	40.09	0.19	139. 2	2.4	14.3 35	0.07 5
IUP -	105 08	X	338-342	La-10	Crystalline bands	340.2 5	20.4	1.0	143.7	1.9	2.5230 8	0.0001 7	20.957	0.029	0.2124 2	0.000 59	78.92	0.25	135. 7	1.7	22.5 19	0.06 4
IUP -	105 09	X	338-342	La-12	Crystalline botryoids	340.7 5	26.79	0.10	137.3	1.3	5.5103 9	0.0003 6	2.5959	0.0038	0.2472 5	0.000 58	1618.8	4.5	127. 3	1.2	26.9 11	0.07 8
IUP -	104 66	XI	392.5-397	La-02	Spheroidal crystalline	394.9 9	24.67	0.31	138.9	2.0	5.9922	0.0027	13.420	0.031	0.2340 0	0.000 94	341.5	1.6	129. 5	1.9	25.2 4	0.12
IUP -	104 67	XI	392.5-397	La-03	Crystalline bands	395.1 8	27.74	0.31	135.4	1.4	6.0728	0.0032	13.188	0.039	0.2579	0.001 0	387.8	1.9	125. 2	1.3	28.2 9	0.14
IUP -	104 68	XI	392.5-397	La-06	Crystalline bands	395.7 5	12.71 8	0.05 2	145.7	1.3	1.9876 31	0.0000 91	n.d.		0.1256 7	0.000 46			140. 5	1.2	12.7 18	0.05 2
IUP -	104 69	XI	392.5-397	La-07	Crystalline bands	395.9 5	8.936	0.09 6	151.2	5.9	0.7775 8	0.0002 8	0.0785 2	0.0003 9	0.0905 4	0.000 81	2916	30	147. 4	5.8	8.96 1	0.09 2
IUP -	110 83	XI	392.5-397	La-09	Crystalline and cryptocrystalline	396.3 3	17.64 1	0.07 8	136.8	1.2	2.9201 4	0.0002 4	0.4168	0.0013	0.1696 1	0.000 65	3620	18	130. 2	1.1	17.6 77	0.06 8
IUP -	104 70	XI	392.5-397	La-10	Crystalline botryoids	396.5 2	9.404	0.06 3	145.9	3.4	1.9720	0.0010	0.0110 07	0.0000 79	0.0944 0	0.000 54	55155	505	142. 0	3.3	9.40 5	0.06 3
IUP -	104 71	XI	392.5-397	La-11	Crystalline bands	396.7 1	8.128	0.07 4	147.8	2.8	1.3103 0	0.0001 0	0.3031 6	0.0008 1	0.0827 8	0.000 63	1157.3	9.3	144. 5	2.7	8.18 6	0.07 0
IUP -	104 72	XII	403-407	La-01	Cryptocrystalline and fractured crystalline botryoids	403	6.673	0.07 7	152.0	5.6	1.2601 7	0.0001 2	0.1906	0.0012	0.0685 8	0.000 66	1486	17	149. 2	5.5	6.71 0	0.07 1
IUP -	110 79	XII	403-407	La-02	Cryptocrystalline and fractured crystalline botryoids	403.1 9	7.671	0.06 4	144.2	3.3	1.4533 9	0.0001 4	0.0281 6	0.0002 4	0.0776 6	0.000 58	12193	138	141. 1	3.2	7.67 6	0.06 3
IUP -	104 73	XII	403-407	La-03	Cryptocrystalline and fractured crystalline botryoids	403.3 7	11.46 2	0.05 7	144.7	1.3	1.8669 8	0.0001 2	n.d.		0.1138 3	0.000 52			140. 1	1.3	11.4 62	0.05 7
IUP -	110 80	XII	403-407	La-04	Cryptocrystalline and fractured crystalline botryoids	403.5 6	6.592	0.03 9	141.8	1.7	1.9297 0	0.0001 5	n.d.		0.0669 0	0.000 36			139. 2	1.7	6.59 2	0.03 9

*Manuscript II: Seep carbonates microfacies and chronology*

IUP -	110 81	XII	403-407	La-05	Cryptocrystalline and fractured crystalline botryoids	403.7 4	8.624	0.05 3	144.6	2.5	2.0835 6	0.0002 0	0.0130 5	0.0001 1	0.0869 2	0.000 48	42276	426	141. 1	2.4	8.62 6	0.05 8
IUP -	110 82	XII	403-407	La-06		Cryptocrystalline and fractured crystalline botryoids	403.9 3	8.949	0.04 8	144.1	1.5	3.1502 2	0.0002 7	n.d.		0.0900 0	0.000 46		140. 5	1.5	8.94 9	0.04 8
IUP -	104 74	XII	403-407	La-07		Cryptocrystalline and fractured crystalline botryoids	404.1 1	15.75	0.10 0.06	138.3 136.1	2.0	3.0911 6	0.0002 0	1.6743	0.0035	0.1536 9	0.000 60	916.1	4.1	132. 3	1.9	15.8 85
IUP -	103 05	--	444-445	--	--	444	20.62 2	0.06 8	136.1 8	0.81	4.2324 5	0.0003 6	2.2585	0.0042	0.1949 4	0.000 55	1119.1	3.8	128. 47	0.76	20.6 34	0.06 9
IUP -	103 39	--	444-445	--	--	444	13.01 3	0.07 7	145.4	1.6	3.7364 4	0.0002 5	0.2492	0.0014	0.1283 9	0.000 70	5874	46	140. 1	1.5	13.0 15	0.07 7
IUP -	103 04	--	444-445	--	--	444.1	18.39 5	0.05 8	137.9 8	0.73	3.8552 3	0.0002 3	0.4880 0	0.0008 9	0.1758 9	0.000 46	4255	14	130. 99	0.70	18.3 98	0.04 8
IUP -	103 06	--	444-445	--	--	444.1	20.77 6	0.08 2	137.5 3	0.84	3.9570 3	0.0002 7	1.6786	0.0035	0.1964 6	0.000 62	1420.4	5.4	129. 69	0.79	20.7 86	0.06 7
IUP -	103 40	--	476	--	--	476	23.70	0.17	139.3	2.1	4.6567 3	0.0003 4	0.7120	0.0037	0.2214 3	0.001 3	4415	35	130. 2	2.0	23.7 1	0.17
IUP -	104 75	XIII	486-490	La-01	Crystalline clotted cryptocrystalline	486	12.87	0.11	142.1 3	0.96	4.8694 6	0.0003 2	3.6076	0.0073	0.1284 1	0.000 49	560.8	2.4	137. 06	0.92	13.0 55	0.05 0
IUP -	104 76	XIII	486-490	La-02	Crystalline clotted cryptocrystalline	486.1 3	12.52 1	0.07 7	140.1 5	0.57	6.0409 8	0.0002 7	3.2421	0.0054	0.1245 0	0.000 35	738.9	2.4	135. 27	0.55	12.6 56	0.03 9
IUP -	110 75	XIII	486-490	La-06	Crystalline bands	488.2 3	14.31	0.33	141.2 3	0.92	7.6087 9	0.0006 4	19.552	0.056	0.1458 6	0.000 65	172.37	0.92	135. 65	0.88	14.9 50	0.07 7
IUP -	110 76	XIII	486-490	La-07	Cryptocrystalline	488.2 7	12.01	0.59	141.2 0	0.77	6.4113 7	0.0005 3	29.510	0.081	0.1295 1	0.000 53	85.55	0.42	136. 50	0.71	13.1 63	0.05 9
IUP -	110 77	XIII	486-490	La-11	Crystalline bands	489.1 3	10.12	0.79	142.6 4	0.80	4.9495 4	0.0003 9	30.825	0.084	0.1159 8	0.000 41	56.65	0.25	138. 63	0.72	11.6 90	0.04 6
IUP -	110 78	XIII	486-490	La-17	Crystalline bands	490.3 4	7.6	1.1	145.5 0	0.91	3.6604 8	0.0002 5	32.201	0.098	0.0981 4	0.000 43	33.97	0.18	142. 43	0.76	9.77 7	0.04 8
IUP -	104 77	XIII	486-490	La-18	Crystalline bands	490.5	2.50	0.18	144.3 6	0.97	3.7870 9	0.0002 3	5.4073	0.0085	0.0295 4	0.000 21	65.52	0.49	143. 34	0.96	2.85 7	0.01 9

Table 5.3. U-Th isotope systematic and geochronology of shells.

IUP ID No.	ID	Depth (cmbsf)	Age <sub>corr.</sub> (ka)	± (abs.)	δ <sup>234</sup> U <sub>ini.</sub> (‰)	± (abs.)	<sup>238</sup> U (μg/g)	± (abs.)	<sup>232</sup> Th (ng/g)	± (abs.)	<sup>230</sup> Th/ <sup>238</sup> U act. Ratio	± (abs.)	<sup>230</sup> Th/ <sup>232</sup> Th act. Ratio	± (abs.)	δ <sup>234</sup> U <sub>m.</sub> (‰)	± (abs.)	Age (ka)	± (abs.)
IUP- 11067	<b>S1</b>	27.5	36.0	1.9	137.9	1.2	1.200828	0.000071	17.642	0.028	0.34568	0.00088	71.39	0.21	124.54	0.89	39.76	0.13
IUP - 10302	<b>S2</b>	45.5	39.95	0.15	143	1.9	0.532985	0.000035	0.03888	0.00012	0.34781	0.00091	14743	59	127.7	1.7	39.97	0.14
IUP- 11069	<b>S3</b>	62.5	40.48	0.26	133.7	2.0	0.16958	0.000059	0.03257	0.00015	0.3495	0.0018	5536	38	119.3	1.8	40.53	0.27
IUP- 11071	<b>S4</b>	98.5	32.71	0.4	93.5	2.3	0.072823	0.000022	0.03894	0.00022	0.2833	0.0028	1609	18	85.3	2.1	32.85	0.36
IUP- 11070	<b>S5</b>	99	41.4	1.5	101.8	6.1	0.045153	0.000050	0.1132	0.0015	0.3504	0.0098	425	13	90.6	5.4	42	1.4



## **Acknowledgments**

We are grateful to the master of the vessel, Lutz Mallon, and leader of MeBo deployment, Tim Freudenthal, and to Janice Malnati, Wei-Rong Chen, Yun-Ju Wang for collecting and analyzing samples during SO266.

### **Funding:**

Ministry of Education and Science, Germany, project TaiDrill – SO266 (Ref. #03G0288A)

Ministry of Science and Technology (MOST), Taiwan, Project TaiGer drill (MOST107-3113-M-002-004).

**Competing interests:** All other authors declare they have no competing interests.

**Data and materials availability:** All data are available in the main text or the supplementary materials.

6. Manuscript III: Seep carbonates environmental archives

**A new  $\delta^{238}\text{U}$  and  $\delta^{18}\text{O}$  record of seawater and isotope decoupling over the last glacial maximum archived by methane seep carbonates offshore Taiwan**

Yiting Tseng<sup>1\*</sup>, Daniel Smrzka<sup>1</sup>, Thomas Pape<sup>1</sup>, Andrea Schröder-Ritzrau<sup>2</sup>, Norbert Frank<sup>2</sup>, Saulwood Lin<sup>3</sup>, Gerhard Bohrmann<sup>1</sup>

<sup>1</sup>MARUM – Center for Marine Environmental Sciences and Faculty of Geosciences, University of Bremen, Germany

<sup>2</sup>Institute of Environmental Physics, Ruprecht-Karls University of Heidelberg, Germany

<sup>3</sup>Institute of Oceanography, National Taiwan University, Taipei, Taiwan

**Abstract**

Marine biogenic carbonates are a valuable archive for global fluctuations of the isotopic composition of seawater. In addition to marine biogenic carbonates such as corals and foraminifera, microbial authigenic carbonates formed at methane seeps may provide an additional archive for the seawater isotopic composition. Massive clear aragonite cements fill up micritic carbonates, and represent an archive for both seep fluids as well as seawater. However, the reliability of seep carbonates as an archive for seawater composition has yet to be assessed. This communication reports high-resolution  $\delta^{238}\text{U}$ ,  $\delta^{18}\text{O}$  and  $\delta^{13}\text{C}$  data from massive aragonite cement layers (>50 cm) within a 5 m-long carbonate core from an active hydrocarbon seepage area, called Yam Seep, located at Four-Way Closure Ridge in a water depth of ~1350 m. This carbonate core provides an extraordinary record of seepage between ~2.50 and 36.65 ka, covering the time period since the Last Glacial Maximum. These authigenic carbonates are unusual in that  $\delta^{238}\text{U}$  and  $\delta^{18}\text{O}$  values can be interpreted with little ambiguity, and show that seep carbonates can be an excellent archive for the stable isotopic composition of seawater over thousands of years. While the  $\delta^{238}\text{U}$  and  $\delta^{18}\text{O}$  values follow a general trend of seawater isotopic composition, the  $\delta^{13}\text{C}$  values suggest a mixing of carbon sources between seeping fluids affected by methane oxidation and seawater, and are thus independent of glacial-interglacial variations. The Yam Seep carbonate core is a prime example of isotope decoupling during carbonate formation and an excellent archive for stable U and O isotopes in seawater. Therefore, this core is very useful for correlation with biogenic carbonates in other deep-sea regions.

**Keywords (max. 6)**

Isotope decoupling, Last Glacial Maximum, Authigenic carbonates, Yam Seep, MeBo sea floor drill rig, Four-Way Closure Ridge

### 6.1. Introduction

Marine biogenic carbonates produced by foraminifera, mollusks, and corals are excellent archives for the composition of seawater in the geologic past (Hillaire-Marcel & Ravel, 2007; Veizer et al., 1997; Kleypas et al., 2015). The stable carbon and oxygen isotopic composition ( $^{13}\text{C}/^{12}\text{C}$  and  $^{18}\text{O}/^{16}\text{O}$ , respectively) of marine biogenic carbonates record fluctuations in seawater salinity, sea ice volume, temperature, pH, as well as the dissolved inorganic carbon (DIC) composition of the ocean (Hillaire-Marcel et al., 2007; Swart et al., 2015). Seawater  $\delta^{18}\text{O}$  has changed significantly over geologic time (Veizer et al., 1997), and the  $\delta^{18}\text{O}$  records of foraminifera and corals show similar fluctuations through the late Quaternary (Clark et al., 2009; Waelbroeck et al., 2002). Different marine carbonate-secreting organisms are used to reconstruct specific isotopic archives. For instance, foraminifera  $\delta^{18}\text{O}$  values are suitable for the reconstruction of open and local seawater  $\delta^{18}\text{O}$  variations, while tropical corals are generally used to reconstruct  $\delta^{18}\text{O}$  values of seawater within specific temperature ranges (Wellington et al., 1996; Swart, 2015). In contrast, the  $\delta^{18}\text{O}$  record of corals does not show a clear covariance with seawater  $\delta^{18}\text{O}$  (Freiwald, 2003). Foraminifera provide a limited archive for uranium (U) isotopes due to commonly encountered thorium (Th) contamination on calcite shells (Delaney & Boyle, 1982), as well as due to alkalinity-dependent U incorporation (Russel et al., 1994; Keul et al., 2013). Corals, on the other hand, are more reliable seawater archives for the U isotopic composition of seawater (Chutcharavan et al., 2017). The reconstruction of seawater  $^{234}\text{U}/^{238}\text{U}$  is essential for marine U-series geochronology and provides global data on continental weathering dynamics. The back-calculated carbonate  $^{234}\text{U}/^{238}\text{U}$  activity ratio is commonly reported as  $\delta^{234}\text{U}_i$ , which represents the parent seawater  $\delta^{234}\text{U}$  value during carbonate precipitation. Studies on shallow- and cold-water corals have changed the previous perception of constant seawater  $\delta^{234}\text{U}$  throughout the Late Quaternary, and revealed non-constant  $\delta^{234}\text{U}_{i \text{ coral}}$  values showing variations in seawater  $\delta^{234}\text{U}$  due to changing ice/land ratios during the Last Glacial Maximum (LGM) (Chutcharavan et al., 2018).

Seep carbonates are commonly found at methane seeps along continental margins worldwide (Suess 2014, 2018), where methane migrates along normal faults or thrusts towards the seafloor (Paull et al., 1992; Whiticar, 1999). When methane comes into contact with seawater in shallow sediments, sulfate-dependent anaerobic oxidation of methane (SD-AOM) is mediated by a syntrophic consortium consisting of sulfate reduction bacteria (SRB) and methanotrophic archaea (ANME) (e.g., Hoehler et al., 1994; Boetius et al., 2000). SD-AOM increases the alkalinity and leads to the precipitation of authigenic carbonates, which are predominantly composed of Mg-calcite and aragonite (Berner, 1975; Bayon et al., 2007; Sun

et al., 2015; Smrzka et al., 2021). Typically, aragonite microcrystals fill up the pore space between sediments and forms micrite (i.e. microcrystalline aragonite), which is a common primary phase in modern seep carbonates (Peckmann et al., 2001; Naehr et al., 2007; Feng et al., 2009; Smrzka et al., 2019). The microcrystalline aragonites, which usually make up most of the volume of many seep carbonates, can be fractured and filled by aragonite cements that are aggregates of clear fibrous crystals devoid of detrital input, described as banded and botryoidal aragonites and yellow aragonites (Bohrmann et al., 1998; Chen et al., 2019; Leefmann et al., 2008; Liebetrau et al., 2014; Teichert et al., 2003, 2005; Tseng et al., 2022b). These aragonite cements can form up to 50 cm-thick banded successions that have been described from chemoherm seep carbonates, and have been documented at Hydrate Ridge from the Cascadia Margin (Teichert et al., 2005; Teichert et al., 2003), at Jaco Scarp from the Central American forearc (Liebetrau et al., 2014) and at Dongsha area from South China Sea (Chen et al., 2019; Deng et al., 2021).

In contrast to marine carbonates whose carbon source is primarily seawater, the carbon ( $\delta^{13}\text{C}$ ) and oxygen ( $\delta^{18}\text{O}$ ) isotopic signature of seep carbonates is usually used to elucidate the carbon and fluid sources for mineral authigenesis during early diagenesis (Ritger et al., 1987; Beauchamp and Savard, 1992; Peckmann et al., 2001; Zwickler et al., 2015). Aragonite cements derived from chemoherms exhibit highly negative  $\delta^{13}\text{C}$  values, seawater-like shale-normalized rare earth element (REE) patterns, as well as seawater-like U isotope ( $\delta^{234}\text{U}$ ) compositions, and have therefore been interpreted as microbially-mediated precipitates growing into the water column (Himmler et al., 2010; Teichert et al., 2003). The age of seep carbonates has usually been determined using U-Th dating, which is a high-precision radiometric method that is widely applied to date terrestrial and marine carbonates including speleothems, corals, and shells (Teichert et al., 2003; Chutcharavan et al., 2018; Spötl et al., 2019). Corals and seep carbonates incorporate uranium from seawater during precipitation therefore allowing radiometric U-Th dating in order to establish their chronology.

In this study we investigate the  $\delta^{18}\text{O}$  and the  $\delta^{234}\text{U}$  isotope proxy in early diagenetic aragonite cement over a time period of ~37 thousand years, and compare these with other biogenic carbonates in order to assess the reliability of seep carbonates as an archive of seawater composition. This study presents an extraordinary record of  $\delta^{234}\text{U}_i$ ,  $\delta^{18}\text{O}$ , and  $\delta^{13}\text{C}$  during the latest glacial-interglacial interval, and provides a new comprehensive assessment on the reliability and potential for early diagenetic aragonite cements at seeps to record changing seawater composition over time.

## 6.2. Study area

The Yam Seep is an active hydrocarbon seepage area ( $\sim 49,000 \text{ m}^2$ ) offshore southwestern Taiwan located at the northern crest of the accretionary Four-way Closure Ridge in a water depth of  $\sim 1350 \text{ m}$  (Klaucke et al., 2016; Chen et al., 2020; Tseng et al., 2022) (Fig. 1a and b). Fault systems at the deformation front of the Eurasian Plate and the Philippine Sea Plates provide pathways for fluid migration that fuel seafloor hydrocarbon seepage at Yam Seep (Kunath et al., 2020), and promote the formation of gas hydrates within the sediments. Seawater temperature and salinity in this region lead to an upper boundary of the gas hydrate stability zone (GHSZ) that is defined by relatively low temperature and high pressure at a water depth of  $\sim 600 \text{ m}$  (Kunath et al., 2020). Despite quaternary sea level fluctuations of up to  $120 \text{ m}$ , the Yam Seep was therefore consistently situated within the GHSZ in the period covered by the study presented here. Therefore, gas hydrate decomposition due to changes in temperature and pressure has most likely contributed little to the level and possible variability of seepage activity at Yam Seep (Kunath et al., 2020). Active seafloor emission of gas bubbles from the Yam Seep was first discovered by Klaucke et al. (2016) and enrichments of dissolved methane in near-bottom water samples collected in 2018 were reported by Mau et al. (2020). Meter-thick, authigenic carbonate crusts are widespread in the seep area and indicate long-lasting methane availability in near-seafloor sediments (Bohrmann et al., 2019; Tseng et al., submitted).

## 6.3. Materials and Methods

Core MeBo-24 (internal station code GeoB23225-1) was drilled using the portable seafloor drill rig MARUM-MeBo200 (University of Bremen) at the northwestern part of the Yam Seep (Fig. 1b) during *R/V SONNE* cruise SO266 in 2018 (Bohrmann et al., 2019). At a drilling depth of  $\sim 5.1 \text{ m}$  below seafloor (mbsf) drilling was terminated due to vigorous free gas ebullition through the borehole. Core MeBo-24 is approx.  $4.9 \text{ m}$  in length and  $61 \text{ mm}$  in diameter consisting of almost pure methane-derived authigenic carbonates (Fig. 2). The carbonates are composed of a paragenetic sequence of various carbonate phases that are almost entirely aragonite (Tseng et al., 2022b). Some sections of pure aragonitic cements are up to several tens of cm thick. Detailed mineralogy and petrography, as well as a core description is given in Tseng et al. (2022b).

All seep carbonate samples are composed of aragonite, therefore the term carbonate is used from hereon when referring to the rock samples. Thirteen sections of carbonate slabs (Fig.

2) were cut from MeBo-24 core which were then cut with a diamond wire saw (wire width 0.28 mm) along isopachous bands of aragonite cement, guided by an electronic controlled stage (STX-202 Diamond Wire Saw MTI corporation). Aragonite chips ( $L \times W \times H = 1.0-1.5 \times 0.1-0.2 \times 0.4$  cm) weighing between 50 to 100 mg were split into two subsamples, one for U-Th dating and one for stable C and O isotope analyses. Powdered samples from thin (width  $<0.1$  cm) and curvy cement layers were obtained from rock samples using a hand-held micro-drill (tungsten carbide,  $\varnothing$  0.6 mm). In total, 104 samples were drilled for U-Th dating and  $^{234}\text{U}/^{238}\text{U}$  ratios, of which 94 were additionally used for stable carbon and oxygen isotope analyses.

U-Th dating of carbonate was conducted following the method of Wefing et al. (2017). Carbonate chips were treated with 1N  $\text{HNO}_3$  for 2-3 seconds to remove possible surface contamination. Subsequently, chips and powders were dissolved using 7N  $\text{HNO}_3$  and the solutions were spiked with a solution containing artificial Th and U isotopes ( $^{229}\text{Th}$ ,  $^{233}\text{U}$ , and  $^{236}\text{U}$ ), which were then used for the determination of U and Th concentrations then. For removal of U and Th the solutions were loaded into a column packed with UTEVA resin. Purified U-Th was washed out from the UTEVA resin using HCl and HF. The purified U and/or Th solutions were diluted with eluent acid ( $\text{HNO}_3$ ) for mass spectrometric analysis.

High-precision U-series age calculation isotopic measurements of  $\text{Th}^{229}$ ,  $\text{Th}^{230}$ ,  $\text{Th}^{232}$ ,  $\text{U}^{233}$ ,  $\text{U}^{234}$ ,  $\text{U}^{235}$ ,  $\text{U}^{236}$ , and  $\text{U}^{238}$  were carried out on a Multi-collector ICP-MS (Thermo Fisher Scientific Neptune Plus) equipped with a desolvator nebulizer (CETAC Aridus) and an autosampler (Elemental Scientific SC-2DX). Sample extraction, purification, and analysis as well as the manual handling of ultra-pure acid ( $\text{HNO}_3$ , HCl, HF) were conducted in a clean laboratory environment.

$\delta^{234}\text{U}_i$  of back-calculated  $^{234}\text{U}/^{238}\text{U}$  activity ratio ( $^{234}\text{U}/^{238}\text{U})_A$ , at the time of precipitation is reported in the standard delta notation relative to secular equilibrium:

$$\delta^{234}\text{U}_i (\text{‰}) = [(^{234}\text{U}/^{238}\text{U})_A - 1] * 1000 \quad (1)$$

Stable carbon and oxygen isotope ratios of aragonite samples were determined at MARUM on a Finnigan MAT 252 or ThermoFisher 253plus gas isotope ratio mass spectrometer (IRMS) connected to a Kiel III or IV automated carbonate preparation device. The sample powder was reacted with 100%  $\text{H}_3\text{PO}_4$  at 75 °C. Results are reported in the  $\delta$ -notation ( $\delta^{13}\text{C}_{\text{carb}}$  and  $\delta^{18}\text{O}_{\text{carb}}$ , respectively) versus Vienna Pee Dee Belemnite (V-PDB) with units in per mill (‰). Calibration of the instruments referred to the house standard (ground



Solnhofen limestone), which in turn was calibrated against the NBS 19 calcite (from IAEA). Standard deviations of the house standard were 0.03-0.05‰ for  $\delta^{13}\text{C}$  and 0.05-0.08‰ for  $\delta^{18}\text{O}$  over the measurement period. Data calibration of the  $\text{CO}_2$  offset from aragonite was calculated after Kim et al. (2007).

Gas that had accumulated in cavities in the MeBo liner ('void gas') was sampled to determine its molecular composition and the C and H isotopic signatures of methane according to procedures detailed in Pape et al. (2020a, 2020b). Gas samples were collected on the ship's deck from two different depths in core 2R (core depth range 274-388 cm) immediately after recovery of MeBo when liners were accessible. Areas where quantities of gas had accumulated in the transparent liners were identified and rubber septa were placed on the liner surfaces in order to minimize escape of void gas and/or the inflow of air from/to the liner during sampling. A steel cannula attached to a gas-tight, valved syringe was pierced through the septum and liner into the void. Gas was slowly drawn into the syringe and the valve was closed then. The gas was transferred to glass serum vials prefilled with saturated NaCl solution, while at the same time, an equivalent volume of the liquid was released from the vial.

The gas molecular composition was analyzed onboard using a 7890B (Agilent Technologies) three-channel gas chromatograph (GC). Stable carbon and hydrogen isotope ratios ( $^{13}\text{C}/^{12}\text{C}$ ,  $^2\text{H}/^1\text{H}$ ) of  $\text{CH}_4$  were determined at MARUM by GC-IRMS.  $\text{CH}_4$  was separated by GC and then either combusted (1,030 °C) or pyrolyzed (1,440 °C) to produce  $\text{CO}_2$  or  $\text{H}_2$ , respectively, which were then transferred to the IRMS. All gas samples were injected at room temperature by manual syringe injection. Isotopic ratios reported are arithmetic means of at least triplicate measurements and are given in the  $\delta$ -notation ( $\delta^{13}\text{C}_{\text{CH}_4}$ ,  $\delta^2\text{H}_{\text{CH}_4}$ ) relative to V-PDB for carbon and Vienna Standard Mean Ocean Water (VSMOW) for hydrogen. Reproducibility was demonstrated using commercial  $\text{CH}_4$  and  $\text{CO}_2$  standards (Isometric Instruments, Canada; Air Liquide GmbH, Germany). Standard deviations of triplicate isotope measurements were  $<0.5\text{‰}$  ( $^{13}\text{C}-\text{CH}_4$ ).

#### 6.4. Results

Dating results for the carbonate samples investigated cover a time period from  $\sim 2.50$  to  $\sim 36.65$  ka (Table 1).  $\delta^{234}\text{U}_i$  values range from 128.8 to 153.4‰ with a mean value of 139.7‰ (Fig. 3, Table 2).  $\delta^{234}\text{U}_i$  values generally decrease with age from  $\sim 145$  to  $\sim 130\text{‰}$ , between 36.65 and 20 ka, and increase from  $\sim 130$  to 157‰ before 20 ka (Fig. 3).

$\delta^{18}\text{O}_{\text{carb}}$  values range from 3.6 to 5.2‰ with a mean value of 4.6‰ and a standard deviation of 0.27‰.  $\delta^{18}\text{O}_{\text{carb}}$  values increase moderately from 36.65 to 17 ka and showed a decrease from 17 to 2.50 ka (Fig. 4).  $\delta^{13}\text{C}_{\text{carb}}$  values average at -46.4‰, and a minimum value of -58.3‰, a median of -46‰, and a maximum of 32.8‰.  $\delta^{13}\text{C}_{\text{carb}}$  values against age show a slight trend towards more negative values from ~36.65 to 2.50 ka (Fig. 5).

The  $\delta^{13}\text{C}_{\text{CH}_4}$ - and  $\delta^2\text{H}_{\text{CH}_4}$ - values of methane in void space gas were -77.4‰ (vs. V-PDB) and -177.5‰ (vs. V-SMOW) at a depth of 306 cmbsf and -78.2‰ (vs. V-PDB) and -174.0‰ (vs. V-SMOW) at a depth of 339 cmbsf (data not illustrated).

## 6.5. Discussion

### 6.5.1. $\delta^{234}\text{U}_i$ of seep carbonates as an archive for retreating and advancing continental ice shields

It is well established that  $\delta^{234}\text{U}_i$  of marine carbonates can archive ambient seawater  $\delta^{234}\text{U}$  during their formation (Chen et al., 2016; Chutcharavan et al., 2018; del Rey et al., 2020). Based on seawater measurements in the Pacific, Indian, and Atlantic Oceans in various water depths, Andersen et al. (2010) reported a uniform modern seawater  $\delta^{234}\text{U}$  value of  $146.8 \pm 0.1$ ‰, which is considered to remain constant through the Late Quaternary. Carbonates with  $\delta^{234}\text{U}_i$  values similar to that of modern seawater are regarded to inherit and preserve primary seawater  $\delta^{234}\text{U}$ , and can be considered reliable sample materials for U-Th dating (Blanchon et al., 2009). For marine carbonates that have experienced post-depositional alteration during diagenesis, the U isotope distribution may deviate from their original distribution during precipitation (Scholz & Mangini, 2007). However, the assumption of a constant seawater  $\delta^{234}\text{U}$  value based on the long residence time of uranium in seawater (500 ka) (Dunk et al., 2002; Henderson et al., 2003) disregards possible deviations from seawater  $\delta^{234}\text{U}$  values due to varying terrigenous input to the ocean during glacial – interglacial intervals. Chutcharavan et al. (2018) investigated  $\delta^{234}\text{U}_i$  trends in corals from multiple sites including Pacific and Atlantic shallow-water corals, and found a general  $\delta^{234}\text{U}_i$  decrease through the last glacial period. Based on these results they suggested that seawater  $\delta^{234}\text{U}$  values were influenced by ice sheet progression and retreat, which would have changed the degree of physical weathering on the continents and thus affected the  $^{234}\text{U}$  input to the oceans.

Similar to the  $\delta^{234}\text{U}_i$  value of corals,  $\delta^{234}\text{U}_i$  values of the Yam Seep carbonates show fluctuations between ~2.50 and 36.65 ka (Fig. 3). In order to understand the difference between

the  $\delta^{234}\text{U}_i$  value of corals and the seep carbonates in terms of  $\delta^{234}\text{U}_i$  archives, we compare the  $\delta^{234}\text{U}_i$  trends between seep carbonates and Pacific Ocean shallow-water corals (Chutcharavan et al., 2018) over the last glacial period. We focused on five time intervals: 2.50-11.7 ka, 11.7-17 ka, 17-21 ka, 21-29 ka, and 29-36.65 ka, which represent interglacial, deglacial, early-deglacial, the LGM, and the pre-LGM stages, respectively (cf. Chutcharavan et al. 2018, Fig. 6). During interglacial times the  $\delta^{234}\text{U}_i$  of seep carbonates ( $\delta^{234}\text{U}_{i \text{ seep}}$ ) and  $\delta^{234}\text{U}_i$  of corals ( $\delta^{234}\text{U}_{i \text{ coral}}$ ) show mean values of  $144.5 \pm 4.4\text{‰}$  and  $144.7 \pm 1.7\text{‰}$ , respectively. The higher variabilities of  $\delta^{234}\text{U}_{i \text{ seep}}$  values are likely due to a lower sample number ( $n=19$ ) compared to the coral samples ( $n=125$ ). Nevertheless, both mean values are similar to that of modern seawater (Andersen et al., 2010). Deglacial  $\delta^{234}\text{U}_{i \text{ seep}}$  and  $\delta^{234}\text{U}_{i \text{ coral}}$  show mean values of  $141.4 \pm 2.6\text{‰}$  and  $143.6 \pm 3.9\text{‰}$ , respectively, which are both lower than mean  $\delta^{234}\text{U}_i$  values during the interglacial stage (Table 2, Fig. 6) when  $\delta^{234}\text{U}_{i \text{ seep}}$  values ( $141.3 \pm 2.5\text{‰}$ ) are  $\sim 2\text{‰}$  lower than  $\delta^{234}\text{U}_{i \text{ coral}}$  values ( $143.6 \pm 0.8\text{‰}$ ). During the early deglacial stage, the mean  $\delta^{234}\text{U}_{i \text{ seep}}$  value ( $136.8 \pm 3.8\text{‰}$ ) is depleted ( $\sim 4\text{‰}$ ) compared to the corresponding deglacial mean  $\delta^{234}\text{U}_i$  coral value ( $140.9 \pm 1.2\text{‰}$ ). During the LGM, both  $\delta^{234}\text{U}_i$  mean values are at their minimum and show a slight decrease from the early deglacial, when  $\delta^{234}\text{U}_{i \text{ seep}}$  is lower than  $\delta^{234}\text{U}_{i \text{ coral}}$  ( $136.3 \pm 2.9\text{‰}$  and  $139.8 \pm 1.4\text{‰}$ , respectively). There is no mean coral data reported during the pre-LGM period, yet the  $\delta^{234}\text{U}_{i \text{ seep}}$  values average at  $138.8 \pm 3.0\text{‰}$ , which is higher than the LGM and deglacial mean values (Fig. 7).

The comparison of  $\delta^{234}\text{U}_i$  of pacific shallow-water corals and seep carbonates shows that both follow the global mean sea level trend that decreases through the last glacial cycle (Lambeck et al., 2001) (Fig. 7). The  $\delta^{234}\text{U}_{i \text{ seep}}$  values support  $\delta^{234}\text{U}_{i \text{ coral}}$  data, confirming a clear non-constant seawater  $\delta^{234}\text{U}$  signature during the glacial period (cf. Chutcharavan et al., 2018). It should be noted, however, that  $\delta^{234}\text{U}_{i \text{ seep}}$  are lower than  $\delta^{234}\text{U}_{i \text{ coral}}$  during the LGM, early deglacial and deglacial periods, in which these values are generally lower than other reported  $\delta^{234}\text{U}_{i \text{ coral}}$  in tropical and deep-water corals (cf. Chen et al., 2016; Chutcharavan et al., 2018). This may be the result of a difference in  $\delta^{234}\text{U}$  values in different geographic locations (cf. Chutcharavan et al., 2018), or due to diagenesis of U under variation of redox conditions (Kigoshi, 1971; Klinkhammer et al., 1991; Chen et al., 2018). The  $\delta^{234}\text{U}$  value of seawater varies due to isotope fractionation between oxidized U(VI) and reduced U(IV), whereby  $^{238}\text{U}$  is preferentially removed from seawater and accumulates in sedimentary pore waters under anoxic conditions (Weyer et al., 2008; Basu et al., 2014; Wang et al., 2015; Stirling et al., 2015; Stylo et al., 2015; Andersen et al., 2017).

The area of the Yam Seep is characterized by uplifting and fracturing of carbonates induced by tectonic activity (Tseng et al., 2022a; 2022b), continuously exposing them to circulating seawater. The interaction and mixing between deep-seated reducing pore waters and seawater may have caused a  $^{238}\text{U}$  enrichment in parent fluids (i.e., the ambient fluid) during carbonate precipitation, and may account for the lower  $\delta^{234}\text{U}$  ambient seawater values at Yam Seep. The higher pre-LGM  $\delta^{234}\text{U}_{\text{i seep}}$  values can be interpreted in terms of a relatively low ice-land ratio during a glacial retreat on the continents, as opposed to an ice sheet advance during the LGM that would result in an higher ice-land ratio. A retreat of continental ice sheets would have allowed for an intensification of physical weathering on the continents, thus causing higher  $\delta^{234}\text{U}$  seawater values during that time (Chen et al., 2016; Chutcharavan et al., 2018, Fig. 7). Although the  $\delta^{234}\text{U}$  ratio of sedimentary pore water tends to be much higher than that of seawater (Kigoshi, 1971; Teichert et al., 2003),  $\delta^{234}\text{U}_{\text{i seep}}$  values generally reflect seawater  $\delta^{234}\text{U}$ . This novel finding has a twofold implication, in that it (1) suggests that seep carbonate can be reliable archives for the uranium isotopic composition of seawater, and that (2) the formation of seep carbonates was significantly impacted by seawater influx during their precipitation.

#### 6.5.2. The $\delta^{18}\text{O}$ archive of Yam Seep carbonates

The trend of  $\delta^{18}\text{O}$  values of Yam Seep carbonates generally follows that of South China Sea benthic foraminifera  $\delta^{18}\text{O}$  from ODP site 184-1143 (Cheng et al., 2004) (Fig. 4), though a wider variability per time interval can be observed. The Yam Seep carbonates are composed of different carbonate phases including clear crystalline banded and botryoidal or spheroidal aragonite, and cryptocrystalline, yellow aragonite (Tseng et al., 2022b), which are typical carbonate phases encountered in seep carbonates (Zwicker et al., 2015, 2018).

The  $\delta^{18}\text{O}$  signature of seep carbonates can be discussed in terms of three factors, which are (i) the  $\delta^{18}\text{O}$  of open ocean, (ii) the  $\delta^{18}\text{O}$  of ambient water during carbonate precipitation, and (iii) the fractionation of oxygen isotopes between the ambient water and the carbonate minerals during precipitation. Environmental factors that contribute to open ocean  $\delta^{18}\text{O}$  include salinity and ice volume, the latter of which is relevant for the composition of the surface water mass and mixing of water masses in the deep ocean (Hillaire-Marcel and Ravelo, 2007). The ambient water during carbonate precipitation at seeps is usually a mixture of seawater and reduced seepage fluids, which are additionally modified by various diagenetic processes

including clay mineral dehydration, meteoric water input, or gas hydrate formation and dissociation (Dähmann et al., 2003). The fractionation of  $\delta^{18}\text{O}$  between ambient water and the mineral during precipitation is influenced by temperature, carbonate mineralogy, vital effects, and the carbonate ion concentration of the water (Swart, 2015; Hillaire-Marcel and Ravelo, 2007; Marchitto et al., 2014). Foraminiferal  $\delta^{18}\text{O}$  values are generally fractionated compared to their parent fluids depending on temperature, and therefore an offset between planktonic and benthic foraminifera is usually observed (Grossman et al., 1986; Marchitto et al.). An offset in the linear regression is also produced by species precipitating either calcitic or aragonitic shells (Grossman et al., 1986; Marchitto et al., 2014; Wiedicke et al., 2006), in which the aragonitic benthic foraminifera *Hoeglundina elegans* (*H. elegans*) is  $\sim 0.6$  to  $1.0\text{‰}$  enriched in  $\delta^{18}\text{O}$  relative to the calcitic foraminifera *Uvigerina* (Grossman and Ku, 1986; Marchitto et al., 2014; Swart, 2015). Planktonic foraminifera (Wiedicke & Weiss, 2006) and shallow-water corals ( $<100$  mbsl) (Fairbanks et al., 1978) are considered a reliable archive for the  $\delta^{18}\text{O}$  signature of subtropical to tropical ( $\sim 20\text{--}28^\circ\text{C}$ ) shallow seawater, which show  $\delta^{18}\text{O}$  intervals between  $-4$  and  $0\text{‰}$ . Calcitic shells of the benthic deep-water ( $>1000$  m) foraminifera *Cibicidoides wuellerstorfi*, that are considered an archive for restricted, deep ocean water with temperatures around and below  $\sim 4^\circ\text{C}$  (Wiedicke & Weiss, 2006) show positive  $\delta^{18}\text{O}$  values of  $\sim 2.5$  to  $4.5\text{‰}$ . Considering the offset of  $\delta^{18}\text{O}$  values of  $0.6\text{‰}$  between calcitic and aragonitic foraminifera shells (Grossman & Ku, 1986; Wiedicke & Weiss, 2006), calculated  $\delta^{18}\text{O}$  values of aragonitic benthic foraminifera shells in deep water ( $>1000$  m) would present the range of  $\sim 3.1$  to  $5.1\text{‰}$ .

Seep carbonates from various locations and water depths in the South China Sea composed of low-Mg calcite, high-Mg calcite, and aragonite exhibit a relatively wide range of  $\delta^{18}\text{O}$  signature ( $-3$  to  $+5\text{‰}$ ) (Feng et al., 2018). The Hydrate Ridge chemohierms growing in water depths of  $\sim 800$  m (Teichert et al., 2005) and the Yam Seep carbonates from a depth of  $\sim 1350$  m show similar  $\delta^{18}\text{O}$  values between  $3.5 - 5.0\text{‰}$  and  $3.6 - 5.2\text{‰}$ , respectively, which are within a similar range as the  $\delta^{18}\text{O}$  values of the aragonitic benthic foraminifera. The generally high variation in  $\delta^{18}\text{O}$  content in seep carbonates is the result of mixing of various oxygen sources such as seawater and pore water, as well as a result of temperature changes during precipitation and variations in carbonate mineralogy (Wiedicke & Weiss, 2006; Naehr et al., 2007). The  $\delta^{18}\text{O}$  values of the aragonite samples from the Yam Seep show a clear overlap with benthic aragonitic foraminifera, suggesting they archive the oxygen isotopic changes of open seawater, which is in turn related to global ice volume changes and mixing of deep-water masses. However, the generally higher variability in  $\delta^{18}\text{O}$  values in seep carbonates of each time interval distinguished herein (Fig. 4) cannot be explained by variable open seawater  $\delta^{18}\text{O}$

values alone. The various carbonate phases within seep carbonates such as micrite, cryptocrystalline yellow aragonite and banded and botryoidal aragonite cement can be distinguished in terms of their formation mechanism. Cryptocrystalline yellow aragonite has been interpreted as being the direct mineralization product of microbial biofilms related to the AOM consortium (e.g., Peckmann et al., 2001; Bahr et al., 2010; Hagemann et al., 2013; Zwicker et al., 2018), whereas clear banded and botryoidal aragonite formed by diffusion of carbonate ions towards the locus of precipitation. Consequently, these two phases show differences in their optical properties, luminescence, organic carbon content, and their trace element and isotopic compositions (Hagemann et al., 2013; Zwicker et al., 2015, 2018). At Yam Seep the cryptocrystalline yellow aragonite bands show more negative  $\delta^{18}\text{O}$  values than their banded and botryoidal counterparts (Fig. 5). Banded and botryoidal cements are voluminous in many seep carbonates and usually fill out large cavities in which they grow from the rims inwards towards the center, whereas the yellow aragonite cements often adhere to these botryoidal cements (e.g., Bahr et al., 2009, 2010; Tseng et al., 2022), and are less relevant in terms of volume. This suggests that the growth of banded and botryoidal cements filling out cavities requires a larger amount of circulating fluids providing a continuous source of calcium and carbonate ions in order to maintain precipitation within the cavities. The up to 50 cm-thick bands of pure banded and botryoidal cements suggest that fluid circulation must have occurred through the available pore space to a considerable extent. This scenario would also have facilitated an isotopic equilibration of fluids within the cavities during the precipitation of banded and botryoidal cements, thus reflecting seawater values. In contrast, the cryptocrystalline yellow aragonites would have received much of their  $\text{CO}_3^{2-}$  from fluids in the direct vicinity, or even within the biofilm harboring the microbial AOM consortium. Various biological processes within this biofilm would have impacted  $\delta^{18}\text{O}$  values of parent fluids, and would have likely prevented a rapid equilibration of  $\delta^{18}\text{O}$  with infiltrating seawater. The difference in formation mechanisms of the two phases may explain the offset in  $\delta^{18}\text{O}$  values between these two phases.

The  $\delta^{18}\text{O}$  values of Yam Seep carbonates were compared to the aragonitic ODP 184-1143 curve, to which a 0.6‰ enrichment shift over the calcitic ODP 184-1143 trend was applied (Grossman & Ku, 1986; Cheng et al., 2004). This comparison shows that the  $\delta^{18}\text{O}$  values of the Yam Seep carbonates show a scatter, but generally follow the South China Sea foraminifera curves with slightly more negative values compared to the aragonitic foraminiferal trend. Variations in  $\delta^{18}\text{O}$  values of seep carbonates often result from clay mineral dehydration in the deep subsurface, meteoric water intrusion, and gas hydrate formation and destabilization

(Bohrmann et al., 1998; Naehr et al., 2007). However, the general correlation of the Yam Seep data and the curve for the South China Sea foraminifera had little or no influence on the  $\delta^{18}\text{O}$  values of the Yam Seep carbonates.

Formation of subsurface gas hydrates is common at many modern seeps situated in the GHSZ (Ruppel et al., 2017; Sloan et al., 2007). During hydrate formation the heavier  $^{18}\text{O}$  water molecules are preferably incorporated into the hydrate structure, causing a relative depletion of the residual ambient fluids in  $^{18}\text{O}$  (Davidson et al., 1983). However, due to the small offsets with respect to the aragonitic foraminiferal trend (Fig. 4), there is no observable influence of gas hydrate dynamics on the  $^{18}\text{O}$  composition of Yam Seep carbonates.

Due to the stability of gas hydrates at these depths, these gas hydrates are more likely to have been consumed at the expense of aragonite formation (cf. Bohrmann et al., 1998; Tseng et al., 2022), rather than by dissociation due to instability. Marcon et al. (2021) showed short-term hydrate formation and dissolution at Hydrate Ridge, probably caused by rapidly changing saturation states of gas hydrate in the sediment. In the case of the Yam Seep such dynamics would have resulted in a constantly changing  $^{18}\text{O}$ -pool of parent fluids. Additionally, the envisaged precipitation mechanism of banded and botryoidal cements growing within large cavities requires large volumes of water to pass through them. The highly dynamic  $^{18}\text{O}$ -pool in conjunction with a constant flux of seawater through the core suggest that the  $^{18}\text{O}$ -inventory of the Yam Seep carbonates reflects seawater composition rather than local hydrate dynamics.

#### 6.5.3. Carbon sources, fluid mixing, and isotope decoupling

Unlike their  $\delta^{234}\text{U}_i$  and  $\delta^{18}\text{O}$  values,  $\delta^{13}\text{C}$  values of authigenic carbonates from the Yam Seep show a large variability between  $-60$  and  $-30\text{‰}$ , and do not show any obvious trends over the time periods between  $\sim 36.65$  ka and  $25.50$  ka (Fig. 6). The  $\delta^{13}\text{C}$  values of carbonates at seeps mostly reflect a mixture between several carbon sources including the carbon isotopic composition of dissolved inorganic carbon (DIC) in seawater, DIC derived from AOM, as well as DIC derived from organoclastic sulfate reduction (Peckmann and Thiel, 2004; Formolo et al., 2004; Naehr et al., 2007; Himmler et al., 2015). Additionally, biogenic methane produced by archaeal methanogenesis is usually typified by  $\delta^{13}\text{C}$  values between  $-110$  to  $-50\text{‰}$ , whereas thermogenic methane derived from decarboxylation reactions and the thermal splitting of organic matter in deeper sediments usually show values between  $-50$  and  $-30\text{‰}$  (Whiticar, 1999).

The fractionation between  $\delta^{13}\text{C}$  of parent methane and carbon incorporated into the mineral usually results in less  $^{13}\text{C}$  depleted minerals compared to methane (Peckmann and Thiel, 2004). Authigenic carbonates are enriched in  $^{13}\text{C}$  relative to methane by  $\sim 10\%$  at the Cascadia subduction zone off Oregon (Bohrmann et al., 1998), by up to  $\sim 16\%$  in seeps at the Makran continental margin in the northern Arabian Sea (Himmeler et al., 2015), and by over  $30\%$  in seeps from the northern Gulf of Mexico (Aharon et al., 1997). This is within a similar magnitude of fractionation as reported from the Black Ridge seeps at the Carolina continental rise, where authigenic carbonates are enriched in  $^{13}\text{C}$  by up to  $20\%$  compared to methane (Naehr et al., 2000). Given the significant fractionation between parent hydrocarbons and the precipitating minerals, it appears that most of the  $\delta^{13}\text{C}$  in seep carbonates is derived from methane, yet the negative  $\delta^{13}\text{C}$  values derived from methane are diluted by various other carbon sources.

To evaluate the carbon source variation during precipitation we applied a carbon isotope mass balance model (Formolo et al. 2004; Krake et al., 2022). This model considers four possible carbon sources that may have contributed to carbonate precipitation, which are DIC from (1) seawater, as well as DIC generated during (2) the oxidation of methane, (3) the oxidation of organic matter in the sediment, and (4) the oxidation of higher molecular weight hydrocarbon compounds. For core MeBo-24 studied herein, organic matter oxidation is likely to have played an insignificant role as a carbon source, because it is nearly entirely composed of aragonite with comparable little micrite and host sediments. Compositions of light hydrocarbons at the eastern margin of Yam Seep (MeBo-28, GeoB23234-1) show a  $\text{C}_1/\text{C}_2$  value exceeding 41.000 with  $\text{C}_3$  compounds being below detection limit between 28 and 59 mbsf (Bohrmann et al., 2019). This finding suggests that methane is by far the dominant light hydrocarbon at Yam Seep. Therefore, the mixing model calculates the fraction of DIC that has contributed to carbonate formation under consideration of two endmember carbon sources, which are seawater DIC, and DIC derived from microbial methane oxidation. The fraction of the respective carbon source (F) is expressed in the  $\delta^{13}\text{C}$  value of the authigenic carbonates (see below):

$$F_{\text{seawater}} + F_{\text{methane}} = 1 \quad (1)$$

$$F_{\text{seawater}} (\delta^{13}\text{C}_{\text{seawater}}) + F_{\text{methane}} (\delta^{13}\text{C}_{\text{methane}}) = \delta^{13}\text{C}_{\text{seep aragonites}} \quad (2)$$

From Eq. (1), the total carbon input from fractions of seawater DIC ( $F_{\text{seawater}}$ ) and methane oxidation DIC ( $F_{\text{methane}}$ ) must equate to 1 (i.e. 100%). This expression is then combined



with Eq. (2) to determine the relative contribution of each carbon pool that produced the measured isotopic composition in any given carbonate sample. The  $\delta^{13}\text{C}$  values used in this method are  $\delta^{13}\text{C}_{\text{seawater}} = 0\text{‰}$  (Cheng et al., 2004), and measured methane  $\delta^{13}\text{C}_{\text{methane}} = -77.8\text{‰}$ , in which the  $\delta^{13}\text{C}_{\text{seawater}}$  value is based on ODP 1143 benthic foraminifera showing  $\delta^{13}\text{C}$  values between 0.243 to  $-0.262\text{‰}$  (Cheng et al., 2004). The very low  $\delta^{13}\text{C}$  values of methane discharged at Yam Seep and the relatively high  $\text{C}_1/\text{C}_2$  value suggest that most of the methane is of biogenic origin (Whiticar, 1999). Additionally, there are no indications for a notable source of thermogenic methane in the area or in its vicinity (Chen et al., 2014), arguing that biogenic methane was the dominant carbon source in the seeping fluids in the past as well. Results of the isotope mass balance calculations for 95 carbonate samples reveal mixing ratios between seawater DIC and DIC derived from SD-AOM in the parent fluids ( $\text{DIC}_{\text{seawater}}/\text{DIC}_{\text{SD-AOM}}$ ) ranging between 57 and 24%, with an average value of  $\sim 40\%$  for all samples (Table 3). We therefore regard the  $\text{DIC}_{\text{seawater}}/\text{DIC}_{\text{SD-AOM}}$  as a measure for the mixing ratio of these two endmember fluids that governed the composition of parent fluids during precipitation of the Yam Seep carbonates.

Further detailed examination of the mixing ratios over the five time intervals between 36.65 and 2.50 ka showed a distinct trend that is directly opposed to the global sea level curve (Fig. 8). The contribution of DIC from inflowing seawater to carbonate precipitation at Yam Seep shows maximum values during the LGM stage, whereas it diminishes in the pre-LGM and deglacial stages (Fig. 8). Flux rates of seep fluids have been shown to depend on global sea level fluctuations, where higher flux rates are facilitated by sea level lowstands and vice versa (e.g., Oppo et al., 2020). At Yam Seep, the opposite trend is observable arguing for a negligible control of sea level on seepage rates at this site. Tseng et al. (2022b) showed how seepage dynamics at Yam Seep changed significantly over the past 38 ka, and distinguished two phases of active seepage between 36.65 and 26.6 ka and 16 to 9 ka, interrupted by a period of relative quiescence between 26.6. and 16 ka (Fig. 8). These periods roughly overlap the pre-LGM, LGM, and deglacial stages, respectively, where the period of quiescence occurred within the LGM at relatively low sea levels. The isotope mass balance calculations can be interpreted either as (i) relatively high seawater influx during the LGM, or that (ii) seepage intensity had diminished during this time period. Either way, the isotope mass balance calculations suggest that the mixing of seawater and seeping fluids at Yam Seep was independent of global sea level change. This agrees with the interpretations of Tseng et al. (2022b) that seepage dynamics were largely controlled by the waxing and waning of tectonic activity. Finally, the calculated fluid mixing ratios during the LGM suggest either a relatively high fraction of injected fluids or a low portion

of seawater during carbonate precipitation. This further underpins the notion that this time interval was a period of tectonic quiescence that triggered less vigorous seepage than in the pre-LGM or in the deglacial stages.

The stable carbon isotopic compositions of Yam Seep carbonates show a decoupling of the behavior of stable C, O, and U isotopes during carbonate precipitation. On the one hand, the highly negative  $\delta^{13}\text{C}$  values argue for a strong influence of AOM leading to the precipitation of thick bands of aragonite within the core. On the other hand, the  $\delta^{234}\text{U}_i$  and  $\delta^{18}\text{O}$  record reflects seawater values showing little to no influence of reduced, seeping fluids. Differences in mobility and behavior of specific isotopes during diagenesis and carbonate formation have been previously reported for U, O and C isotopes. Oxygen isotopes in particular are more mobile than C isotopes during early diagenesis and carbonate formation, as the carbon pool in parent fluids is much smaller than that of oxygen (Banner and Hanson, 1990; Swart, 2015). Uranium isotopes are also known to experience variable offsets during early diagenesis (Chen et al., 2018; Del Rey et al., 2020). The mobility of isotopes and elements during the early diagenesis of carbonates is further a function of open-system versus closed-system diagenesis, which describes the degree of fluid circulation through sedimentary pore water during carbonate formation (Banner and Hanson, 1990). Studies from cold seep carbonates have shown how fluid circulation may retain specific elements or compounds within the authigenic mineral phases, while leading to an exchange and loss of other elements (Zwicker et al., 2018). In the case of the Yam Seep, the record of U and O isotopes in authigenic carbonates suggests a strong and continuous influence of seawater that overprinted any isotopic signal derived from pore fluids. Moreover, the thick aragonite bands would have required large amounts of fluids to continuously circulate through open pore spaces to provide the necessary ions for carbonate precipitation (cf. Luff and Wallmann, 2003). The retention of the highly negative  $\delta^{13}\text{C}$  values can be explained by the precipitation of banded and botryoidal carbonate cements at the expense of gas hydrates containing highly  $^{13}\text{C}$ -depleted biogenic methane (cf. Bohrmann et al., 1998), which is the most likely mechanism of carbonate formation at Yam Seep (Tseng et al., 2022b). In contrast to the carbon isotopes, the U and O isotopic inventory of the Yam Seep carbonates appears to be largely sourced from seawater. This notion is strengthened by the similarities of both isotope curves to those of benthic foraminifera and corals (Figs. 3, 4), as well as by carbon isotope mass balance calculations suggesting a significant seawater fraction in parent fluids between ~30 and 60% over the past 36.65 ka (Fig. 5).

## 6.6. Conclusion

Stable U, O and C isotopes of authigenic carbonates from the Yam Seep at the accretionary wedge SW offshore Taiwan revealed three distinct isotopic profiles during precipitation throughout the Last Glacial Maximum (LGM).  $\delta^{234}\text{U}$  values of seep carbonates show similar trends as corals. This suggests that seep carbonates are valuable archives of the seawater U isotopic composition. In a similar fashion,  $\delta^{18}\text{O}$  values of authigenic carbonates appear to reliably record the seawater O isotopic composition over the LGM. In contrast to the U and O isotopic systems, the C isotopic composition records the degree of mixing between seawater and methane-rich fluids during carbonate precipitation. Evaluating the fluid mixing ratio via isotope mass balance calculations shows that seepage activity was largely independent of global sea level, but depended more strongly on local tectonic activity. The decoupling of O and U isotopes from C isotopes further shows their respective tendency to be exchanged during fluid circulation and mineral formation at seeps. Whereas the stable C isotopic composition reflects a typically seepage-derived signature, O and U isotopes are more prone to record an influence of seawater circulation. The excellent isotopic archive and their decoupling in Yam Seep carbonates provides a new record for the isotopic composition of seawater and offers new constraints on the mobility of stable C, O, and U isotopes during the early diagenesis of microbially-mediated carbonates.

## **Acknowledgments**

- master of *RV SONNE*, L. Mallon, during SO266
- leader of the MARUM-MeBo team, T. Freudenthal, and his crew
- J. Malnati (Faculty of Geosciences, Univ. of Bremen), Wei-Rong Chen and Yun-Ju Wang for collecting and analyzing samples.
- Henning Kuhnert (MARUM, Univ. of Bremen) for C and O isotope measurements on aragonites

## **Funding**

Ministry of Education and Science, Germany, project TaiDrill – SO266 (Ref. #03G0288A)

Ministry of Science and Technology (MOST), Taiwan, Project TaiGer drill (MOST107-3113-M- 002-004).

## **Declaration of competing interest**

Authors declare that they have no competing interests.

## **Data availability**

- All data are available in the main text or the supplementary materials
- PANGAEA

## **Author contributions**

Conceptualization: YT, GB

Methodology: ASR, NF, YT

Investigation: YT, ASR (?), TP

Visualization: YT

Supervision: GB, SL

Writing—original draft: YT

Writing—review & editing: YT, DS, TP, SL, ASR, NF, GB

## Figures and Tables

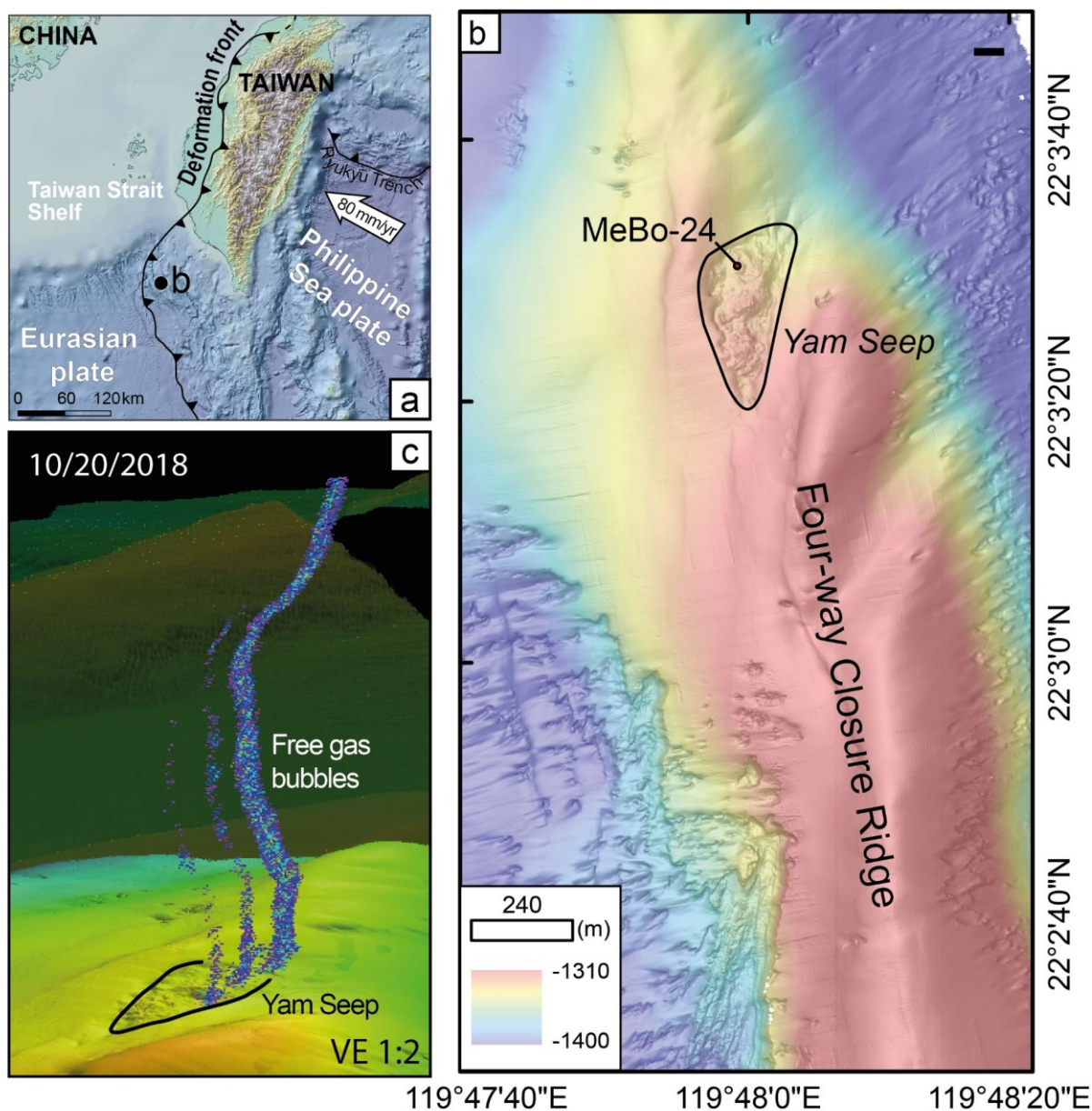


**Fig. 6.1** Location of the active Yam Seep at Four-way Closure Ridge. (a) Tectonic setting showing the deformation front of Eurasian plate and Philippine Sea plate. The black dot denotes the location of the study site. (b) MeBo-24 drill site at Yam Seep on the crest of the Four-way Closure Ridge. (c) Modern seepage at Yam Seep. Rising gas bubbles causing hydroacoustic anomalies in the water column (called “flares”) detected by means of multi-beam echosounder during cruise SO266 in 2018. Vertical exaggeration is 1:2 (modified after Tseng et al., 2022a).

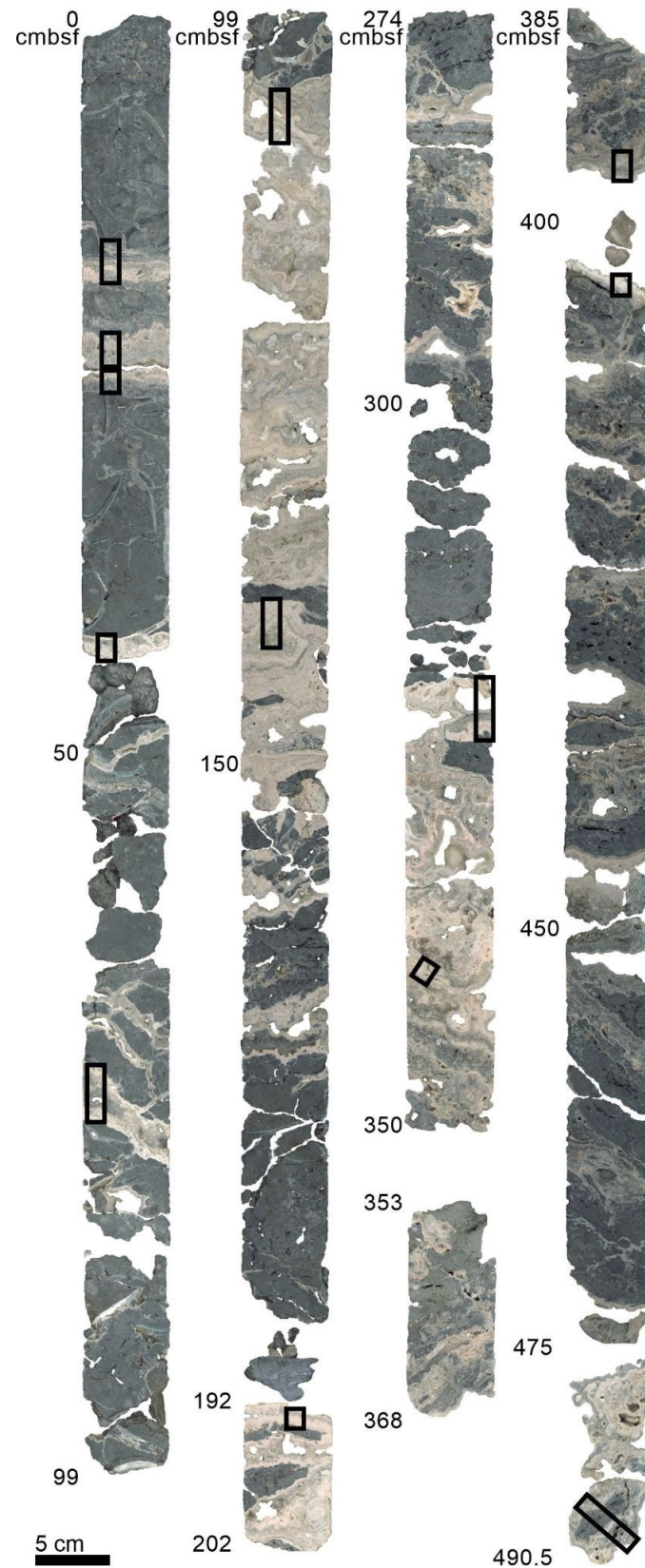


**Fig. 6.2** Overview of the MeBo-24 carbonate core. Detailed sample locations of thirteen sections are highlighted by the black rectangles.



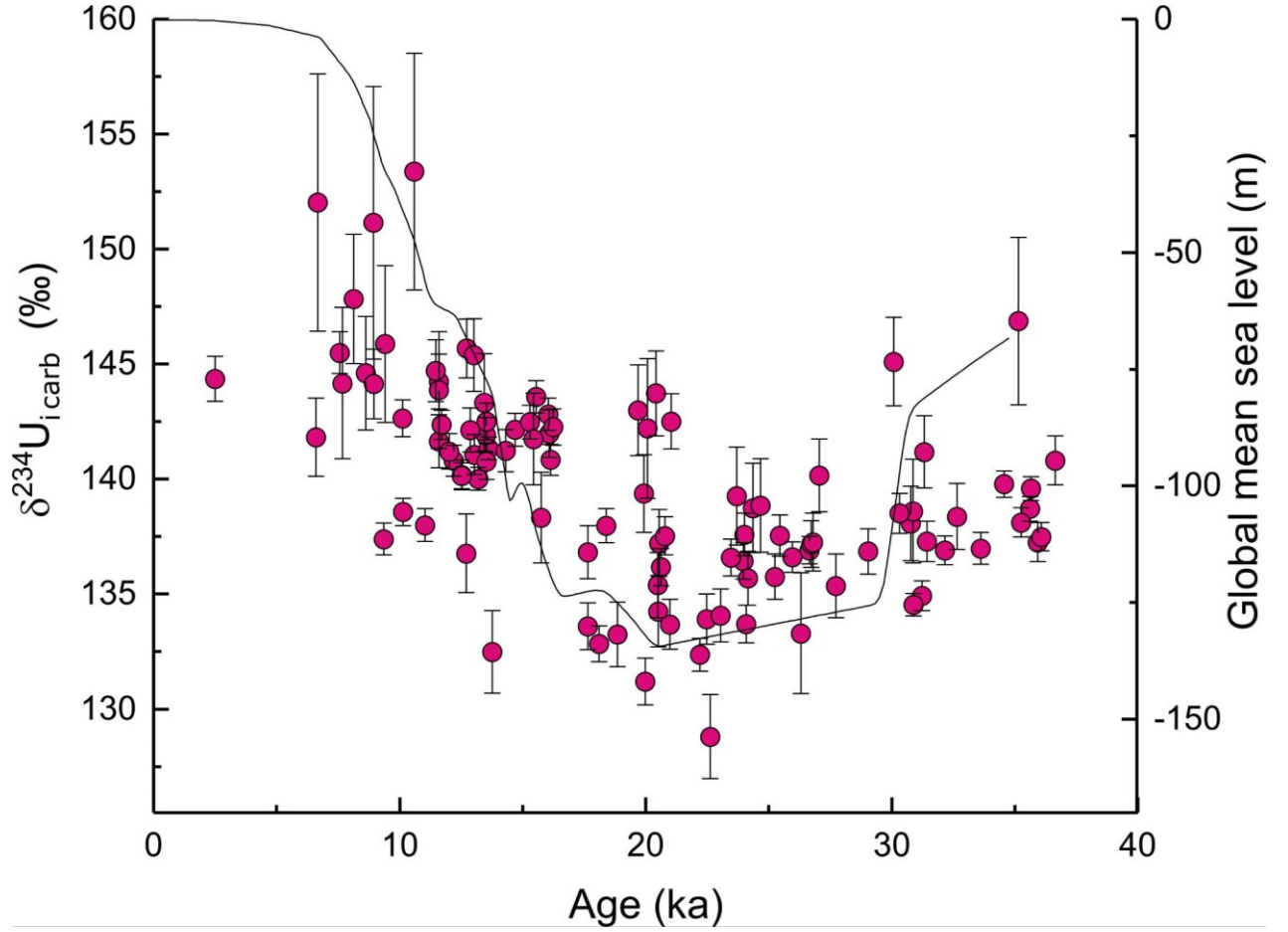


**Fig. 6.3**  $\delta^{234}\text{U}_{\text{i}}$  values of seep carbonates plotted against age. The evolution of the Global Mean Sea Level (nowadays - 0 m) is also shown (black line).

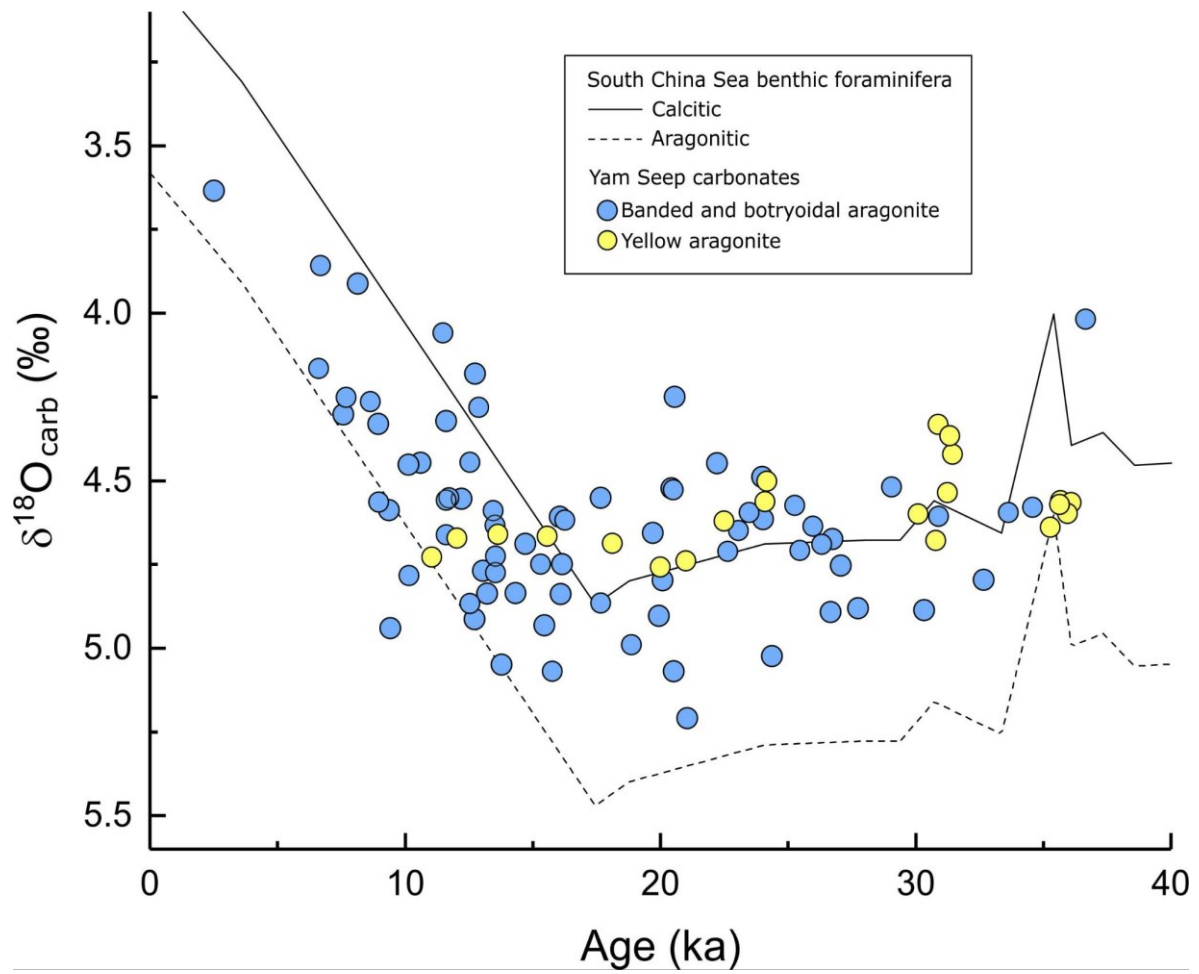


**Fig. 6.4**  $\delta^{18}\text{O}$  values of seep carbonates plotted against age. The curve for calcite-shelled foraminifera is from Cheng et al. 2004. For comparison, the corresponding aragonite values were converted according to Grossman and Kuh (1986).



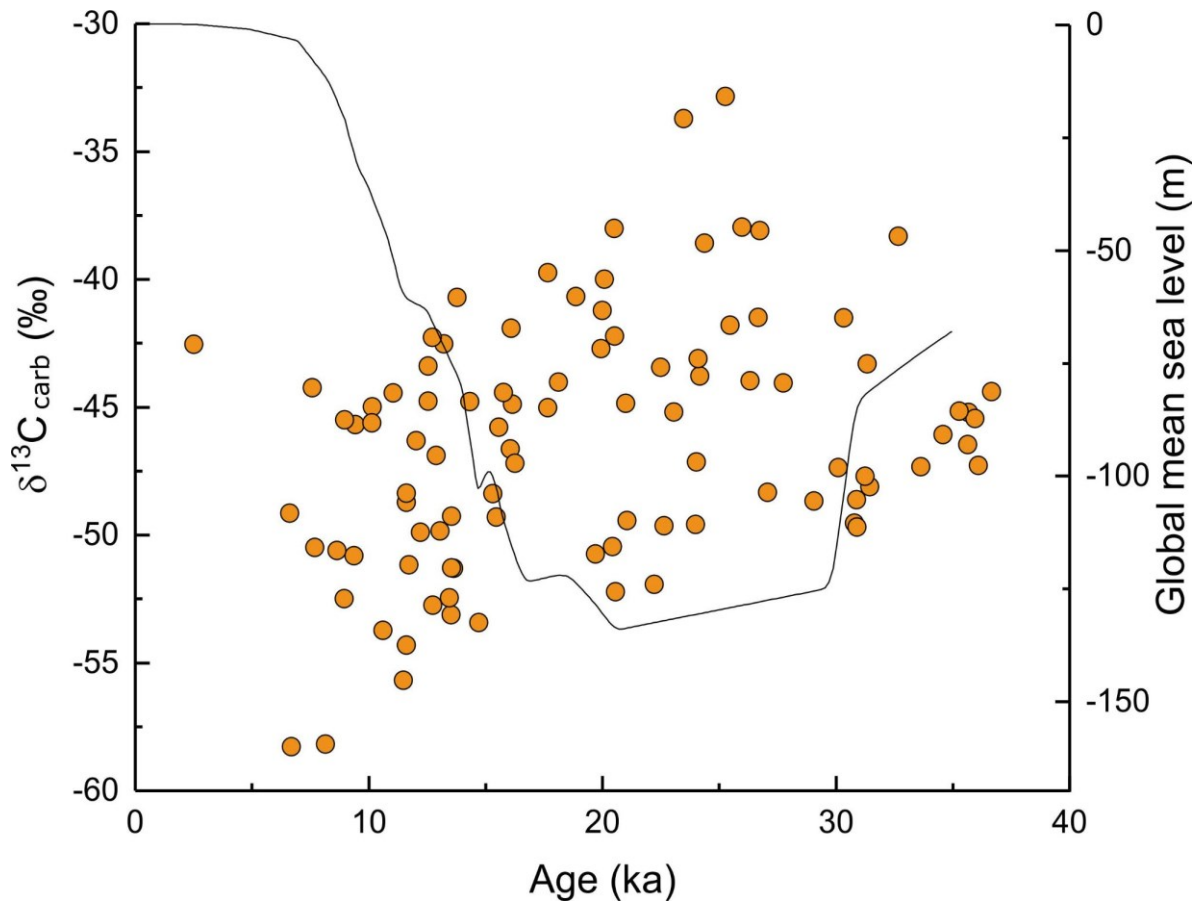


**Fig. 6.5**  $\delta^{13}\text{C}$  values of seep carbonates plotted against age. The evolution of the Global Mean Sea Level (nowadays - 0 m) is also shown (black line).

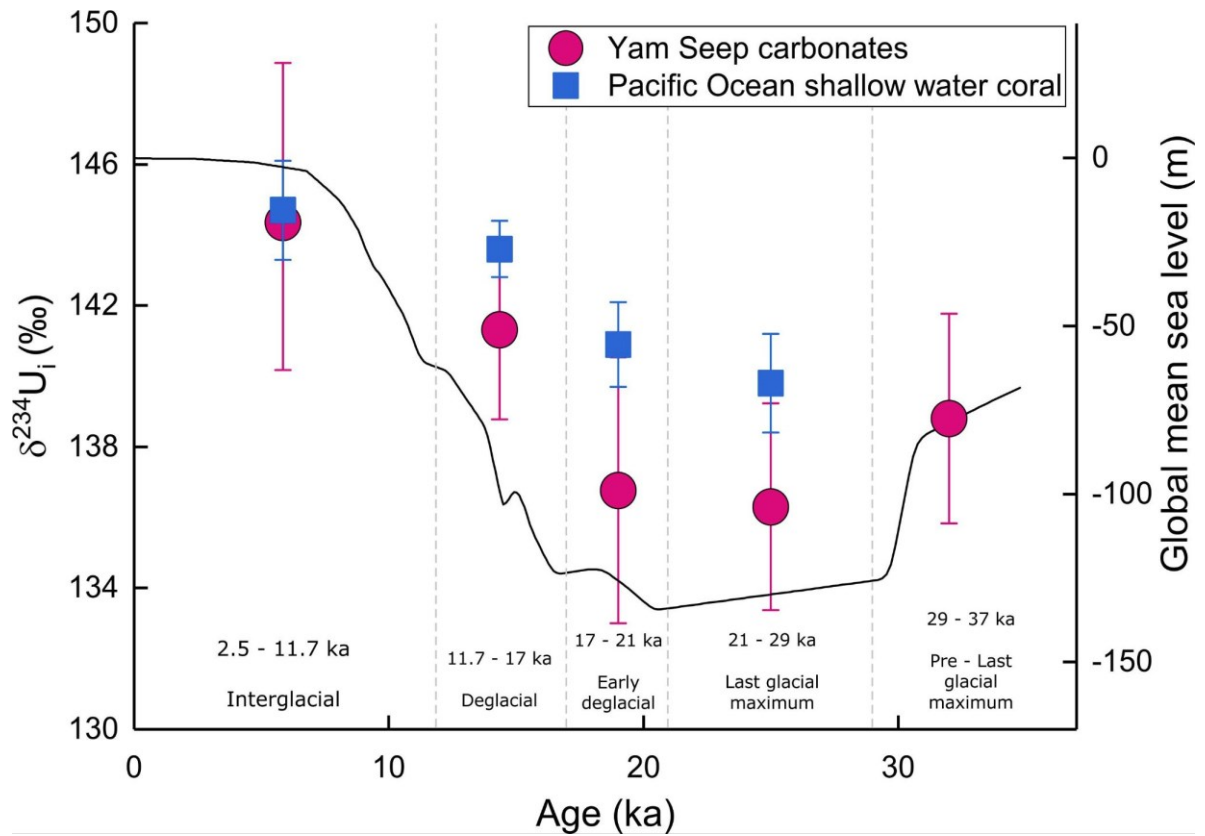


**Fig. 6.6** Averaged  $\delta^{234}\text{U}_i$  values of corals and seep carbonates from the five time intervals determined. Red squares are Yam Seep carbonates and blue squares are pacific shallow-water corals. Error bars are standard deviations. Black line represents the evolution of the Global Mean Sea Level (nowadays - 0 m).

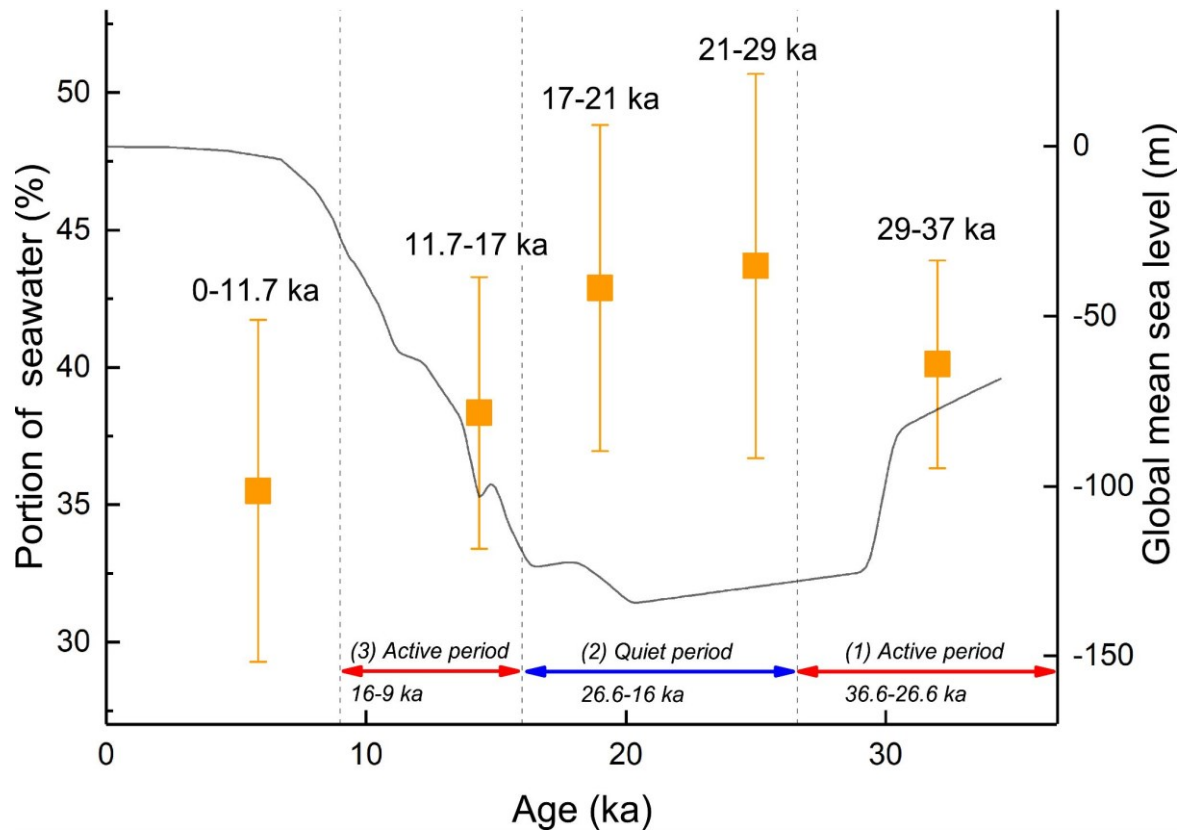


**Fig. 6.7** Averaged portion of seawater in parent fluids of authigenic carbonates calculated from stable carbon isotope mass balance for the five time intervals. Error bars are standard deviations. See text for further details. The evolution of the Global Mean Sea Level (nowadays - 0 m) is also shown (black line).

**Table 6.1 Aragonites U-Th dating age, mineral form,  $\delta^{234}\text{U}_{\text{ini.}}$ ,  $\delta^{18}\text{O}$  and  $\delta^{13}\text{C}$**

ID Sequ- ence			Core depth (cm)	Age (ka)	$\pm$ (abs.)	$\delta^{234}\text{U}_{\text{ini.}}$ (‰)	$\pm$ (abs.)	$^{238}\text{U}$ ( $\mu\text{g/g}$ )	$\pm$ (abs.)	$\delta^{18}\text{O}$ (‰)	$\pm$ (‰)	$\delta^{13}\text{C}$ (‰)	$\pm$ (‰)
I	15-19	La-04	15.88	13.20	0.07	140.02	0.50	4.35	1.8E-04	4.84	0.02	-42.51	0.01
I	15-19	La-05	16.04	16.08	0.28	141.98	1.04	4.28	1.8E-03	4.84	0.02	-41.89	0.01
I	15-19	La-07	16.36	13.03	0.06	141.07	0.87	5.62	2.3E-04	4.77	0.04	-49.83	0.04
I	15-19	La-08	16.52	11.02	0.04	138.00	0.71	4.78	1.8E-04	4.73	0.04	-44.43	0.02
I	15-19	La-11	17	12.20	0.06	140.80	0.67	6.06	2.7E-04	4.55	0.01	-49.88	0.02
I	15-19	La-12	17.16	11.60	0.05	141.65	1.15	5.58	3.5E-04	4.66	0.01	-48.72	0.01
I	15-19	La-13	17.32	11.60	0.06	144.24	1.18	6.17	2.9E-04	4.56	0.01	-48.35	0.02
I	15-19	La-15	17.64	13.61	0.03	141.34	0.49	6.43	2.8E-04	4.66	0.02	-51.29	0.01
I	15-19	La-17	17.96	9.35	0.05	137.40	0.70	4.84	2.0E-04	4.59	0.01	-50.79	0.02
II	19-23	La-07	21.18	14.69	0.06	142.15	0.71	4.91	2.0E-04	4.69	0.03	-53.42	0.03
II	19-23	La-10	21.65	11.71	0.06	142.36	0.64	5.10	4.0E-04	4.55	0.03	-51.16	0.02
II	19-23	La-12	22.3	13.51	0.06	141.92	0.76	5.83	3.3E-04	4.63	0.03	-53.11	0.02
II	19-23	La-13	22.6	13.44	0.16	143.33	2.12	5.05	2.5E-03	4.59	0.01	-52.45	0.01
II	19-23	La-18	22.99	10.13	0.11	138.58	0.59	4.63	2.3E-04	4.78	0.00	-44.98	0.03
III	24-28	La-01	24	15.55	0.14	143.58	0.71	4.13	2.4E-04	4.67	0.05	-45.78	0.04
III	24-28	La-03	24.33	16.04	0.05	142.81	0.70	4.10	2.0E-04	4.61	0.01	-46.62	0.00
III	24-28	La-04	24.49	16.24	0.06	142.26	0.79	4.86	2.8E-04	4.62	0.05	-47.18	0.04
III	24-28	La-06	24.82	16.14	0.11	140.84	0.67	4.62	3.6E-04	4.75	0.02	-44.88	0.01
III	24-28	La-07	24.98	15.30	0.71	142.48	0.73	5.11	3.8E-04	4.75	0.01	-48.36	0.01
III	24-28	La-08	25.15	13.53	1.41	142.50	0.80	5.21	4.3E-04	4.73	0.04	-49.26	0.04
III	24-28	La-09	25.31	12.53	0.92	140.19	0.64	5.36	3.8E-04	4.45	0.05	-44.76	0.02
III	24-28	La-10	25.47	13.53	0.39	140.78	0.79	5.22	3.6E-04	4.78	0.03	-51.28	0.02
IV	42-43	--	42	23.98	0.05	136.44	0.79	3.35	2.8E-04	4.49	0.03	-49.57	0.02
IV	42-43	--	42.25	30.77	0.17	138.08	1.62	3.75	2.8E-04	4.68	0.03	-49.52	0.03
IV	42-43	--	42.5	30.86	0.20	138.61	2.25	3.59	3.2E-04	4.33	0.02	-48.61	0.02
IV	42-43	--	42.75	31.32	0.15	141.18	1.57	4.35	3.8E-04	4.37	0.04	-43.30	0.01

V	70-75	La-03	70.7	30.09	0.20	145.11	1.93	4.00	3.1E-04	4.60	0.03	-47.35	0.02
V	70-75	La-16	71	21.04	0.20	142.52	1.21	2.21	8.7E-05	5.21	0.02	-49.42	0.01
V	70-75	La-17	71.1	27.05	0.16	140.17	1.58	3.34	1.8E-04	4.75	0.03	-48.31	0.01
V	70-75	La-08	72.7	15.44	2.52	141.75	1.99	2.49	1.6E-04	4.93	0.04	-49.30	0.02
V	70-75	La-13	74	24.16	0.45	135.69	1.17	4.47	2.7E-04	4.50	0.02	-43.76	0.02
VI	103-108	La-02	104.3	35.14	0.23	146.87	3.64	3.86	2.5E-03	--	--	--	--
VI	103-108	La-03	104.5	32.64	0.13	138.38	1.44	3.32	1.9E-04	4.80	0.03	-38.30	0.01
VI	103-108	La-04	104.7	30.32	0.07	138.51	0.87	3.59	1.6E-04	4.89	0.02	-41.49	0.02
VI	103-108	La-06	105.1	26.65	0.06	136.90	0.59	3.61	1.3E-04	4.89	0.04	-41.49	0.01
VI	103-108	La-09	105.7	18.85	0.07	133.25	1.41	3.00	1.7E-04	4.99	0.03	-40.66	0.03
VI	103-108	La-10	105.9	20.52	0.12	134.26	1.55	2.64	2.0E-04	5.07	0.00	-42.20	0.02
VI	103-108	La-11	106.1	12.70	0.08	136.77	1.71	2.51	1.2E-04	4.91	0.01	-42.25	0.01
VI	103-108	La-12	106.3	19.92	0.15	139.38	1.69	3.06	1.9E-04	4.90	0.01	-42.70	0.01
VI	103-108	La-17	107.3	13.76	0.10	132.49	1.79	2.93	1.8E-04	5.05	0.05	-40.70	0.02
VI	103-108	La-18	107.5	24.36	0.17	138.74	1.94	2.54	2.0E-04	5.02	0.01	-38.58	0.01
VII	138-144	La-03	139.51	31.43	0.13	137.28	0.88	4.72	3.5E-04	4.42	0.02	-48.09	0.01
VII	138-144	La-09	140.45	22.21	0.05	132.36	0.71	3.99	1.3E-04	4.45	0.04	-51.92	0.02
VII	138-144	La-10	140.61	31.23	0.08	134.93	0.65	4.51	2.3E-04	4.54	0.01	-47.70	0.01
VII	138-144	La-16	141.54	29.05	0.09	136.85	0.99	4.83	3.0E-04	4.52	0.02	-48.66	0.01
VII	138-144	Lb-05	141.6	33.62	0.08	136.99	0.70	4.24	1.9E-04	4.60	0.04	-47.32	0.02
VII	138-144	Lb-11	141.6	30.88	0.08	134.54	0.48	6.65	2.3E-04	4.61	0.01	-49.68	0.01
--	52-53	--	152	32.16	0.09	136.91	0.63	5.18	5.3E-04	--	--	--	--
VIII	192-202	La-01	192	36.65	0.12	140.81	1.06	3.82	3.4E-04	4.02	0.02	-44.38	0.01
VIII	192-202	La-02	192.14	34.56	0.09	139.78	0.58	4.75	3.4E-04	4.58	0.01	-46.06	0.01
VIII	192-202	La-03	192.29	35.65	0.10	139.59	0.52	4.89	3.9E-04	4.56	0.03	-45.19	0.04
VIII	192-202	La-04	192.43	35.63	0.10	138.71	0.54	4.50	3.5E-04	4.57	0.04	-46.46	0.02
VIII	192-202	La-05	192.57	35.94	0.14	137.26	0.85	3.89	3.8E-04	4.60	0.01	-45.44	0.01
VIII	192-202	La-06	192.71	36.08	0.15	137.50	0.62	4.52	3.4E-04	4.57	0.02	-47.28	0.05
VIII	192-202	La-07	192.86	35.27	0.16	138.12	0.63	4.78	3.3E-04	4.64	0.01	-45.15	0.01
IX	319-326	Lb-02	319.64	26.31	0.15	133.30	2.63	3.37	2.6E-04	4.69	0.04	-43.95	0.02

IX	319-326	Lb-07	320.86	20.08	0.24	142.21	3.03	1.69	1.2E-04	4.80	0.01	-39.98	0.01
IX	319-326	Lc-01	321.6	20.56	0.37	137.22	1.45	2.40	1.4E-04	4.25	0.06	-52.20	0.03
IX	319-326	Lc-02	321.73	19.98	0.21	131.20	1.01	5.26	3.1E-04	4.76	0.04	-41.21	0.01
IX	319-326	Lc-03	321.86	26.73	0.34	137.18	1.02	6.01	4.0E-04	4.67	0.02	-38.08	0.03
IX	319-326	Lc-04	321.99	24.09	0.18	133.70	0.82	6.03	4.5E-04	4.56	0.02	-43.09	0.02
IX	319-326	Lc-05	322.13	17.65	0.11	133.61	1.01	7.22	4.4E-04	4.55	0.03	-39.72	0.04
IX	319-326	Lc-06	322.26	20.50	0.26	135.40	1.41	3.63	2.3E-04	4.53	0.03	-37.99	0.04
IX	319-326	Lc-07	322.39	18.11	0.10	132.84	0.79	5.39	4.7E-04	4.69	0.01	-44.00	0.01
IX	319-326	Lc-08	322.52	20.99	0.10	133.69	1.09	4.67	3.0E-04	4.74	0.06	-44.84	0.06
IX	319-326	Lc-09	322.65	22.48	0.09	133.91	1.10	4.02	2.3E-04	4.62	0.01	-43.43	0.02
IX	319-326	Lc-10	322.78	23.05	0.11	134.07	1.16	3.65	1.7E-04	4.65	0.02	-45.19	0.01
IX	319-326	Lc-11	322.91	22.63	0.09	128.81	1.83	3.47	1.8E-04	4.71	0.01	-49.63	0.02
IX	319-326	Lf-01	326	25.45	0.11	137.54	0.90	3.24	2.0E-04	4.71	0.01	-41.78	0.01
IX	319-326	Lf-08	326	23.47	0.10	136.59	0.80	5.33	4.7E-04	4.60	0.02	-33.70	0.02
IX	319-326	Lf-09	326	25.24	0.19	135.76	0.99	4.77	2.9E-04	4.57	0.04	-32.83	0.04
IX	319-326	Lf-07	326	25.96	0.11	136.61	0.67	4.86	5.9E-04	4.64	0.02	-37.94	0.01
X	338-342	La-06	339.25	24.01	0.13	137.59	0.93	3.84	2.1E-04	4.62	0.04	-47.14	0.02
X	338-342	La-07	339.5	19.69	0.51	143.00	1.97	2.27	1.1E-04	4.66	0.02	-50.73	0.01
X	338-342	La-08	339.75	10.59	1.98	153.37	5.15	1.13	7.5E-05	4.45	0.04	-53.72	0.01
X	338-342	La-09	340	11.59	1.49	143.88	2.53	1.28	1.2E-04	4.32	0.01	-54.30	0.01
X	338-342	La-10	340.25	20.42	1.03	143.73	1.85	2.52	1.7E-04	4.52	0.01	-50.44	0.01
X	338-342	La-12	340.75	26.79	0.10	137.26	1.25	5.51	3.6E-04	--	--	--	--
XI	392.5-397	La-02	394.99	24.67	0.31	138.86	2.04	5.99	2.7E-03	--	--	--	--
XI	392.5-397	La-03	395.18	27.74	0.31	135.36	1.39	6.07	3.2E-03	4.88	0.02	-44.04	0.02
XI	392.5-397	La-06	395.75	12.72	0.05	145.68	1.28	1.99	9.1E-05	4.18	0.03	-52.74	0.02
XI	392.5-397	La-07	395.95	8.94	0.10	151.15	5.92	0.78	2.8E-04	4.33	0.04	-52.47	0.01
XI	392.5-397	La-09	396.33	17.64	0.08	136.82	1.15	2.92	2.4E-04	4.87	0.02	-45.00	0.01
XI	392.5-397	La-10	396.52	9.40	0.06	145.88	3.40	1.97	1.0E-03	4.94	0.03	-45.66	0.03
XI	392.5-397	La-11	396.71	8.13	0.07	147.84	2.81	1.31	9.8E-05	3.91	0.04	-58.17	0.03
XII	403-407	La-01	403	6.67	0.08	152.03	5.59	1.26	1.2E-04	3.86	0.05	-58.26	0.02

XII	403-407	La-02	403.19	7.67	0.06	144.17	3.29	1.45	1.4E-04	4.25	0.02	-50.47	0.03
XII	403-407	La-03	403.37	11.46	0.06	144.72	1.34	1.87	1.2E-04	4.06	0.02	-55.67	0.01
XII	403-407	La-04	403.56	6.59	0.04	141.82	1.70	1.93	1.5E-04	4.17	0.01	-49.13	0.01
XII	403-407	La-05	403.74	8.62	0.05	144.61	2.47	2.08	2.0E-04	4.26	0.01	-50.60	0.00
XII	403-407	La-06	403.93	8.95	0.05	144.14	1.51	3.15	2.7E-04	4.57	0.01	-45.49	0.01
XII	403-407	La-07	404.11	15.75	0.10	138.33	1.98	3.09	2.0E-04	5.07	0.01	-44.42	0.00
--	59-60	01	444	20.62	0.07	136.18	0.81	4.23	3.6E-04	--	--	--	--
--	59-60	02	444	13.01	0.08	145.40	1.59	3.74	2.5E-04	--	--	--	--
--	59-60	01	444.1	18.40	0.06	137.98	0.73	3.86	2.3E-04	--	--	--	--
--	59-60	02	444.1	20.78	0.08	137.53	0.84	3.96	2.7E-04	--	--	--	--
--	476	--	476	23.70	0.17	139.27	2.13	4.66	3.4E-04	--	--	--	--
XIII	486-490	La-01	486	12.87	0.11	142.13	0.96	4.87	3.2E-04	4.28	0.04	-46.87	0.02
XIII	486-490	La-02	486.13	12.52	0.08	140.15	0.57	6.04	2.7E-04	4.87	0.02	-43.38	0.00
XIII	486-490	La-06	488.23	14.31	0.33	141.23	0.92	7.61	6.4E-04	4.84	0.03	-44.77	0.02
XIII	486-490	La-07	488.27	12.01	0.59	141.20	0.77	6.41	5.3E-04	4.67	0.03	-46.30	0.02
XIII	486-490	La-11	489.13	10.12	0.79	142.64	0.80	4.95	3.9E-04	4.45	0.03	-45.60	0.01
XIII	486-490	La-17	490.34	7.56	1.12	145.50	0.91	3.66	2.5E-04	4.30	0.01	-44.23	0.00
XIII	486-490	La-18	490.5	2.50	0.18	144.36	0.97	3.79	2.3E-04	3.64	0.04	-42.53	0.03

**Table 6.2 Descriptive statistics of  $\delta^{234}\text{U}_i$  during five time intervals determined**

Time interval (ka)	No. of samples	Mean (‰)	Standard Deviation	Minimum (‰)	Median (‰)	Maximum (‰)
All time	104	139.6	4.4	128.8	139.3	153.4
2.50-11.7	19	144.5	4.4	137.4	144.2	153.4
11.7-17	27	141.3	2.5	132.5	141.7	145.7
17-21	16	136.8	3.8	131.2	136.5	143.7
21-29	22	136.3	2.9	128.8	139.6	142.5
29-36.65	20	138.8	3.0	134.5	138.2	146.9

**Table 6.3 Descriptive statistics of ratio of mixing seawater during five time intervals determined**

Time interval (ka)	No. of samples	Mean (%)	Standard Deviation	Minimum (%)	Median (%)	Maximum (%)
All time	95	39.8	6.2	24.3	40.2	57.4
2.50-11.7	19	35.5	6.2	24.3	36.2	44.8
11.7-17	26	38.3	4.9	30.6	38.9	47.1
17-21	13	42.9	5.9	32.2	44.5	50.7
21-29	19	43.7	7.0	32.6	43.2	57.34
29-36.65	18	40.1	3.8	35.5	39.1	50.3



7. Computer tomography scanning of carbonate consolidated gas hydrates bearing sediments at Yam Seep, Four-way Closure Ridge SW offshore Taiwan

## **Computer tomography scanning of carbonate consolidated gas hydrates bearing sediments at Yam Seep, Four-way Closure Ridge SW offshore Taiwan**

Yiting Tseng<sup>1\*</sup>, Jürgen Titschack<sup>1</sup>, Saulwood Lin<sup>2</sup>, Gerhard Bohrmann<sup>1</sup>

<sup>1</sup>MARUM – Center for Marine Environmental Sciences and Faculty of Geosciences, University of Bremen, Germany

<sup>2</sup>Institute of Oceanography, National Taiwan University, Taiwan

### **Abstract**

At cold seeps, carbonate precipitation consolidates the sediments that potentially consist of gas hydrate, free gas, and also of fauna debris, shells, or breccias. Gas migrating to the subsurface, change of geotechnical properties of the sediment had potentially allowed the formation of gas hydrate to push the sediments aside and form massive hydrate with the co-existence of free gas bubbles. However, the consequence of gas bearing sediments after consolidation and the evidence of the coexisting of gas hydrate and gas bubbles have yet little been studied due to the limit of in-situ environment and the complicated structure of cemented carbonate cores. Here, we present the results of CT scan on a 5-meter-long carbonate core, MeBo-24 from Yam Seep at Four-Way Closure accretionary Ridge in SW offshore Taiwan. The non-intrusive analysis provides comprehensive core deposition and stratification archives, in which the variation of density between different microfacies is not obvious. However, the pore space in the carbonate core present two distinct signal intensities that represent the open pores and filled pores, x-ray attenuation <800 HU and 900 - 1500 HU, respectively. The column percentages of open pores and filled pores are difference between different microfacies (A, B and C), in which microfacies B composed mostly pure aragonite is less porous comparing to sediment consolidated microcrystalline aragonite microfacies A and high (~>87%) aragonite microfacies C. Whereby present evolution of the fluid transportation during precipitate consolidation. The highest open pores and filled pores at the section of the oldest precipitates in MeBo-24 provide a critique for supporting the gas hydrate expansion in the sediments, in which the scale not only causing the fracturing of sediments but also individual pores within sediments.

## Method

Whole rounds of core GeoB23225-1 were scanned by a Toshiba Aquilion 64™ computer tomograph (CT) at the hospital Klinikum Bremen-Mitte, with an X-ray source voltage of 120 kV and a current of 600 mA and a resolution of 0.351 mm in xy-direction and 0.5 mm resolution in z-direction (resolution of scaled reconstruction: 0.195 x 0.195 x 0.3 mm). Images were reconstructed using Toshiba's patented helical cone beam reconstruction technique. The obtained CT data were processed using the ZIB edition of the Amira software (version 2019.51; Stalling et al., 2005).

Within Amira, the CT scans of the core sections were merged when necessary and core liners, including about 2 mm of the core rims, were removed from the dataset until all marginal artefacts from the coring process were removed. Subsequently, the air-filled pore space within the sediment was separated from the surrounding air by using the *Ambient Occlusion* module (Baum et al., 2016; Titschack et al., 2018). Open pores and pores filled with low density sediments were segmented with the marker-based watershed tool of the *Segmentation Editor*. For the water-shedding, markers were set in the respective materials by thresholding (open pores: <770 HU; filled pores 900 – 1500 HU; sediment/rock: 2300 – 3250 HU). Individual pore spaces were identified and separated with the *Connected Component* module for open pores, and for joined open and filled pores. The results were visualised in 2D and 3D. The porosity and the number of individual pores within every xy-slice was quantified with the Material Statistics and the GrainSizeDistribution modules, respectively.

## Result

MeBo-24 present obvious porosity variation from the top to the bottom that the porosity increase from 0 to 200 cmbsf and higher ratio of porosity can be observed below 200 cmbsf (Fig. 7.1). Open pores and filled pores were defined to distinguish the intensity of void pore space and the pore space that are filled by loose acicular crystal. The filled pores are not as well consolidated as carbonate rocks. Results of open pores and filled pores were shading with color blue and green (Fig. 7.2).

Distinguished microfacies, microfacies I, II and III of a selective section (274-283 cmbsf) present distinct porosity variation (Fig. 7.3) Microfacies I, the micritic carbonate characterize with highest porosity and the high aragonite composition (> 87%) microfacies III (Chapter 6) also present relatively high porosity. The clear aragonite microfacies II is however present the low porosity ratio.

We analysed porosity (open and filled pores) of 16 segments (Fig. 7.4) with selective micritic carbonate sections and clear aragonite sections. The porosities of open and filled pores are generally increasing from the top to the deeper depth. Means of the lowest and the highest porosities are 2.5 and 15.4 % at the segments of 0-5 and 154-188 cmbsf. The deepest dark grey and white carbonates present mean porosities of 9.9 and 9.1 % at 418-475 and 475-490 cmbsf, respectively. Mean, maximum and minimum of each segment are shown in Table. 7.1 and Fig. 7.4.

#### Potential topics for discussion

1. Sediment porosity featuring gas hydrate bearing sediments
2. Characteristics of microfacies I, II, and III
3. Evolution and mechanism of porous dark aragonite (microfacies III)
4. Exposed sediments surface and the development in correlate with the encounter of gas hydrates
5. Fluid migration during consolidation

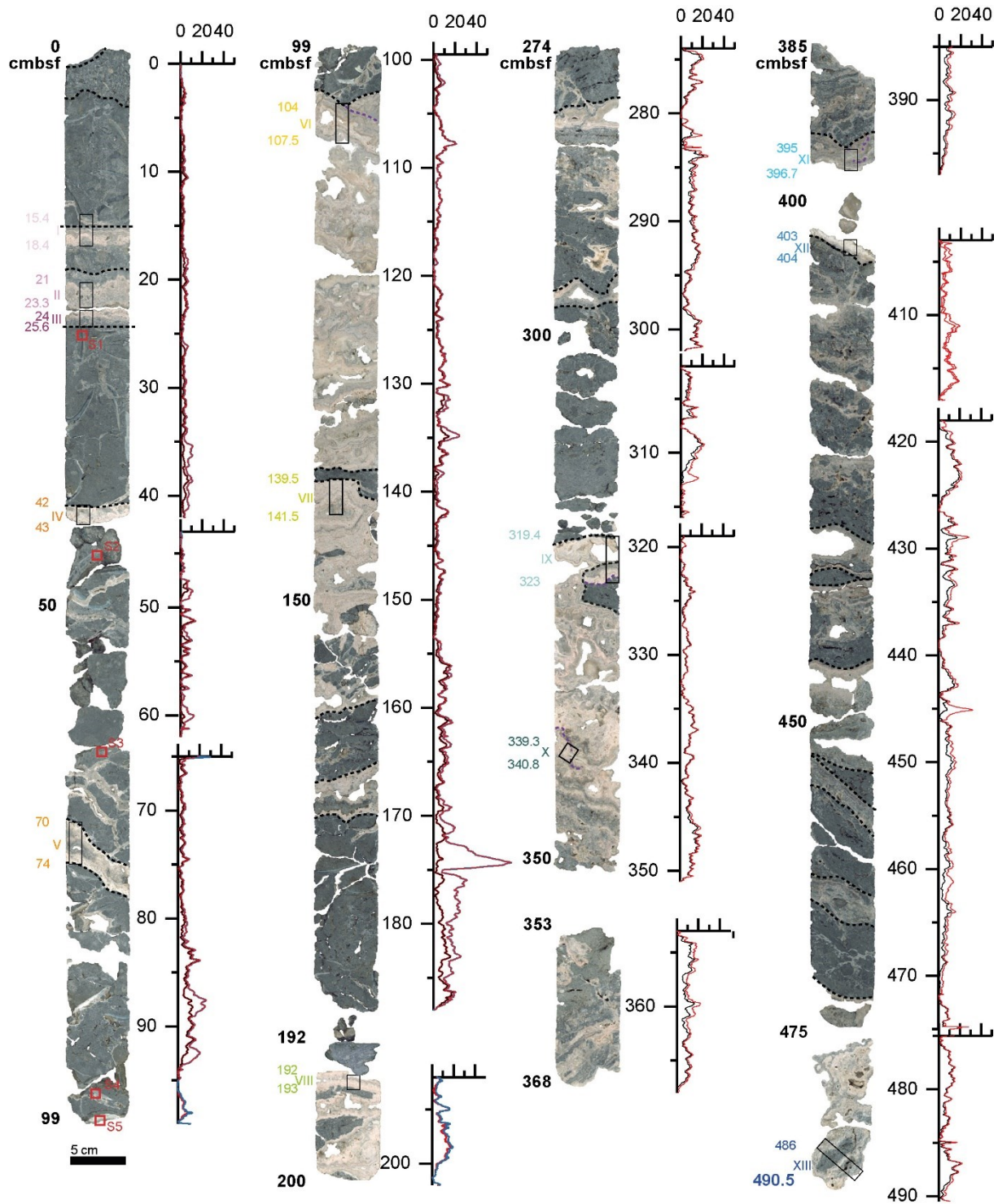
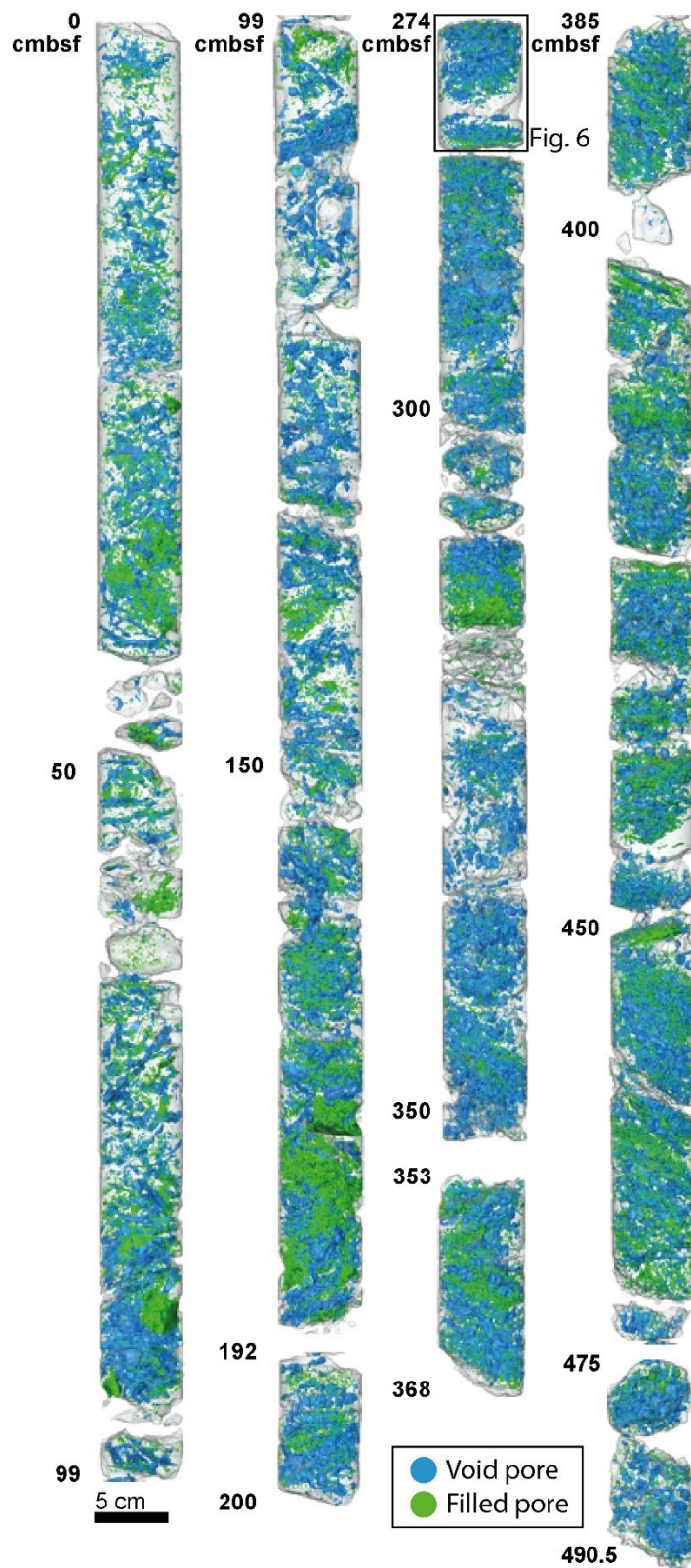
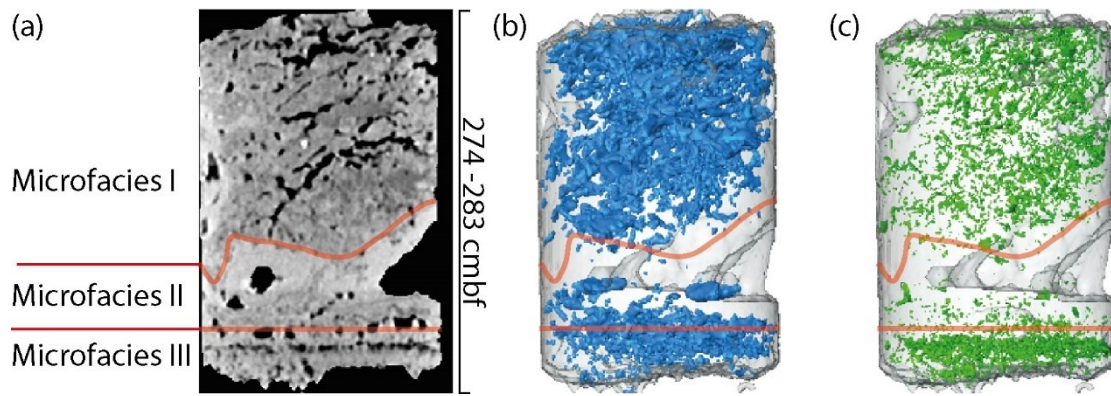


Fig. 7.1. MeBo-24, GeoB23225-1 and CT-scan porosity profile



**Fig 7.2.** CT-Scan of MeBo-24,



**Fig. 7.3.** Microfacies and CT scan results at 274-283 cmbsf. (a) Orthoslice with grey values in the range from 1000 - 3500 HU (b) Open pores (blue) x-ray attenuation <800 HU (c) Filled pores (green) x-ray attenuation 900 - 1500 HU

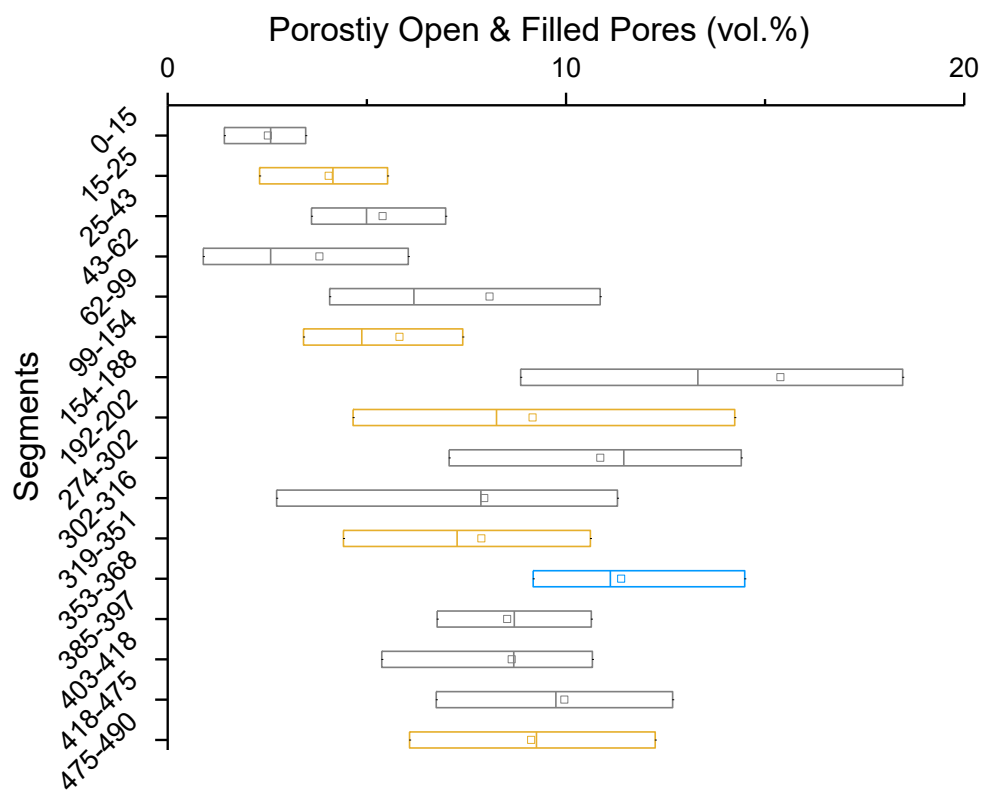


**Fig. 7.4.** Box plots porosities of 16 segments at GeoB23225-1. Grey boxes are micrites, yellow boxes are light aragonites, and blue box is dark aragonites.



Table 7.1 Statistic n, mean, standard deviation, minimum, median, and maximum of porosity (%) in each segments.

<b>Data</b>	<b>N total</b>	<b>Mean</b>	<b>Standard Deviation</b>	<b>Minimum</b>	<b>Median</b>	<b>Maximum</b>
<b>0-43</b>	1416	2.554998	1.497863	0.030831	2.446426	10.21923
	1416	4.066599	2.326195	0.158658	3.67784	11.70953
<b>43-62</b>	712	2.106478	3.010056	0	1.000042	26.99282
	712	3.810036	3.806036	0	2.584609	29.86535
<b>62-99</b>	979	5.530559	3.715768	0	4.287372	19.16228
	979	8.082684	5.51248	0.052678	6.179869	25.92836
<b>99-188</b>	2912	5.652618	3.530856	0	4.963159	20.64719
	2912	9.482391	8.543257	0	6.947347	72.30749
<b>192-200</b>	321	7.96032	4.744408	0.338086	7.190496	17.99903
	321	9.163257	5.110572	0.48018	8.258119	19.56826
<b>274-302</b>	925	9.069684	4.563307	0	9.265737	21.24518
	925	10.86409	4.995562	0.031287	11.44975	25.24111
<b>302-316</b>	561	5.49942	4.995282	0	5.050001	20.29077
	561	7.951226	5.497151	0	7.865169	21.87553
<b>319-351</b>	1022	7.026978	4.031278	0.051871	6.527187	18.18937
	1022	7.878116	4.3179	0.056381	7.267401	19.89966
<b>353-368</b>	479	8.552416	3.659187	0	8.905285	16.66326
	479	11.38941	4.32765	0	11.11475	21.79818
<b>385-397</b>	316	6.378539	2.731709	0.438778	6.389106	12.89202
	316	8.5241	3.233518	0.740155	8.702891	15.34677
<b>403-418</b>	672	6.302482	3.892663	0	5.771477	17.5425
	672	8.639944	4.151873	0	8.687884	19.41878
<b>418-475</b>	1749	7.206849	4.231346	0	7.039945	27.11864
	1749	9.960957	4.861898	0.129734	9.744999	32.05298
<b>475-490</b>	466	7.787633	4.381697	0	7.949003	20.75003
	466	9.124817	4.313086	0.619082	9.260767	22.07011



## 8. Conclusion and outlook

### 8.1. Summary of findings

This cumulative thesis investigates seepage from the past to the present at Yam Seep at Four-Way Closure Ridge, offshore southwestern Taiwan. The entire work focuses on geochemical cycling and geodynamic activity in Yam Seep as an individual seep area (based on bathymetry and backscatter maps at the meter-scale resolution) of gas bubble emissions, high concentration methane anomalies, distribution of chemosynthetic communities and authigenic carbonates morphologies (based on water-column hydroacoustic data, seafloor image system and water sample analysis) which showcase the tectonic influence (based on petrography and detail dating on the carbonate core), and authigenic seep aragonites provides environmental archives of paleo seawater and seepage (based on environmental proxy isotopes analysis on aragonite samples from carbonate core). The data and samples were collected from research cruise SO266 RV Sonne to the Four-Way Closure Ridge in October, 2018. The detailed observation and mapping are complemented by the AUV survey of research cruise OR1-1163 RV Ocean researcher I during May 2017. The deployment of drill-rig recovered a 5-meter-long carbonate core, MeBo-24, through the carbonate pavement at north western Yam Seep. This was the first seep carbonate core retrieved from the active margin south western Taiwan. The investigation and sampling revealed the active and long-term seepage of ~40 thousand-year history at the 49,000 m<sup>2</sup> carbonate paved Yam Seep area.

The three manuscripts respectively show an application of distinctive research methods to understand the (i) morphology, active seepages, and evolution of Yam Seep, (ii) the carbonates petrography and chronology and (iii) the archives of carbonate uranium, oxygen and carbon isotopes in MeBo-24. The first manuscript aims to provide a comprehensive morphology of Yam Seep by correlating hydroacoustic data (maps of high-resolution bathymetry, backscatter, side-scan profile, and water column data), images (photos and videos), and sediment and rock samples (seawater, sediments, carbonates). The second and the third manuscripts focus on the investigation and examination on the carbonate core MeBo-24. The second manuscript looks into petrography, stratigraphy and chronology of the carbonate and the indications of fracturing and precipitation mechanisms. The third manuscript aims to develop a better understanding of seep carbonate precipitation archives interplay fluid sources of seawater, seepages and gas hydrates via studying seep aragonites isotope archived  $\delta^{234}\text{U}$ ,  $\delta^{18}\text{O}$  and  $\delta^{13}\text{C}$ .

Significant findings presented in the three manuscripts are summarized in Fig 8.1. Yam Seep at Four-Way Closure Ridge is a carbonate paved seep area, in which the morphology of exposed

carbonate crusts and build-ups indicates the influence of tectonic fracturing and erosion. This study showed that the chemosynthetic communities within cracks or deepest ground between build-ups, gas bubble “flares” at the east flank of Yam Seep, and high methane concentrations at the rim of the seep area. The results suggested that the distinct characteristics and distribution of the active seepages and detailed carbonate morphology can be extended to the whole area through analyzing hydroacoustic backscatter signals. At the rim of Yam Seep, partially exposed carbonate crusts and wide extension of reduced sediment and microbial patches indicate an initial stage of occurrence of methane and a potential expansion of the seep area. We illustrated a four-stage schematic evolution of Yam Seep: initial seepage, carbonate precipitation, increasing precipitation and seafloor sealing, and erosion and seafloor morphology re-shaping (Fig 8.1 A).

In the separate manuscript, the critique of the long-term seepage at Yam Seep is revisited with dating on carbonate and bivalve shells in MeBo-24 that indicate a persistent ~40-thousand-year seeping history across the LGM and suggest non-climate-perturbed seepages. Petrography of carbonates within MeBo-24 revealed different precipitation environments that result in three different microfacies: A, B and C. Microfacies A, the banded and botryoidal (crystalline) and yellow (cryptocrystalline) aragonites, intercalate between microfacies B, micritic carbonate consisting of microcrystalline aragonites consolidated sediments. And microfacies C succeed below microfacies A that present a different aragonite form. Chronology correlation with petrography revealed the cementing sequence within carbonate fractures and unconformities. The deep water (>1000m) setting provides no ambiguity of fractures causing by gas hydrate dynamic but are producing by tectonic activities. Ages of the aragonites precipitates on the fracture boundaries determine the episodes of tectonic and seepage activity. Combining petrography and chronology, we propose that tectonic fracturing the consolidated micritic carbonates and the open spaces are later filled by gas hydrates which are replaced and cemented by microfacies B, resulting in the formation of MeBo-24 (Fig 8.1 B). Repeating such mechanisms further showcase the tectonic and seepage activity variations that indicate an active period between ~37 and 27 ka followed by a quiet period between ~27 and 16 ka, and a lateral active period between ~16 and 12 ka (Fig 8.1 B).

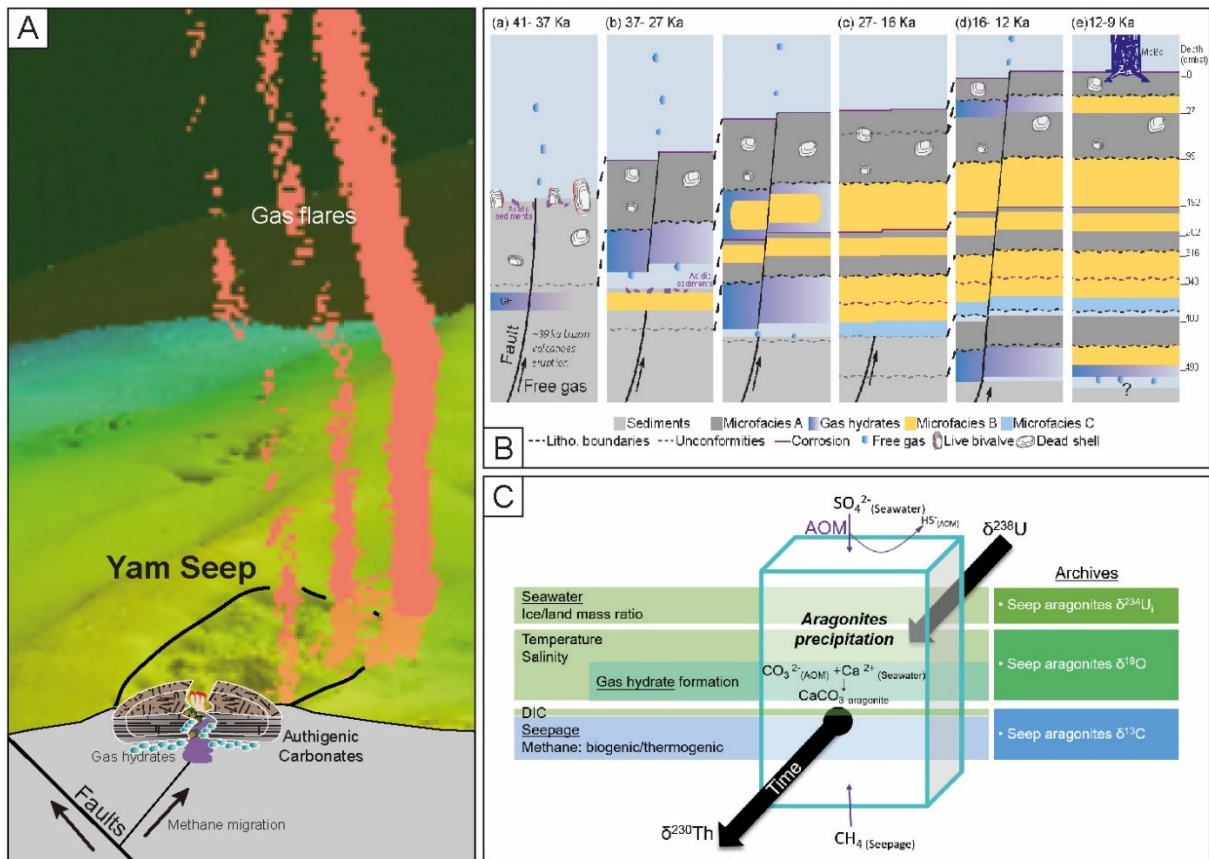


**Fig. 8.1** Summary of main results of this thesis. A) AUV bathymetry map, gas flares and schematic carbonate crusts and distribution of chemosynthetic communities (below). B) formation of aragonites replacing gas hydrates within fractured carbonates (micrites). C) Seep aragonites  $\delta^{234}\text{U}_i$ ,  $\delta^{18}\text{O}$  and  $\delta^{13}\text{C}$  reflect an interplay of seawater archived ice/land ratio, temperature, salinity, DIC, gas hydrates and methane.

In the third manuscript, the seep aragonite (microfacies B) isotopes  $\delta^{234}\text{U}_i$ ,  $\delta^{18}\text{O}$  and  $\delta^{13}\text{C}$  profile archived three different patterns that represent the decoupling of  $\delta^{234}\text{U}$ ,  $\delta^{18}\text{O}$  and  $\delta^{13}\text{C}$  during precipitation. The archiving of isotopes is resulted from the interplay of seawater, seepage and gas hydrates in the past  $\sim 37$  thousand years. Seep aragonites  $\delta^{234}\text{U}_i$ ,  $\delta^{18}\text{O}$  and  $\delta^{13}\text{C}$  reflect the interplay of open seawater and ambient water that archives ice/land ratio, temperature, salinity, DIC, gas hydrates, and methane (Fig 8.1 C). The similarity between seep aragonites  $\delta^{234}\text{U}_i$ ,  $\delta^{18}\text{O}$  profiles and foraminifera and corals profiles revealed the characteristic of seep aragonites archived open seawater  $\delta^{234}\text{U}$ ,  $\delta^{18}\text{O}$  variations. Seep aragonites  $\delta^{234}\text{U}_i$  shows high similarity with coral  $\delta^{234}\text{U}_i$  and potentially extend the archiving period that indicates the ice-land ratio variation during glacial-interglacial. Seep aragonites  $\delta^{18}\text{O}$  present a similar trend as the benthic foraminifera  $\delta^{18}\text{O}$  archives; however, a group of relatively depleted seep aragonites show the influence of the gas hydrate formation environment. The extremely low seep aragonites  $\delta^{13}\text{C}$  values suggest the dominant influence of seepage methane. However, the variations of  $\delta^{13}\text{C}$  values are resulted from the waxing and waning of the influence from the methane oxidation DIC and seawater DIC. The increase of seawater mixing ratio during the LGM presents a negative correlation with the sea level variations but an overlap with the results of quiet period ( $\sim 27$  to  $16$  ka) in manuscript II. The increase of seawater flux can also be interpreted as the diminishing of seepage intensity. Both interpretations suggest the independency of seepage and sea level variation, which leads to further assessment of the influence of the tectonic controlled seepage in the manuscript II.

Density and porosity of the carbonate core MeBo-24 was studied using CT-scan. Representing consolidated sediments, MeBo-24 consist of a piece of 5-meter-long carbonate rock with varied porosity and density. Some sections present a mousy-sediments-like structure which indicates the presence of previous gas hydrate bearing sediments. The porosity variations provided insights for distinguishing microfacies and stratigraphy of MeBo-24. Ample correlations between porosity, density and stratigraphy of MeBo-24 potentially allow for deciphering the evolution and formation of carbonate precipitation with the interplay of gas bubbles, gas hydrates, fluid migrations and chemosynthetic shells cementation. Further analysis is needed for a more holistic discussion before a concrete conclusion can be reached

In summary, reshaping of seafloor morphology and the carbonate precipitations under fracturing caused the intercalation of different carbonate microfacies and aragonite forms. These seep aragonites archive important environmental variation that interplay seawater, gas hydrate, and methane. The relevance of this study is not restricted to seepage and early

diagenesis at seepage. Evidence from this study has contributed more broadly to understanding the geochemical cycles and geodynamics activities at active margin seep.

### 8.1. Outlook

We have conducted a detailed study on the Yam Seep area in which massive deposition of authigenic carbonates can be found. This study has provided new insights into paleo seepage and the environmental archives. However, this is merely a start of calling for more evidence from other seep sites to broaden our understanding regarding the influences of seepage locally and globally. Many questions have been posed and require further investigation. More studies and broader knowledge on seeps and gas hydrates remain crucial in the time of climate change as an urgent response for a sustainable earth. A plenty of carbon budget from nature input remains unclear while how the global atmosphere and ocean system responds to climate change is under debate. Detailed investigation on aragonite precipitation rate, AOM conditions and the potential oldest archives that a seep carbonate can reach are crucial for a more holistic understanding. Further research would be needed to consider the potential causes of tectonic influence and effects of seepage episodes as well as the variation of the marine environment linked to deep water alkalinity buffering and other regional and global geodynamics.

## 9. References

- Aharon, P., Schwarcz, H. P., & Roberts, H. H. (1997). Radiometric dating of submarine hydrocarbon seeps in the Gulf of Mexico. *GSA Bulletin*, 109(5), 568-579. doi:10.1130/0016-7606(1997)109<0568:rdoshs>2.3.co;2
- Alford, M. H., Peacock, T., MacKinnon, J. A., Nash, J. D., Buijsman, M. C., Centurioni, L. R., . . . Tang, T.-Y. (2015). The formation and fate of internal waves in the South China Sea. *Nature*, 521(7550), 65-69. doi:10.1038/nature14399
- Aloisi, G., Pierre, C., Rouchy, J. M., Foucher, J. P., Woodside, J., & Party, M. S. (2000). Methane-related authigenic carbonates of eastern Mediterranean Sea mud volcanoes and their possible relation to gas hydrate destabilisation. *Earth and Planetary Science Letters*, 184(1), 321-338. doi:10.1016/s0012-821x(00)00322-8
- Andersen, M. B., Stirling, C. H., & Weyer, S. (2017). Uranium isotope fractionation. *Reviews in mineralogy and geochemistry*, 82(1), 799-850.
- Andersen, M. B., Stirling, C. H., Zimmermann, B., & Halliday, A. N. (2010). Precise determination of the open ocean  $^{234}\text{U}/^{238}\text{U}$  composition. *Geochemistry, Geophysics, Geosystems*, 11(12). doi:10.1029/2010gc003318
- Bahr, A., Pape, T., Abegg, F., Bohrmann, G., van Weering, T., & Ivanov, M. K. (2010). Authigenic carbonates from the eastern Black Sea as an archive for shallow gas hydrate dynamics - Results from the combination of CT imaging with mineralogical and stable isotope analyses. *Marine and Petroleum Geology*, 27(9), 1819-1829. doi:10.1016/j.marpetgeo.2010.08.005
- Bahr, A., Pape, T., Bohrmann, G., Mazzini, A., Haeckel, M., Reitz, A., & Ivanov, M. (2007). Authigenic carbonate precipitates from the NE Black Sea: a mineralogical, geochemical, and lipid biomarker study. *International Journal of Earth Sciences*, 98(3), 677. doi:10.1007/s00531-007-0264-1
- Banner, J. L., & Hanson, G. N. (1990). Calculation of simultaneous isotopic and trace element variations during water-rock interaction with applications to carbonate diagenesis. *Geochimica Et Cosmochimica Acta*, 54(11), 3123-3137.
- Barbieri, R., Ori, G. G., & Cavalazzi, B. (2004). A Silurian Cold-Seep Ecosystem from the Middle Atlas, Morocco. *PALAIOS*, 19(6), 527-542. <http://www.jstor.org/stable/3515872>
- Barry, M. A., Boudreau, B. P., & Johnson, B. D. (2012). Gas domes in soft cohesive sediments. *Geology*, 40(4), 379-382. doi:10.1130/g32686.1
- Baum, D., & Titschack, J. (2016). Cavity and pore segmentation in 3D images with Ambient Occlusion. Paper presented at the Eurographics Conference on Visualization (EuroVis) 2016.
- Bayon, G., Henderson, G. M., & Bohn, M. (2009). U-Th stratigraphy of a cold seep carbonate crust. *Chemical Geology*, 260(1-2), 47-56. doi:10.1016/j.chemgeo.2008.11.020
- Bayon, G., Henderson, G. M., Etoubleau, J., Caprais, J. C., Ruffine, L., Marsset, T., . . . Sultan, N. (2015). U-Th isotope constraints on gas hydrate and pockmark dynamics at the Niger delta margin. *Marine Geology*, 370, 87-98. doi:10.1016/j.margeo.2015.10.012
- Bayon, G., Pierre, C., Etoubleau, J., Voisset, M., Cauquil, E., Marsset, T., . . . Fouquet, Y. (2007). Sr/Ca and Mg/Ca ratios in Niger Delta sediments: Implications for authigenic carbonate genesis in cold seep environments. *Marine Geology*, 241(1-4), 93-109. doi:10.1016/j.margeo.2007.03.007
- Beauchamp, B., & Savard, M. (1992). Cretaceous Chemosynthetic Carbonate Mounds in the Canadian Arctic. *Palaios*, 7(4), 434-450. doi:10.2307/3514828
- Bergquist, D. C., Williams, F. M., & Fisher, C. R. (2000). Longevity record for deep-sea invertebrate. *Nature*, 403(6769), 499-500. doi:10.1038/35000647

- Berner, R. A. (1975). The role of magnesium in the crystal growth of calcite and aragonite from sea water. *Geochimica Et Cosmochimica Acta*, 39(4), 489-504. doi:[https://doi.org/10.1016/0016-7037\(75\)90102-7](https://doi.org/10.1016/0016-7037(75)90102-7)
- Berner, R. A. (1980). Early diagenesis: a theoretical approach: Princeton University Press.
- Berner, R. A. (1982). Burial of organic carbon and pyrite sulfur in the modern ocean; its geochemical and environmental significance. *American Journal of Science*, 282(4), 451-473. doi:10.2475/ajs.282.4.451
- Berner, R. A. (1990). Atmospheric Carbon Dioxide Levels Over Phanerozoic Time. *Science*, 249(4975), 1382-1386. doi:doi:10.1126/science.249.4975.1382
- Berner, R. A., & Raiswell, R. (1983). Burial of organic carbon and pyrite sulfur in sediments over phanerozoic time: a new theory. *Geochimica Et Cosmochimica Acta*, 47(5), 855-862. doi:[https://doi.org/10.1016/0016-7037\(83\)90151-5](https://doi.org/10.1016/0016-7037(83)90151-5)
- Blanchon, P., Eisenhauer, A., Fietzke, J., & Liebetrau, V. (2009). Rapid sea-level rise and reef back-stepping at the close of the last interglacial highstand. *Nature*, 458(7240), 881-884. doi:10.1038/nature07933
- Boetius, A., Ravensschlag, K., Schubert, C. J., Rickert, D., Widdel, F., Gieseke, A., . . . Pfannkuche, O. (2000). A marine microbial consortium apparently mediating anaerobic oxidation of methane. *Nature*, 407(6804), 623-626.
- Boetius, A., & Wenzhöfer, F. (2013). Seafloor oxygen consumption fuelled by methane from cold seeps. *Nature Geoscience*, 6(9), 725-734. doi:10.1038/ngeo1926
- Bohrmann, G., Greinert, J., Suess, E., & Torres, M. (1998). Authigenic carbonates from the Cascadia subduction zone and their relation to gas hydrate stability. *Geology*, 26(7), 647-650. doi:10.1130/0091-7613(1998)026<0647:acftcs>2.3.co;2
- Bohrmann, G., Heeschen, K., Jung, C., Weinrebe, W., Baranov, B., Cailleau, B., . . . Masson, D. (2002). Widespread fluid expulsion along the seafloor of the Costa Rica convergent margin. *Terra Nova*, 14(2), 69-79.
- Bohrmann, G., Lin, S., & Berndt, C. (2019). MeBo200 Methane Hydrate Drillings Southwest of Taiwan - First Results from the R/V Sonne Cruise SO266. <https://ui.adsabs.harvard.edu/abs/2019AGUFMOS43A..01B>
- Bohrmann, G., & Torres, M. E. (2006). Gas hydrates in marine sediments *Marine geochemistry* (pp. 481-512): Springer.
- Borowski, W. S., Paull, C. K., & Ussler III, W. (1996). Marine pore-water sulfate profiles indicate in situ methane flux from underlying gas hydrate. *Geology*, 24(7), 655-658.
- Bowin, C., Lu, R. S., Lee, C.-S., & Schouten, H. (1978). Plate convergence and accretion in Taiwan-Luzon region. *Aapg Bulletin*, 62(9), 1645-1672.
- Caress, D. W., & Chayes, D. N. (1996). Improved processing of Hydrosweep DS multibeam data on the R/V Maurice Ewing. *Marine Geophysical Researches*, 18(6), 631-650.
- Caress, D. W., Thomas, H., Kirkwood, W. J., McEwen, R., Henthorn, R., Clague, D. A., . . . Reynolds, J. (2008). High-resolution multibeam, sidescan, and subbottom surveys using the MBARI AUV D. Allan B. Marine habitat mapping technology for Alaska, 47-69.
- Chen, F., Wang, X., Li, N., Cao, J., Bayon, G., Peckmann, J., . . . Feng, D. (2019). Gas Hydrate Dissociation During Sea-Level Highstand Inferred From U/Th Dating of Seep Carbonate From the South China Sea. *Geophysical Research Letters*, 46. doi:10.1029/2019GL085643
- Chen, J., Edwards, R. L., & Wasserburg, G. J. (1986). 238U, 234U and 232Th in seawater. *Earth and Planetary Science Letters*, 80(3-4), 241-251.
- Chen, N. C., Yang, T. F., Hong, W. L., Chen, H. W., Chen, H. C., Hu, C. Y., . . . Su, C. C. (2017). Production, consumption, and migration of methane in accretionary prism of southwestern Taiwan. *Geochemistry, Geophysics, Geosystems*, 18(8), 2970-2989.

- Chen, N.-C., Yang, T. F., Hong, W.-L., Yu, T.-L., Lin, I.-T., Wang, P.-L., . . . Lin, L.-H. (2020). Discharge of deeply rooted fluids from submarine mud volcanism in the Taiwan accretionary prism. *Scientific Reports*, 10(1), 381. doi:10.1038/s41598-019-57250-9
- Chen, S.-C., Hsu, S.-K., Wang, Y., Chung, S.-H., Chen, P.-C., Tsai, C.-H., . . . Lee, Y.-W. (2014). Distribution and characters of the mud diapirs and mud volcanoes off southwest Taiwan. *Journal of Asian Earth Sciences*, 92, 201-214. doi:https://doi.org/10.1016/j.jseaes.2013.10.009
- Chen, T., Robinson, L. F., Beasley, M. P., Claxton, L. M., Andersen, M. B., Gregoire, L. J., . . . Harpp, K. S. (2016). Ocean mixing and ice-sheet control of seawater  $^{234}\text{U}/^{238}\text{U}$  during the last deglaciation. *Science*, 354(6312), 626-629.
- Chen, T.-T., Paull, C. K., Liu, C.-S., Klaucke, I., Hsu, H.-H., Su, C.-C., . . . Caress, D. W. (2019). Discovery of numerous pingos and comet-shaped depressions offshore southwestern Taiwan. *Geo-Marine Letters*. doi:10.1007/s00367-019-00577-z
- Chen, W.-S., Lee, W. C., Huang, N. W., Yen, I. C., Yang, C. C., Yang, H. C., . . . Sung, S. H. (2005). Characteristics of accretionary prism of Hengchun Peninsula, southern Taiwan: Holocene activity of the Hengchun Fault. *West. Pac. Earth Sci.*, 5, 129-153.
- Chen, X., Romaniello, S. J., Herrmann, A. D., Hardisty, D., Gill, B. C., & Anbar, A. D. (2018). Diagenetic effects on uranium isotope fractionation in carbonate sediments from the Bahamas. *Geochimica Et Cosmochimica Acta*, 237, 294-311. doi:10.1016/j.gca.2018.06.026
- Cheng, H., Edwards, R. L., Hoff, J., Gallup, C. D., Richards, D., & Asmerom, Y. (2000). The half-lives of uranium-234 and thorium-230. *Chemical Geology*, 169(1-2), 17-33.
- Cheng, H., Lawrence Edwards, R., Shen, C.-C., Polyak, V. J., Asmerom, Y., Woodhead, J., . . . Calvin Alexander, E. (2013). Improvements in  $^{230}\text{Th}$  dating,  $^{230}\text{Th}$  and  $^{234}\text{U}$  half-life values, and U–Th isotopic measurements by multi-collector inductively coupled plasma mass spectrometry. *Earth and Planetary Science Letters*, 371-372, 82-91. doi:https://doi.org/10.1016/j.epsl.2013.04.006
- Cheng, X., Tian, J., & Wang, P. (2004). (Table T2) Oxygen and carbon isotope ratios for benthic foraminifers of ODP Site 184-1143. Retrieved from: https://doi.org/10.1594/PANGAEA.784149
- Chiu, J.-K., Wei-Hao, T., & Liu, C.-S. (2006). Distribution of gassy sediments and mud volcanoes offshore southwestern Taiwan. *TAO: Terrestrial, Atmospheric and Oceanic Sciences*, 17(4), 703.
- Chuang, P. C., Dale, A. W., Wallmann, K., Haeckel, M., Yang, T. F., Chen, N. C., . . . Sun, C. H. (2013). Relating sulfate and methane dynamics to geology: Accretionary prism offshore SW Taiwan. *Geochemistry, Geophysics, Geosystems*, 14(7), 2523-2545.
- Chuang, P. C., Yang, T., Hong, W. L., Lin, S., Sun, C. H., Lin, A. S., . . . Chung, S. H. (2010). Estimation of methane flux offshore SW Taiwan and the influence of tectonics on gas hydrate accumulation. *Geofluids*, 10(4), 497-510.
- Chuang, P.-C., Yang, T. F., Wallmann, K., Matsumoto, R., Hu, C.-Y., Chen, H.-W., . . . Dale, A. W. (2019). Carbon isotope exchange during anaerobic oxidation of methane (AOM) in sediments of the northeastern South China Sea. *Geochimica Et Cosmochimica Acta*, 246, 138-155. doi:10.1016/j.gca.2018.11.003
- Chutcharavan, P. M., Dutton, A., & Ellwood, M. J. (2018). Seawater  $^{234}\text{U}/^{238}\text{U}$  recorded by modern and fossil corals. *Geochimica Et Cosmochimica Acta*, 224, 1-17.
- Clark, P. U., Dyke, A. S., Shakun, J. D., Carlson, A. E., Clark, J., Wohlfarth, B., . . . McCabe, A. M. (2009). The Last Glacial Maximum. *Science*, 325(5941), 710-714. doi:10.1126/science.1172873
- Claypool, G. E., & Kaplan, I. (1974). The origin and distribution of methane in marine sediments *Natural gases in marine sediments* (pp. 99-139): Springer.



- Cochran, J. K., Carey, A. E., Sholkovitz, E. R., & Surprenant, L. D. (1986). The geochemistry of uranium and thorium in coastal marine sediments and sediment pore waters. *Geochimica Et Cosmochimica Acta*, 50(5), 663-680. doi:[https://doi.org/10.1016/0016-7037\(86\)90344-3](https://doi.org/10.1016/0016-7037(86)90344-3)
- Cordes, E. E., Arthur, M. A., Shea, K., Arvidson, R. S., & Fisher, C. R. (2005). Modeling the mutualistic interactions between tubeworms and microbial consortia. *PLoS Biol*, 3(3), e77.
- Cordes, E. E., Bergquist, D. C., Shea, K., & Fisher, C. R. (2003). Hydrogen sulphide demand of long-lived vestimentiferan tube worm aggregations modifies the chemical environment at deep-sea hydrocarbon seeps. *Ecology Letters*, 6(3), 212-219.
- Crémière, A., Bayon, G., Ponzevera, E., & Pierre, C. (2013). Paleo-environmental controls on cold seep carbonate authigenesis in the Sea of Marmara. *Earth and Planetary Science Letters*, 376, 200-211. doi:<https://doi.org/10.1016/j.epsl.2013.06.029>
- Cutler, K., Gray, S., Burr, G., Edwards, R., Taylor, F., Cabioch, G., . . . Moore, J. (2004). Radiocarbon calibration and comparison to 50 kyr BP with paired <sup>14</sup>C and <sup>230</sup>Th dating of corals from Vanuatu and Papua New Guinea. *Radiocarbon*, 46(3), 1127-1160.
- Dadson, S. J., Hovius, N., Chen, H., Dade, W. B., Hsieh, M.-L., Willett, S. D., . . . Lin, J.-C. (2003). Links between erosion, runoff variability and seismicity in the Taiwan orogen. *Nature*, 426(6967), 648-651. doi:10.1038/nature02150
- Dählmann, A., & De Lange, G. (2003). Fluid–sediment interactions at Eastern Mediterranean mud volcanoes: a stable isotope study from ODP Leg 160. *Earth and Planetary Science Letters*, 212(3-4), 377-391.
- Davidson, D. W., Leaist, D. G., & Hesse, R. (1983). Oxygen-18 enrichment in the water of a clathrate hydrate. *Geochimica Et Cosmochimica Acta*, 47(12), 2293-2295. doi:[https://doi.org/10.1016/0016-7037\(83\)90053-4](https://doi.org/10.1016/0016-7037(83)90053-4)
- del Rey, Á., Havsteen, J. C., Bizzarro, M., & Dahl, T. W. (2020). Untangling the diagenetic history of uranium isotopes in marine carbonates: A case study tracing the  $\delta^{238}\text{U}$  composition of late Silurian oceans using calcitic brachiopod shells. *Geochimica Et Cosmochimica Acta*, 287, 93-110. doi:<https://doi.org/10.1016/j.gca.2020.06.002>
- Delaney, M. L., & Boyle, E. A. (1983). Uranium and thorium isotope concentrations in foraminiferal calcite. *Earth and Planetary Science Letters*, 62(2), 258-262. doi:[https://doi.org/10.1016/0012-821X\(83\)90088-2](https://doi.org/10.1016/0012-821X(83)90088-2)
- Deng, Y., Chen, F., Guo, Q., Hu, Y., Chen, D., Yang, S., . . . Zhu, J. (2021). Possible Links Between Methane Seepages and Glacial-Interglacial Transitions in the South China Sea. *Geophysical Research Letters*, 48. doi:10.1029/2020GL091429
- Deng, Y., Chen, F., Li, N., Jin, M., Cao, J., Chen, H., . . . Cheng, S. (2019). Cold-Water Corals in Gas Hydrate Drilling Cores from the South China Sea: Occurrences, Geochemical Characteristics and Their Relationship to Methane Seepages. *Minerals*, 9, 742. doi:10.3390/min9120742
- Derkachev, A. N., Nikolaeva, N. A., Baranov, B. V., Barinov, N. N., Mozherovskiy, A. V., Minami, H., . . . Shoji, H. (2015). Manifestation of carbonate-barite mineralization around methane seeps in the Sea of Okhotsk (the western slope of the Kuril Basin). *Oceanology*, 55(3), 390-399. doi:10.1134/s0001437015030029
- Douville, E., Sallé, E., Frank, N., Eisele, M., Pons-Branchu, E., & Ayrault, S. (2010). Rapid and accurate U–Th dating of ancient carbonates using inductively coupled plasma-quadrupole mass spectrometry. *Chemical Geology*, 272(1), 1-11. doi:<https://doi.org/10.1016/j.chemgeo.2010.01.007>
- Dubilier, N., Bergin, C., & Lott, C. (2008). Symbiotic diversity in marine animals: the art of harnessing chemosynthesis. *Nature Reviews Microbiology*, 6(10), 725-740. doi:10.1038/nrmicro1992

- Dunk, R., Mills, R., & Jenkins, W. (2002). A reevaluation of the oceanic uranium budget for the Holocene. *Chemical Geology*, 190(1-4), 45-67.
- Duperron, S., Nadalig, T., Caprais, J.-C., Sibuet, M., Fiala-Médioni, A., Amann, R., & Dubilier, N. (2005). Dual symbiosis in a *Bathymodiolus* sp. mussel from a methane seep on the Gabon continental margin (Southeast Atlantic): 16S rRNA phylogeny and distribution of the symbionts in gills. *Applied and Environmental Microbiology*, 71(4), 1694-1700.
- Duplessy, J. C., Lalou, C., & Vinot, A. C. (1970). Differential isotopic fractionation in benthic foraminifera and paleotemperatures reassessed. *Science*, 168(3928), 250-251.
- Dupre, S., Scalabrin, C., Grall, C., Augustin, J. M., Henry, P., Sengor, A. M. C., . . . Geli, L. (2015). Tectonic and sedimentary controls on widespread gas emissions in the Sea of Marmara: Results from systematic, shipborne multibeam echo sounder water column imaging. *Journal of Geophysical Research-Solid Earth*, 120(5), 2891-2912. doi:10.1002/2014jb011617
- Esat, T. M., & Yokoyama, Y. (2006). Variability in the uranium isotopic composition of the oceans over glacial–interglacial timescales. *Geochimica Et Cosmochimica Acta*, 70(16), 4140-4150.
- Fairbanks, R. G., & Matthews, R. K. (1978). The marine oxygen isotope record in Pleistocene coral, Barbados, West Indies. *Quaternary Research*, 10(2), 181-196. doi:https://doi.org/10.1016/0033-5894(78)90100-X
- Fan, L. F., Lin, S., Hsu, C.-W., Tseng, Y.-T., Yang, T., & Huang, K.-M. (2018). Formation and preservation of authigenic pyrite in the methane dominated environment. *Deep Sea Research Part I: Oceanographic Research Papers*, 138. doi:10.1016/j.dsr.2018.07.004
- Feng, D., Chen, D. F., & Roberts, H. H. (2009). Petrographic and geochemical characterization of seep carbonate from Bush Hill (GC 185) gas vent and hydrate site of the Gulf of Mexico. *Marine and Petroleum Geology*, 26(7), 1190-1198. doi:10.1016/j.marpetgeo.2008.07.001
- Feng, D., Cheng, M., Kiel, S., Qiu, J. W., Yang, Q. H., Zhou, H. Y., . . . Chen, D. F. (2015). Using *Bathymodiolus* tissue stable carbon, nitrogen and sulfur isotopes to infer biogeochemical process at a cold seep in the South China Sea. *Deep-Sea Research Part I-Oceanographic Research Papers*, 104, 52-59. doi:10.1016/j.dsr.2015.06.011
- Feng, D., Qiu, J. W., Hu, Y., Peckmann, J., Guan, H. X., Tong, H. P., . . . Chen, D. F. (2018). Cold seep systems in the South China Sea: An overview. *Journal of Asian Earth Sciences*, 168, 3-16. doi:10.1016/j.jseaes.2018.09.021
- Feng, D., Roberts, H. H., Cheng, H., Peckmann, J., Bohrmann, G., Edwards, R. L., & Chen, D. F. (2010). U/Th dating of cold-seep carbonates: An initial comparison. *Deep-Sea Research Part II-Topical Studies in Oceanography*, 57(21-23), 2055-2060. doi:10.1016/j.dsr2.2010.09.004
- Feng, J. X., Yang, S. X., Liang, J. Q., Fang, Y. X., He, Y. L., Luo, M., & Chen, D. F. (2018). Methane seepage inferred from the porewater geochemistry of shallow sediments in the Beikang Basin of the southern South China Sea. *Journal of Asian Earth Sciences*, 168, 77-86. doi:10.1016/j.jseaes.2018.02.005
- Fisher, C. R., Urcuyo, I. A., Simpkins, M. A., & Nix, E. (1997). Life in the Slow Lane: Growth and Longevity of Cold-seep Vestimentiferans. *Marine Ecology*, 18(1), 83-94. doi:https://doi.org/10.1111/j.1439-0485.1997.tb00428.x
- Flügel, E. (2004). *Microfacies of carbonate rocks : analysis, interpretation and application*: Berlin ; New York : Springer, [2004] ©2004.
- Formolo, M. J., Lyons, T. W., Zhang, C. L., Kelley, C., Sassen, R., Horita, J., & Cole, D. R. (2004). Quantifying carbon sources in the formation of authigenic carbonates at gas hydrate sites in the Gulf of Mexico. *Chemical Geology*, 205(3-4), 253-264. doi:10.1016/j.chemgeo.2003.12.021

- Frank, N., & Hemsing, F. (2021). Dating of Corals and Other Geological Samples via the Radioactive Disequilibrium of Uranium and Thorium Isotopes. In G. Ramstein, A. Landais, N. Bouttes, P. Sepulchre, & A. Govin (Eds.), *Paleoclimatology* (pp. 89-100). Cham: Springer International Publishing.
- Freiwald, A. (2003). Reef-Forming Cold-Water Corals. In G. Wefer, D. Billett, D. Hebbeln, B. B. Jørgensen, M. Schlüter, & T. C. E. van Weering (Eds.), *Ocean Margin Systems* (pp. 365-385). Berlin, Heidelberg: Springer Berlin Heidelberg.
- Freytag, J. K., Girguis, P. R., Bergquist, D. C., Andras, J. P., Childress, J. J., & Fisher, C. R. (2001). A paradox resolved: Sulfide acquisition by roots of seep tubeworms sustains net chemoautotrophy. *Proceedings of the National Academy of Sciences*, 98(23), 13408. doi:10.1073/pnas.231589498
- Fujikura, K., Tsuchida, S., Huang, C.-Y., Nunoura, T., Lin, L.-H., Soh, W., . . . Machiyama, H. (2007). Vent-type chemosynthetic community associated with methane seep at the Formosa Ridge, off southwest Taiwan. ICGH, Taipei, *Proceedings of the International Conference on Gas Hydrate~Energy, Climate and Environment*, 30-31.
- Gasse, F. (2000). Hydrological changes in the African tropics since the Last Glacial Maximum. *Quaternary Science Reviews*, 19(1-5), 189-211. doi:10.1016/s0277-3791(99)00061-x
- Greinert, J., Bohrmann, G., & Elvert, M. (2002). Stromatolitic fabric of authigenic carbonate crusts: result of anaerobic methane oxidation at cold seeps in 4,850 m water depth. *International Journal of Earth Sciences*, 91(4), 698-711. doi:10.1007/s00531-001-0244-9
- Greinert, J., Bohrmann, G., & Suess, E. (2001). Gas hydrate-associated carbonates and methane-venting at Hydrate Ridge: classification, distribution and origin of authigenic lithologies. *GEOPHYSICAL MONOGRAPH-AMERICAN GEOPHYSICAL UNION*, 124, 99-114.
- Greinert, J., Lewis, K. B., Bialas, J., Pecher, I. A., Rowden, A., Bowden, D. A., . . . Linke, P. (2010). Methane seepage along the Hikurangi Margin, New Zealand: Overview of studies in 2006 and 2007 and new evidence from visual, bathymetric and hydroacoustic investigations. *Marine Geology*, 272(1-4), 6-25. doi:10.1016/j.margeo.2010.01.017
- Grossman, E. L., & Ku, T.-L. (1986). Oxygen and carbon isotope fractionation in biogenic aragonite: Temperature effects. *Chemical Geology: Isotope Geoscience section*, 59, 59-74. doi:https://doi.org/10.1016/0168-9622(86)90057-6
- Grottoli, A. G. (2000). Stable Carbon Isotopes ( $\delta^{13}\text{C}$ ) in Coral Skeletons. *Oceanography*, 13(2), 93-97.
- Haas, A., Peckmann, J., Elvert, M., Sahling, H., & Bohrmann, G. (2010). Patterns of carbonate authigenesis at the Kouilou pockmarks on the Congo deep-sea fan. *Marine Geology*, 268, 129-136. doi:10.1016/j.margeo.2009.10.027
- Hagemann, A., Leefmann, T., Peckmann, J., Hoffmann, V. E., & Thiel, V. (2013). Biomarkers from individual carbonate phases of an Oligocene cold-seep deposit, Washington State, USA. *Lethaia*, 46(1), 7-18. doi:10.1111/j.1502-3931.2012.00316.x
- Han, X., Suess, E., Huang, Y., Wu, N., Bohrmann, G., Su, X., . . . Fang, Y. (2008). Jiulong methane reef: microbial mediation of seep carbonates in the South China Sea. *Marine Geology*, 249(3-4), 243-256.
- Han, X., Suess, E., Liebetrau, V., Eisenhauer, A., & Huang, Y. (2014). Past methane release events and environmental conditions at the upper continental slope of the South China Sea: constraints by seep carbonates. *International Journal of Earth Sciences*, 103(7), 1873-1887. doi:https://doi.org/10.1007/s00531-014-1018-5
- Han, X., Suess, E., Sahling, H., & Wallmann, K. (2004). Fluid venting activity on the Costa Rica margin: New results from authigenic carbonates. *International Journal of Earth Sciences*, 93, 596-611. doi:10.1007/s00531-004-0402-y

- Han, X. Q., Yang, K. H., & Huang, Y. Y. (2013). Origin and nature of cold seep in northeastern Dongsha area, South China Sea: Evidence from chimney-like seep carbonates. *Chinese Science Bulletin*, 58(30), 3689-3697. doi:10.1007/s11434-013-5819-x
- Henderson, G. M. (2002). Seawater (234U/238U) during the last 800 thousand years. *Earth and Planetary Science Letters*, 199(1-2), 97-110.
- Henderson, G. M., & Anderson, R. F. (2003). The U-series toolbox for paleoceanography. *Reviews in mineralogy and geochemistry*, 52(1), 493-531.
- Hillaire-Marcel, C., & Ravelo, A. (2007). The use of Oxygen and Carbon isotopes of Foraminifera in Paleoceanography. *Developments in Marine Geology: Proxies in Late Cenozoic Paleoceanography*. Burlington: Elsevier Science.
- Himmler, T., Bach, W., Bohrmann, G., & Peckmann, J. (2010). Rare earth elements in authigenic methane-seep carbonates as tracers for fluid composition during early diagenesis. *Chemical Geology*, 277(1), 126-136. doi:https://doi.org/10.1016/j.chemgeo.2010.07.015
- Himmler, T., Bayon, G., Wangner, D., Enzmann, F., Peckmann, J., & Bohrmann, G. (2016). Seep-carbonate lamination controlled by cyclic particle flux. *Scientific Reports*, 6(1), 1-8.
- Himmler, T., Birgel, D., Bayon, G., Pape, T., Ge, L., Bohrmann, G., & Peckmann, J. (2015). Formation of seep carbonates along the Makran convergent margin, northern Arabian Sea and a molecular and isotopic approach to constrain the carbon isotopic composition of parent methane. *Chemical Geology*, 415, 102-117. doi:10.1016/j.chemgeo.2015.09.016
- Himmler, T., Brinkmann, F., Bohrmann, G., & Peckmann, J. (2011). Corrosion patterns of seep-carbonates from the eastern Mediterranean Sea. *Terra Nova*, 23(3), 206-212. doi:https://doi.org/10.1111/j.1365-3121.2011.01000.x
- Himmler, T., Sahy, D., Martma, T., Bohrmann, G., Plaza-Faverola, A., Bünz, S., . . . Lepland, A. (2019). A 160,000-year-old history of tectonically controlled methane seepage in the Arctic. *Science Advances*, 5(8), eaaw1450. doi:doi:10.1126/sciadv.aaw1450
- Himmler, T., Smrzka, D., Zwicker, J., Kasten, S., Shapiro, R. S., Bohrmann, G., & Peckmann, J. (2018). Stromatolites below the photic zone in the northern Arabian Sea formed by calcifying chemotrophic microbial mats. *Geology*, 46(4), 339-342. doi:10.1130/g39890.1
- Hinrichs, K. U., & Boetius, A. (2003). The Anaerobic Oxidation of Methane: New Insights in Microbial Ecology and Biogeochemistry. In G. Wefer, D. Billett, D. Hebbeln, B. B. Jørgensen, M. Schlüter, & T. C. E. van Weering (Eds.), *Ocean Margin Systems* (pp. 457-477). Berlin, Heidelberg: Springer Berlin Heidelberg.
- Hoehler, T. M., Alperin, M. J., Albert, D. B., & Martens, C. S. (1994). Field and laboratory studies of methane oxidation in an anoxic marine sediment: Evidence for a methanogen-sulfate reducer consortium. *Global Biogeochemical Cycles*, 8(4), 451-463.
- Hovland, M. (2002). On the self-sealing nature of marine seeps. *Continental Shelf Research*, 22(16), 2387-2394. doi:https://doi.org/10.1016/S0278-4343(02)00063-8
- Hovland, M., & Risk, M. (2003). Do Norwegian deep-water coral reefs rely on seeping fluids? *Marine Geology*, 198, 83-96. doi:10.1016/S0025-3227(03)00096-3
- Hsu, C.-W., MacDonald, I. R., Römer, M., Pape, T., Sahling, H., Wintersteller, P., & Bohrmann, G. (2019). Characteristics and hydrocarbon seepage at the Challenger Knoll in the Sigsbee Basin, Gulf of Mexico. *Geo-Marine Letters*, 39(5), 391-399. doi:10.1007/s00367-019-00595-x
- Jørgensen, B. B., Weber, A., & Zopfi, J. (2001). Sulfate reduction and anaerobic methane oxidation in Black Sea sediments. *Deep Sea Research Part I: Oceanographic Research Papers*, 48(9), 2097-2120.

- Judd, A., & Hovland, M. (2007). Seabed Fluid Flow: The Impact on Geology, Biology and the Marine Environment.
- Kastner, M., Solomon, E., Harris, R., & Torres, M. (2014). Fluid Origins, Thermal Regimes, and Fluid and Solute Fluxes in the Forearc of Subduction Zones.
- Keul, N., Langer, G., de Nooijer, L. J., Nehrke, G., Reichart, G.-J., & Bijma, J. (2013). Incorporation of uranium in benthic foraminiferal calcite reflects seawater carbonate ion concentration. *Geochemistry, Geophysics, Geosystems*, 14(1), 102-111. doi:<https://doi.org/10.1029/2012GC004330>
- Kigoshi, K. (1971). Alpha-recoil thorium-234: dissolution into water and the uranium-234/uranium-238 disequilibrium in nature. *Science*, 173(3991), 47-48. doi:10.1126/science.173.3991.47
- Kim, S.-T., Mucci, A., & Taylor, B. E. (2007). Phosphoric acid fractionation factors for calcite and aragonite between 25 and 75 C: revisited. *Chemical Geology*, 246(3-4), 135-146.
- Klaucke, I., Berndt, C., Crutchley, G., Chi, W.-C., Lin, S., & Muff, S. (2016). Fluid venting and seepage at accretionary ridges: the Four Way Closure Ridge offshore SW Taiwan. *Geo-Marine Letters*, 36(3), 165-174. doi:10.1007/s00367-015-0431-5
- Klaucke, I., Sahling, H., Weinrebe, W., Blinova, V., Burk, D., Lursmanashvili, N., & Bohrmann, G. (2006). Acoustic investigation of cold seeps offshore Georgia, eastern Black Sea. *Marine Geology*, 231(1-4), 51-67. doi:10.1016/j.margeo.2006.05.011
- Kleypas, J. A., Mcmanus, J. W., & Menez, L. A. B. (2015). Environmental Limits to Coral Reef Development: Where Do We Draw the Line?1. *American Zoologist*, 39(1), 146-159. doi:10.1093/icb/39.1.146
- Klinkhammer, G. P., & Palmer, M. R. (1991). Uranium in the oceans: Where it goes and why. *Geochimica Et Cosmochimica Acta*, 55(7), 1799-1806. doi:[https://doi.org/10.1016/0016-7037\(91\)90024-Y](https://doi.org/10.1016/0016-7037(91)90024-Y)
- Ku, Y.-P., Chen, C.-H., Song, S.-R., Iizuka, Y., & Shen, J. J.-S. (2009). A 2 Ma record of explosive volcanism in southwestern Luzon: Implications for the timing of subducted slab steepening. *Geochemistry, Geophysics, Geosystems*, 10(6). doi:<https://doi.org/10.1029/2009GC002486>
- Kunath, P., Chi, W.-C., Berndt, C., Chen, L., Liu, C.-S., Kläschen, D., & Muff, S. (2020). A Shallow Seabed Dynamic Gas Hydrate System off SW Taiwan: Results From 3-D Seismic, Thermal, and Fluid Migration Analyses. *Journal of Geophysical Research: Solid Earth*, 125(11), e2019JB019245-T. doi:<https://doi.org/10.1029/2019JB019245>
- Kuo, M.-Y., Kang, D.-R., Chang, C.-H., Chao, C.-H., Wang, C.-C., Chen, H.-H., . . . Lin, S. (2019). New Records of Three Deep-Sea Bathymodiolus Mussels (Bivalvia: Mytilida: Mytilidae) From Hydrothermal Vent and Cold Seep in Taiwan. *Journal of Marine Science and Technology*, 27(4), 352-358.
- Kutterolf, S., Liebetrau, V., Morz, T., Freundt, A., Hammerich, T., & Garbe-Schonberg, D. (2008). Lifetime and cyclicity of fluid venting at forearc mound structures determined by tephrostratigraphy and radiometric dating of authigenic carbonates. *Geology*, 36(9), 707-710. doi:10.1130/g24806a.1
- Kvenvolden, K. A. (1993). Gas hydrates—geological perspective and global change. *Reviews of Geophysics*, 31(2), 173-187. doi:<https://doi.org/10.1029/93RG00268>
- Kvenvolden, K. A., & McMenamin, M. A. (1980). Hydrates of natural gas; a review of their geologic occurrence (825). Retrieved from <http://pubs.er.usgs.gov/publication/cir825>
- Lambeck, K., & Chappell, J. (2001). Sea Level Change Through the Last Glacial Cycle. *Science*, 292(5517), 679-686. doi:10.1126/science.1059549
- Leefmann, T., Bauermeister, J., Kronz, A., Liebetrau, V., Reitner, J., & Thiel, V. (2008). Miniaturized biosignature analysis reveals implications for the formation of cold seep carbonates at Hydrate Ridge (off Oregon, USA). *Biogeosciences*, 5(3), 731-738. doi:10.5194/bg-5-731-2008

- Leloup, J., Loy, A., Knab, N. J., Borowski, C., Wagner, M., & Jørgensen, B. B. (2007). Diversity and abundance of sulfate-reducing microorganisms in the sulfate and methane zones of a marine sediment, Black Sea. *Environmental Microbiology*, 9(1), 131-142. doi:<https://doi.org/10.1111/j.1462-2920.2006.01122.x>
- Liang, Q., Hu, Y., Feng, D., Peckmann, J., Chen, L., Yang, S., . . . Chen, D. (2017). Authigenic carbonates from newly discovered active cold seeps on the northwestern slope of the South China Sea: Constraints on fluid sources, formation environments, and seepage dynamics. *Deep Sea Research Part I: Oceanographic Research Papers*, 124, 31-41.
- Liebetrau, V., Augustin, N., Kutterolf, S., Schmidt, M., Eisenhauer, A., Garbe-Schonberg, D., & Weinrebe, W. (2014). Cold-seep-driven carbonate deposits at the Central American forearc: contrasting evolution and timing in escarpment and mound settings. *International Journal of Earth Sciences*, 103(7), 1845-1872. doi:10.1007/s00531-014-1045-2
- Liebetrau, V., Eisenhauer, A., & Linke, P. (2010). Cold seep carbonates and associated cold-water corals at the Hikurangi Margin, New Zealand: New insights into fluid pathways, growth structures and geochronology. *Marine Geology*, 272(1-4), 307-318. doi:10.1016/j.margeo.2010.01.003
- Lim, Y. C., Lin, S., Yang, T. F., Chen, Y.-G., & Liu, C.-S. (2011). Variations of methane induced pyrite formation in the accretionary wedge sediments offshore southwestern Taiwan. *Marine and Petroleum Geology*, 28(10), 1829-1837.
- Lin, C.-C., Lin, A. T.-S., Liu, C.-S., Horng, C.-S., Chen, G.-Y., & Wang, Y. (2014). Canyon-infilling and gas hydrate occurrences in the frontal fold of the offshore accretionary wedge off southern Taiwan. *Marine Geophysical Research*, 35(1), 21-35. doi:10.1007/s11001-013-9203-7
- Lin, S., Lim, Y. C., Liu, C.-S., Yang, T. F., Chen, Y.-G., Machiyama, H., . . . Fujikura, K. (2007). Formosa Ridge, A cold seep with densely populated chemosynthetic community in the passive margin, southwest of Taiwan. *Goldschmidt Conference, Cologne, Geochim. Cosmochim. Acta*, 71(15).
- Liu, C.-S., Huang, I. L., & Teng, L. S. (1997). Structural features off southwestern Taiwan. *Marine Geology*, 137(3-4), 305-319.
- Liu, C.-S., Schnurle, P., Wang, Y., San-Hsiung, C., Song-Chuen, C., & Hsuan, T.-H. (2006). Distribution and characters of gas hydrate offshore of southwestern Taiwan. *TAO: Terrestrial, Atmospheric and Oceanic Sciences*, 17(4), 615.
- Liu, S.-C., Shyu, J. B. H., & Shen, C.-C. (2021). Paleo-earthquake records of the Hengchun offshore structure, southern Taiwan, revealed by uplifted coral colonies. *Tectonophysics*, 817, 229049. doi:<https://doi.org/10.1016/j.tecto.2021.229049>
- Loher, M., Marcon, Y., Pape, T., Romer, M., Wintersteller, P., Ferreira, C. D., . . . Bohrmann, G. (2018). Seafloor sealing, doming, and collapse associated with gas seeps and authigenic carbonate structures at Venere mud volcano, Central Mediterranean. *Deep-Sea Research Part I-Oceanographic Research Papers*, 137, 76-96. doi:10.1016/j.dsr.2018.04.006
- Luff, R., & Wallmann, K. (2003). Fluid flow, methane fluxes, carbonate precipitation and biogeochemical turnover in gas hydrate-bearing sediments at Hydrate Ridge, Cascadia Margin: Numerical modeling and mass balances. *Geochimica Et Cosmochimica Acta*, 67(18), 3403-3421. doi:10.1016/s0016-7037(03)00127-3
- MacAvoy, S. E., Carney, R. S., Fisher, C. R., & Macko, S. A. (2002). Use of chemosynthetic biomass by large, mobile, benthic predators in the Gulf of Mexico. *Marine Ecology Progress Series*, 225, 65-78.
- MacDonald, I. R., Reilly, J. F., Guinasso, N. L., Brooks, J. M., Carney, R. S., Bryant, W. A., & Bright, T. J. (1990). Chemosynthetic mussels at a brine-filled pockmark in the northern Gulf of Mexico. *Science*, 248(4959), 1096-1099.

- Machiyama H., S. L., K. Fujikura, C.-Y. Huang, C.-Y. Ku, L.-H. Lin, S. Morita, T. Nunoura, W. Soh, T. Toki, and T. F. Yang. (2007). Discovery of "Hydrothermal" Chemosynthetic Community in a Cold Seep Environment, Formosa Ridge: Seafloor Observation Results from First ROV Cruise, off Southwestern Taiwan. EOS Trans. AGU, 88 (52), Fall Meet. Suppl., Abstract OS23A-1041.
- Marchitto, T., Curry, W., Lynch-Stieglitz, J., Bryan, S., Cobb, K., & Lund, D. (2014). Improved oxygen isotope temperature calibrations for cosmopolitan benthic foraminifera. *Geochimica Et Cosmochimica Acta*, 130, 1-11.
- Marcon, Y., Kelley, D., Thornton, B., Manalang, D., & Bohrmann, G. (2021). Variability of natural methane bubble release at southern hydrate ridge. *G3: Geochemistry, Geophysics, Geosystems*, 22(10).
- Marcon, Y., Ondréas, H., Sahling, H., Bohrmann, G., & Olu, K. (2014). Fluid flow regimes and growth of a giant pockmark. *Geology*, 42(1), 63-66. doi:10.1130/g34801.1
- Matsumoto, R., Okuda, Y., Hiruta, A., Tomaru, H., Takeuchi, E., Sanno, R., . . . Komatsubara, J. (2009). Formation and Collapse of Gas Hydrate Deposits in High Methane Flux Area of the Joetsu Basin, Eastern Margin of Japan Sea. *Chigaku Zasshi (journal of Geography)*, 118, 43-71. doi:10.5026/jgeography.118.43
- Mau, S., Tu, T.-H., Becker, M., dos Santos Ferreira, C., Chen, J.-N., Lin, L.-H., . . . Bohrmann, G. (2020). Methane Seeps and Independent Methane Plumes in the South China Sea Offshore Taiwan. *Frontiers in Marine Science*, 7, 543.
- Mazzini, A., Ivanov, M. K., Nermoen, A., Bahr, A., Bohrmann, G., Svensen, H., & Planke, S. (2008). Complex plumbing systems in the near subsurface: Geometries of authigenic carbonates from Dolgovskoy Mound (Black Sea) constrained by analogue experiments. *Marine and Petroleum Geology*, 25(6), 457-472. doi:https://doi.org/10.1016/j.marpetgeo.2007.10.002
- Moerz, T., Fekete, N., Kopf, A., Brückmann, W., Kreiter, S., Hühnerbach, V., . . . R. Ranero, C. (2005). Styles and productivity of mud diapirism along the Middle American margin Part II: Mound Culebra and Mounds 11, and 12 (pp. 40-76).
- Moore, J. C., & Vrolijk, P. (1992). FLUIDS IN ACCRETIONARY PRISMS. *Reviews of Geophysics*, 30(2), 113-135. doi:10.1029/92rg00201
- Mucci, A. (1983). The solubility of calcite and aragonite in seawater at various salinities, temperatures, and one atmosphere total pressure. *American Journal of Science*, 283. doi:10.2475/ajs.283.7.780
- Naehr, T., Rodriguez, N., Bohrmann, G., Paull, C., & Botz, R. (2000). 29. Methanederived authigenic carbonates associated with gas hydrate decomposition and fluid venting above the Blake Ridge Diapir. Paper presented at the Proceedings of the Ocean Drilling Program, Scientific Results.
- Naehr, T. H., Eichhubl, P., Orphan, V. J., Hovland, M., Paull, C. K., Ussler, W., . . . Greene, H. G. (2007). Authigenic carbonate formation at hydrocarbon seeps in continental margin sediments: A comparative study. *Deep-Sea Research Part II-Topical Studies in Oceanography*, 54(11-13), 1268-1291. doi:10.1016/j.dsr2.2007.04.010
- Oppo, D., De Siena, L., & Kemp, D. B. (2020). A record of seafloor methane seepage across the last 150 million years. *Scientific Reports*, 10(1), 2562. doi:10.1038/s41598-020-59431-3
- Orange, D. L., Yun, J., Maher, N., Barry, J., & Greene, G. (2002). Tracking California seafloor seeps with bathymetry, backscatter and ROVs. *Continental Shelf Research*, 22(16), 2273-2290. doi:10.1016/s0278-4343(02)00054-7
- Pape, T., & Bohrmann, G. (2022). Shallow Gas Hydrates Associated to Pockmarks in the Northern Congo Deep-Sea Fan, SW Africa World Atlas of Submarine Gas Hydrates in Continental Margins (pp. 359-371): Springer.

- Pape, T., Buenz, S., Hong, W. L., Torres, M. E., Riedel, M., Panieri, G., . . . Wallmann, K. (2020). Origin and transformation of light hydrocarbons ascending at an active pockmark on Vestnesa Ridge, Arctic Ocean. *Journal of Geophysical Research: Solid Earth*, 125(1), e2018JB016679.
- Pape, T., Haeckel, M., Riedel, M., Kölling, M., Schmidt, M., Wallmann, K., & Bohrmann, G. (2020). Formation pathways of light hydrocarbons in deep sediments of the Danube deep-sea fan, Western Black Sea. *Marine and Petroleum Geology*, 122, 104627.
- Papenmeier, S., Darr, A., Feldens, P., & Michaelis, R. (2020). Hydroacoustic Mapping of Geogenic Hard Substrates: Challenges and Review of German Approaches. *Geosciences*, 10(3), 100.
- Paull, C. K., Caress, D. W., Thomas, H., Lundsten, E., Anderson, K., Gwiazda, R., . . . Herguera, J. C. (2015). Seafloor geomorphic manifestations of gas venting and shallow subbottom gas hydrate occurrences. *Geosphere*, 11(2), 491-513. doi:10.1130/ges01012.1
- Paull, C. K., Chanton, J. P., Neumann, A. C., Coston, J. A., Martens, C. S., & Showers, W. (1992). Indicators of Methane-Derived Carbonates and Chemosynthetic Organic Carbon Deposits: Examples from the Florida Escarpment. *Palaios*, 7(4), 361-375. doi:10.2307/3514822
- Paull, C. K., Ussler III, W., Borowski, W. S., & Spiess, F. N. (1995). Methane-rich plumes on the Carolina continental rise: Associations with gas hydrates. *Geology*, 23(1), 89-92.
- Paull, C. K., Ussler, W., Greene, H. G., Barry, J., & Keaten, R. (2005). Bioerosion by chemosynthetic biological communities on Holocene submarine slide scars. *Geo-Marine Letters*, 25(1), 11-19. doi:10.1007/s00367-004-0184-z
- Peckmann, J., Goedert, J. L., Thiel, V., Michaelis, W., & Reitner, J. (2002). A comprehensive approach to the study of methane-seep deposits from the Lincoln Creek Formation, western Washington State, USA. *Sedimentology*, 49(4), 855-873. doi:10.1046/j.1365-3091.2002.00474.x
- Peckmann, J., Reimer, A., Luth, U., Luth, C., Hansen, B. T., Heinicke, C., . . . Reitner, J. (2001). Methane-derived carbonates and authigenic pyrite from the northwestern Black Sea. *Marine Geology*, 177(1-2), 129-150. doi:10.1016/s0025-3227(01)00128-1
- Peckmann, J., & Thiel, V. (2004). Carbon cycling at ancient methane-seeps. *Chemical Geology*, 205(3), 443-467. doi:https://doi.org/10.1016/j.chemgeo.2003.12.025
- Peckmann, J., Thiel, V., Michaelis, W., Clari, P., Gaillard, C., Martire, L., & Reitner, J. (1999). Cold seep deposits of Beauvoisin (Oxfordian; southeastern France) and Marmorito (Miocene; northern Italy): microbially induced authigenic carbonates. *International Journal of Earth Sciences*, 88(1), 60-75. doi:10.1007/s005310050246
- Ritger, S., Carson, B., & Suess, E. (1987). METHANE-DERIVED AUTHIGENIC CARBONATES FORMED BY SUBDUCTION INDUCED PORE-WATER EXPULSION ALONG THE OREGON WASHINGTON MARGIN. *Geological Society of America Bulletin*, 98(2), 147-156. doi:10.1130/0016-7606(1987)98<147:macfbs>2.0.co;2
- Roberts, H. H., & Aharon, P. (1994). HYDROCARBON-DERIVED CARBONATE BUILDUPS OF THE NORTHERN GULF-OF-MEXICO CONTINENTAL-SLOPE - A REVIEW OF SUBMERSIBLE INVESTIGATIONS. *Geo-Marine Letters*, 14(2-3), 135-148. doi:10.1007/bf01203725
- Roberts, H. H., Feng, D., & Joye, S. B. (2010). Cold-seep carbonates of the middle and lower continental slope, northern Gulf of Mexico. *Deep-Sea Research Part II-Topical Studies in Oceanography*, 57(21-23), 2040-2054. doi:10.1016/j.dsr2.2010.09.003
- Roberts, J., Wheeler, A., Freiwald, A., & Cairns, S. (2009). Cold Water Corals: The Biology and Geology of Deep-Sea Coral Habitats. *Cold-Water Corals: The Biology and Geology of Deep-Sea Coral Habitats*, 1-350. doi:10.1017/CBO9780511581588



- Robinson, L. F., Belshaw, N. S., & Henderson, G. M. (2004). U and Th concentrations and isotope ratios in modern carbonates and waters from the Bahamas. *Geochimica Et Cosmochimica Acta*, 68(8), 1777-1789.
- Robinson, L. F., Henderson, G. M., Hall, L., & Matthews, I. (2004). Climatic control of riverine and seawater uranium-isotope ratios. *Science*, 305(5685), 851-854.
- Roder, C., Berumen, M. L., Bouwmeester, J., Papathanassiou, E., Al-Suwailem, A., & Voolstra, C. R. (2013). First biological measurements of deep-sea corals from the Red Sea. *Scientific Reports*, 3(1), 2802. doi:10.1038/srep02802
- Römer, M., Sahling, H., Pape, T., Bohrmann, G., & Spieß, V. (2012). Quantification of gas bubble emissions from submarine hydrocarbon seeps at the Makran continental margin (offshore Pakistan). *Journal of Geophysical Research: Oceans*, 117(C10).
- Römer, M., Sahling, H., Pape, T., dos Santos Ferreira, C., Wenzhöfer, F., Boetius, A., & Bohrmann, G. (2014). Methane fluxes and carbonate deposits at a cold seep area of the Central Nile Deep Sea Fan, Eastern Mediterranean Sea. *Marine Geology*, 347, 27-42. doi:https://doi.org/10.1016/j.margeo.2013.10.011
- Rubin-Blum, M., Antony, C. P., Borowski, C., Sayavedra, L., Pape, T., Sahling, H., . . . Dubilier, N. (2017). Short-chain alkanes fuel mussel and sponge *Cycloclostus* symbionts from deep-sea gas and oil seeps. *Nature Microbiology*, 2(8), 17093. doi:10.1038/nmicrobiol.2017.93
- Ruppel, C. D., & Kessler, J. D. (2017). The interaction of climate change and methane hydrates. *Reviews of Geophysics*, 55(1), 126-168. doi:https://doi.org/10.1002/2016RG000534
- Russell, A. D., Emerson, S., Nelson, B. K., Erez, J., & Lea, D. W. (1994). Uranium in foraminiferal calcite as a recorder of seawater uranium concentrations. *Geochimica Et Cosmochimica Acta*, 58(2), 671-681. doi:https://doi.org/10.1016/0016-7037(94)90497-9
- Sahling, H., Bohrmann, G., Spiess, V., Bialas, J., Breitzke, M., Ivanov, M., . . . Schneider, R. (2008). Pockmarks in the Northern Congo Fan area, SW Africa: Complex seafloor features shaped by fluid flow. *Marine Geology*, 249(3-4), 206-225. doi:10.1016/j.margeo.2007.11.010
- Sahling, H., Borowski, C., Escobar-Briones, E., Gaytán-Caballero, A., Hsu, C. W., Loher, M., . . . Bohrmann, G. (2016). Massive asphalt deposits, oil seepage, and gas venting support abundant chemosynthetic communities at the Campeche Knolls, southern Gulf of Mexico. *Biogeosciences*, 13(15), 4491-4512. doi:10.5194/bg-13-4491-2016
- Sahling, H., Masson, D. G., Ranero, C. R., Hühnerbach, V., Weinrebe, W., Klauke, I., . . . Suess, E. (2008). Fluid seepage at the continental margin offshore Costa Rica and southern Nicaragua. *Geochemistry, Geophysics, Geosystems*, 9(5). doi:https://doi.org/10.1029/2008GC001978
- Sahling, H., Rickert, D., Lee, R. W., Linke, P., & Suess, E. (2002). Macrofaunal community structure and sulfide flux at gas hydrate deposits from the Cascadia convergent margin, NE Pacific. *Marine Ecology Progress Series*, 231, 121-138.
- Sato, H., Hayashi, K., Ogawa, Y., & Kawamura, K. (2012). Geochemistry of deep sea sediments at cold seep sites in the Nankai Trough: Insights into the effect of anaerobic oxidation of methane. *Marine Geology*, 323, 47-55. doi:10.1016/j.margeo.2012.07.013
- Schnürle, P., Liu, C.-S., Lin, A. T., & Lin, S. (2011). Structural controls on the formation of BSR over a diapiric anticline from a dense MCS survey offshore southwestern Taiwan. *Marine and Petroleum Geology*, 28(10), 1932-1942.
- Scholl, D. W., & von Huene, R. (2007). Crustal recycling at modern subduction zones applied to the past—Issues of growth and preservation of continental basement crust, mantle geochemistry, and supercontinent reconstruction. *Geological Society of America Memoirs*, 200, 9-32.

- Scholz, D., & Mangini, A. (2007). How precise are U-series coral ages? *Geochimica Et Cosmochimica Acta*, 71(8), 1935-1948.
- Shakhova, N., Semiletov, I., Sergienko, V., Lobkovsky, L., Yusupov, V., Salyuk, A., . . . Panteleev, G. (2015). The East Siberian Arctic Shelf: towards further assessment of permafrost-related methane fluxes and role of sea ice. *Philosophical Transactions of the Royal Society A: Mathematical, Physical and Engineering Sciences*, 373(2052), 20140451.
- Sherwood, O. A., Travers, P. D., & Dolan, M. P. (2013). Chapter 15 - Compound-Specific Stable Isotope Analysis of Natural and Produced Hydrocarbon Gases Surrounding Oil and Gas Operations. In I. Ferrer & E. M. Thurman (Eds.), *Comprehensive Analytical Chemistry* (Vol. 61, pp. 347-372): Elsevier.
- Sibuet, J.-C., Zhao, M., Wu, J., & Lee, C.-S. (2021). Geodynamic and plate kinematic context of South China Sea subduction during Okinawa trough opening and Taiwan orogeny. *Tectonophysics*, 817, 229050. doi:<https://doi.org/10.1016/j.tecto.2021.229050>
- Sibuet, M., & Olu, K. (1998). Biogeography, biodiversity and fluid dependence of deep-sea cold-seep communities at active and passive margins. *Deep Sea Research Part II: Topical Studies in Oceanography*, 45(1), 517-567. doi:[https://doi.org/10.1016/S0967-0645\(97\)00074-X](https://doi.org/10.1016/S0967-0645(97)00074-X)
- Skarke, A., Ruppel, C., Kodis, M., Brothers, D., & Lobecker, E. (2014). Widespread methane leakage from the sea floor on the northern US Atlantic margin. *Nature Geoscience*, 7(9), 657-661. doi:10.1038/ngeo2232
- Sloan Jr, E. D., & Koh, C. A. (2007). *Clathrate hydrates of natural gases*: CRC press.
- Smrzka, D., Kraemer, S. M., Zwicker, J., Birgel, D., Fischer, D., Kasten, S., . . . Peckmann, J. (2015). Constraining silica diagenesis in methane-seep deposits. *Palaeogeography, Palaeoclimatology, Palaeoecology*, 420, 13-26. doi:<https://doi.org/10.1016/j.palaeo.2014.12.007>
- Smrzka, D., Zwicker, J., Klügel, A., Monien, P., Bach, W., Bohrmann, G., & Peckmann, J. (2016). Establishing criteria to distinguish oil-seep from methane-seep carbonates. *Geology*, 44(8), 667-670. doi:10.1130/g38029.1
- Smrzka, D., Zwicker, J., Lu, Y., Sun, Y., Feng, D., Monien, P., . . . Peckmann, J. (2021). Trace element distribution in methane-seep carbonates: The role of mineralogy and dissolved sulfide. *Chemical Geology*, 580, 120357. doi:<https://doi.org/10.1016/j.chemgeo.2021.120357>
- Smrzka, D., Zwicker, J., Misch, D., Walkner, C., Gier, S., Monien, P., . . . Peckmann, J. (2019). Oil seepage and carbonate formation: A case study from the southern Gulf of Mexico. *Sedimentology*, 66(6), 2318-2353. doi:<https://doi.org/10.1111/sed.12593>
- Solomon, E. A., Kastner, M., Jannasch, H., Robertson, G., & Weinstein, Y. (2008). Dynamic fluid flow and chemical fluxes associated with a seafloor gas hydrate deposit on the northern Gulf of Mexico slope. *Earth and Planetary Science Letters*, 270(1-2), 95-105. doi:10.1016/j.epsl.2008.03.024
- Spötl, C., & Boch, R. (2019). Chapter 128 - Uranium series dating of speleothems. In W. B. White, D. C. Culver, & T. Pipan (Eds.), *Encyclopedia of Caves* (Third Edition) (pp. 1096-1102): Academic Press.
- Stalling, D., Westerhoff, M., & Hege, H.-C. (2005). 38 - Amira: A Highly Interactive System for Visual Data Analysis. In C. D. Hansen & C. R. Johnson (Eds.), *Visualization Handbook* (pp. 749-LXXVIII). Burlington: Butterworth-Heinemann.
- Stirling, C. H., Andersen, M. B., Warthmann, R., & Halliday, A. N. (2015). Isotope fractionation of <sup>238</sup>U and <sup>235</sup>U during biologically-mediated uranium reduction. *Geochimica Et Cosmochimica Acta*, 163, 200-218. doi:<https://doi.org/10.1016/j.gca.2015.03.017>

- Stylo, M., Neubert, N., Wang, Y., Monga, N., Romaniello, S. J., Weyer, S., & Bernier-Latmani, R. (2015). Uranium isotopes fingerprint biotic reduction. *Proceedings of the National Academy of Sciences*, 112(18), 5619-5624. doi:doi:10.1073/pnas.1421841112
- Suess, E. (2014). Marine cold seeps and their manifestations: geological control, biogeochemical criteria and environmental conditions. *International Journal of Earth Sciences*, 103(7), 1889-1916. doi:10.1007/s00531-014-1010-0
- Suess, E. (2018). Marine Cold Seeps: Background and Recent Advances. In H. Wilkes (Ed.), *Hydrocarbons, Oils and Lipids: Diversity, Origin, Chemistry and Fate* (pp. 1-21). Cham: Springer International Publishing.
- Suess, E., Bohrmann, G., Von Huene, R., Linke, P., Wallmann, K., Lammers, S., . . . Orange, D. (1998). Fluid venting in the eastern Aleutian subduction zone. *Journal of Geophysical Research: Solid Earth*, 103(B2), 2597-2614.
- Suess, E., Carson, B., Ritger, S. D., Moore, J. C., Jones, M. L., Kulm, L. D., & Cochrane, G. R. (1985). Biological communities at vent sites along the subduction zone off Oregon. *Bulletin of the Biological Society of Washington*, 6, 475-484.
- Suess, E., Torres, M., Bohrmann, G., Collier, R., Rickert, D., Goldfinger, C., . . . Heeschen, K. (2001). Sea floor methane hydrates at Hydrate Ridge, Cascadia margin. *GEOPHYSICAL MONOGRAPH-AMERICAN GEOPHYSICAL UNION*, 124, 87-98.
- Sun, N., Brandon, A. D., Forman, S. L., Waters, M. R., & Befus, K. S. (2020). Volcanic origin for Younger Dryas geochemical anomalies ca. 12,900 cal B.P. *Science Advances*, 6(31), eaax8587. doi:doi:10.1126/sciadv.aax8587
- Sun, W., Jayaraman, S., Chen, W., Persson, K. A., & Ceder, G. (2015). Nucleation of metastable aragonite  $\text{CaCO}_3$  in seawater. *Proceedings of the National Academy of Sciences*, 112(11), 3199-3204. doi:doi:10.1073/pnas.1423898112
- Swart, P. K. (2015). The geochemistry of carbonate diagenesis: The past, present and future. *Sedimentology*, 62(5), 1233-1304. doi:https://doi.org/10.1111/sed.12205
- Teichert, B. M. A., Eisenhauer, A., Bohrmann, G., Haase-Schramm, A., Bock, B., & Linke, P. (2003). U/Th systematics and ages of authigenic carbonates from Hydrate Ridge, Cascadia Margin: recorders of fluid flow variations. *Geochimica Et Cosmochimica Acta*, 67(20), 3845-3857. doi:https://doi.org/10.1016/S0016-7037(03)00128-5
- Teichert, B. M. A., Gussone, N., Eisenhauer, A., & Bohrmann, G. (2005). Clathrites: Archives of near-seafloor pore-fluid evolution ( $\delta^{44}\text{Ca}$ ,  $\delta^{13}\text{C}$ ,  $\delta^{18}\text{O}$ ) in gas hydrate environments. *Geology*, 33(3), 213-216. doi:10.1130/g21317.1
- Teng, L. S. (1990). Geotectonic evolution of late Cenozoic arc-continent collision in Taiwan. *Tectonophysics*, 183(1-4), 57-76.
- Thiel, V., Peckmann, J., Richnow, H. H., Luth, U., Reitner, J., & Michaelis, W. (2001). Molecular signals for anaerobic methane oxidation in Black Sea seep carbonates and a microbial mat. *Marine Chemistry*, 73(2), 97-112. doi:10.1016/s0304-4203(00)00099-2
- Thompson, W. G., Allen Curran, H., Wilson, M. A., & White, B. (2011). Sea-level oscillations during the last interglacial highstand recorded by Bahamas corals. *Nature Geoscience*, 4(10), 684-687.
- Timmis, K. N., McGenity, T., Van Der Meer, J. R., & de Lorenzo, V. (2010). *Handbook of hydrocarbon and lipid microbiology*: Springer Berlin.
- Titschack, J., Baum, D., Matsuyama, K., Boos, K., Färber, C., Kahl, W. A., . . . Stock, S. R. (2018). Ambient occlusion – A powerful algorithm to segment shell and skeletal intrapores in computed tomography data. *Computers & Geosciences*, 115, 75-87. doi:https://doi.org/10.1016/j.cageo.2018.03.007
- Tong, H., Feng, D., Cheng, H., Yang, S., Wang, H., Min, A. G., . . . Chen, D. (2013). Authigenic carbonates from seeps on the northern continental slope of the South China Sea: New insights into fluid sources and geochronology. *Marine and Petroleum Geology*, 43, 260-271. doi:https://doi.org/10.1016/j.marpetgeo.2013.01.011

- Torres, M. E., Bohrmann, G., & Suess, E. (1996). Authigenic barites and fluxes of barium associated with fluid seeps in the Peru subduction zone. *Earth and Planetary Science Letters*, 144(3-4), 469-481.
- Tseng, Y., Römer, M., Lin, S., Pape, T., Berndt, C., Chen, T. T., . . . Bohrmann, G. (2022). Yam Seep at Four-Way Closure Ridge – a prominent active gas seep system at the accretionary wedge SW offshore Taiwan. *International Journal of Earth Sciences*, Accepted.
- Tseng, Y., Schröder-Ritzrau, A., Lin, S., Frank, N., & Bohrmann, G. (2020). Authigenic Seep Carbonates of the South China Sea – Archives for Geochemical Cycling and Geodynamic Activity.
- Urey, H. C. (1947). The thermodynamic properties of isotopic substances. *Journal of the Chemical Society (Resumed)*, 562-581.
- Ustaszewski, K., Wu, Y.-M., Suppe, J., Huang, H.-H., Chang, C.-H., & Carena, S. (2012). Crust–mantle boundaries in the Taiwan–Luzon arc-continent collision system determined from local earthquake tomography and 1D models: implications for the mode of subduction polarity reversal. *Tectonophysics*, 578, 31-49.
- Vacelet, J., Boury-Esnault, N., Fiala-Medioni, A., & Fisher, C. (1995). A methanotrophic carnivorous sponge. *Nature: International Weekly Journal of Science*(6547).
- Veizer, J., Bruckschen, P., Pawellek, F., Diener, A., Podlaha, O. G., Carden, G. A. F., . . . Ala, D. (1997). Oxygen isotope evolution of Phanerozoic seawater. *Palaeogeography, Palaeoclimatology, Palaeoecology*, 132(1), 159-172. doi:[https://doi.org/10.1016/S0031-0182\(97\)00052-7](https://doi.org/10.1016/S0031-0182(97)00052-7)
- Waelbroeck, C., Labeyrie, L., Michel, E., Duplessy, J. C., McManus, J. F., Lambeck, K., . . . Labracherie, M. (2002). Sea-level and deep water temperature changes derived from benthic foraminifera isotopic records. *Quaternary Science Reviews*, 21(1-3), 295-305. doi:[10.1016/s0277-3791\(01\)00101-9](https://doi.org/10.1016/s0277-3791(01)00101-9)
- Wang, B., Du, Z., Luan, Z., Zhang, X., Wang, M., Wang, X., . . . Yan, J. (2021). Seabed features associated with cold seep activity at the Formosa Ridge, South China Sea: Integrated application of high-resolution acoustic data and photomosaic images. *Deep Sea Research Part I: Oceanographic Research Papers*, 177, 103622. doi:<https://doi.org/10.1016/j.dsr.2021.103622>
- Wang, C.-H., & Burnett, W. C. (1990). Holocene Mean Uplift Rates Across an Active Plate-Collision Boundary in Taiwan. *Science*, 248(4952), 204-206.
- Wang, X., Johnson, T. M., & Lundstrom, C. C. (2015). Isotope fractionation during oxidation of tetravalent uranium by dissolved oxygen. *Geochimica Et Cosmochimica Acta*, 150, 160-170. doi:<https://doi.org/10.1016/j.gca.2014.12.007>
- Wefing, A.-M., Arps, J., Blaser, P., Wienberg, C., Hebbeln, D., & Frank, N. (2017). High precision U-series dating of scleractinian cold-water corals using an automated chromatographic U and Th extraction. *Chemical Geology*, 475, 140-148. doi:<https://doi.org/10.1016/j.chemgeo.2017.10.036>
- Wei, J., Li, J., Wu, T., Zhang, W., Li, J., Wang, J., . . . Chen, W. (2020). Geologically controlled intermittent gas eruption and its impact on bottom water temperature and chemosynthetic communities—A case study in the “HaiMa” cold seeps, South China Sea. *Geological Journal*, 55(9), 6066-6078. doi:<https://doi.org/10.1002/gj.3780>
- Wei, K.-Y., Chiu, T.-C., & Chen, Y.-G. (2003). Toward establishing a maritime proxy record of the East Asian summer monsoons for the late Quaternary. *Marine Geology*, 201(1), 67-79. doi:[https://doi.org/10.1016/S0025-3227\(03\)00209-3](https://doi.org/10.1016/S0025-3227(03)00209-3)
- Wellington, G. M., Dunbar, R. B., & Merlen, G. (1996). Calibration of stable oxygen isotope signatures in Galápagos corals. *Paleoceanography*, 11(4), 467-480. doi:<https://doi.org/10.1029/96PA01023>

- Weyer, S., Anbar, A. D., Gerdes, A., Gordon, G. W., Algeo, T. J., & Boyle, E. A. (2008). Natural fractionation of  $^{238}\text{U}/^{235}\text{U}$ . *Geochimica Et Cosmochimica Acta*, 72(2), 345-359. doi:<https://doi.org/10.1016/j.gca.2007.11.012>
- Whiticar, M. J. (1999). Carbon and hydrogen isotope systematics of bacterial formation and oxidation of methane. *Chemical Geology*, 161(1), 291-314. doi:[https://doi.org/10.1016/S0009-2541\(99\)00092-3](https://doi.org/10.1016/S0009-2541(99)00092-3)
- Whiticar, M. J., Faber, E., & Schoell, M. (1986). Biogenic methane formation in marine and freshwater environments:  $\text{CO}_2$  reduction vs. acetate fermentation—Isotope evidence. *Geochimica Et Cosmochimica Acta*, 50(5), 693-709. doi:[https://doi.org/10.1016/0016-7037\(86\)90346-7](https://doi.org/10.1016/0016-7037(86)90346-7)
- Wiedicke, M., & Weiss, W. (2006). Stable carbon isotope records of carbonates tracing fossil seep activity off Indonesia. *Geochemistry Geophysics Geosystems*, 7. doi:[10.1029/2006gc001292](https://doi.org/10.1029/2006gc001292)
- Yu, H.-S., & Chang, J.-F. (2002). The Penghu submarine canyon off southwestern Taiwan: Morphology and origin. *Terrestrial Atmospheric and Oceanic Sciences*, 13(4), 547-562.
- Zwicker, J., Smrzka, D., Gier, S., Goedert, J. L., & Peckmann, J. (2015). Mineralized conduits are part of the uppermost plumbing system of Oligocene methane-seep deposits, Washington State (USA). *Marine and Petroleum Geology*, 66, 616-630. doi:<https://doi.org/10.1016/j.marpetgeo.2015.05.035>
- Zwicker, J., Smrzka, D., Himmler, T., Monien, P., Gier, S., Goedert, J., & Peckmann, J. (2018). Rare earth elements as tracers for microbial activity and early diagenesis: a new perspective from carbonate cements of ancient methane-seep deposits. *Chemical Geology*, 501, 77-85.

## Acknowledgments

Before concluding this thesis, I would like to thank my supervising professor Prof. Dr. Gerhard Bohrmann, and second reviewer Dr. Ingo Klaucke; colleagues in Heidelberg Dr. Andrea Schröder-Ritzrau and Prof. Dr. Norbert Frank; teacher in Taiwan: Dr. Saulwood Lin; my GLOMAR committee members, Dr. Andreas Klügel, Dr. Miriam Römer and Dr. Thomas Pape; working group's postdoc: Dr. Daniel Smrzka. I am truly grateful for your scientific supports and guidance and suggestions on other off-topic issues. Also, many thanks to my wonderful colleagues: Janice, Vicky, Nina, Meggie, Katharina and Angelika; former colleagues, Steffie and Ines; friends in Bremen: Lena, Matthias, Katharine, Sina, Thorsten, Connie, Bryan, Muhan, Mu-Han, A-Ling, Kai Jing, A-Bei, TK, Jian-min; a good old friend: Wei Fang. Thank you all for creating such a pleasant atmosphere scientifically and socially during my PhD, during the research cruises and during my time in Bremen. Last but not the least, my family and friends in Taiwan: my parents, grandma, my brothers and Amber for providing me unconditional love and be my heartfelt support. And also, my lovely friends, Sophia, En-min, Sunny, Chick, Palmela, and Sandy. Thanks to your faithful trust, I was able to complete this thesis.

This year, at the age of 32, I am finishing this thesis after four years living in Germany. Looking back to these times, or even back to ten years ago since I decided to study “ocean”, from the age of 22, I can recall so many memories. Most of the time, I feel like I was constantly on my way to somewhere without a clear destination. Fortunately, along the whole journey from Taipei to Munich, from Munich to Bremen and from Bremen to Heidelberg, to South China Sea, to Antarctic Ocean, to Mediterranean Sea, I had met so many kind people. Those memories with snow, whales and crazy weather, those people offering me cakes and even more cakes, those time we sitting in the office and praising the lovely weather in Bremen (especially in January and February) are all so remarkable. However, with the completion of this thesis, I know I'm ready to go ashore.

This trip, the four years of the doctoral program, I learned that there are far more unknown than we know. And perhaps this is the thing that writing this thesis had taught me. It might take years and years for scientist to revealed a question and takes longer time to observe and to have the results. By the time to conclude the finding, the results might be however perceived as limited in time and space within our eyesight. The development of technology, newer research methods, and newly discovered research sites are either verify the conclusion of the past or may revealing the previous misunderstanding. One of the most important things I had learned in the process

of completing my doctoral dissertation is that one should never give up. Results may not be perfect, but it's the process that matter. The process that we had been through, we recorded it faithfully and then we are ready to move on.

In the meantime, I would like to thank DAAD for the support of the four-year scholarship.

## 致謝 Acknowledgments in Mandarin

在這本論文結尾以前，我想要感謝指導教授傑哈；台灣的老師林曉武；海德堡大學德安德烈雅和諾貝特；工作團隊的博士後們：丹尼爾、米力安、湯瑪士、卡塔琳娜；同事：雅妮絲、薇琪、妮娜、美姬、安潔莉卡；前同事兼好友，史黛妃，依內斯；其他在布萊梅的好朋友們：麗娜、馬提亞斯、卡特琳娜、西娜、托斯坦、康寧、布萊恩、睦涵、牧函、阿令、凱晶、阿北、之青、又軒、TK、介民。還有在法蘭克福的摯友維方。最後，給我底氣和勇氣的在台灣和家人、伴侶和朋友：我的父母、阿罵、弟弟們、阿淳、炯糞、妍旻、芙雯、小雞、小皮、綉綦。謝謝你們對我的信任和支持，這本論文才得以完成。

今年 32 歲的我，花了四年完成了這本論文。回想這四年，又甚至是從 22 到 32 這十年，很難去講述經歷了些甚麼。腦袋滿滿的回憶，只是有一種總是在移動，甚至載浮載沉感覺。然而這次隨著這本論文的完成，感覺像是真正要上岸了。好像 22 歲那年，我看著太平洋就這樣從花蓮出海了，而且一直都沒回去過。很幸運的，這一路上，從倫敦到台北，從台北到慕尼黑，再從台北到布萊梅甚至去了海德堡。在這些城市裡，與我相遇的那些人們，那一張張善良的臉，給予我幫助，那些大雪的回憶，讓我驚嘆著。去了好多地方，碰到了好多好人，頭髮白了好多，威溪河划了好幾遍，還划到了威尼斯，許多時刻被簇擁著，有時也會失落孤獨。

這一趟，博士班四年，發覺我懂得最多的就是那些無解的問題的存在。但這或許就是努力完成這本博士論文唯一教會我的事情：問題往往沒有標準答案。一個問題，需要好幾年的時間去驗證與了解，常常難以輕易下結論，即使有了結論，也有可能只是受限時間和空間的認知。隨著時間，科技的發展，更新的研究方法，新發現的研究地點來驗證過往的鐵證如山都可能只是誤會一場。完成博士論文的過程中我學會最重要的是，即使千頭萬緒，但千萬不能放棄。即使可能不夠完美，但此時此刻得出來的結果，在詳細的討論和誠實地記錄之後才有機會在往後被了解，這些問題在未來才有被突破的可能。

同時，以此文感謝 DAAD 四年獎學金的支持。



## Appendix

Conference contribution

Virtual oral contribution to the Goldschmidt Conference, 21-26 June 2020.

### **Authigenic seep carbonates of the South China Sea - archives for geochemical cycling and geodynamic activity**

YITING TSENG<sup>1\*</sup>, ANDREA SCHRÖDER-RITZRAU<sup>2</sup>, SAULWOOD LIN<sup>3</sup>, NORBERT FRANK<sup>2</sup>, GERHARD BOHRMANN<sup>1</sup>

<sup>1</sup>MARUM, Center of Environmental Sciences, University of Bremen, Germany (\*correspondence: ytseng@marum.de)

<sup>2</sup>Institute of Environmental Physics, University Heidelberg, Germany

<sup>3</sup>Institute of Oceanography, National Taiwan University, Taiwan

A continuous 4.9-meter-long authigenic carbonate core was drilled on board R/V Sonne (SO266) at a water depth of 1347 m, using the portable MARUM drilling system MeBo200. The core was drilled at the YAM cold seep field, offshore SW Taiwan, where active seepage is ongoing and a carbonate paved seafloor is located and exposed at the northern top of the accretionary ridge, known as Four Way Closure Ridge. 78 flare sites were observed over the pavement area (~40,000 m<sup>2</sup>). Within the carbonate core, cemented shells, aragonites (~37.7%) and micrites (~62.3%) can be distinguished. Cemented matrixs and veins consist of mainly pure aragonite. Results from 52 aragonite U-Th dating show the absolute chronology from  $2.5 \pm 0.18$  ka to  $33.62 \pm 0.08$  ka BP, indicating the precipitation of carbonate via anaerobic oxidation of methane (AOM). AOM had been dominated at the site archiving the methane emanation variations throughout Late Quaternary. Calculated initial  $^{234}\text{U}/^{238}\text{U}$  activity ratios ( $\delta^{234}\text{U}_i$ ) range between  $128.8\text{‰} \pm 1.8\text{‰}$  and  $153.4\text{‰} \pm 5.2\text{‰}$  (mean  $140.4\text{‰}$ , std. dev.  $5.3\text{‰}$ ). They reveal marine  $\delta^{234}\text{U}$  values in the range from modern seawater ( $146.8 \pm 0.1\text{‰}$ , [1]), as well as modern and last glacial values as documented e.g. in cold water corals (modern  $146.7 \pm 0.4\text{‰}$ , last glacial  $140.6 \pm 0.9\text{‰}$ , [2]). These results indicate, that we not only acquire the seepage chronology but also the direct correlation of paleocean scenario from authigenic carbonate. Additionally, certain unconformities in the precipitation rings occurred at the depth of 338 cmbsf (age ~10 to 26 ka) and 403 cmbsf (age ~20 to 26 ka), showing cracks and the introduced of lateral aragonite vein precipitation. These structures imply the potential of tremendous physical forcing at a certain time and causing the non-continuous precipitation results.

[1]Andersen, M.B., et al. (2010) *Geochem. Geophys. Geosyst.* 11(12). [2]Wefing A.M. et al. (2017) *Chem. Geol.* 475: 140-148.

Oral contribution to EGU 2022, 23–27 May 2022, Vienna, Austria.

The MARUM graduate school GLOMAR and Prof. Dr. Gerhard Bohrmann is thanked for funding to attend this conference.

**The YAM seep area – an active carbonate-paved gas seep field at the accretionary margin SW offshore Taiwan**

Yiting Tseng<sup>1</sup>, Miriam Römer<sup>1</sup>, Saulwood Lin<sup>2</sup>, Thomas Pape<sup>1</sup>, Christian Berndt<sup>3</sup>, Tzu-Ting Chen<sup>1</sup>,  
Gerhard Bohrmann<sup>1</sup>

<sup>1</sup>MARUM, Center for Marine Environmental Sciences and Department of Geosciences University of Bremen, Klagenfurter Str., 28359 Bremen, Germany

<sup>2</sup>Institute of Oceanography, National Taiwan University, Roosevelt Road, 10617 Taipei, Taiwan

<sup>3</sup>GEOMAR, Helmholtz-Zentrum for Ocean Research Kiel, Wischhofstr. 1-3, 24148 Kiel, Germany

The YAM seep area is an active gas seep region among the widespread seep sites offshore south-western Taiwan. The seep area covers a seafloor region of 49,000 m<sup>2</sup> at the northern crest of Four-Way Closure Ridge in 1,347 m water depth. During several research cruises (ORI-1163, SO266), shipborne and AUV-related hydro-acoustic investigations revealed that the area of seepage is well documented by high backscatter and a changing micro-bathymetry between rough and flat in the otherwise very flat seabed in the area.

During expedition SO266, RV Sonne, gas emission sites were observed at the center and eastern flank of the area using ship-borne multi-beam data in the water column. Seawater methane concentrations above the seafloor were collected from the middle west to east of the central transect, revealing concentrations ranging 5.5-18.2 nmol/L with general higher methane concentrations at the rim of the area. Authigenic carbonate samples were collected during gravity coring and MeBo drilling. MeBo drilling was stopped below 5 mbsf because of continuous release of free gas out of the borehole. Carbon isotope measurements of the carbonates showed  $\delta^{13}\text{C}$  values between -38.25 to -52.17 ‰, indicating a mixing of biogenic and thermogenic gas in the methane-derived carbonates. Seismic investigations of the Four-Way Closure Ridge show a well-defined fault below the ridge crest which extends from below the gas hydrate stability zone to the seafloor and acts as a pathway for the methane ascent to the seafloor.

Seafloor observation using a TV-sled showed a seafloor paved by carbonate rocks consisting of different featured crusts, slabs, and irregular build-ups. Thin-layered crusts were mainly observed at the paved area's rim, while thick-layered slabs and free-standing build-ups were the main features at the elevated region. Chemosynthetic communities, like mussels and clams, mainly were observed within certain carbonate fractures. At the same time, other animals, bacterial mats, and tube worms are presented generally along the whole survey path among the rough seep area. Hydro-acoustic data correlated with visual observation results indicate wide variation through the region of the seep area. Based on our interpretation, the YAM seep area developed over a longer time at the crest of the accretionary ridge, seepage, uplifting of the ridge, tectonic fracturing, and seafloor erosion highly influenced the seafloor manifestation.

Cruise participation

**2018: SO266 (34 days) TAIDRILL**

Taiwanese-German Expedition to study the influence of tectonic processes on hydrate distribution and

dynamics southwest of Taiwan

**2019: PS119 (48 days)**

Seeps and vents from trench to the back-arc of the sandwich plate - Fluid and gas circulation of mid-ocean ridge

**2020: SO278 (50 days)**

Fluid-rock interaction at the backstop to the Mediterranean Ridge Accretionary Complex South of Crete

Affirmation in lieu of an oath

**Versicherung an Eides Statt / *Affirmation in lieu of an oath***

**gem. § 5 Abs. 5 der Promotionsordnung vom 18.06.2018 /  
according to § 5 (5) of the Doctoral Degree Rules and Regulations of 18 June, 2018**

Ich / I, Yiting Tseng,

(Vorname / First Name, Name / Name, Anschrift / Address, ggf. Matr.-Nr. / student ID no., if applicable)

versichere an Eides Statt durch meine Unterschrift, dass ich die vorliegende Dissertation selbständig und ohne fremde Hilfe angefertigt und alle Stellen, die ich wörtlich dem Sinne nach aus Veröffentlichungen entnommen habe, als solche kenntlich gemacht habe, mich auch keiner anderen als der angegebenen Literatur oder sonstiger Hilfsmittel bedient habe und die zu Prüfungszwecken beigelegte elektronische Version (PDF) der Dissertation mit der abgegebenen gedruckten Version identisch ist. / *With my signature I affirm in lieu of an oath that I prepared the submitted dissertation independently and without illicit assistance from third parties, that I appropriately referenced any text or content from other sources, that I used only literature and resources listed in the dissertation, and that the electronic (PDF) and printed versions of the dissertation are identical.*

Ich versichere an Eides Statt, dass ich die vorgenannten Angaben nach bestem Wissen und Gewissen gemacht habe und dass die Angaben der Wahrheit entsprechen und ich nichts verschwiegen habe. / *I affirm in lieu of an oath that the information provided herein to the best of my knowledge is true and complete.*

Die Strafbarkeit einer falschen eidesstattlichen Versicherung ist mir bekannt, namentlich die Strafandrohung gemäß § 156 StGB bis zu drei Jahren Freiheitsstrafe oder Geldstrafe bei vorsätzlicher Begehung der Tat bzw. gemäß § 161 Abs. 1 StGB bis zu einem Jahr Freiheitsstrafe oder Geldstrafe bei fahrlässiger Begehung. / *I am aware that a false affidavit is a criminal offence which is punishable by law in accordance with § 156 of the German Criminal Code (StGB) with up to three years imprisonment or a fine in case of intention, or in accordance with § 161 (1) of the German Criminal Code with up to one year imprisonment or a fine in case of negligence.*

**Bremen, 12.9.2022**

Ort / Place, Datum / Date

Unterschrift / Signature

---